Assessment of the applicability of reduced-order models to simulate corrosion processes and protection mechanisms

A Dissertation

Presented to

The Faculty of The School of Engineering and Applied Science

University of Virginia

In Partial Fulfillment

Of the Requirements for the Degree of

Doctor of Philosophy in Materials Science and Engineering

By

Carolina Moraes

May 2023

Abstract

Corrosion is a complex phenomenon that involves coupled electrochemical, chemical, and mass transport processes interacting with the complexities of material metallurgy and microstructure. The intricate interdependence between the variables and processes makes the prediction of corrosion damage very challenging. To gain knowledge about the underlying mechanisms, advanced characterization and electrochemical methods, and computational models are used. Experimental techniques and computational models can work synergistically to improve the fundamental understanding of corrosion processes. The use of reduced-order models for simulating potential, current density, and species distribution in an electrolyte are attractive due to the high computational costs required to solve the intricate set of highly nonlinear partial differential equations and boundary conditions characteristic of electrochemistry problems.

Aluminum alloys utilized in the aerospace industry are susceptible to localized corrosion due to their heterogeneous microstructure. In airframe components, these alloys are also susceptible to galvanic corrosion at joint locations, where the Al panels are joined together by fasteners made of dissimilar, more noble alloys. To protect these structures, organic coatings with inhibiting pigments are commonly used, such as Mg-rich primers. These primers can provide protection to Al alloys via galvanic and chemical mechanisms. The means and effectiveness of the protection mechanisms depend on a myriad of parameters; thus, a large volume of experimental work is necessary to unravel individual and synergistic effects between the variables, and the development of models that describe such mechanisms can be used to efficiently screen the large parameter space.

In this work, the applicability of reduced-order models in simulating complex interdependent mechanisms occurring in galvanic systems was tested. The work focused on developing computational models that simulate galvanic and chemical processes important for the corrosion and corrosion protection mechanisms of aerospace Al alloys. The impact of the governing equations utilized to describe the transport of ionic species in a galvanic cell was investigated. The Laplace, Nernst-Planck solved with the electroneutrality condition, and Nernst-Planck-Poisson equations were utilized to solve the potential, current density, and species spatiotemporal distributions in the electrolyte. In addition, a modified Laplace approach was developed, in which the mass and charge transport equations were partially decoupled; the Laplace equation was utilized to solve for charge conservation, while Nernst-Planck equations were utilized to solve for mass transport and calculate the electrolyte conductivity at each position and time-step. The importance of each term that describes the mass and charge transport in the electrolyte in varying supporting electrolyte concentrations was discussed. It was found that the reduced-order models saved substantial computational time without significant loss in accuracy for electrolyte concentrations typical of most environments of interest in corrosion and electrochemistry.

Reduced-order models were applied to model corrosion and corrosion protection mechanisms relevant to aerospace aluminum alloys. The applicability of the Laplace equation to model the galvanic coupling of aluminum alloy 7050 (AA7050) and stainless-steel type 316 (SS316) was assessed. The Scanning Vibrating Electrode Technique (SVET) was utilized to

measure the current density distribution across the Al alloy and the SS316 electrodes, and the measurements were compared with the calculated results. The validated finite element model was used to investigate the impact of the SVET experimental limitations in measuring the current density at the electrode/electrolyte interface.

The Laplace equation was complemented by the addition of the transport of minor species and homogeneous reactions in the electrolyte to model conditions in which the evolving electrolyte chemistry plays an important role in the corrosion behavior of an Al alloy. A comprehensive framework was developed to model the chemical and electrochemical mechanisms offered by Mg-based organic coatings. Chemistry-dependent boundary conditions were developed to simulate the change in the corrosion behavior of an aluminum alloy 2024 (AA2024) when exposed to a solution containing Mg-based pigments. The model predicted the change in the corrosion potential of AA2024 as a function of pH, water layer thickness, chloride concentration, and the inhibition of oxygen reduction reaction. The pH in the solution was calculated taking into account Mg dissolution, precipitation of $Mg(OH)_2$, $Al(OH)_3$ dissolution, and hydrolysis of Al^{3+} ions. The predicted critical pH at which the corrosion potential of AA2024-T351 sharply decreases to values below pitting and repassivation potentials under full immersion conditions was in accordance with experimental observations performed in varying sodium chloride concentrations. In higher sodium chloride concentrations, the critical pH decreases due to the reduced concentration of dissolved oxygen and the higher passive current density in higher sodium chloride concentrations.

In the study of the cathodic protection mechanism offered by Mg-rich primers, the galvanic coupling between the aluminum alloy 2024 and the Mg pigments was modeled as a function of coating resistance, water layer thickness, and electrolyte chemistry. The impact of the coating resistance on the galvanic coupling was also simulated experimentally by coupling the Al alloy and Mg electrodes and resistors of varying resistances via a zero resistance ammeter. Good agreement was found between the modeled and experimentally-determined coupled potential and current for all the resistances evaluated. Finally, the phenomenon of Al dissolution under cathodic polarization was modeled utilizing the developed pH-dependent electrochemical kinetics. The modeling results qualitatively agree with experimental data reported in the literature.

The comprehensive framework developed in this work was utilized to assess the parameter space. The impact of environmental and coating parameters on the corrosion and corrosion protection mechanisms of Al alloys was investigated. The conditions under which the protection mechanisms are hampered were highlighted and discussed. The robustness of reduced-order models was increased by the development of chemistry-dependent boundary conditions that were adaptive to changes in the electrolyte composition.

To my parents and sister, Gastão, Fatima, and Adriana, for their unconditional love and support.

Acknowledgments

I would like to sincerely thank my advisor, Professor Robert Kelly, for granting me the opportunity of being a part of his group and of pursuing a Ph.D. under his guidance. In addition to his brilliance, his pragmatism, kindness, and humbleness inspire me to be a better person, scientist, and engineer. I am profoundly grateful for your support that began even before I was your student.

I would also like to thank the members of my committee, Prof. John Scully, Prof. Jimmy Burns, Prof. Bicheng Zhou, and Prof. Jill Venton for their time, insightful comments, and advice.

The funding programs from the United States Air Force Academy and Navy Research Laboratory and their respective program managers, Dr. Gregory Shoales, and Dr. Christine Sanders, are gratefully acknowledged. I would also like to thank Dr. R.J. Santucci, who collaborated with this research in both funding programs.

I am grateful to the faculty, students, and staff of the Materials Science and Engineering department and the University of Virginia, for creating a great environment for learning and conducting research.

Additionally, I thank my fellow colleagues from the Kelly group and from the Center for Electrochemical Science and Engineering, Dr. Pedro Atz Dick, Dr. Rebecca Marshall, Dr. Gilbert Liu, Dr. Carol Glover, Dr. Utibe-Eno Charles-Granville, Dr. Ryan Katona, Dr. Sanjay Choudhary, and Armando Shehi for the companionship, help, and shared learning. Special thanks go to the undergraduate researcher, Emma Laubengayer, for her consistent hard work and help.

I wish to thank my colleague and father-in-law, Prof. Luis Frederico P. Dick, for his genuine interest and curiosity in my work, countless insightful discussions, and for sharing his passion for research, electrochemistry, and corrosion science.

I am especially grateful for my parents for providing me with all the means and guidance for me to succeed in my academic, professional, and personal life.

Finally, I would like to express my deepest gratitude to my loving husband, brilliant colleague, best friend, and love of my life, Pedro Atz Dick, for his unfailing support, and for being my inspiration in all spheres of my life.

Table of Contents

List of Tables

List of Figures

Chapter 1. Introduction

Corrosion is a complex phenomenon that involves coupled electrochemical, chemical, and mass transport processes interacting with the complexities of material metallurgy and microstructure. The intricate interdependence between the variables and processes makes the prediction of corrosion damage very challenging. Although corrosion damage can be measured with field and accelerated laboratory exposures, they are specific to the materials and environment in which the tests are performed. Additionally, they provide limited mechanistic insight into the processes governing the corrosion mechanisms, as it is very difficult to unravel the individual impact of the parameters that influence the corrosion processes. To gain knowledge about the underlying mechanisms, advanced characterization methods, electrochemical techniques, and computational models are used. Experimental techniques and computational models can work synergistically to improve the fundamental understanding of corrosion processes. Experimental techniques can be used to formulate and understand underlying mechanisms that govern a given corrosion process. Once an underlying mechanism is understood, computational models that describe the physicochemical phenomena that govern the corrosion processes can be used to further investigate the impact of a wide range of variables on the mechanisms of interest. At the same time, models can be used to better understand the limitations of experimental techniques. The work described herein focused on developing computational models in combination with experimental techniques to advance the understanding of selected processes important to the corrosion and protection of Al alloys applied in the aerospace industry.

1.1. Corrosion susceptibility of high-strength Al alloys in aircraft assemblies and corrosion protection methods

1.1.1. Corrosion of aerospace Al alloys

Aluminum and its alloys generally have good corrosion resistance in neutral aqueous solutions due to the instantaneous formation of a protective, non-conducting oxide film that protects the underlying metal from the environment and hinders cathodic charge-transfer electrochemical reactions [1]. The reactivity of Al is strongly correlated to the thermodynamic stability of the oxide/hydroxide film, which has an amphoteric nature [1,2]. In acidic environments, the oxide dissolves, forming the more stable, aqueous Al cationic species. In alkaline environments, the oxide /hydroxide film dissolves into aqueous aluminate species ($Al(OH)_4^-$). Additionally, aggressive species, such as Cl^-, induce local breakdown of the passive film, which leads to an accelerated dissolution at localized sites [3].

Precipitation-hardened aluminum alloys, such as AA2024 and AA7050, are the most utilized materials employed in aircraft structural components due to their high strength-to-weight ratio [4]. The high

strength offered by these materials arises from the intermetallic particles (IMPs) formed by the Al matrix and alloying elements, such as Cu, Zn, and Mg. Unfortunately, although this approach improves the mechanical properties of Al alloys, it is detrimental to their corrosion resistance. The presence of IMPs can induce localized corrosion, such as pitting, intergranular corrosion, and environmentally-assisted cracking [2,5]. The increased susceptibility to localized corrosion results from the different electrochemical properties of IMPs (e.g., standard potentials) and the Al matrix, which causes the development of microgalvanic interactions, leading to the corrosion of the IMP or the surrounding matrix [5–8].

The susceptibility to pitting corrosion can be assessed by a few parameters, such as pitting and repassivation potentials. The pitting potential is generally regarded as the potential above which the accelerated dissolution on the localized sites (pits) is stable, and pits can grow and propagate. The repassivation potential is the potential below which pits repassivate, and pitting corrosion is stifled. Between the pitting and repassivation potentials, pits can nucleate, but the propagation is not stable, and they can repassivate (metastable pits) [9]. If the corrosion potential (the potential at which the rate of cathodic and anodic reactions occurring on the metal are balanced) of a passive metal is below the repassivation potential, the metal is passive and not susceptible to pitting corrosion at the open-circuit potential. If the corrosion potential is above the repassivation potential but below the pitting potential, the metal is susceptible to metastable pitting. The corrosion of high-strength aluminum alloys, such as AA2024, is near the pitting potential in neutral, aerated chloride-containing solutions. Thus, at open-circuit potential, the alloy easily undergoes pitting corrosion.

Besides localized corrosion, the Al alloys present in airframe components are susceptible to additional corrosion processes. The airframe components are often constructed by joining Al alloys with the use of fasteners made of dissimilar alloys, such as stainless steel. Because stainless steel is more noble than the Al alloy, galvanic corrosion can occur when the alloys are in electrical contact and exposed to an electrolyte [10–13]. In addition, the susceptibility to localized corrosion is increased, as noble fasteners can polarize the Al alloy anodically, which can drive the potential to potentials above the pitting potential. At these joints, there is an additional susceptibility to corrosion. The tight gap formed by the fastener and the Al alloy plate can assist in the wicking of electrolyte. Due to the physical constriction in these locations, aggressive solutions, different from the bulk, can form and accelerate the corrosion attack [10,14,15]. The corrosion damage within the crevice formed by the fastener and the Al alloy can lead to stress corrosion cracking [16]. Thus, localized and galvanic corrosion are important corrosion processes occurring on aerospace Al alloys.

1.1.2. Corrosion protection methods applied to Al alloys

The high susceptibility to localized corrosion of the high-strength Al alloys requires the application of corrosion protection methods. The most common means of protecting these aircraft structures is the application of multilayered coating systems that can provide corrosion protection by a variety of mechanisms, such as barrier protection, active corrosion inhibition by the release of corrosion inhibitors, and sacrificial cathodic protection [17,18]. Traditionally, Al alloys have been protected against corrosion by chromate-based coating systems. However, hexavalent chromium is detrimental to human health, and environmental regulations require the substitution of chromate-based protection systems [19].

Mg-rich primers (MgRP) have emerged as one promising alternative to chromate-based coatings in the protection of Al substrates [20]. Mg-rich primers are a type of metal-rich sacrificial coatings, which are composed of metal pigments dispersed in an organic matrix. The Mg pigments are less noble than the Al substrate. Therefore, they can provide sacrificial cathodic protection when the pigments are in electrical contact with the substrate. In addition to reducing the corrosion reaction rate of the substrate, the polarization to potentials below critical threshold potentials protects the passive substrate from localized corrosion [21]. A challenge in utilizing cathodic protection methods in Al alloys is the amphoteric nature of the Al oxide/hydroxide protective layer. The cathodic reactions occurring at the Al surface ,when cathodically polarized, increase the local pH, which leads to the chemical dissolution of the protective oxide layer, a phenomenon referred to as cathodic corrosion [22]. Mixing of the active metallic pigments with the polymer resin can mediate the galvanic interactions by imposition of an ohmic resistance, limiting the extent of the cathodic polarization and retarding the depletion of the fast-dissolving Mg pigment [20,23] Additionally, metal-rich primers can provide protection by secondary mechanisms, such as chemical inhibition and barrier protection [20,24]. In MgRP/AA2024 systems, Mg^{2+} can provide cathodic inhibition by the precipitation of $Mg(OH)_2$ and $MgCO_3$ on the Cu-rich IMP, which can mitigate the deleterious interaction between the IMP and the less noble Al matrix [24–26]. Another mechanism of chemical inhibition is based on the influence of the Mg dissolution products on the local electrolyte pH that reduces the susceptibility to localized corrosion by lowering the corrosion potential of the Al alloy [24].

The distance over which a Mg pigment can cathodically polarize the substrate is termed the galvanic throwing power, and it is influenced by geometric, environmental, and coating proprieties [23,27]. The conditions in which chemical protection mechanisms can be provided will also depend on the local chemistry. The electrolyte composition and geometry significantly vary in atmospheric environments due to the small volume of solution that causes dramatic changes in the composition due to the accumulation of dissolved species and drying and wetting events driven by changes in the temperature and relative humidity in diurnal cycles [28].

The complex interplay between coating properties, alloy systems, the geometry of the component, and environmental variables makes it difficult to predict the corrosion of the substrate and coating performance. The design of an optimal coating system is challenged by the myriad of variables that influence corrosion and protection mechanisms.

1.2. Potential and current density distributions in a galvanic cell

Many of the processes important to the corrosion and protection mechanisms presented in the previous section involve the formation of a galvanic cell, in which there is a physical separation of anode and cathode. The separation of the anode and cathode happens when oxidation and reduction reactions are favorable in different locations on a conductive surface in the presence of an electrolyte. This can be caused by: (i) the electrical contact of conductive materials of different electrode potentials; (ii) differences in local chemistry in the solution that lead to differences in the electrochemical behavior. These processes are important to understand the accelerated damage of Al alloys near noble fasteners and the corrosion protection mechanisms provided by sacrificial anodes. The high dissolution rates observed in pits and crevices can be explained by a cascade of autocatalytic processes that occur due to the localized anodic reaction, consequent acidification due to the metal hydrolysis associated with the constricted transport, and migration of chloride ions to the anode [3,29–31].

While the electronic transport between the connected anode and cathode is fast, the ionic transport in the electrolyte is much slower. The (ionic) resistance in the electrolyte creates a potential gradient in the solution and limits the coupling between the anode and the cathode. **Figure 1.1** (a) shows a schematic drawing of a galvanic couple and respective Evans diagrams at different points in space. Near the point of contact between the anode and the cathode, the current path in the electrolyte is short. The potential established will be close to the mixed potential - the potential at which the line that describes the reduction kinetics at the cathode crosses the line that describes the oxidation kinetics at the anode. That is, the potential at which the sum of the cathode and anodic currents is zero. The coupling causes the cathode and anode to be polarized in different directions, away from their equilibrium potentials. This increases the driving force for both anodic and cathodic reactions, increasing the rate of the reactions (current density). The longer the distance between a point on the cathode and a point on the anode, the higher the total electrolyte resistance between them. The resistance in the solution decreases their polarization and the rate of the electrochemical reactions due to these ohmic losses in the electrolyte. Thus, in galvanic processes, there is a spatial distribution of the corrosion and reduction rates. The distributions depend on the kinetics of the anode and the cathode, the solution conductivity, and the geometry of the component.

Because what conducts current in the electrolyte is the transport of ions, the products of the electrochemical reactions will also impact the conductivity of the electrolyte, which in turn affects the rate

(and distributions) of the electrochemical reactions. In addition, the electrochemical kinetics can be a strong function of the local chemistry at the electrode/electrolyte interface. **Figure 1.1** (b) shows an example of the how the concentration of a species can significantly impact the rate of electrochemical reactions. The local chemistry is determined by the electrochemical reactions, homogeneous reactions in solution (e.g., precipitation), and mass transport. The interdependency of all these processes poses a significant challenge to the complete comprehension of corrosion mechanisms.

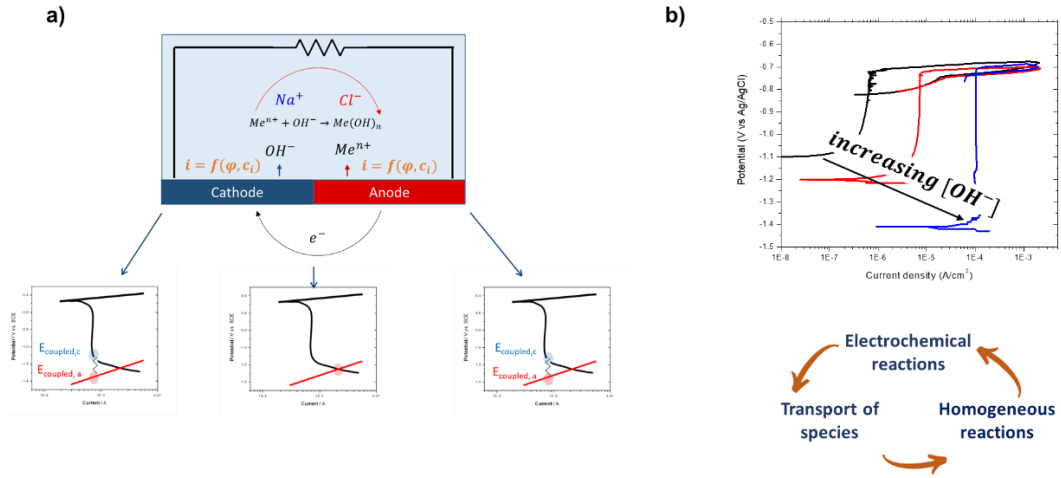

Figure 1.1. (a) Schematic drawing of the processes occurring in a galvanic cell; (b) example of the impact of the local chemistry on the electrochemical kinetics

The investigation of the potential, current density, and species distribution is crucial for the understanding of both deleterious galvanic corrosion and cathodic protection mechanisms, the protection mechanisms provided by inhibitors, and for the understanding of localized corrosion processes, such as pitting and crevice corrosion. The development of in-situ local electrochemical techniques, such as scanning vibrating electrode technique (SVET) [23,32–35], coupled multielectrode array technique (CMEA) [14,36–38], atomic emission spectroelectrochemistry (AESEC)[22,39–41] , which allows for the spatial and/or temporal resolution of local currents and chemical species, has greatly improved the understanding of corrosion processes. A review of these techniques, along with other important experimental techniques used in the corrosion field, can be read elsewhere [42–45].

Still, there are significant challenges in accurately predicting the corrosion damage of the materials in real-life service conditions and in the effective design of new corrosion protection methods. The small length scales in which localized corrosion events occur and the complex geometries of the actual structures undergoing corrosion damage pose a significant experimental challenge. The complex and dynamic electrolyte geometry and chemistry in atmospheric environments convolute the understanding of the impact of each environmental parameter, in addition to increasing the experimental difficulties related to measuring

the relevant variables in thin film environments. The myriad of coupled parameters that influence the local electrochemical conditions, which change with space and time, makes it challenging to understand the role of each parameter, or the synergistic impact of a combination of parameters.

The development of computational models that accurately describe chemical and physical processes involved in the corrosion and corrosion protection mechanisms can help understand the individual and combined effects of environmental, coating, and substrate parameters. Thus, significant efforts are being dedicated to the development of computational models that accurately describe phenomena important to corrosion processes [46–48]. The combination of advanced in-situ electrochemical techniques and computational models has deepened the understanding of complex corrosion mechanisms [49–52].

1.3. Finite element modeling applied to corrosion science

The complex interdependence and the spatiotemporal nature of the processes governing corrosion processes require the use of numerical methods to solve for the variables of importance. The most popular approach to calculating the spatiotemporal distributions of potential, current density, and solution composition is the Finite Element Method (FEM). FEM is a technique used to numerically solve sets of partial differential equations that describe various physical phenomena. The method is based on the discretization of the physical domain of interest into smaller, finite elements, in which the differential equations are more easily solved, and the variables of interest are approximated [53]. Iterations of the set of solutions continue until a solution applicable across the entire domain is achieved to within a certain tolerance. The advancement of computational power and the development of commercial software that offers robust solvers have allowed the development of increasingly complex models that solve the variables of interest for a wide range of conditions and geometries [53].

1.3.1.1. Governing equations

There are different governing equations that can be used to solve for potential, current density, and species distribution in an electrochemistry problem. The choice of the governing equation is dependent upon the degree of simplification desired. As discussed in the previous section, the conduction of current between an anode and a cathode in the electrolyte is governed by the transport of ionic species. Thus, the potential and current density distributions are solved by mass and charge conservation laws. Mass transport is governed by mass conservation:

$$\frac{\partial c_i}{\partial t} = -\nabla \cdot \mathbf{N}_i + R_i \quad (1)$$

where $\mathbf{N}_i$is the flux of the species i and R_i is the homogeneous production or consumption of species i. The flux of the ionic species in dilute solutions is given by the Nernst-Planck (NP) equations [54]:

$$\boldsymbol{N_i} = -D_i \nabla c_i - z_i u_i F c_i \nabla \varphi + c_i \mathbf{u} \tag{2}$$

where, D_i is the diffusivity of species i, $z_i$is the charge number of species i, $u_i$is the mobility of species i, c_i is the concentration of species i, φ is the electrostatic potential, and $\mathbf{u}$ is the fluid bulk velocity. The three terms are descriptions of the impact of diffusion, migration, and convection processes on the current.

The electrolyte current density is calculated by multiplying Faraday's constant by the summation of the flux of each ionic species multiplied by their respective charge number:

$$i_{electrolyte} = F \sum z_i \boldsymbol{N_i} \tag{3}$$

Because of potential gradient term in the NP equations, one more equation is needed to solve for mass conservation, as there are *i* equations (Equation 1), and *i*+1 variables (*i* species concentrations and φ). The means by which the electric field and charge conservation is solved dictates the different governing equations utilized in electrochemical problems.

There are mainly three options for governing equations: the Nernst-Planck-Poisson (**NPP**) equations, Nernst-Planck coupled with the electroneutrality condition **(NPE)**, and the Laplace (**Lk**) equation. The NPP approach is the most general description of the charge, and mass transport of species of an infinitely dilute electrolyte solutions [53,54]. In the **NPP** approach, charge conservation is solved by Poisson's equation (Equation 4), which relates the charge density in the electrolyte and the electric potential. The mass and charge conservation equations have to be coupled and solved simultaneously.

$$\nabla^2 \Phi = -\frac{\mathrm{F}}{\epsilon} \sum_i z_i c_i \tag{4}$$

where ϵ is the dieletric constant of the medium [54].

The Nernst-Planck-Poisson equations are difficult to solve because they are highly nonlinear and exhibit an extremely wide range of lengths and time scales [53]. The problem can be simplified if the electrolyte is assumed to be electroneutral which results in the Nernst-Planck with Electroneutrality (**NPE)** approach. The electroneutrality condition (Equation 5) is the additional equation required to solve for the charge and mass transport:

$$\sum_{\boldsymbol{i}} z_i c_i = 0 \tag{5}$$

The electroneutrality condition is not a fundamental law of nature but is an accurate approximation for length scales larger than the double layer (1-10 nm) [54]. Therefore, it is a reasonable approach to describe the bulk of a solution for most of the engineering problems related to corrosion processes. By assuming electroneutrality, the conservation of charge is implied in the conservation of mass. Multiplying Equation 1 by $z_i F$ and considering electrically-balanced homogeneous reactions yields:

$$\nabla \cdot \mathbf{i} = 0 \tag{6}$$

Inserting Equation 3 in Equation 6 yields Equation 7, as the convection term is nulled by the electroneutrality condition:

$$\nabla \cdot F \sum_{\boldsymbol{i}} z_i D_i \nabla \mathrm{c}_i + \nabla \cdot \nabla \Phi F^2 \sum_{\boldsymbol{i}} z_i^2 u_i c_i = 0 \tag{7}$$

Equation 7 shows that the potential and current density distributions are governed by diffusion (first term of the left side of Equation 7) and migration processes (second term of the left side of Equation 7). While the **NPE** approach alleviates some of the complexities of solving the Nernst-Planck-Poisson equations, it can still be highly nonlinear, especially with highly nonlinear electrochemical kinetics commonly observed and used as boundary conditions at the electrode/solution interface. In commercial software, such as COMSOL Multiphysics ®, the **NPE** method is solved by the method of elimination, in which a species of choice (the make-up ion), is removed from the conservation equations, and it is used to solve the electroneutrality condition. Besides not having a physics basis, it has been reported discrepancies between the potential, current density, and species distributions by the use of different make-up ions [55,56].

Equation 7 can be further reduced if the electrolyte is spatially- and temporally uniform, with negligible concentration gradients in the solution, which results in Equation 8:

$$\nabla \cdot \nabla \Phi F^2 \sum_{\boldsymbol{i}} z_i^2 u_i c_i = 0 \tag{8}$$

where the constant and uniform electrolyte conductivity, κ, is:

$$\kappa = \mathrm{F}^2 \sum_{\boldsymbol{i}} z_i^2 u_i c_i \tag{9}$$

and thus Equation 7 is reduced to the Laplace equation (Equation 9):

$$\nabla^2 \Phi = 0 \tag{10}$$

Under these conditions, the current density in the electrolyte can be reduced to Ohm's law (Equation 6);

$$\mathbf{i} = \kappa \nabla \Phi \tag{11}$$

The Laplace equation treats the electrolyte as an ohmic resistor and describes a linear relationship between current density and potential. The assumption of ohmic behavior is appropriate if the solution is well-mixed and there are negligible concentration gradients in the electrolyte. The Laplace equation is easier to solve; it requires much less computational power so that complex geometries can be built and solved with reasonable computational times.

The **NPP** and **NPE** provide information on the spatiotemporal distributions of the species concentration, potential, and current density. With the use of Laplace equation, only steady-state potential and current density profiles can be calculated, as the assumption of a uniform electrolyte is made. This assumption becomes incorrect for corrosion problems in which the electrolyte solution changes spatially and/or temporally. Besides the effects on the solution conductivity, the use of Laplace equation becomes problematic if the changes in the local chemistry have a signficiant impact on the electrochemical kinetics of the electrodes.

A way to approach this problem is to use the Laplace approach with the transport of minor species. If the electrolyte solution is considerably conductive and most current is carried by species that are not participating in the electrode reactions, then the transport of minor species can be calculated separately from the current and potential distributions using Fick's second law, and the current density and potential distributions can be calculated using Laplace equation. Even though minor species do not contribute to the current significantly, they can have a significant impact on the kinetics of the electrodes.

The development of commercially available software, such as COMSOL Multiphysics ®, has promoted the use of physics-based FEM models to solve research and industry-related problems in various fields of engineering. With the robust solvers developed, research can focus better on the development of the boundary conditions and the implications and limits of the governing equations. In electrochemistry, the computational costs associated with the highly nonlinear governing equations and boundary conditions can be prohibitively high, even with the use of supercomputers. Thus, the use of reduced-order models is attractive.

Despite the increased use in electrochemistry applications, little guidance has been given regarding what the costs in accuracy are with the various reduced-order approaches and how that accuracy may be affected by system variables such as electrolyte concentration. Guidance on the choice of the governing equations and methods to acquire adequate boundary conditions is needed in order to develop adequate models as the use of these finite element models becomes more accessible.

1.3.1.2. The boundary conditions at the electrode/electrolyte interface

In order to be solved, the differential equations that describe the electrolyte require boundary conditions for the behavior of an electrochemical system [54]. The boundary conditions at the

electrode/electrolyte interface describe the electrochemical behavior of the reactions occurring on them. If the rate of the electrochemical reaction is infinitely fast, then the electrode will be at its equilibrium potential, and its boundary condition is simply its equilibrium potential. For most cases, however, the rate of the electrochemical reaction is limited by charge transfer, diffusion of species, or both. In those cases, one needs to describe the relationship between the rate of the reaction (current density) as a function of the overpotential at the surface and/or concentration of species.

Accurately representing the electrochemical behavior of materials is one of the critical challenges in developing reliable and robust models. The boundary conditions are often described mathematically via Butler-Volmer or Tafel equations, for example, in cases where the parameters used to describe the equations can be found in the literature or fitted to experimental data obtained from potentiodynamic or potentiostatic techniques, experiments from which the relationship between current density and potential of an electrode can be obtained [54]. If the electrochemical behavior is more complex and cannot be described by common equations, the boundary conditions can be defined by the interpolation of experimental potentiodynamic polarization data performed on the material and solution of interest .

However, the polarization behavior is valid only for the conditions in which the experiment that generated it is performed. The electrochemical behavior of a material is affected by many variables, such as the local chemistry, microstructure, and environmental conditions [26,57–60]. For alloys that have a heterogeneous microstructure, such as the aerospace Al alloys, the polarization behavior will also be dictated by the IMPs and their area relative to the matrix [61]. For reactions that are controlled by charge transfer and diffusion of reactant species, the transport of such species in the electrolyte will dictate the rate of the reactions. Oxygen reduction reaction (ORR), for example, is an important cathodic reaction that controls the corrosion rate and current density distributions in many systems. In many alloys, it is controlled by the diffusion of O_2 in the electrolyte. The ORR rate will change depending on the solubility and diffusivity of O_2 in the solution and also on the thickness of the electrolyte if the electrolyte thickness is within the O_2 diffusional boundary layer thickness, which is usually the case in atmospheric corrosion problems [60,62,63]. Thus, for processes in which one or more of these conditions change over time, the initial boundary conditions might become incorrect. Additionally, the local chemical conditions are not always known. For example, it is difficult to determine what are the local conditions at pits and crevices due to their small length scales.

1.3.1.3. Applications of FEM in the study of corrosion mechanisms relevant to Al alloys

FEM has been largely applied in the study of corrosion processes relevant to corrosion and corrosion protection methods. In the study of localized corrosion, Nernst-Planck equations have been used to simulate chemical conditions in localized corrosion processes in Al alloys [64–68]. The studies focused

on calculating the potential, current density, and pH distributions in the localized sites. Guseva, et al. [65] modeled the transient chemistry during the initial stage of localized corrosion in Al alloys considering various homogeneous reactions. Using non-equilibrium expressions in the reaction rates, the authors showed that steady-state conditions were not reached depending on the species, suggesting that steady-state approximations can give inaccurate values for species concentrations.

Murer et al. [69] utilized modeling and experimental approaches to study the current density distributions between Al and Al%4Cu couple to gain insights on the local conditions which lead to microgalvanic corrosion mechanisms occuring in Al-Cu alloys. The authors discussed the differences in modeling results obtained depending on the method utilized to determine the boundary conditions at the Al electrode. Voltammetry performed via a microcapillary electrochemical cell differed significantly from the results obtained using polarization curves obtained in a large-scale cell. They highlighted the challenges associated with determining appropriate Al dissolution rates and the need to describe those as a function of solution chemistry. Yin et al. [67,70,71] developed a comprehensive model describing multiple processes occurring as a result of the microgalvnic coupling in Al alloys. The model took into consideration the impact of the chemistry of the electrolyte on the electrochemical reactions, the effect of the Al dissolution on the geometry, and the deposition of corrosion products and their blocking effect on the electrochemical reactions. The chemistry-dependent boundary conditions describing the influence of pH and O_2 concentration on the Al dissolution were obtained using an interpolation surface (relating 3 variables) and volume (relating 4 variables) extracted from polarization curves obtained in different conditions. The authors were able to describe the interdependence between geometrical, chemical, and electrochemical factors and their impact on the mechanisms of microgalvanic corrosion. Although the authors creatively approached the challenge of the interdependence between local chemical conditions and electrochemical reactions, the use of linear interpolation to create the boundary condition surface and volume can lead to approximation errors.

In the study of galvanic corrosion and galvanic protection provided by sacrificial anodes, both Laplace [62,72–77] and Nernst-Planck with electroneutrality [78–82] approaches have been utilized. King et al. [74] utilized a Laplacian approach to calculate the potential and current density distribution of Mg coupled to AA2024 in different water layer thicknesses and solution concentrations, using experimental polarization curves obtained in quiescent electrolyte solutions with varying chloride concentrations as boundary conditions. The effect of electrolyte concentration, water layer thickness, and film resistance over Mg on the galvanic throwing power of Mg was investigated. The magnitude and distribution of cathodic and anodic current densities predicted by the model were in accordance with experimental measurements [83]. However, the model did not account for the impact of the water layer thickness on the cathodic behavior of AA2024 and for evolving electrolyte chemistry in the electrolyte due to the corrosion reactions.

It has been observed that the change in the electrolyte chemistry due to Mg dissolution can change the corrosion behavior of AA2024, and it is an important aspect of the protection mechanisms provided by the primer [24].

Thébault et al. [49,84] utilized various local electrochemical techniques and FEM modeling to investigate the protection mechanisms provided by zinc to a steel sheet in the case of cut-edge corrosion. The comparison between current density distributions obtained by SVET and by FEM, utilizing both Laplace and Nernst-Planck approaches, yielded an interesting result: although more rigorous, the Nernst-Planck approach provided more discrepant distributions., and the simplified Laplace solution was in better agreement with the experimental data. The authors suggested that the convection caused by the movement of the SVET microelectrode probe homogenized the solution, decreasing the concentration gradients. By the use of Nernst-Planck equations with the electroneutrality condition, however, they were able to solve for the species distribution over the cut-edge. They calculated the pH distribution of the solution, taking into account the heterogeneous and homogenous reactions occurring at the electrode surface and in the bulk electrolyte, and compared them with in-situ pH measurements. The pH profile matched the experimental data only when the boundary conditions over the steel were adapted in accordance with "post" experimental observations.

In the study of atmospheric corrosion, Liu et al. [62] developed a Laplace model to investigate the effect of the electrolyte layer thickness on the galvanic coupling between stainless-steel type 316L (SS316) and AA7050. In the model, the effect of the faster ORR kinetics in the thin film environment is taken into account. The relationship between the ORR diffusion-limited current density and the diffusion boundary layer thickness was obtained by performing cathodic polarization scans on SS316 using the rotating disk electrode technique and the Levich equation. The FEM study showed that, in sufficiently thin films, the ohmic resistance in the solution dominated the galvanic coupling current.

In more realistic scenarios, the electrolyte film thickness, composition, and conductivity are dynamic due to wetting and drying events. As both the film thickness and the electrolyte composition can affect the ORR kinetics [85], an accurate description of the boundary conditions requires an enormous amount of experimental work. The use of interpolated experimental potentiodynamic polarization data would also complicate the simulation of the dynamic behavior of the electrolyte, as a large interpolation set of polarization scans would be required.

1.4. Scope of the research

The overarching research question of this dissertation is to what extent and under what circumstances it is possible to accurately describe corrosion processes and their transients by using reduced-order model approaches, in which the current density and potential distributions are decoupled from the transport of species in the electrolyte, thus reducing the nonlinearity and computational demand of Nernst-Planck-Poisson and Nernst-Planck coupled with electroneutrality condition. The applicability of the reduced-order approaches to the development of adaptive boundary conditions used to describe transients of selected corrosion mechanisms is also evaluated. The models developed were applied to investigate the impact of environmental, geometric, and materials variables on mechanisms that describe the corrosion and protection of aerospace Al alloys.

The work is divided into six chapters. In Chapter 2, the accuracy of reduced-order models is assessed by the comparison between the potential, current density, and species distributions in a galvanic cell obtained with the use of different governing equations of varying levels of simplification. A simplified method that takes into account the local variations in the electrolyte chemistry, without the need to use NPP or NPE methods, is proposed. The trade-offs between computational power demands and model accuracy are discussed, and the conditions under which the most simplified equation can be used to model the charge and mass transport are suggested. The work is based on two publications submitted to *Electrochimica Acta*, currently under review.

In Chapter 3, the Laplace equation is utilized to model the current density distribution between an AA7050 and SS316. The modeling results are compared with SVET measurements. The limitations of both the modeling approach and SVET techniques are discussed. The results corroborate with the findings of Chapter 2 and indicate that the simplifications used to describe the electrochemical reactions occurring at the electrodes (boundary conditions) have a larger impact on the calculations in comparison to the simplification of the governing equations. The work is based on a paper published in the *Journal of the Electrochemical Society* [86].

In Chapter 4, a comprehensive framework that simulates chemical and electrochemical protection mechanisms provided by Mg-based coatings is developed. Chemistry-dependent boundary conditions are developed by empirical abstractions to describe the dependence of the Al anodic dissolution on pH. The electrolyte chemistry transient as a result of the electrochemical reactions occurring on the Al alloy and on Mg is simulated. The work is based on a paper published in the *Journal of the Electrochemical Society* [87]

In Chapter 5, the applicability of the developed framework is tested over different parameters. In Part I, the chemistry-dependent boundary conditions are expanded to include the impact of Cl^- concentration. In Part II, the impact of an ohmic resistance of known value between the AA2024 and Mg electrical connection on the galvanic potential and currents is verified by a modeling and experimental

approach. In Part III. the applicability of the pH-dependent anodic kinetics to simulate the Al dissolution under cathodic polarization is verified by comparison between model results and data available from the literature. In Chapter 6, a summary of the main findings and recommendations of future work are presented.

Chapter 2. A Comparison of FEM Results from the Use of Different Governing Equations in a Galvanic Cell

General introduction

The use of reduced-order models for simulating potential, current density, and species distribution in an electrolyte are attractive due to the high computational costs required to solve the intricate set of highly nonlinear partial differential equations and boundary conditions characteristic of electrochemistry problems. Although the use of finite element models has been increasingly popular by the easier access to robust solvers available on commercial software, a thorough investigation on the impacts of the available methods for solving potential, current density, and distribution has not been reported. As such, the accuracy of reduced-order models is assessed by the comparison between the potential, current density, and species distributions in a galvanic cell obtained with the use of different governing equations of varying levels of simplification. A simplified, pseudo-Laplace method that takes into account the local variations in the electrolyte chemistry is developed. The impact of the concentration of inert ionic species (NaCl) on the accuracy of the reduced-order model approaches is assessed. The concentration of the NaCl was varied from 0.1 to 1000 mM and the results were compared. The following hypotheses were tested: (i) in solutions of importance to most corrosion problems, the loss in accuracy in the calculations of potential, current density, and species distributions is small due to the relatively high ratio between the inert and the electrochemically active species; (ii) if the electrolyte conductivity spatiotemporal evolution is taken into account, the Laplace approach can provide good answers even in low inert to electrochemically active species ratio.

The chapter is organized in two parts. In Part I, the analysis was performed in the NaCl concentration range relevant to most corrosion problems. In Part II, analysis is extended to lower concentrations of supporting electrolyte. The work is based on two publications submitted to *Electrochimica Acta*, currently under review. The results are presented in the form in which the publications were submitted.

2.1. A Comparison of FEM Results from the Use of Different Governing Equations in a Galvanic Cell

Part I In the Presence of a Supporting Electrolyte

C. V. Moraes[a] and R. G. Kelly[a]

[a] Center for Electrochemical Science and Engineering, Department of Materials Science and Engineering, University of Virginia, Charlottesville, VA 22904, USA

Corresponding author: rgk6y@virginia.edu

2.2. Abstract

The use of reduced-order models for simulating potential, current density, and species distribution in an electrolyte are attractive due to the high computational costs required to solve the intricate set of highly nonlinear partial differential equations and boundary conditions characteristic of electrochemistry problems. The loss in accuracy of the reduced-order models is assessed in this work by the comparison of the results obtained by these reduced-order models to those obtained by the most general model of an infinitely dilute solution. The models were performed using the governing equations available on COMSOL Multiphysics®. For electrolyte concentrations typical of most environments of interest in corrosion and electrochemistry, the reduced-order models saved substantial computational time without significant loss in accuracy.

Keywords: Modeling, Nernst-Planck equation, Laplace equation, Finite element method, Galvanic cell

2.3. Introduction

The accelerated development of computational power and commercial software that efficiently solves increasingly complex partial differential equations (PDE) disseminate the use of physics-based models to approach research and industry-related problems. This advancement has greatly benefited the fields of corrosion science and battery development due to the intricate set of PDE and nonlinear boundary conditions necessary to solve electrochemical problems. With the robust solvers developed, research can focus better on the development of the boundary conditions and the implications and limits of the governing equations. Guidance on the choice of the governing equations and methods to acquire adequate boundary conditions is needed in order to develop adequate models as the use of these finite element models becomes more accessible.

In systems in which there is a separation of anode and cathode, such as those occurring in galvanic corrosion, localized corrosion, batteries, and fuel cells, current density and potential distributions are established in the electrolyte. The conditions are governed by the transport of reactant species to or from

the electrode surface, ohmic potential drop in the solution, or charge-transfer electrochemical kinetics at the metal/solution interface. Charge-transfer-controlled electrochemical kinetics can be a strong function of the local chemistry at the interface. The local chemistry is determined by the electrochemical reactions, homogeneous reactions in solution (e.g., precipitation), and mass transport. Coupling all these processes together leads to a deeper understanding of the controlling processes and can inform the design of corrosion protection schemes or power sources.

The most popular approach to calculating the spatiotemporal distributions of potential, current density and solution composition is the Finite Element Method (FEM) [88]. In the corrosion science field, the method has been applied to study, for example, galvanic corrosion [69,72,73,84,86,89–92], atmospheric corrosion [62,93,94], localized corrosion [64,65,67,80,94–101], and corrosion protection mechanisms [49,74,76,87,102]. Reviews are available [46,48,53,88,103–105], but in short, the FEM applied to electrochemical systems divides the solution volume of interest into a set of interconnected elements. The method involves computationally solving the governing differential equations of interest at each node connecting the elements in a self-consistent manner. The boundary conditions at the electrode/electrolyte interface boundaries are the electrochemical kinetics of the interfacial reactions of interest. Homogeneous reactions occurring in the electrolyte can also be included. The selection of the governing equations used determines not only what characteristics of the system are considered but also what parameters can be determined. More accurate governing equations generally require more computational power, to the point that some systems of interest cannot be managed with conventional computational resources.

Reduced-order governing equations, while not as rigorous, can provide important insights into desired parameters at a greatly reduced computational cost [62,74,76,106,107]. However, each level of simplification brings with it trade-offs in accuracy that should be understood before the selection of the governing equations. In many cases, the loss of accuracy is trivial, being far less than the uncertainty in the electrochemical kinetics, for example.

2.3.1. Governing equations for solving potential, current density, and species concentration in the electrolyte

The conduction of current in the electrolyte is the transport of the charged species. Thus, mass transport laws in the electrolyte are required to solve for the potential and current density. Mass transport is governed by mass conservation:

$$\frac{\partial c_i}{\partial t} = -\nabla \cdot \mathbf{N}_i + R_i \tag{1}$$

where $\mathbf{N}_i$is the flux of the species i and R_i is the homogeneous production or consumption of species i. The flux of the ionic species in dilute solutions is given by the Nernst-Planck equation:

$$\boldsymbol{N_i} = -D_i \nabla c_i - z_i u_i F c_i \nabla \varphi + c_i \mathbf{u} \quad (2)$$

where, D_i is the diffusivity of species i, $z_i$is the charge number of species i, $u_i$is the mobility of species i, c_i is the concentration of species i, φ is the electrostatic potential, and **u** is the fluid bulk velocity. The three terms are descriptions of the impact of diffusion, migration, and convection processes on the current.

The electrolyte current density is calculated by multiplying Faraday's constant by the summation of the flux of each ionic species multiplied by their respective charge number:

$$i_{electrolyte} = F \sum z_i \boldsymbol{N_i} \quad (3)$$

For *i* species, Equation 2 generates *i* equations. However, due to the need to calculate potential in the migration term, one more equation is needed to solve for mass conservation, as there are *i* equations (Equation 1), and *i*+1 variables (*i* species concentrations and φ). The means by which the electric field is solved dictates the different governing equations utilized in electrochemical problems. There are mainly three governing equations: the Nernst-Planck-Poisson equations, Nernst-Planck coupled with the electroneutrality condition, and the Laplace equation. The Nernst-Planck-Poisson approach is the most general description of the charge and mass transport of species of an infinitely dilute electrolyte solution. It uses the set of Nernst-Planck equations (Equation (2)) to solve for the transport of species, along with the mass conservation (Equation (1)), and Poisson's equation to solve for the potential field [53,54]. The Poisson's equation relates the charge density to the electric potential [54]. For a medium of uniform dielectric constant, the Poisson equation can be described by:

$$\nabla^2 \Phi = -\frac{\mathrm{F}}{\epsilon} \sum_i z_i c_i \quad (4)$$

The Nernst-Planck-Poisson equations are difficult to solve because they are highly nonlinear and exhibit a wide range of lengths and time scales. The large value of the proportionality constant $\frac{\mathrm{F}}{\epsilon}$ (1.4 x 10^{16} V□cm for a relative dielectric constant of water) implies that any small deviation from electroneutrality yields large electric forces [54]. Thus, any initial charge density can be very rapidly neutralized through migration on a timescale much smaller than the sluggish diffusion. Unfortunately, that speed requires the computational engine to use very small time steps, which greatly lengthens computation time.

The most utilized approach to circumvent the need of solving the Poisson equation coupled with Nernst-Planck equations is by assuming that the electrolyte is electroneutral:

$$\sum_i z_i c_i = 0 \quad (5)$$

Although the electroneutrality condition is not a fundamental law of nature, it is an accurate approximation for length scales larger than the double layer (1-10 nm) [54]. Therefore, it is a reasonable

approach to describe the bulk of a solution for most of the engineering problems related to corrosion processes. Equation 5 provides the additional equation to the set of Nernst-Planck equations necessary to solve for the electric field.

The conservation of charge is implied in the conservation of mass when assuming the electroneutrality condition [54]. Multiplying Equation 1 by $z_i F$ and considering electroneutrality for electrically balanced homogeneous reactions yields:

$$\nabla \cdot \mathbf{i} = 0 \tag{6}$$

Inserting Equation 3 in Equation 6 yields:

$$\nabla \cdot F \sum_{i} z_i D_i \nabla \mathrm{c}_i + \nabla \cdot \nabla \Phi F^2 \sum_{i} z_i^2 u_i c_i = 0 \tag{7}$$

as the convection term is nulled by the electroneutrality assumption.

In the absence of concentration gradients and in a uniform electrolyte composition, Equation 7 reduces to the **Laplace** equation:

$$\nabla^2 \Phi = 0 \tag{8}$$

Under these conditions, the current density in the electrolyte can be described to Ohm's law (Equation 6);

$$\mathbf{i} = \kappa \nabla \Phi \tag{9}$$

where κ is the electrolyte conductivity and is expressed by Equation 10:

$$\kappa = \mathrm{F}^2 \sum_{i} z_i^2 u_i c_i \tag{10}$$

The Laplace equation is easier to solve; it requires much less computational power so that complex geometries can be built and solved in very reasonable computational times. However, the Laplace Equation is steady state; in its original form, no time dependence can be calculated for any of the variables. Thus, any evolution of chemical composition as a result of homogeneous reactions involving the products of the electrochemical reactions is outside the reach of the original equation.

2.3.2. The boundary conditions at the electrode/electrolyte interface

To fully describe the electrochemical problem, the kinetics of the electrochemical reactions occurring at the electrodes must be defined as the boundary conditions of the problem, which are often nonlinear. The electrochemical kinetics can often be described by the Butler-Volmer equation:

$$i = i_0 \left[\exp\left(\frac{\alpha_a F \eta}{RT}\right) - \exp\left(\frac{-\alpha_c F \eta}{RT}\right)\right] \tag{11}$$

where i_0 is the exchange current density, α_a is the anodic charge transfer coefficient, α_c is the cathodic charge-transfer coefficient, η is the overpotential, R is the universal gas constant, and T is the absolute temperature.

The nonlinearity of the boundary conditions further complicates the problem. In addition, the current density at a given point will be dependent on the overpotential and/or on the composition of the solution. The overpotential will depend on the ohmic drop in the solution and on the polarization behavior of the anode and the cathode. At the same time, the ohmic drop in the solution can also depend on the solution composition.

2.3.3. Advantages and disadvantages of different governing equations

Before discussing the possible advantages and disadvantages of the different governing equations, a general description of their implementation will inform the discussion. The Nernst-Planck-Poisson equations provide a description of the transients of potential, current densities, and species concentration distributions. This approach requires solutions of highly nonlinear sets of equations, especially with nonlinear electrochemical kinetics, such as those described by Butler-Volmer equations, are used as boundary conditions at the electrode/solution interface. Replacing the Poisson equation with electroneutrality eases the computational load.

A common solution method applied to solve the electroneutrality condition is called the equation elimination method. In this method, an ion of choice, the "make-up" ion, is removed from the mass conservation equations, and then it is used to solve for the electroneutrality condition, from which its concentration is retrieved. In COMSOL Multiphysics (v. 6.1), for example, the equation elimination method is used to solve for the electroneutrality [56,108]. One can choose any of the species present in the model as the make-up ion, or one can use the "Water-based with electroneutrality" option, in which the electroneutrality is solved by H^+ and OH^- species coupled with the water auto-ionization equilibrium condition. One of the disadvantages of this method is that one cannot use an ion that is directly involved in any homogeneous or electrochemical reactions; its concentration has to be solely used to solve the electroneutrality condition. Thus, the choice of the make-up ion might be limited depending on the system that is being modeled. Additionally, a few studies have reported discrepancies in results when choosing different make-up ions [56,88].

The Laplace equation treats the electrolyte as an ohmic resistor and describes a linear relationship between current density and potential, reducing the nonlinearity of the model. The assumption of ohmic behavior is appropriate if the solution is well-mixed and there are negligible concentration gradients in the electrolyte. This assumption becomes limiting for corrosion problems where the electrolyte solution changes, especially when local electrolyte chemistry has a significant impact on the electrochemical kinetics of the materials of interest. One means of modifying the Laplace equation to make it more amenable to important problems is to take advantage of the supporting electrolyte effect, where appropriate, using a method referred to as the Laplace approach with the transport of minor species. If the electrolyte solution

is considerably conductive and most current is carried by species that are not participating in the electrode reactions, then the transport of minor species can be calculated separately from the current and potential distributions using Fick's second law, and the current density and potential distributions can be calculated using Laplace equation [54]. Even though the contribution of the minor species to the current might be negligible, they can have a significant impact on the electrochemical kinetics.

Yet if there are compositional changes with time and/or space, the assumption of a constant electrolyte conductivity is no longer valid, and the Laplace equation is not suitable. Fu and Chan [97] expanded the Laplace approach to circumvent this limitation without solving for the Nernst-Planck and charge conservation equations simultaneously by implementing a sub-routine to their computations. In the first time step, electrolyte chemistry was assumed uniform, and the initial potential distribution was calculated using the Laplace equation by assigning a uniform conductivity to each element. The potential distribution calculated in this initial step was used to calculate the ionic flux for every species at each element. Then, the new concentrations were used to calculate the electrolyte conductivity at each element, which was then used in the following time step to calculate the new potential distribution using the Laplace equation. The calculations of the flux of each species included a term to account for the diffusion potential caused by the concentration gradient. The diffusion potential is a driving force that ensures electroneutrality in the diffusion processes of ionic species.

Understanding the conditions in which the assumptions made to reduce the complexity of the models are valid is important to ensure the accuracy of the solutions obtained by the reduced-order models. However, few guidelines have been given regarding what the costs in accuracy are with the various reduced-order approaches and how that accuracy may be affected by system variables such as electrolyte concentration. As such, the objective of this work is to assess the accuracy of the reduced-order methods by comparing the potential, current density, and species distributions obtained by these reduced-order methods with those obtained by the most general equation. The governing equations for solving electrochemical systems available on commercial software (COMSOL Multiphysics, v. 6.1) are compared for a range of supporting electrolyte concentrations. The two methods for solving the coupled mass and charge conservation equations are used – the Nernst-Planck-Poisson (**NPP**) and the Nernst-Planck solved by the electroneutrality condition (**NPE**). In addition, two methods that solve mass and charge conservation *separately* are used. In these methods, the Laplace equation is used to solve for the charge conservation, decoupled from mass conservation equations. The transport of the ionic species is solved using Nernst-Planck equations, in which the potential term is retrieved from the results of the Laplace equation. The difference between these two simplified methods is the treatment of the electrolyte conductivity. In the most simplified method, the electrolyte conductivity is assumed to be spatially and temporally uniform (**Lk**). In the second method, referred to as **Lvk**, the spatial and temporal variations in the electrolyte

conductivity will be taken into account. As performed by Fu and Chan [97], the Laplace equation will be used to solve for the potential and current density distribution. The potential term calculated with the Laplace equation will then be used to solve for the species transport using Nernst-Planck equations. Then, the electrolyte conductivity will be calculated at each time step using Equation 10. In this way, the changes in the electrolyte composition due to the electrochemical reactions and homogeneous reactions occurring in the electrolyte will impact the local and temporal solution conductivity. However, the contribution of the diffusion potential term on the species and potential distribution will be neglected, and the error associated with this simplification will be calculated. Note that, using this method, the conductivity throughout the geometry is not constant, invalidating the Laplace equation. However, at each element and time step, the conductivity is constant. Hence, the Laplace equation is valid for each element.

The potential, current density, and species distributions in the electrolyte obtained by the **NPP**, **NPE**, **Lvk**, and **Lk** approaches will be compared, and the implications of separating mass and charge transfer equations in the electrolyte for a galvanic system will be investigated. The results presented herein were calculated for a specific system and geometry, and the conclusions regarding the accuracy of the simplified methods are system-specific.

2.4. Model description

The different governing equations were used to calculate the potential, current density, and species distributions resulting from the galvanic coupling of two metals in a simple, 2D geometry. The concentration of the supporting electrolyte, NaCl, was varied. The model was originally developed to investigate the galvanic coupling of an Al alloy and Mg for the study of protection mechanisms provided by Mg-rich primers [87]. As such, the geometry represented a cross-section of a scratch on a coated panel, exposing the bare Al in contact with the Mg particles present in a 20 μm-thick primer to a quiescent electrolyte. **Figure 2.1** (a) shows the geometry used in the work. The 10-mm scribe is centered in the geometry and lies within the two 5 mm portions of the MgRP-coated panel. At the scribe, hydrogen evolution reaction (HER) occurs. At the coating and the cut edges, anodic dissolution of Mg occurs. The geometry has also been used to model galvanic processes between Zn and Fe occurring in galvanized steels [84,92].

2.4.1. Governing equations

COMSOL Multiphysics (v. 6.1) was used to solve the partial differential equations. The Nernst-Planck-Poisson (**NPP)** and the (**NPE**) methods were solved using the Tertiary Current Distribution module. The charge conservation was solved using either the Poisson equation (**NPP**) (Equation 4) or the

electroneutrality condition (Equation 5) with the method of elimination (**NPE**). Na^+ was used as the make-up ion unless otherwise noted.

The Laplace (**Lk**) and pseudo-Laplace (**Lvk**) methods were solved by coupling the Secondary Current Distribution and the Transport of Diluted Species. The potential and current density distributions were calculated using the Laplace equation. The Transport of Diluted Species module was used to solve for mass conservation and transport using Nernst-Planck equations, where the potential gradient term was retrieved from the Secondary Current Distribution module. The local current densities at the electrodes were used in the Transport of Diluted Species interface to calculate the production of the electrochemically active species (Mg^{2+} and OH^-) at the electrodes through Faraday's law. In the **Lk** approach, the electrolyte conductivity was constant and given by the concentration of the supporting electrolyte – essentially, the electrolyte conductivity at t = 0 s.

In the **Lvk** approach, a conductivity variable was introduced. The electrolyte conductivity was calculated at each time step and position according to Equation 10, where c_i and u_i were calculated by the Transport of Diluted Species module. The mobility was calculated using the Nernst-Einstein relation (Equation 12):

$$u_i = \frac{D_i}{RT} \tag{12}$$

Using the **NPP** and **NPE** methods, charge and mass conservation equations were solved simultaneously, but different equations were used to solve charge conservation. In the **Lk** and **Lvk** approaches, the model does not treat the ionic species as charges to solve the charge conservation equation, so mass and charge conservation equations are decoupled in the aspect of charge conservation. The transport of species is coupled with Laplace, as the potential in the electrolyte is used in the migration term, and the current density at the electrodes is used to calculate the production of the ionic species. In the **Lvk** case, the Laplace equation is also coupled with the mass transport equations, as the concentrations and mobility terms are used to calculate the local electrolyte conductivity.

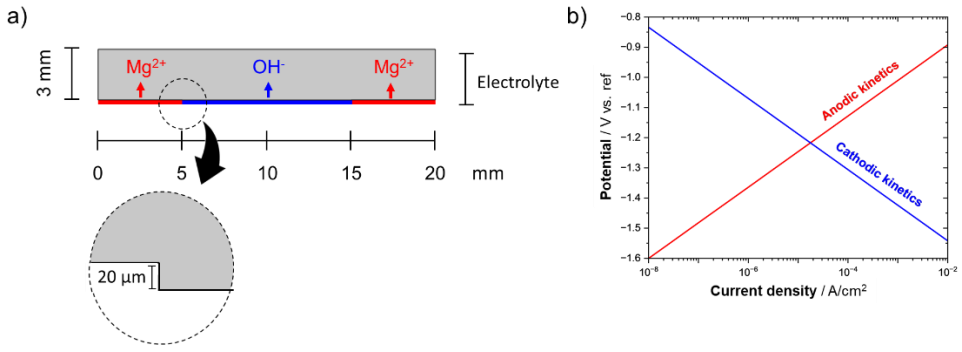

Figure 2.1. (a) Geometry utilized in the model; (b) Boundary conditions at the electrode/electrolyte interface: Tafel kinetics are used to describe the electrochemical behavior of the anode and cathode.

The model solved for the concentration of five species: Mg^{2+}, OH^-, H^+, Na^+, and Cl^-. The species diffusivities were acquired utilizing OLI Studios (v. 11), calculated for [NaCl] = 0.1 M at 25 ˚C and 1 atm. The diffusivities are shown in **Table 2.1.**

The model is developed under the following assumptions of quiescent electrolyte: that is, there is no forced or natural convection (the electrolyte layer is thinner than the diffusion layer), and infinite dilution: there is no interaction between the ions, apart from that necessary to maintain electroneutrality (in the **NPP** and **NPE** approaches).

Table 2.1. Parameters utilized in the model.

Parameter	Parameter description	Value	Reference
$\mathbf{D_{Na^+}}$	Diffusion coefficient of Na^+	1.18×10^{-9} m^2/s	OLI Studios (v. 11)
$\mathbf{D_{Cl^-}}$	Diffusion coefficient of Cl^-	1.75×10^{-9} m^2/s	OLI Studios (v. 11)
$\mathbf{D_{H^+}}$	Diffusion coefficient of H^+	9.30×10^{-9} m^2/s	OLI Studios (v. 11)
$\mathbf{D_{OH^-}}$	Diffusion coefficient of OH^-	5.22×10^{-9} m^2/s	OLI Studios (v. 11)
$\mathbf{D_{Mg^{2+}}}$	Diffusion coefficient of Mg^{2+}	0.72×10^{-9} m^2/s	OLI Studios (v. 11)
$\boldsymbol{i_0}$	Exchange current density of the anodic and cathodic reaction	10^{-8} A/cm^2	Arbitrarily chosen
$\mathbf{E_{0,\ cathodic}}$	Reversible potential of the cathodic reaction	-0.346 V vs. ref	Arbitrarily chosen
$\mathbf{E_{0,\ anodic}}$	Reversible potential of anodic reaction	-1.60 V vs. ref	Arbitrarily chosen
B	Tafel slope of the anodic and cathodic dissolution	-118 mV	Arbitrarily chosen
k	Sink term reaction rate constant	3.7 $m^6/(s \cdot mol^2)$	[87]
$\mathbf{k_{sp,\ app}}$	Apparent solubility product of $Mg(OH)_2$	4.12×10^{-12} mol^3/dm^9	OLI Studios (v. 11)

2.4.2. Boundary conditions

The electrochemical reactions occurring at the anode and cathode boundaries were described using charge transfer kinetics according to Equation 13:

$$i = i_o 10^{\frac{(E-E_0)}{B}} \tag{13}$$

where i_o is the exchange current density, E is the local potential at the electrode, E_0 is the reversible potential, and B is the pseudo-Tafel slope of the electrochemical reactions.

The kinetic parameters were arbitrarily chosen, and the anodic and cathodic reactions had equivalent kinetics, i.e., the pseudo-Tafel and exchange current density were equal. Thus, even though we reference the reactions as Mg anodic dissolution and HER, the parameters chosen for their kinetics were not completely based on the actual kinetics of these reactions in the conditions in which the model is performed. **Figure 2.1** (b) shows the kinetics of the cathode and anode.

The rate of the production of the electrochemically active species was calculated using the local current densities through Faraday's law (Equation 14):

$$\mathrm{J}_i = \frac{-\nu_i i}{nF} \tag{14}$$

where J_i is the flux of species i at the electrode, ν_i is the stoichiometric coefficient of the reaction, i is the local current density, and n is the number of participating electrons. The stoichiometric coefficient is defined by the following convention:

$$|\nu_{ox}|Ox + ne^- \rightleftharpoons \nu_{red}Red$$
$$\nu_{ox} < 0 \qquad \nu_{red} > 0$$

At the anode, Mg^{2+} is produced from the anodic dissolution of Mg (Reaction I)

$$Mg \rightarrow {Mg^{2+}}_{(aq)} + 2e^- \tag{I}$$

At the cathode, hydroxide ions are produced as products of the hydrogen evolution reaction in alkaline media (Reaction II).

$$2H_2O + 2e^- \rightarrow H_{2(g)} + 2{OH^-}_{(aq)} \tag{II}$$

At the top, right, and left boundaries, no flux boundary conditions were applied.

2.4.3. Homogeneous reactions in the electrolyte domain: Case II

The models were performed with and without homogeneous reactions. In Case I, no homogeneous reactions are considered, although the creation of the soluble species from the electrochemical reactions was calculated and tracked. In Case II, water autoionization (Reaction III) and precipitation of hydroxides, $Mg(OH)_2$ (Reaction IV) were considered. The precipitation of corrosion products was simulated by a sink term that removed Mg^{2+} and OH^- at the time and locations in which the solubility product was reached. The reaction only took place if the conditions for precipitation were met and a Heaviside function was used to impose the sink reaction "switch" condition. More details can be found in previously published work [87].

$$H^+ + OH^- \rightleftharpoons H_2O \tag{III}$$

$$Mg^{2+} + 2OH^- \longrightarrow Mg(OH)_2 \quad \text{(IV)}$$

The reaction rate and equilibrium constants are shown in **Table 2.1.**

2.4.4. Description of the cases evaluated

The goal of this work is to compare the solutions obtained with the most general model (**NPP**) to the most reduced-order model (**Lk**) under varying NaCl concentrations – the supporting electrolyte (SE). The models were performed for 0.01, 0.1, and 1 M NaCl in three different cases. In Case I, homogeneous reactions were not considered. Thus, the electrolyte composition changed due to the electrochemical reactions, and the minor species accumulated with time in the closed system. In Case II, homogeneous reactions were considered. In Case III, the models were performed with and without homogeneous reactions, but the diffusivities of all ions were equal to 10^{-9} m^2/s. In the present paper, the results pertaining to the 0.01 – 1 M NaCl will be shown and compared. In a following publication, the comparison will be extended to the lower NaCl concentrations.

2.5. Results

The results are organized into six sections. In the first, the impact of the governing equation selected on the computational time is described for a range of solution compositions. The second section compares the results of **NPP** to **NPE** in order to assess the loss of accuracy in using the electroneutrality assumption in place of solving Poisson's Equation for the potential. The next two sections compare the potential, current density, electrolyte conductivity, and chemical species spatiotemporal distributions calculated with the two Laplace approaches (**Lk** and **Lvk**) to one another and to the results from **NPP**. In the first, no homogeneous reactions are considered, whereas, in the second, the impact of homogeneous reactions is discussed. In the following section, the differences between the Laplace approaches and **NPP** for a case in which all the ions have equivalent diffusivities are shown. Finally, a summary and discussion of the error in the potential and current density distributions calculated by the reduced-order models is presented. In all cases, the electrolyte concentrations of interest are those most commonly encountered in corrosion and electrochemical systems, represented by NaCl concentrations of 0.01 M and above.

2.5.1. Comparison between the computational time of each calculation method

Table 2.2 shows the computational time of each calculation method in the various NaCl concentration for Case I and Case II. The computational time was generally inversely correlated to the number of simplifications of each approach: **Lk** was the fastest to compute, followed by **Lvk**, **NPE,** and **NPP**, in increasing order. The **NPP** approach took up to ca. nine times longer to compute in comparison to

the **Lk** approach. The **Lvk** approach took about twice the time to compute compared to **Lk**. In comparison to **NPE**, **NPP** took up to three times longer.

Table 2.2. Comparison between the computational times (in seconds) of the different governing equations

		Computational time / s		
	NaCl concentration / M	0.01	0.1	1
Case I	Lk	13	11	10
	Lvk	27	24	22
	NPE	30	28	29
	NPP	87	84	88
Case II	Lk	766	823	858
	Lvk	310	1,693	1,663
	NPE	4,800	6,528	6,711
	NPP	6,105	6,270	6,288

The addition of homogeneous reactions (Case II) considerably increased the computational time, especially at high NaCl concentrations. The homogeneous reactions increase the impact of simultaneously solving for mass and charge conservation equations, as seen by the large ratios between **NPE** and **Lvk** in Case II vs. Case I. For example, in the 1 M NaCl solution, **NPE** took four times longer than **Lvk** for Case II, whereas, in the absence of homogeneous reactions, **NPE** took almost the same amount of time as **Lvk**. There are some apparent anomalies as well. In the lowest concentration considered, 0.01 M, the **Lvk** method is twice as fast as the more reduced model **Lk** in Case II, whereas it is slower by a factor of two in Case I. In addition, in the higher NaCl concentrations, the **NPP** is actually slightly faster than the **NPE**, albeit by < 10%.

2.5.2. Comparison between Nernst-Planck-Poisson and Nernst-Planck solved with electroneutrality

The solutions obtained by solving the Nernst-Planck equations utilizing the electroneutrality condition (**NPE**) yielded results that were nearly identical to the results obtained by solving for the charge conservation utilizing Poisson's equation (**NPP**). **Figure 2.2**(a)-(d) compare the results of selected variables calculated with the **NPE** and **NPP** approach for a case in which the concentration of the supporting electrolyte (the non-reacting species), NaCl, was 0.01 M. **Figure 2.2** (a) and (b) show the potential (a) and absolute value of the current density (b) distribution along the electrodes adjacent to the electrode/electrolyte interface (y = 0 mm) after 7200 s. As it can be seen from the superposition of the lines

showing the results of **NPP** and **NPE**, the methods yielded virtually identical results. Even the transient and profile of the Na^+ concentration (**Figure 2.2** (c) and (d), respectively), which is artificially calculated using the **NPE** method, were nearly identical in both approaches. The largest difference between the Na^+ concentration found among all the cases modeled was less than 0.01% (an absolute difference of less than 0.1 μM).

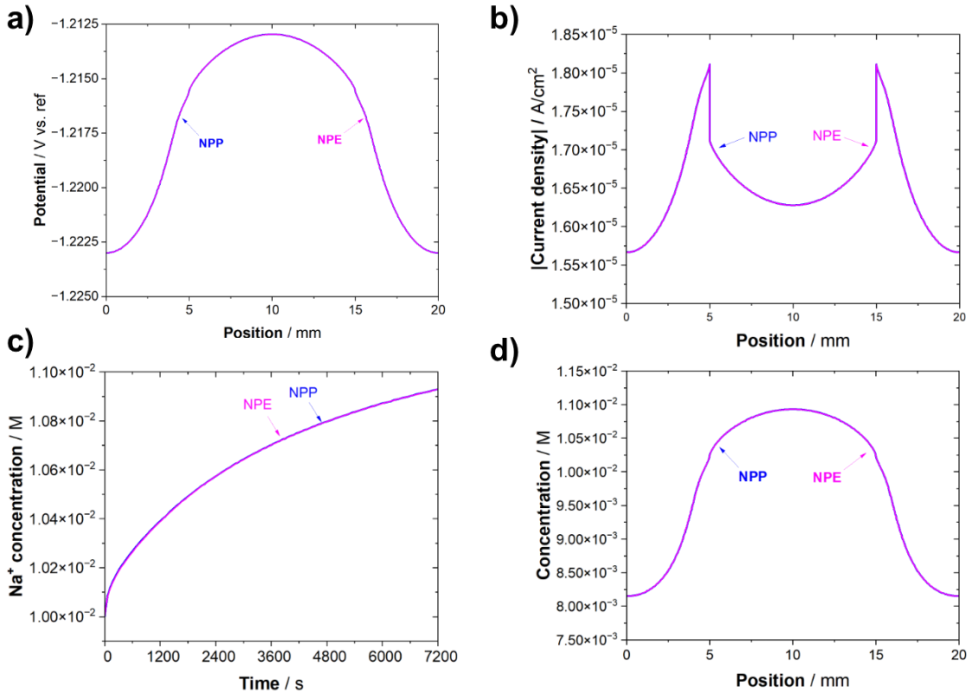

Figure 2.2. Solutions obtained by the **NPP** and **NPE** method utilizing Na^+ as the make-up ion for a NaCl concentration of 0.01 M. (a) Potential and current density (b) profiles across the electrodes; (c) Na^+ concentration transient at x = 10 mm (center of the cathode); (d) Na^+ concentration profile adjacent to the electrode/electrolyte interface after 7200 s.

Figure 2.3 (a) shows the result of the summation of the product of the concentration of each species and its charge number ($\sum c_i z_i$) near the electrode/electrolyte interface. The **NPE** method enforces electroneutrality, so the sum of the product of the concentration of each species and its charge is necessarily nearly zero, i.e., below the specified error. The **NPP** approach allows for charge separation, as charge conservation is solved by Poisson's equation and not by enforcing electroneutrality. However, as shown in **Figure 2.3** (a), there is a minute excess charge separation ($+3x10^{-13}$ equiv/dm^3) at the point of contact between the anode and the cathode. **Figure 2.3** (b) shows the charge density in the electrolyte calculated by the **NPP** method. Again, the calculation shows a small charge density at the anode and cathode point of contact – ca. 10^{-11} C/m^2.

Because of the similarity between the results obtained by the **NPP** and **NPE** approaches, the Laplace (**Lk**) and pseudo-Laplace (**Lvk**) approaches are only compared to the **NPP** approach unless otherwise noted.

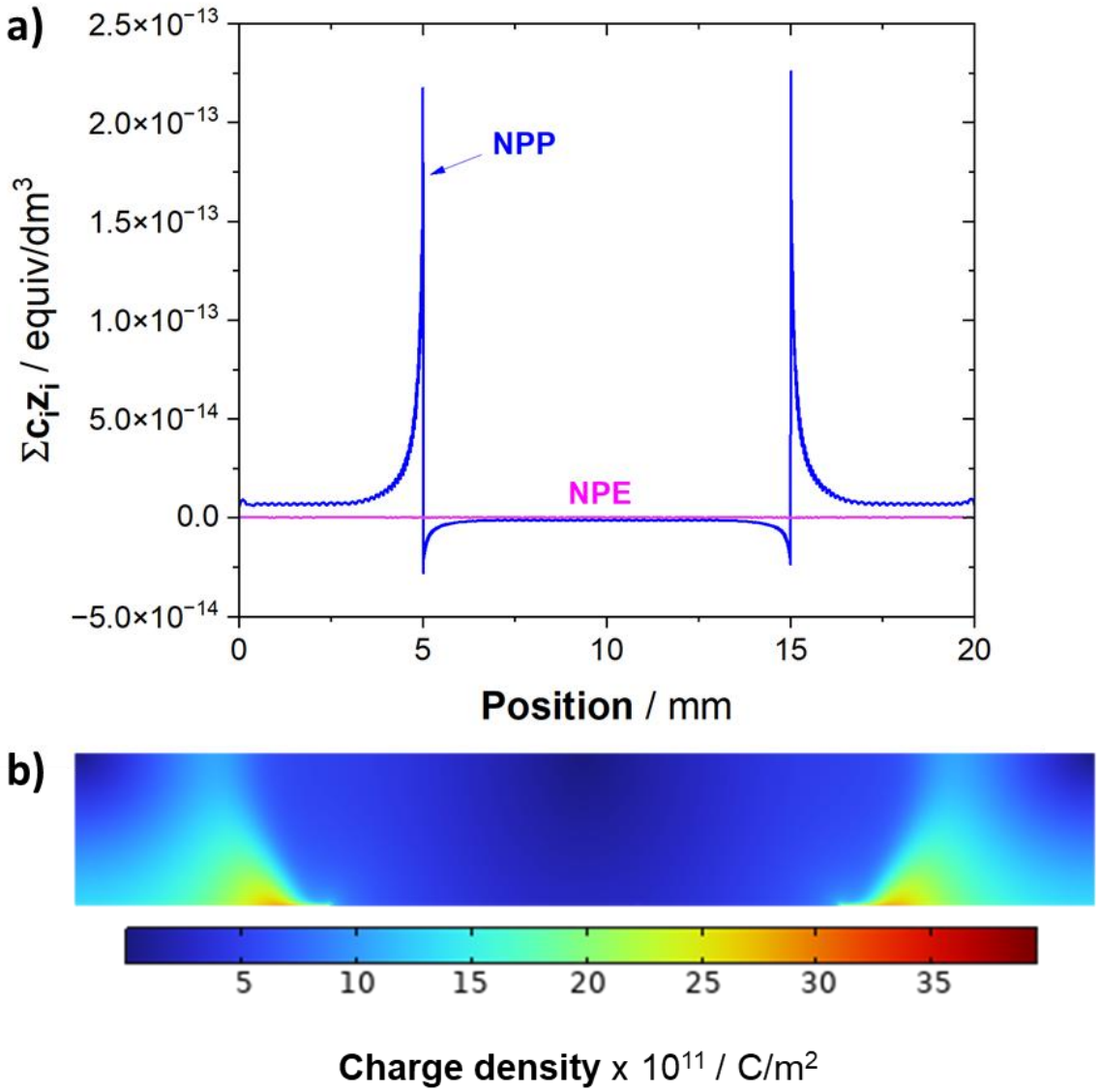

Figure 2.3. (a) Summation of the concentration of each species multiplied by its respective charge number adjacent to the electrode/electrolyte interface after 7200 s of simulation for [NaCl] = 0.01 M; (b) charge density calculated by the NPP approach after 7200 s of simulation for [NaCl] = 0.01 M.

2.5.3. Comparison between the approaches in the absence of homogenous reactions (Case I)

The aim of the following section is to compare the results of selected variables obtained using the reduced-order model approaches, **Lk** and **Lvk**, to the most general method, **NPP,** as a function of supporting

electrolyte concentration. All the transients presented were calculated at the midpoint of the cathode (x = 10 mm), and the positional distributions were calculated adjacent to the electrode/electrolyte interface (y = 0 mm) after 7200 s of simulation. First, the impacts of the NaCl concentration on the potential, current density, and species distributions calculated by the **NPP** approach are briefly presented. Then, the impact of the NaCl concentration on the differences between the calculation methods is described.

2.5.3.1. Potential, current density, and electrolyte conductivity transients

Figure 2.4 shows the potential (a) and current density (b) at the center of the cathode as a function of time at varying NaCl concentrations calculated by the **Lk**, **Lvk,** and **LPP** methods. **Figure 2.4** (c) shows the electrolyte conductivity (κ) normalized by the initial electrolyte conductivity as a function of time calculated with the **NPP** and **Lvk** methods, calculated by Equation 10. In the **Lk** method, the electrolyte conductivity is constant and equal to the initial electrolyte conductivity, by definition.

By analyzing the results provided by the **NPP** approach, which are illustrated by the solid line on the graphs displayed in **Figure 2.4**, it is possible to see that the change with time in the potential, current density, and electrolyte conductivity is not noticeable in the 1 M NaCl case within the 7200 s. The potential in the middle of the cathode is nearly constant at -1.217 V vs. ref, and the respective current density is -1.760x10^{-5} A/cm^2 . As the NaCl concentration decreases, the temporal changes of these variables are more apparent. For a NaCl concentration of 0.01 M, the electrolyte conductivity at the center of the cathode increases by almost 50% after 7200 s. As a result, the potential and current density at the cathode decrease as the increase in the electrolyte conductivity increases the anodic polarization at the cathode by the anode. However, the change is arguably small – the potential decreases by 1 mV, starting at -1.210 V and lowering to to -1.211 V vs. ref after 7200 s. Accordingly, the current density decreases from -1.53x10^{-5} A/cm^2 to -1.59 x10^{-5} A/cm^2. Please note that the cathodic current density is negative, following the sign convention of a galvanic cell – thus, the more negative cathodic current density signifies an increase in the cathodic reaction rate.

The divergence between the **Lk** and the **NPP** approaches decreases as the temporal changes in the potential, current density, and electrolyte conductivity lessen as the **Lk** approach assumes a steady-state condition. In the NaCl concentration of 1 M, it is not possible to see differences between the methods in the scale shown. In the lowest NaCl, initial potential and current density calculated by **Lk**, **Lvk**, and **NPP** are equal, as their initial electrolyte conductivities are equal. However, with time, the **Lk** solution diverges from **Lvk** and **NPP**, as the electrolyte conductivity increases as a result of the electrochemical reactions occurring at the electrodes, leading to a decrease in the potential and current density at the cathode.

The solutions provided by the **Lvk** method are in good agreement with the **NPP** solution. The **Lvk** method calculates a slightly lower electrolyte conductivity at the center of the cathode in the 0.01 M and

0.1 M NaCl case. The potential and current density decrease linearly with time and are slightly overestimated for t < 6000 s. At t = 6000 s, the **Lvk** method slightly underestimates the potential and current density in the middle of the cathode. The differences are small, and after 7200 s, the **Lvk** method underestimated the potential by 0.19 mV and the current density by 5.88 x10^{-8} A/cm^2. In 0.1 M NaCl, **Lvk** and **Lk** potential and current densities are almost undistinguishable in the scale used in the graph, whereas the solutions provided by **NPP** show a slightly lower potential and current density (a difference of 0.09 mV and 0.03 μA/cm^2, respectively).

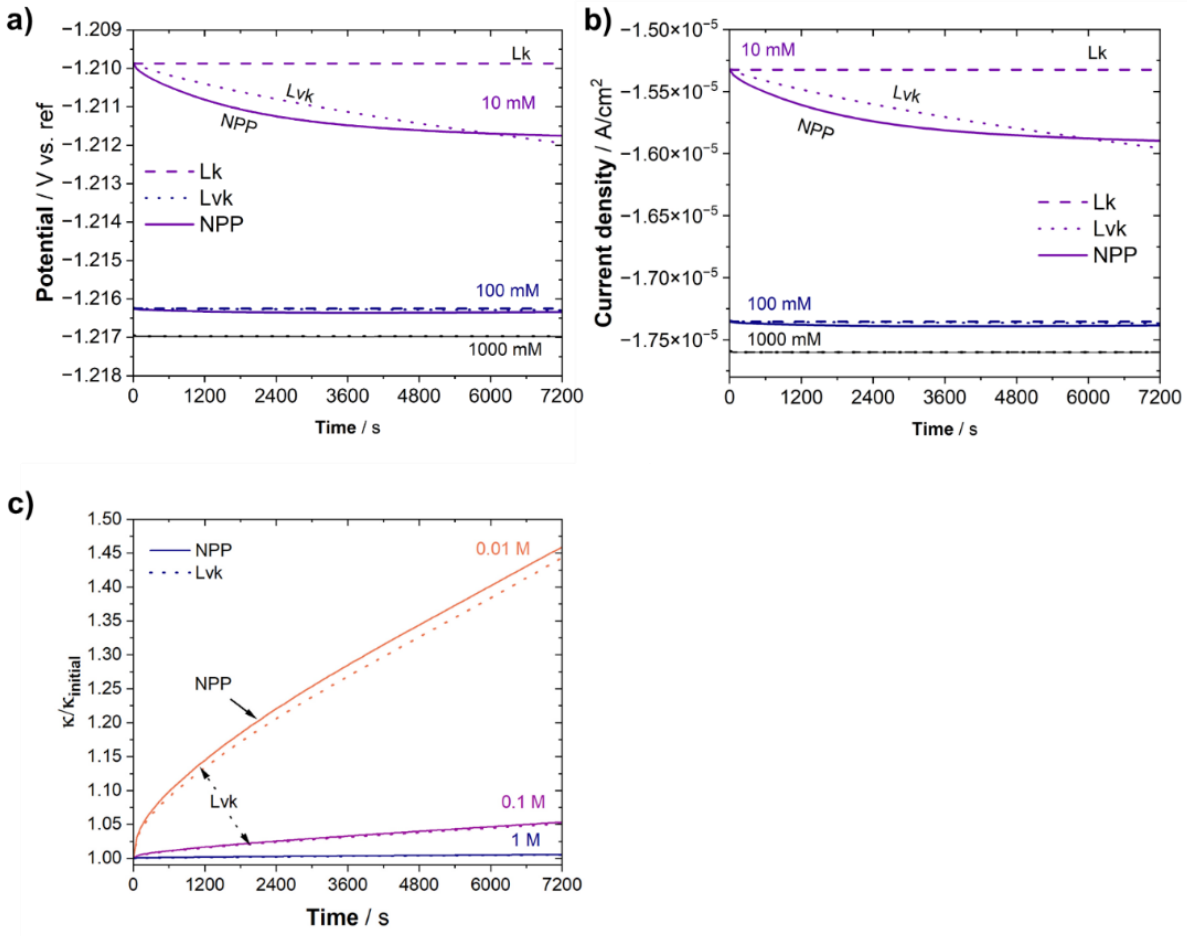

Figure 2.4. Potential (a) and current density (b) transients at the center of the cathode (x = 10 mm) calculated by the **Lk**, **Lvk**, and **NPP** for varying NaCl concentrations (0.01, 0.1, and 1 M). In (c), the transient of the electrolyte conductivity normalized the electrolyte conductivity at t = 0 s is shown for the **NPP** and **Lvk** methods for the varying NaCl concentrations.

2.5.3.2. Potential, current density, and electrolyte conductivity distributions near the electrode/electrolyte interface after 7200 s

Figure 2.5 (a)-(d) shows the potential at the electrodes as a function of position near the electrode/electrolyte interface (y = 0 mm) after 7200 s calculated by the different methods for varying NaCl concentrations. The y-axis scale changes for each NaCl concentration to better observe the differences between the calculation methods. In **Figure 2.5** (d), the potential distributions for the NaCl concentrations of 1, 0.1, and 0.01 M are shown on the same scale to put in perspective the impact of the NaCl on the solutions.

In the highest NaCl concentration (1 M), there is a small potential difference across the electrolyte. The difference between the lowest potential (at the outer edges of the anode at x = 0 mm and x = 20 mm) and the highest potential (in the middle of the cathode at x = 10 mm) is ca. 0.15 mV, as calculated by **NPP**. With the decrease in the NaCl concentration, the potential difference across the electrodes increases as the electrolyte becomes less conductive. At the lowest NaCl concentration, **NPP** calculates a potential difference of ca. 9 mV across the electrolyte.

The differences between the potentials calculated by the different methods are higher at the outer edges of the anodes (x = 0 and 20 mm), and at the center of the cathode (x = 10 mm). Near the cathode and anode junction, the calculated potentials are closer in value. The potential distributions resulting from the **Lk** and **Lvk** methods are virtually equal in the NaCl concentration of 1 M. The reduced-order approaches calculate a slightly higher ohmic drop across the electrodes (ca. 0.16 mV), but the potential distribution only marginally differs from the **NPP** solution. The greatest difference between the potential calculated by **NPP** and the reduced-order methods is 7 μV, and it is located in the middle of the cathode (x = 10 mm). As the concentration of the supporting electrolyte decreases, the differences between the solutions obtained by the different methods increase. For [NaCl] ≤ 0.1 M, the **Lk** and **Lvk** solutions differ from each other. The **Lvk** solution is closer to that of **NPP**. In the [NaCl] = 0.01 M, **Lvk** is in very good agreement with the **NPP** solution, although it calculates a slightly lower ohmic drop across the electrodes. There is a higher discrepancy between the potential distribution calculated by the **Lk** and **NPP** approaches at the lowest NaCl. The **Lk** approach overestimates the potential difference across the electrodes; at the anodes, the **Lk** approach underestimates the potential at the anode and overestimates the potential at the cathode.

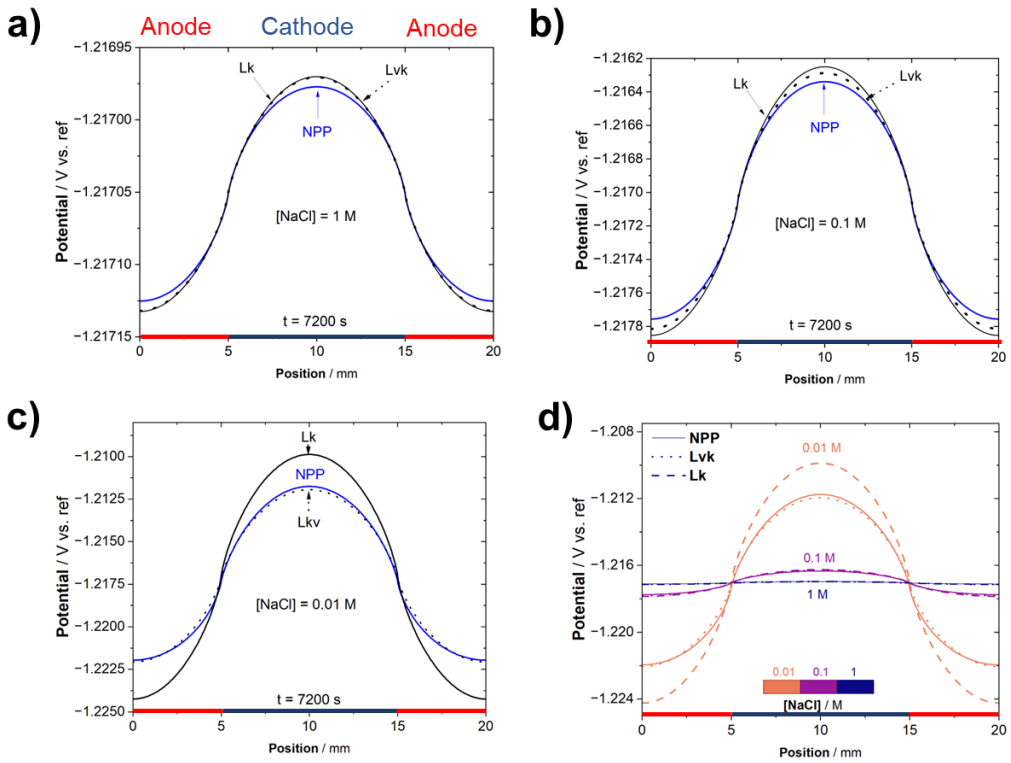

Figure 2.5. Potential distribution after 7200 s obtained by the different calculation methods (**NPP**, **Lvk**, and **Lk**) for varying supporting electrolyte concentration (NaCl): a) 1 M; b) 0.1 M; c) 10 mM. Please note that the potential scale on the y-axis changes in the (a)-(e) graphs.

Figure 2.6 displays the absolute value of the current density as a function of position after 7200 s for the NaCl concentrations of 1 M (a), 0.1 M (b), and 0.01 M (c). **Figure 2.6** (d) shows the potential distribution obtained for all the NaCl concentrations plotted in the same scale. The current density is the highest at the point of contact between the anode and the cathode, and it decreases as the cathode and anode separate from one another due to the resistance to the current flow in the solution. As the NaCl concentration increases and the electrolyte becomes more conductive, the absolute value of the current density becomes more uniform across the electrodes and is generally higher, except at the junction between the anode and cathode, in which the current density is higher in the lowest NaCl case.

Consistent with the potential distribution observations, the difference between the current density profiles calculated by the different governing equations decreases as the NaCl concentration increases. Additionally, the difference between the current densities calculated by the different methods increases with increasing distance from the anode and cathode junctions (x = 5 and 15 mm).

It is not possible to distinguish between the current densities calculated by the **Lk** and **Lvk** approach in the 1 M NaCl case, as seen in **Figure 2.6** (a). The difference between the reduced-order approaches and

the **NPP** approach is also very small – the largest current density difference was 10^{-9} A/cm^2 – and the solutions are only distinguishable due to the narrow current density range in the y-axis. In the NaCl concentration of 0.01 M, the **Lk** method current densities deviate more significantly from the **NPP** and **Lvk** approaches.

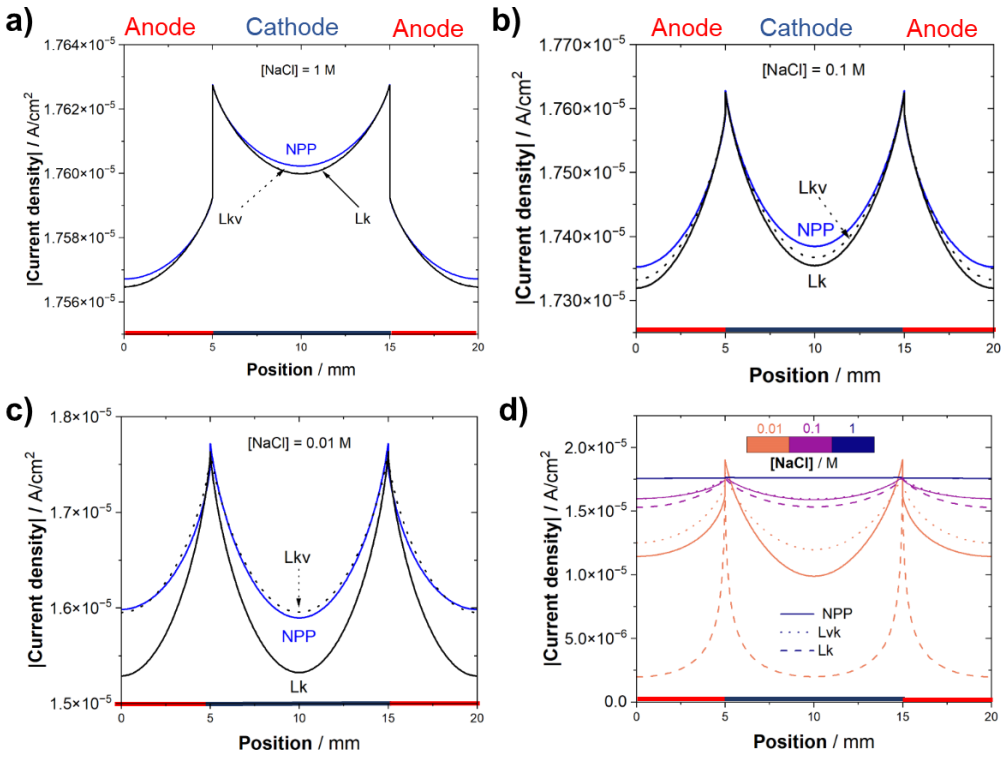

Figure 2.6. The absolute value of current density as a function of position after 7200 s obtained by the different calculation methods (**NPP**, **Lvk**, and **Lk**) for varying supporting electrolyte concentration (NaCl): a) 1 M; b) 0.1 M; c) 0.01 M; d) 1, 0.1, and 0.01 M the same current density scale. Please note that the current density scale on the y-axis changes in the (a)-(c) graphs.

Figure 2.7 shows the electrolyte conductivity profile after 7200 s for the different NaCl concentration cases: 1 M (a), 0.1 M (b), and 0.01 M (c). On the right y-axis, the ratio between the electrolyte conductivity at t = 7200 s and at t = 0 s is shown. The electrolyte conductivity increases in lockstep with the NaCl concentration. In the **Lk** approach, the electrolyte conductivity is constant and uniform. The **NPP** and **Lvk** approaches show that the electrolyte conductivity is higher at the anodes than at the cathode. The difference between the electrolyte conductivities at the cathode and at the anode increases as the NaCl concentration decreases. The electrolyte conductivity calculated using the **Lvk** approach is in good agreement with the **NPP** solution, albeit slightly smaller in all cases.

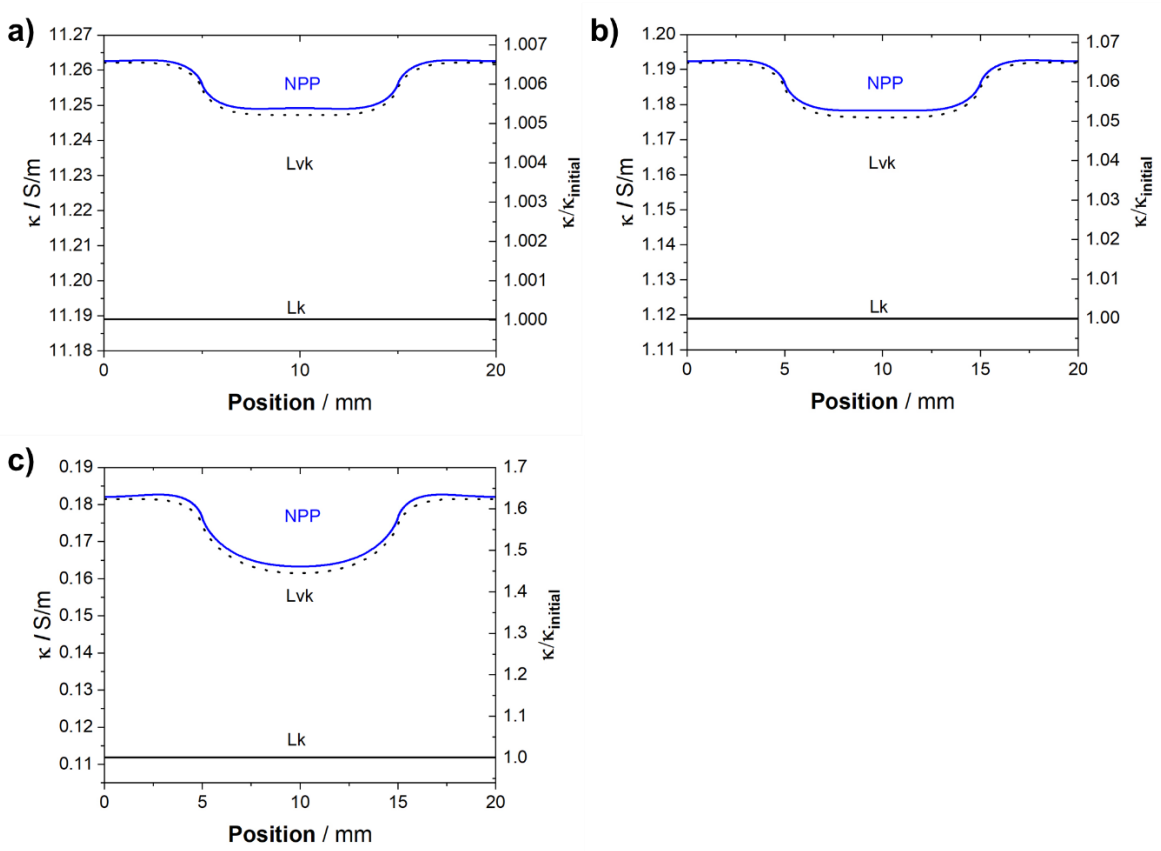

Figure 2.7. Electrolyte conductivity profile after t = 7200 s as a function of NaCl concentration: (a) 1 M, (b), 0.1 M, (c) 0.01 M.

2.5.3.3. Species transient and profile

This section presents the results comparing the concentration of the chemical species (Na+, Cl-, Mg2+, and OH-) as a function of time and position calculated with the different methods. As a reminder, for the Lk and Lvk methods, the transport by migration and diffusion and the production of the reacting species (Mg2+ and OH-) via electrochemical reactions were calculated by coupling the Transport of Diluted Species and the Secondary Current Density modules of COMSOL (v. 6.1). The rate of production of Mg2+ and OH- were calculated using the calculated current density through Faraday's Law. The potential gradient calculated using Laplace's equation is applied to solve for the migration term in the transport of species. In the Lvk method, the computed concentrations are used in the Secondary Current Distribution module to update the local electrolyte conductivity using Equation 10.

Reacting species

Figure 2.8 shows the concentration transients of Mg^{2+} and OH^- at the center of the cathode (x = 10 mm) for NaCl concentrations varying from 0.01 to 1 M. Mg^{2+} and OH^- concentrations increase as the electrochemical reactions occurring at the electrodes progress and the species accumulate in the closed system. The concentration of Mg^{2+} was low in the first 1800 s, after which it increased. The Mg^{2+} rate at which the Mg^{2+} concentration increases as the NaCl concentration decreases. After 7200 s, the Mg^{2+} concentration at the center of the cathode is higher in the 0.01 M NaCl solution. The OH^- concentration increases more rapidly in the first ca. 100 s. After 7200 s, the OH^- concentration increases as the NaCl concentration increases.

There are negligible differences between the methods for the 0.1 and 1 M NaCl cases (**Figure 2.8** (a1, a2, b1, and b2)). For the NaCl concentration of 0.01 M, there is a small discrepancy between the results. The **Lk** and **Lvk** methods overestimate the Mg^{2+} concentration (**Figure 2.8** (c1)) and underestimate the OH^- concentration (**Figure 2.8** (c2)) at the cathode. The **Lvk** method yields results closer to the **NPP** solution.

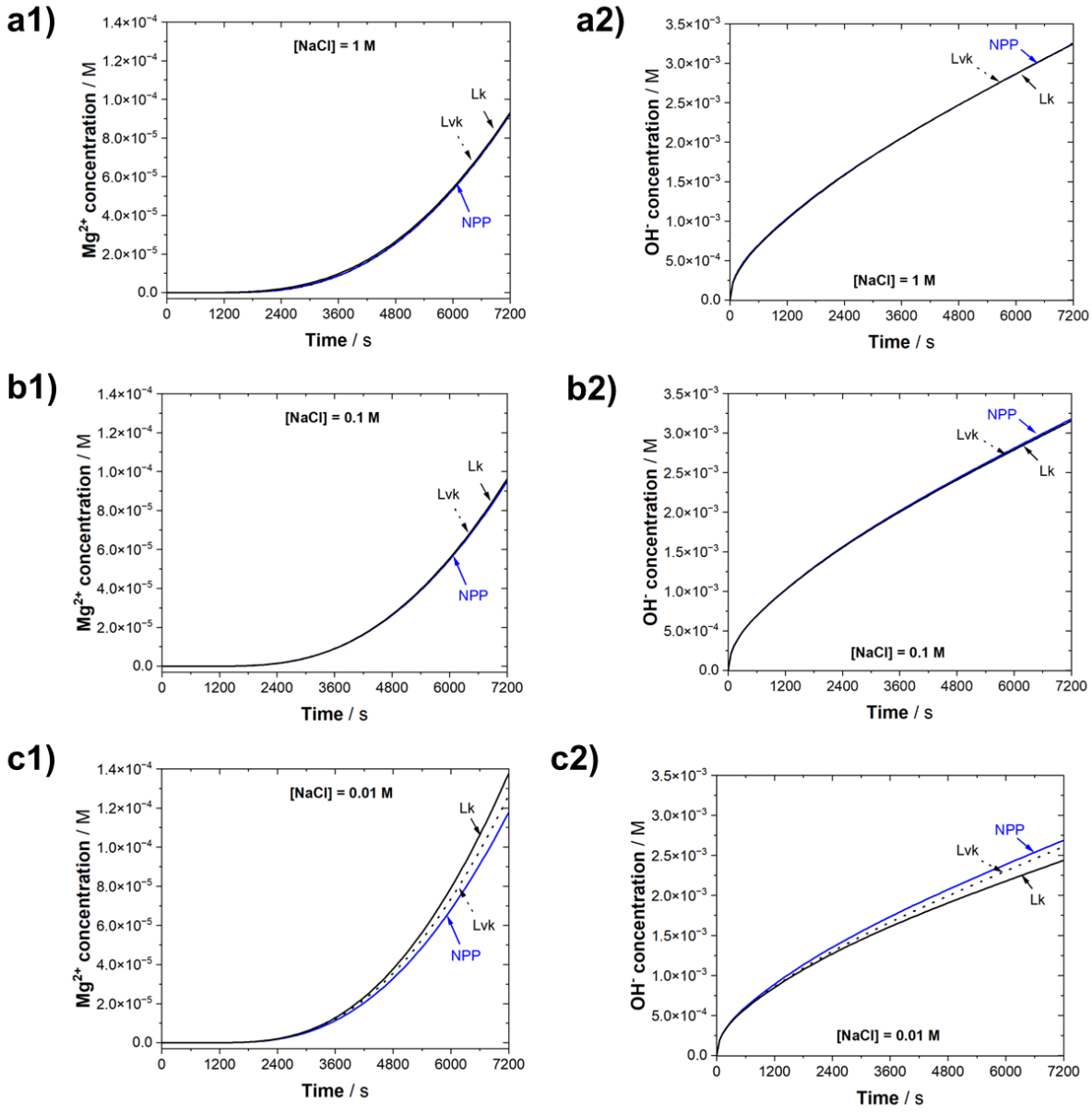

Figure 2.8. Transient of Mg^{2+} (a1, b1, and c1) and OH^- (a2, b2, c2) in the middle of the cathode (x = 10 mm) calculated by the **Lk**, **Lvk**, and **NPP** methods in varying NaCl concentrations: (a1 and a2) 1 M, (b1 and b2) 0.1 M, and 0.01 M (c1 and c2).

The concentration profiles of the reacting species, Mg^{2+} and OH^-, adjacent to the electrode/electrolyte interface after 7200 s are displayed in **Figure 2.9**. The concentration of Mg^{2+} is higher at the anodes; the highest Mg^{2+} concentration is found at the edges of the anodes (x = 0 and 20 mm), and it decreases with the distance from the edges of the anode, reaching a minimum value at the center of the cathode (x = 10 mm). The OH^- concentration profile displays the opposite behavior: the maximum

concentration is found at the center of the cathode, and the lowest concentrations are found at the edges of the anode.

For the 1 M NaCl case, it is not possible to distinguish the concentration profiles of Mg^{2+} (**Figure 2.9** (a1))and OH^- (**Figure 2.9** (a2)) obtained by the **Lk**, **Lvk**, and **NPP** methods. For the 0.1 M NaCl case, it is possible to see a small difference in the OH^- concentration profile at the cathode calculated by the **NPP** approach in comparison to **Lk** and **Lvk**, which underestimate the OH^- concentration **Figure 2.9** (b2). For the lowest NaCl concentration, the concentration profiles obtained by the different approaches are more distinguishable. The concentration of Mg^{2+} at the edges of the anode is overestimated by the **Lvk** method and underestimated by the **Lk** method **Figure 2.9** (c1). At the cathode, the Mg^{2+} concentration calculated by the reduced-order methods agrees better with the **NPP** solution. The concentration of OH^- at the cathode is underestimated by the **Lk,** and **Lvk** approaches **Figure 2.9** (c2). At the edges of the cathode, the concentration of OH- is overestimated by the **Lk** approach and underestimated by the **Lvk** approach.

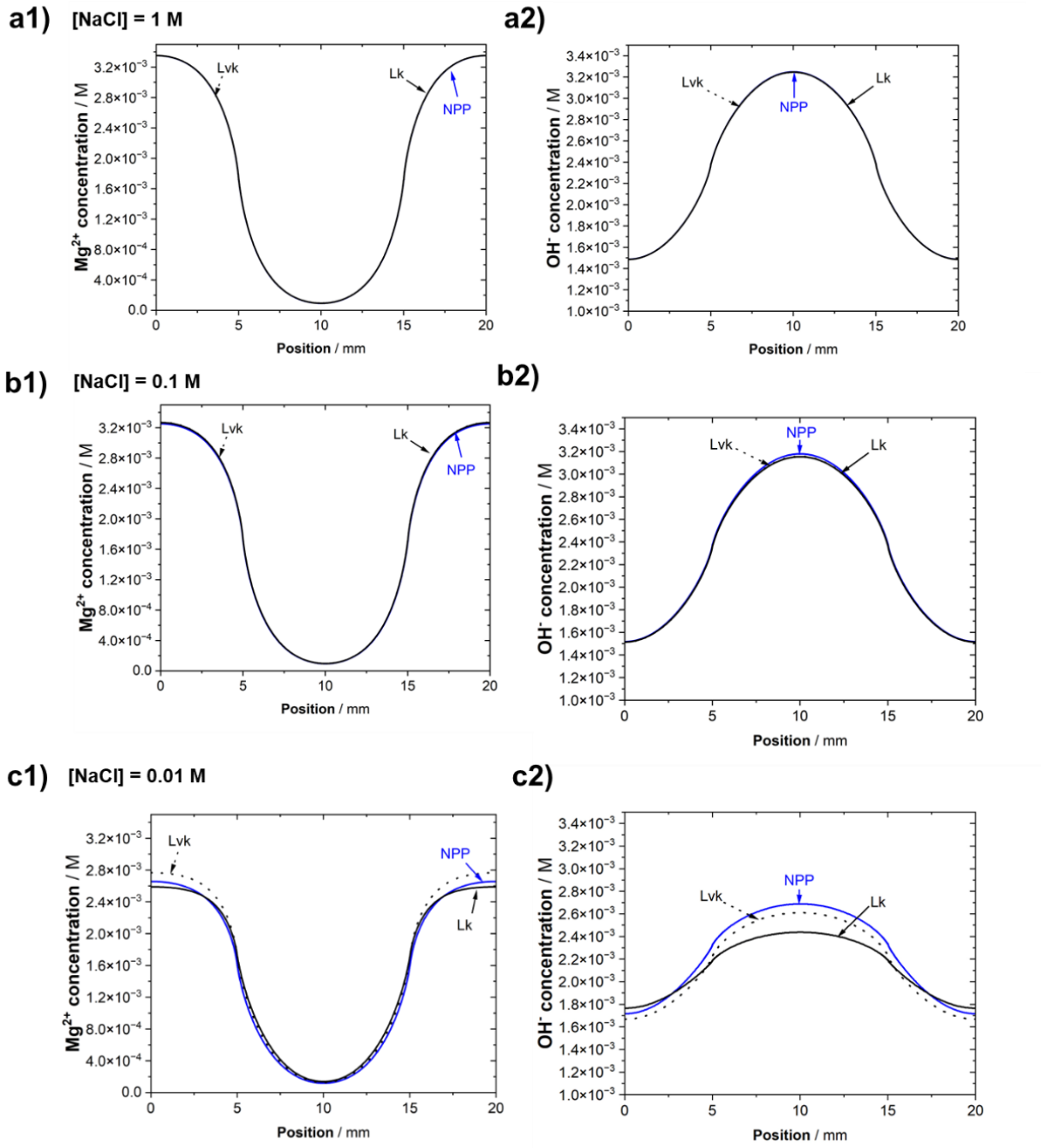

Figure 2.9. Mg^{2+} (a1, b1, c1) and OH^- (a2, b2, c2) concentration profile adjacent to the electrode/electrolyte interface after 7200 s in the NaCl concentrations of 1 M (a1 and a2), 0.1 M (b1 and b2), and 0.01 M (c1 and c2).

Supporting electrolyte

Figure 2.10 shows the Na^+ and Cl^- concentration profiles adjacent to the electrode/electrolyte interface after 7200 s. Please note that the y-axis concentration scale changes at each plot. The concentration

of Cl^- shows a maximum at the edges of the anode, and it decreases with increasing distance from the edges of the anode, reaching a minimum at the center of the cathode. Na^+ displays the opposite behavior, with its maximum reached in the middle of the cathode and the minimum at the edges of the anodes.

The reduced-order models overestimate the Na^+ concentration at all positions and underestimate the Cl^- at all positions in the 0.1 and 1 M NaCl cases. The highest deviation in the Na^+ and Cl^- concentrations calculated by the reduced-order models is less than 1% in the 0.1 M NaCl case, and 0.1% in the 1 M NaCl case. The Na^+ and Cl^- concentration profiles calculated using **Lk** and **Lvk** are nearly identical in the 1 M NaCl case, and they start to deviate from each other at lower NaCl concentrations.

In the 0.01 M NaCl case, the differences between the Na^+ and Cl^- concentrations calculated by the **Lk** and **Lvk** are more noticeable. Compared to the **NPP** solution, the **Lk** method overestimates the Na^+ concentration at the cathode and underestimates its concentration at the edges of the anode. The Cl^- concentration calculated by the **Lk** approach is underestimated at the cathode and overestimated at the edges of the anode. The **Lvk** approach overestimates the Na^+ concentration and underestimates the Cl concentration at all positions adjacent to the electrode/electrolyte interface. The deviations of the **Lk** and **Lvk** methods from the **NPP** approach are higher at the center of the cathode.

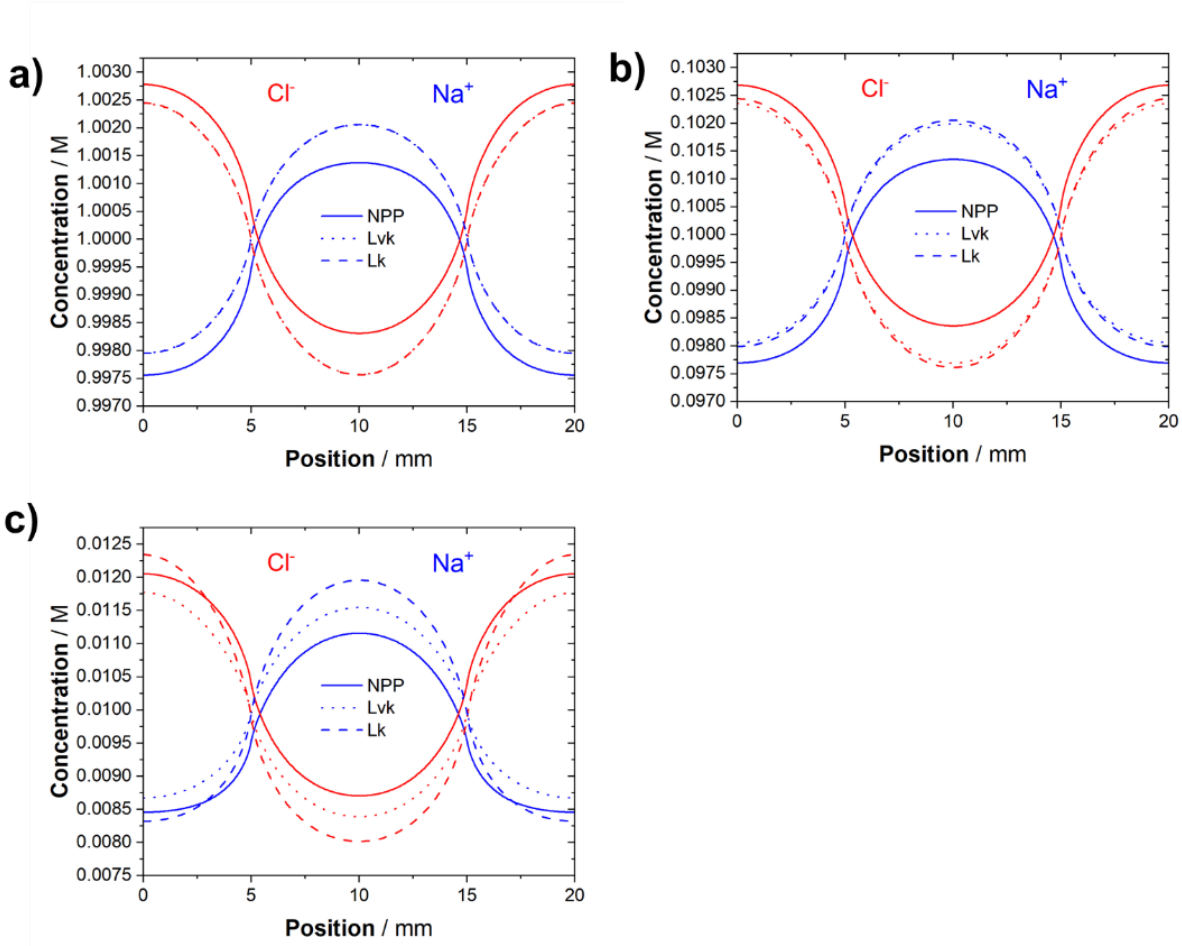

Figure 2.10. Na^+ and Cl^- concentration profiles adjacent to the electrode/electrolyte interface for varying NaCl concentrations calculated by the **Lk**, **Lvk**, and **NPP** methods: (a) 1 M, (b) 0.1 M, (c), 0.01 M.

2.5.4. Case II: the addition of homogeneous reactions in the electrolyte

The results shown above were obtained without considering any homogeneous reactions occurring in the electrolyte. In the absence of homogeneous reactions, the concentration of the species originating from the electrochemical reactions (Mg^{2+} and OH^-) increases indefinitely because of their accumulation in the closed system. However, in most systems relevant to corrosion, corrosion products, such as hydroxides and oxides, will precipitate after a solubility limit is reached, leading to a ceiling on the solution concentrations of some species. The homogeneous reactions will change the local composition of the electrolyte, impacting the electrolyte conductivity, potential, and current density distributions.

2.5.4.1. Impact of homogeneous reactions on the potential, current density, and species concentration calculated by the NPP method

The addition of homogeneous reactions affects the distributions of interest; in the higher concentration solutions, however, the differences are negligible (<1%), with the exception of the Mg^{2+} and OH^- as they are reactive ions whose maximum concentrations are limited by the solubility product of $Mg(OH)_2$. **Figure 2.11** compares the reacting species transient at the anode and cathode junction and at the center of the cathode, and the profiles adjacent to the electrode/electrolyte interface after 7200 s of potential, reacting and supporting electrolyte species concentrations, and electrolyte conductivity obtained in Case I and Case II for [NaCl] = 1 M.

The addition of the sink term simulating the precipitation of $Mg(OH)_2$ limited the increase in the concentration of Mg^{2+} and OH^-. **Figure 2.11** (a) and (b) show the Mg^{2+} and OH^- concentration transients at the anode and cathode junction (**Figure 2.11** (a)) and at the center of the cathode (**Figure 2.11** (b) calculated in Case I and II. At the beginning of the simulation, the concentration transient of Mg^{2+} and OH^- calculated in Case I and Case II follow the same profile. After the $Mg(OH)_2$ solubility limit is reached, the concentrations calculated in Case II start to deviate from those obtained in Case I. The solubility limit of $Mg(OH)_2$ is reached after 120 s at the junction, after which the concentration of Mg^{2+} starts to decrease, and the increase in the OH^- slows down. At the center of the cathode, the solubility limit is reached after 1000 s; the increase in the OH^- concentration slows down, and the concentration of Mg^{2+} remains low in the 7200 s. The Mg^{2+} and OH^- concentration profiles adjacent to the electrode/electrolyte interface after 7200 s obtained in Case I and II are displayed in **Figure 2.11** (c). The concentrations are lower in Case II, and their distributions are less uniform. The Mg^{2+} concentration adjacent to the cathode is very low and negligible. At the anodes, the concentration increases from 0.02 mM to 3 mM from the anode and cathode junctions (x = 5, 15 mm) to the edges of the anode (x = 0, 20 mm). Likewise, the concentration of OH^- is low at the anodes, and its concentration increases sharply near the cathode and anode junction, reaching a maximum of 40 μM at the center of the cathode, almost two order of magnitude higher than at the edges of the anode.

The addition of the homogeneous reactions slightly flattened the potential distribution profile, as displayed in **Figure 2.11** (d)**.** The same effect can be seen in the distribution of the supporting electrolyte ions shown in **Figure 2.11** (e). **Figure 2.11** (f) shows the electrolyte conductivity as a function of position adjacent to the electrode/electrolyte interface calculated in Case I and Case II. The electrolyte conductivity is higher in Case I, and its distribution is more uniform along the electrodes. In Case II, the electrolyte conductivity displays a minimum at the junctions between the anode and the cathode.

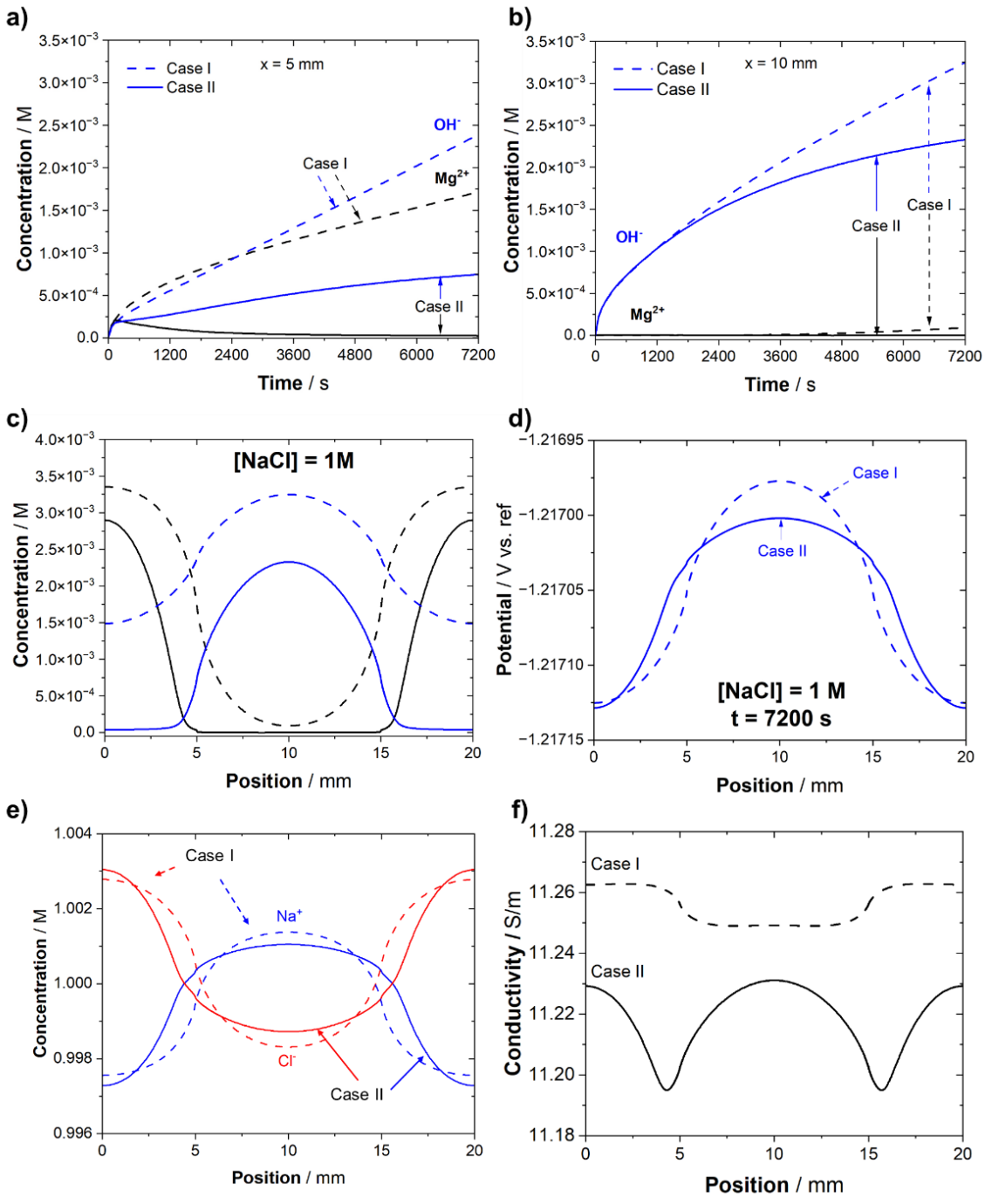

Figure 2.11. The impact of the addition of homogeneous reactions on the potential, species distribution, and the electrolyte conductivity profiles after 7200 s for [NaCl] = 1 M.

2.5.4.2. Comparison between the calculation methods in the calculated potential with reactions: Potential, current density, and electrolyte conductivity profile

In the presence of a homogeneous reaction, the differences between the profiles of parameters of interest are larger for the reduced-order methods than in the absence of a homogeneous reaction, although in most cases the differences are still trivial.

Figure 2.12 shows the potential and current density distribution after 7200 s adjacent to the electrode/electrolyte interface for the various NaCl concentrations. In comparison to Case I, the potential and current density profiles calculated using the reduced-order approaches deviate more from the **NPP** solution. The reduced-order models calculate a higher potential difference across the electrodes and lower current densities. As observed in Case I, the **Lk** and **Lvk** approaches are indistinguishable in the 1 M NaCl case (**Figure 2.12** (a1) and (a2)). However, differently from Case I, the solutions obtained by **Lk** and **Lvk** are more similar to each other in the lower NaCl concentrations. All that said, at these concentrations of NaCl, the differences are <1% in the current density for 0.1 M and 1 M NaCl and <10% for 0.01M NaCl. The differences in the potential distributions are even smaller (<0.03%).

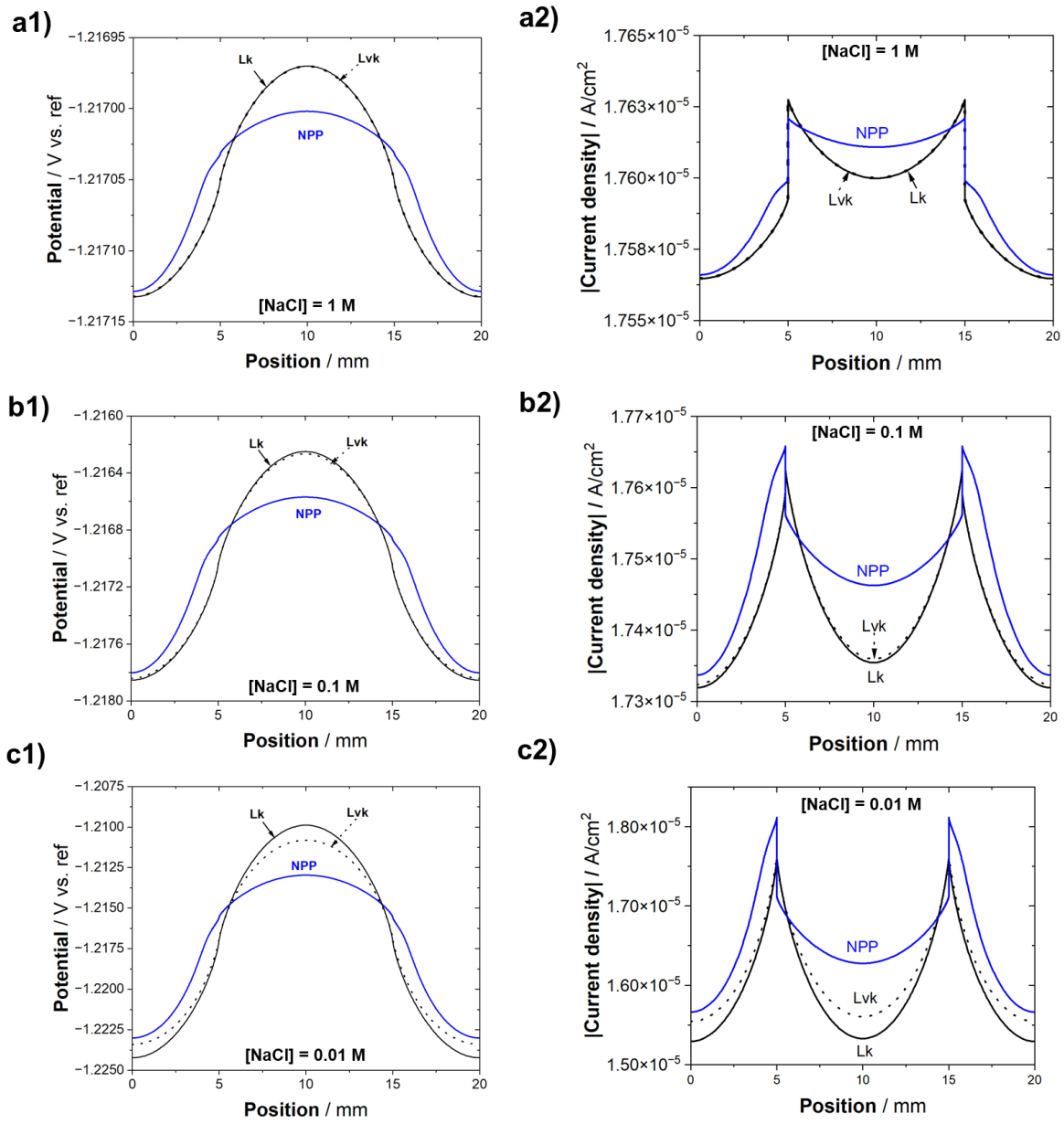

Figure 2.12. Potential (a1, b1, c1) and current density (a2, b2, c2) distributions adjacent to the electrode/electrolyte interface after 7200 s for [NaCl] = 1 M (a1 and 22), 0.1 M (b1 and b2), and 0.01 M (c1 and c2).

Figure 2.13 (a) shows the ratio between the electrolyte conductivity at $t = t_x$ and the initial electrolyte conductivity in the middle of the cathode calculated by the **NPP** and **Lvk** approaches. In the 0.01 M NaCl case, the electrolyte conductivity increases by 32.5% after 7200 s (**NPP**). The increase is smaller than the increase observed in Case I (50% increase). The **Lvk** solution yields a smaller electrolyte conductivity in the 0.01 M NaCl case, and the deviation from the **NPP** approach increases with time.

Figure 2.13 (b), (c), and (d) show the electrolyte conductivity as a function of position for [NaCl] = 1, 0.1, and 0.01 M, respectively. The right y-axis shows the electrolyte conductivity normalized by its initial value. Note that the y-axis scale changes in each graph. For all NaCl concentrations, the electrolyte conductivity exhibits two minimum near the anode and cathode junctions and a maximum at the edges of the anode and middle of the cathode. The relative local variation in the electrolyte conductivity increases with decreasing NaCl concentration.

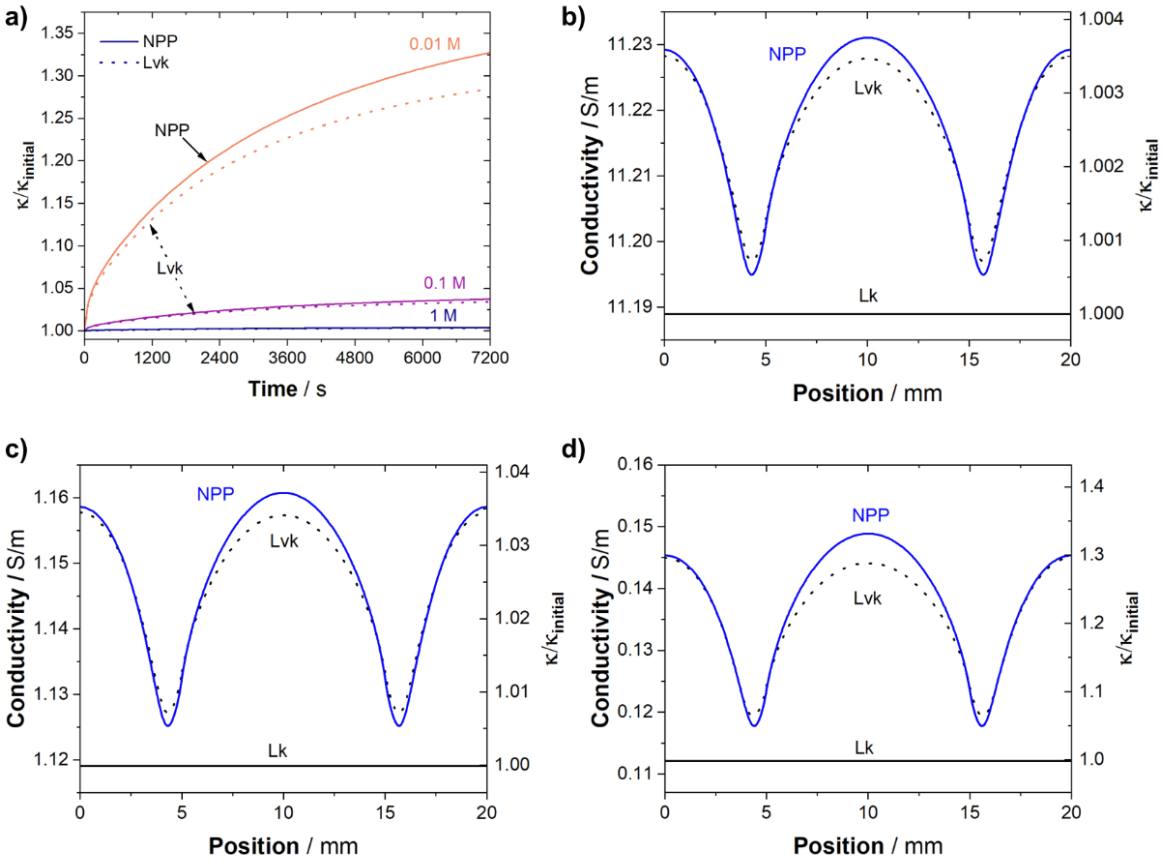

Figure 2.13. (a) Ratio between the electrolyte conductivity at t = t_x and the initial electrolyte conductivity in the middle of the cathode as a function of time for [NaCl] = 1, 0.1, 0.01 M; electrolyte conductivity profile after 7200 s adjacent to the electrode/electrolyte interface for [NaCl] = 1 (b), 0.1 (c), 0.01 M (d).

2.5.4.3. Reacting species distribution near the electrode/electrolyte interface after 7200 s

Figure 2.14 illustrates the concentration of the reacting species adjacent to the electrode/electrolyte interface calculated by the different methods with the addition of homogeneous reactions for the varying NaCl concentrations.

There is an excellent agreement between the reacting species concentration profiles between the solutions obtained by the reduced-order and **NPP** models for the NaCl concentrations of 1 M and 0.1 M (**Figure 2.14** (a1, a2, b1, and b2)). The Mg^{2+} concentration profile obtained by the reduced-order approaches is also in good agreement with the **NPP** solution in the NaCl concentration of 0.01 M, although the **Lvk** approach slightly overestimates (by 4%) the Mg^{2+} concentration at the positions adjacent to the anode (**Figure 2.14** (c1)). The OH^- concentration profile resulting from the **Lk** and **Lvk** calculations displays higher deviations to **NPP** in comparison to the Mg^{2+} concentration profile (**Figure 2.14** (c2)). At the center of the cathode, the reduced-order approaches underestimate the OH^- concentration by 9%.

The concentrations of the major species, Na^+ and Cl^-, calculated in Case II are shown in **Figure S1** in the Supplementary Information.

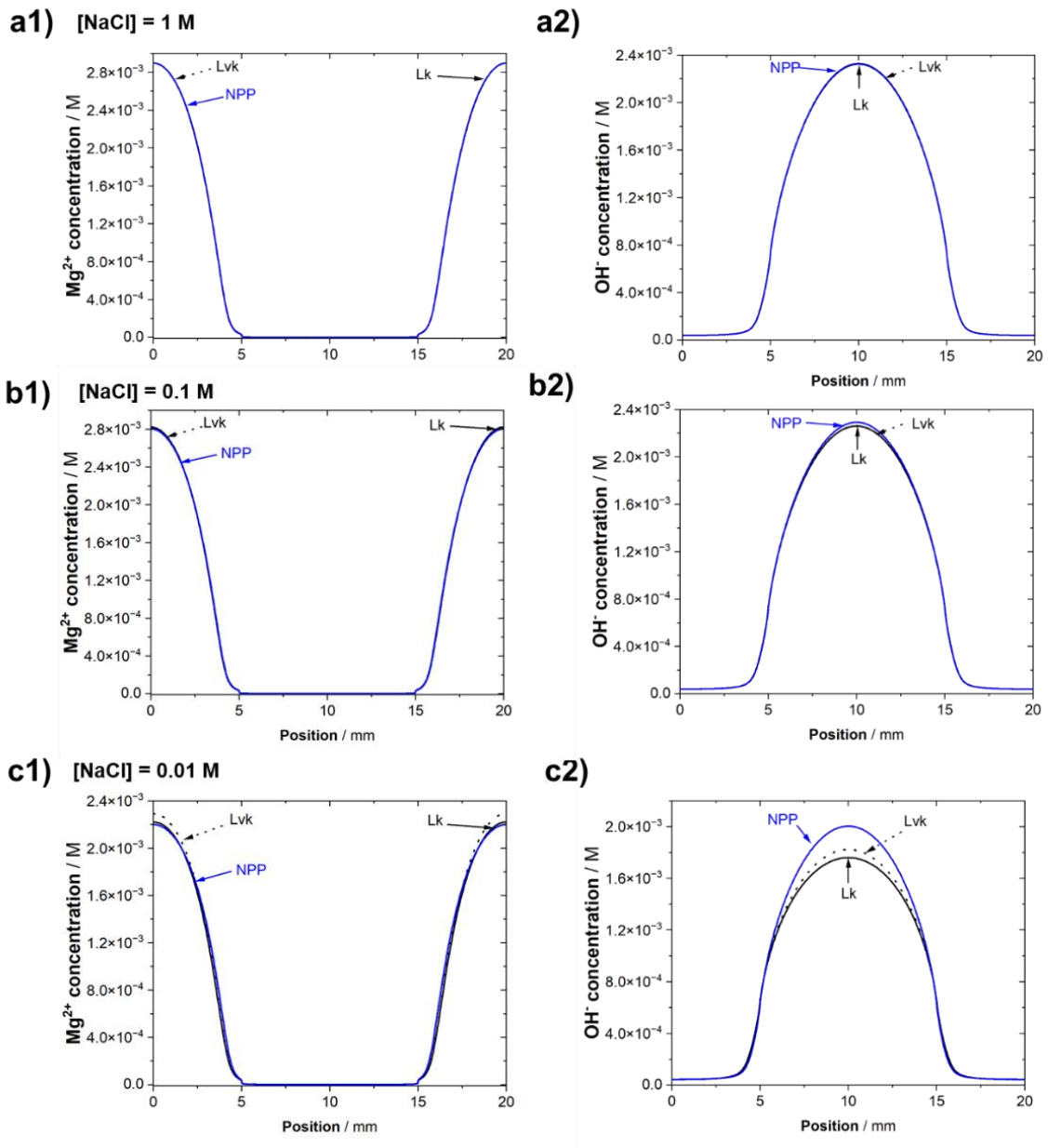

Figure 2.14. Concentration profile of the reacting species, Mg^{2+} (a1, b1, c1) and OH^- (a2, b2, c2) adjacent to the electrode/electrolyte interface after t = 7200 s calculated by **NPP**, **Lvk**, and **Lk** methods in Case II.

2.5.5. Case III: All species have the same diffusivity

In Case III, the calculations were performed with different methods for a case in which all the ions had the same diffusivities ($D = 10^{-9}$ m^2/s). The homogeneous reactions were considered in the calculations. **Figure 2.15** shows the potential, current density, and supporting electrolyte species concentration calculated for a [NaCl] = 1 M.

When equalling the diffusion coefficients of all species, the **Lvk** and **NPP** yield the same solutions. As **Figure 2.15** shows, the potential, current density, and species distributions calculated by **Lvk** and **NPP** overlap and are virtually equal. The **Lk** solutions, however, deviate from the **NPP** and **Lvk**. The **Lk** method calculated a lower ohmic drop across the electrodes and higher current densities. Additionally, the concentrations of the supporting electrolyte ions also deviated from the **NPP** and **Lvk** solutions: the **Lk** method underestimated the anions at the anode and the cations at the cathode.

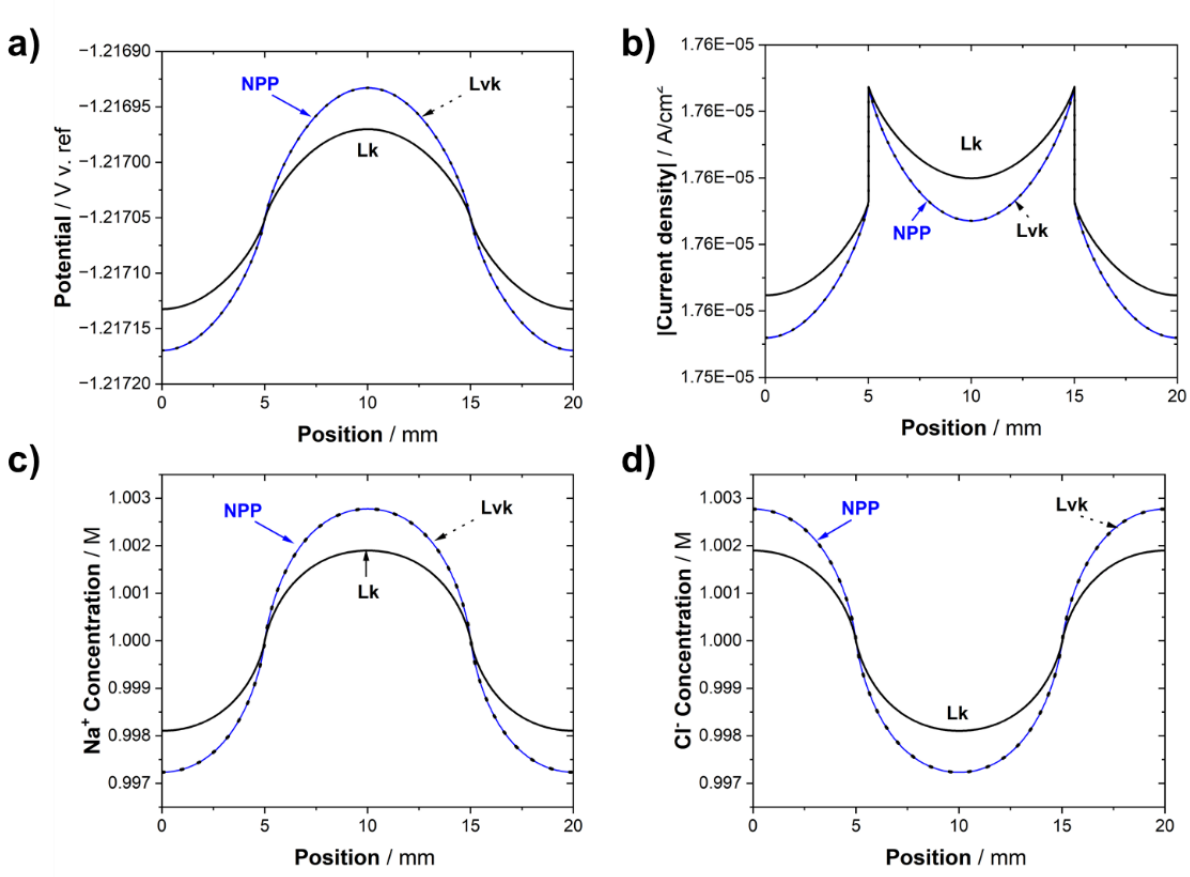

Figure 2.15. Potential (a), current density (b), Na+ concentration (c), and Cl- concentration (d) calculated adjacent to the electrode/electrolyte interface boundary after t = 7200 s for the **NPP**, **Lvk**, and **Lk** method in Case III, in which the diffusivities of all ions were equal.

2.5.6. Deviations in the potential, current density, and species concentration calculated by the reduced-order models

The errors associated with the reduced-order approaches were evaluated quantitatively by comparing the values of selected variables with those obtained with the **NPP** approach. The values of potential, current density, and concentration of Mg^{2+} and OH^- at the center of the cathode (x = 10 mm) after 7200 s calculated with the **Lk** and **Lvk** approaches were compared against those obtained by the **NPP**

approach. The results are shown in **Figure 2.16**, in which the differences are plotted against the ratio between the supporting electrolyte to the reactive species (SER ratio). The ratio was calculated by summing the average of the Na^+ and Cl^- concentrations in the electrolyte domain and dividing the sum of the average of the remaining species.

There was a greater error associated with the concentration of Mg^{2+} at the center of the cathode in comparison to the other variables **Figure 2.16** (a) and (b)). In Case II, however, the concentration of Mg^{2+} at the center of the cathode is negligible, as seen in **Figure 2.14** – ca. 0.4 μM. Thus, an error of 10% represents an absolute difference of 0.04 μM. For the range of NaCl concentrations considered in this work, the errors associated with the reduced-order models are small. For the lowest NaCl case, the deviation from the potential was ca. 3 mV, with the respective error in the current density being 5% and 10% error in the species concentration for the most simplified approach (**Lk**). The increase in the concentration of the supporting electrolyte substantially decreases the deviation of the reduced-order models from the **NPP** method. Increasing the NaCl concentration from 0.01 M to 1 M decreased the error in current density from ca. 3% to 0.01% in Case I – with an absolute difference of $2x10^{-9}$ A/cm^2 for the 1 M NaCl case. The error associated with OH^- decreases from 10% to 0.07% - representing an absolute difference of 2 μM. The error associated with the concentration of Mg^{2+} falls from 17% to 0.9%.

The errors associated with the **Lvk** method are lower than those of the **Lk** method. The difference between the accuracy of the methods is lowered in Case II, in which there is a small difference between the **Lk** and **Lvk** solutions for [NaCl] ≥ 0.1 M. The addition of the homogeneous reactions increased the difference between the reduced-order approaches and **NPP**, especially for the **Lvk** case. In the [NaCl] = 0.01 M case, for example, the current density difference is ca. 0.5% in Case I, in comparison to 4% in Case II, as seen in **Figure 2.16** (d).

If all species have the same diffusivities, the solutions obtained by **Lvk** are virtually identical to those obtained by the **NPP** approach. In comparison to Case II (as in Case III the homogeneous reactions were included in the calculations), the errors associated with the **Lk** approach decreased. In SER ratios < 30, the Lk error obtained in Case III is similar to those obtained in Case I. For SER ratios > 30, the error obtained in Case III is smaller than in Case I. At a SER ratio of 1000, the error of **Lk** in Case III is more than two orders of magnitude lower than in Case II and more than one order of magnitude lower than in Case I.

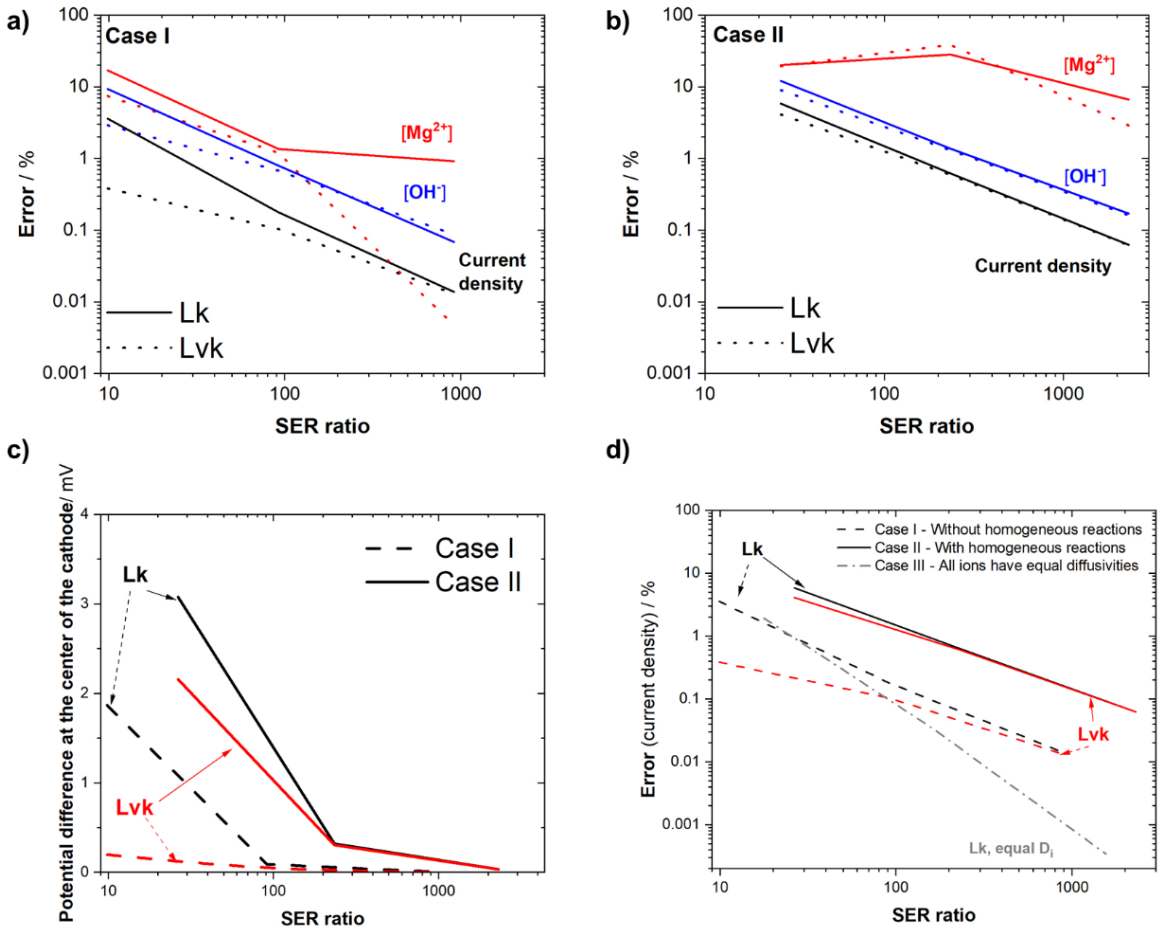

Figure 2.16. Percent error associated with the concentration of Mg^{2+} and OH^-, and the current density at the center of the cathode in Case I (a) and Case II (b) as a function of the supporting electrolyte to the reactive species ratio (SER). In (c), the absolute difference between the potential calculated at the center of the cathode is shown. In (d), the error in the current density associated with the reduced-order approaches is shown.

2.6. Discussion

The accuracy with which numerical models describe electrochemical phenomena depends not only on the governing equations used but also (and sometimes more importantly) on the accuracy of the properties of the solution and the interfacial reactions of interest. In this work, we are interested in determining the conditions in which simplifications regarding ionic transport can be made to model the galvanic coupling of two hypothetical metals in a planar geometry in a thin electrolyte solution. The objective is to find the parameter space in which we can separate the charge and mass transport calculations without losing much accuracy. The motivation for understanding the impact of simplifications on the

accuracy of the solution is the immense computational time savings possible with reduced-order models. As shown in **Table 2.2**, factors of almost 10 exist between the time required to calculate the most accurate solutions (via **NPP**) and the most simple governing equation (**Lk**), even for the simple geometry and electrochemical kinetics used here. Understanding the trade-offs between speed and accuracy is critical in deciding, for a given electrochemical system, which governing equations to use. This paper focuses on electrolyte conditions of most relevance to corrosion and electrochemical studies in which the baseline environment has ionic concentrations on the order of 0.1 M or more. In a following publication, the impact of low ionic concentrations on the accuracy of reduced-order modeling approaches will be analyzed.

To orient the reader, this section first compares the results of calculations using the most accurate governing equations, **NPP**, and the two variants of the fastest governing equations to solve, **Lk** and **Lvk**, showing that they result in virtually identical results but with **NPP** taking up to 10x longer to converge. The requirements for the supporting electrolyte effect to occur are described in terms of the ratio of the non-reactive/supporting electrolyte ions to (SER) to those involved in heterogeneous and homogeneous reactions. It is shown that in the demanding geometry used herein, ratios of greater than five are required for the error to be < 1% in current density. For most environments of interest in corrosion and electrochemistry, this magnitude SER is generally observed. The next section describes the impacts of homogeneous reactions which create sinks for species, such as precipitation reactions, on the error in the solutions from the reduced-order governing equations. The presence of a precipitation reaction increases the error of the reduced-order approaches, and a ratio of >100 is required for a <1% error in current density. The third section compares the results from **NPE** to **NPP** and shows that for all cases considered, the error is negligible, but the computation time can be reduced by up to a factor of 3 with the NPE.

2.6.1. The Lvk and Lk approaches can provide acceptable results in electrolytes with concentrations typically of importance in corrosion and electrochemistry problems

As described above and shown in **Table 2.2**, the reduction in computation time using either the **Lvk** or **Lk** as governing equations relative to the **NPP** governing equations is substantial. For electrolytes of sufficiently high conductivity, the loss of accuracy of potential, current density, and species concentration distributions is negligible when using the reduced-order models. Under these conditions, the migration flux of the Na^+ and Cl^- is ~90- 95% of the total migration flux; i.e., these ions essentially carry all of the current. The ratio between the migration flux of the Na^+ and Cl^- over the sum of the migration fluxes of all species is shown in **Figure S3**. Such situations are common in corrosion problems where background electrolyte concentrations on the order of 0.5 M are common, and minor species concentrations are on the order of mM or less. Even in electrochemical power sources, the supporting electrolyte used is often at quite high concentrations relative to the minor species.

As can be seen in **Figures 3.5**, **3.6**, **3.12**, and **3.14**, there are negligible differences between the results using the different governing equations in the distribution of the potential, current density, and species concentration after 7200 s for [NaCl] ≥ 0.1 M for the system studied. While for the most complex case shown in this work (Case II), the savings in computational time seem small (in the range of minutes for using **Lvk** in the lowest NaCl concentration), they might be determining for the feasibility of solving more complex models, in which the addition of multiple ions and subsequent homogeneous reactions, and/or 3D geometries are necessary and substantially increase the computational power necessary to solve the problem.

The value of the ratio of the supporting electrolyte species to the minor species that ensures the desired accuracy will depend on the type of system investigated. For example, a ratio of only 5 is needed when there are no homogeneous reactions (Case I), and the **Lvk** approach is used, as shown in **Figure 2.16** . The faster **Lk** approach requires a ratio of 25 for a maximum error in the current density of 1%.

2.6.2. The Lvk approach errors are due to the absence of the diffusion potential term in the calculation of the potential distribution

The errors associated with the **Lvk** approach are due to the absence of the diffusion potential term in the calculation of the charge conservation equation. In the view of electroneutrality, the governing equation of the coupled charge and mass conservation is described by Equation 7. Using the **Lvk** approach, the second term on the left side of the equation is taken into account, as the **Lvk** approach uses the local concentration and mobility of the species to calculate the spatiotemporal evolution of the electrolyte conductivity. However, the second term on the left side of the equation, which describes the additional driving force that prevents the separation of charge in a diffusing system, is neglected. The diffusion potential term alters the potential, current density, and species distributions. Thus, the distribution of species and resulting electrolyte conductivity calculated by the **Lvk** and **NPP** approaches will not be the same, but it is only due to the absence of the diffusion potential term. The proof of that is shown in Case III, in which the calculations of **NPP** and **Lvk** yielded the same results. In Case III, the models were performed for a case in which the diffusivities of the species were equal. If all species have the same diffusivity, the diffusion potential term is zero due to electroneutrality.

In a following publication, the consequences of the absence of the diffusion potential term on the species concentration and local electroneutrality will be discussed.

2.6.3. Systems involving precipitation reactions require higher ratios of non-reactive to reactive ions for low errors

The addition of the sink term and the equilibrium between H^+ and OH^- species increased the errors associated with the reduced-order approaches for the same supporting electrolyte to minor species ratio, as illustrated in **Figure 2.16.** For the same 1% maximum error in current density, the SER ratio increases from 25 to 145 and from 5 to 130 using the **Lk** and **Lvk** methods, respectively. For [NaCl] = 1 M, the addition of homogeneous reactions increased the error by almost one order of magnitude.

The sink term generated inhomogeneities in the electrolyte, which increased the errors of the reduced-order models. As seen in **Figure 2.14**, the distribution of the concentrations of Mg^{2+} and OH^- are more non-uniform in Case II; there is a higher concentration gradient of OH^- and Mg^{2+} across the electrodes near the electrolyte/electrolyte interface. The consumption of Mg^{2+} and OH^- at locations where the solubility product was reached caused a local decrease in the concentrations of Mg^{2+} and OH, which led to a local decrease in the electrolyte conductivity. As it can be observed in **Figure 2.11** (f), there is a minimum in the electrolyte conductivity at the anode and cathode junctions (x = 5 and 15 mm). Due to the higher currents near the junction of the anode and the cathode, there is a higher production of Mg^{2+} and OH^-, leading to a higher sink reaction rate. The species that cause most of the inhomogeneity of the electrolyte conductivity are the same that cause most of the diffusion potential. The higher the disparity between the diffusion coefficients of the ionic species, the higher the diffusion potential. As it can be seen in **Table 2.1**, the most discrepant diffusion coefficients pertain to Mg^{2+} and OH^-.

The higher electrolyte inhomogeneity is sufficient to explain the increased error of the **Lk** approach, as the calculations are performed assuming a uniform conductivity across the electrolyte. The increased error in Case II associated with the **Lvk** approach can be explained by the higher inhomogeneity in the Mg^{2+} and OH^- distributions; the higher concentration gradients lead to higher diffusion potential terms. Because in the **Lvk** method, the diffusion potential term is neglected, there will be discrepancies in the potential, current density, and species concentrations spatiotemporal distributions. So even though the electrolyte conductivity is calculated locally, the deviation in the species concentrations will lead to errors in the electrolyte conductivity calculation. Due to the strong interdependence between the potential, current density, and species spatiotemporal distributions, minor discrepancies in any of those variables can compound the error.

In Case III, even though the homogeneous reactions were implemented, the error associated with the **Lk** approach was similar to that of Case I at lower SER ratios. In higher SER ratios, the **Lk** error was much smaller in Case III than in Case I. These observations indicate that the higher error observed in Case II is associated with the diffusion potential term, corroborating the explanation that the higher concentration gradients of the Mg^{2+} and OH^- species due to the sink reaction increased the importance of the diffusion

potential and that, in high SER ratios, the errors of the reduced-order approaches are dominated by the absence of the diffusion potential term.

It is important to put in perspective the magnitude of the errors discussed here in comparison to the impact of the boundary conditions on the potential, current density, and species distributions. The typical exponential behavior of the relationship between the rate of electrochemical reactions with the overpotential will cause a much larger impact on the results for small discrepancies in the reaction parameters (*e.g.*, Tafel slope). For example, a 1% difference in the Tafel slope of the anodic kinetics leads to a 3.6% difference in the calculated current density; a difference of 10% in the Tafel slope leads to a 48% difference in the current density. As a contrast, the reduced-order approaches error is 0.07% in Case II, and 0.01% in Case I for the 1 M NaCl simulation.

2.6.4. Nernst-Planck solved with the electroneutrality condition using the method of elimination is a robust approach for the studied system

The solutions obtained with the **NPE** method were in excellent agreement with the **NPP** solutions, the latter being the gold standard governing equation. The length scales of the geometry of the system described herein are orders of magnitude larger than the length scales in which significant charge density is observed – typically 1-10 nm from the electrode surface (i.e., the double layer). The smallest mesh size utilized in the model is 7 μm, ca. 3 to 4 orders of magnitude larger than the typical double layer. The largest charge density calculated by the **NPP** approach was $8x10^{-19}$ C/mm^2 for the 1 M NaCl case, caused by a minute separation of the cations and anions summing to $3x10^{-15}$ equiv/dm^3, which is clearly negligible and could likely be reduced further with even finer meshing in those areas. Thus, electroneutrality is an appropriate assumption for the length scales of the problem considered and very likely would be for a wide range of corrosion phenomena of interest. In addition, the phenomena related to capacitive effects near the electrodes can be taken into account via the boundary conditions at the electrode/electrolyte interface [54].

The implementation of **NPE** method via the method of elimination is a robust approach to solving for the electroneutrality. Although the concentration of the make-up ion is artificially calculated by the electroneutrality condition, the difference in the concentration of the Na^+ (the chosen make-up ion for **NPE**) calculated using **NPP,** and that calculated using **NPE** was 0.0002%. It has been previously reported that there were discrepancies in modeling results when utilizing different make-up ions [56]for a case in which ionic equilibrium reactions were included in the calculations, as well as having a sink term. Those errors were not observed in the present work when either Na^+ or Cl^- were used as make-up ions for all cases modeled. **Figure 2.17** (a) shows the [Na^+] and [Cl^-] calculated with the **NPE** method using Na^+ and Cl^- as make-up ions in Case II. There was a negligible difference between the solutions. **Figure S2** shows that even if the make-up ions have significantly different diffusivities, the results were essentially identical.

The source of the discrepancy in using the **NPE** is the charge balance of the solution at t = 0 s. If the solution is not charge-balanced, then the choice of make-up ions does impact the results. Such a condition can occur when, for example, one adjusts the initial concentration of the ions to satisfy the equilibrium reactions according to their equilibrium constants, a common practice to aid convergence when modeling chemical reactions [109]. One can even perform a separate step involving only the solution of the mass conservation using equilibrium reactions in order to obtain the initial electrolyte composition [56]. Although this makes sense mathematically in terms of mass conservation, it might not necessarily obey charge conservation.

We can take the specific case presented in this work as an example, in which water autoionization and $Mg^{2+} + OH^- \leftrightarrow Mg(OH)_2$ are the homogeneous reactions considered to occur in the electrolyte. The water auto-ionization reaction associated with the relatively fast OH^- production at the cathode introduced numerical instability when the initial solution pH was 7. In the first 0.1 s, the concentrations of H^+ and OH^- change substantially, and the H^+ concentration becomes negative (i.e., -0.1 μM). It was observed that the faster the transient, the more negative the H^+ became. Thus, the initial pH was changed to a higher value to aid model convergence. In doing so, the initial concentration of Mg^{2+} also had to be changed to maintain equilibrium. If we assume the reactions are in equilibrium at t = 0 s with an initial pH of 10, and we use the equilibrium constants to calculate the initial values of the other species in a way that satisfies the equilibrium equations, the initial concentration of OH^- will be 10^{-4} M, according to K_w (10^{-14}); and Mg^{2+} would be $4.12x10^{-4}$ M according to a K_{sp} of $4.12x10^{-12}$, as simulated in OLI Studios. These concentrations satisfy the imposed equilibrium expressions, but they disturb electroneutrality, as the summation of the product between the species concentrations and their respective charge number yields a net charge of $+7.24x10^{-4}$ equiv/dm^3.

For the initially unbalanced electrolyte case, the **NPP** method did not converge, as it has no means by which to correct the initial, non-physical net charge in the electrolyte. The **NPE** method did converge, but discrepancies were found when using different make-up ions.

Figure 2.17 (a) shows the initial concentrations of the ions in the unbalanced electrolyte, and **Figure 2.17** (b)-(e) compares the solutions obtained when using either Na^+ (**NPE-Na**) or Cl^- (**NPE-Cl**) as the make-up ion for a [NaCl] = 1 M. **Figure 2.17** (b) shows the concentration of Na^+ and Cl^- calculated by **NPE-Na** and **NPE-Cl** methods for a 1 M NaCl solution. When Na^{+-} is used as the make-up ion, the overall Na^+ concentration is lower than that resulting from the **NPE-Cl**$^-$; the average Na^+ concentration calculated by the **NPE-Na** method was 0.99928 M, while the average Cl^- concentration is 1.0000 M. When Cl^- is used as the make-up ion, the overall Cl^- is higher than that resulting from the **NPE-Na** method; the calculated averaged Cl^- concentration is 1.00072 M, while the averaged Na^+ is 1.0000 M, equal to its initial concentration. That is, there is a deficit of 0.00072 M of Na^+ when Na^+ is used as the make-up ion and a

surplus of 0.00072 M of Cl^- when Cl^- is used as the make-up ion. The deficit of the cation and the surplus of the anion balance the excess of the positive charge of the initial electrolyte condition. **Figure 2.17** (d) and (e) display the discrepancies in the potential distributions obtained by **NPE-Na** and **NPE-Cl** and the potential distribution obtained via **NPP**, for the case in which the electrolyte was charge-balanced. In the 1 M NaCl case, there were negligible differences between the potentials calculated by the different make-up ions, both of which differed from the **NPP** solution, albeit marginally.

It should also be noted that although the **NPE** method provided solutions in close agreement with **NPP** while requiring far less computational time (by a factor of up to 3), it requires the use of a species to which no explicit boundary conditions can be applied. In the present study, Na^+ and Cl^- were the only options available, as Mg^{2+} and OH^- had explicit boundary conditions at the electrodes through Faraday's law, and their concentrations, in addition to H^+, were subject to reaction terms in the electrolyte domain.

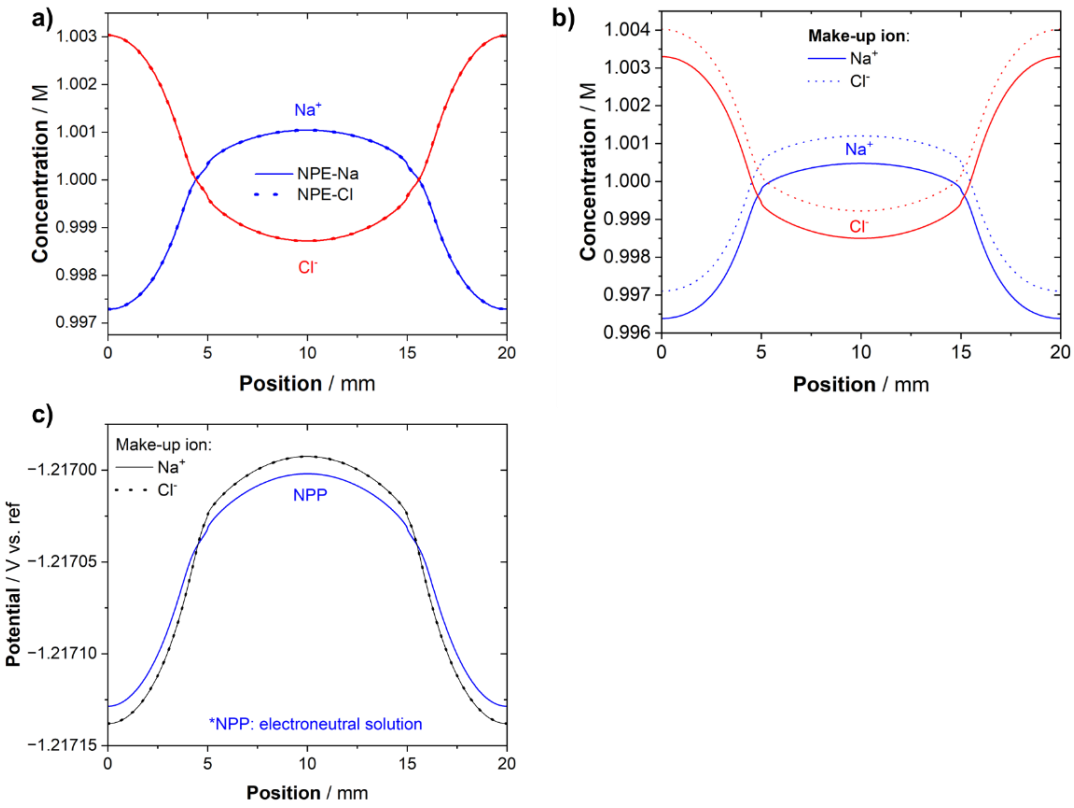

Figure 2.17. Impact of the make-up ion on the species concentration and potential distributions. In (a), the concentration profiles of Na^+ and Cl^- obtained when using either Na^+ (**NPE-Na**) or Cl^- (**NPE-Cl**) as the make-up ions in Case II for a NaCl concentration of 1 M are shown. The concentration profiles of Na^+ and Cl^- (b) and the potential distribution at the electrodes (c) obtained using NPE-Na and NPE-Cl are shown for a case in which the electrolyte is not electroneutral at t = 0s.

Table 2.3. Initial concentration of the ionic species and the product of the their concentration and their respective charge number used in a case in which the electrolyte was not electroneutral at t = 0 s.

Species	Initial concentration / M	$z_i c_i$ / equiv/dm^3
Mg^{2+}	4.2×10^{-4}	8.24×10^{-4}
Na^+	1[a]	1
Cl^-	1[b]	-1
H^+	1.0×10^{-10}	1×10^{-9}
OH^-	1.0×10^{-4}	-1×10^{-4}
	$\sum z_i c_i$	7.24×10^{-4}

a. Initial concentration of Na^+ when Cl^- is used as the make-up ion

b. Initial concentration of Cl^- when Na^+ is used as the make-up ion

2.6.5. Limitations

Because of the strong interdependency between the potential, current density, and species distribution, the conclusions made herein are applied to the specific system investigated. Changes in the electrochemical kinetics of the materials, ions of interest, and geometry may result in different conclusions regarding the minimal supporting electrolyte-to-reacting species (SER) ratio required to obtain the desired accuracy. However, qualitatively, the conclusions can be generalized to other systems.

In a system in which the hydrolysis of metal cations leads to local acidification, the error associated with the diffusion potential term may be higher due to the faster rate at which H^+ diffuses relative to the other ions ($D_{H^+} \sim 9.3 \times 10^{-9} m^2/s$). In the presence of large concentration gradients, the minimum ratio between the supporting electrolyte to the electrochemically active species might be much higher. Such conditions can be found in pits and crevices, in which the dissolution of metal and the subsequent hydrolysis of the metal cations in an occluded geometry cause local acidification and high concentration gradients.

The model does not take into account convection in the electrolyte. The model simulates the diffusion layer of a quiescent electrolyte and assumes that the thickness of the diffusion layer is 3000 µm. In quiescent solutions, the thickness of the diffusion boundary layer was found to be close to 800 µm, beyond which natural convection dominated the mass transport [62]. The decrease in the diffusion boundary layer increases the concentration gradients, leading to an increase in the diffusion potential [84], which causes deviations in the reduced-order model from the most rigorous modeling approaches.

Even though the model was performed considering relatively high concentrations of supporting electrolyte, the calculations were performed using an infinite dilution assumption. In more concentrated solutions, activity gradients should be used as the driving force for diffusion processes (and not concentration), and additional composition-dependent transport parameters become necessary [54].

2.7. Conclusions

In this work, the potential, current density, and species spatiotemporal distributions obtained by different governing equations used to solve for mass and charge conservation in the electrolyte in a galvanic cell were compared. The errors associated with the assumptions typically taken to simplify the calculations were quantitatively described. The impact of a supporting electrolyte concentration, in a range commonly found in corrosion problems, was verified.

- The reduced-order models can save substantial computational time without significant loss in accuracy in a sufficiently high ratio of non-reactive to electrochemically active ions concentrations (SER).
- The critical SER above which the error is below a desired threshold depends on the system; the critical ratio increased for the same percent error in the case in which a sink term simulating a precipitation reactions were modeled. For the systems considered herein, SER >50 led to errors in potential of < 3mV, and in current density and species concentrations <10%.
- The error associated with the **Lvk** approach is solely due to the absence of the diffusion potential term in the electric field calculation, and its solution can be used to investigate the impact of diffusion potential on the potential, current density, and species distributions.
- The method of elimination is a robust approach to solve for the **NPE** approach if the electrolyte is initially charge balanced.

In a following publication, the analysis is extended to lower concentrations of supporting electrolyte, and a discussion of the relative importance of the migration and diffusion terms on the potential distributions calculated by the two Laplace approaches gives context to the sources of the errors and the issue of local and global charge balance in the electrolyte is addressed

2.8. Acknowledgments

Financial support from the SERDP program through the Office of Naval Research (C. Sanders) via Contract N00173-19-1-G011 as well as the DOD Corrosion Program Office through the US Air Force Academy via Contract FA7000-18-2-0006 is gratefully acknowledged.

A Comparison of FEM Results from the Use of Different Governing Equations in a Galvanic Cell

Part II: Impact of Low Supporting Electrolyte Concentration

C. V. Moraes[a] and R. G. Kelly[a]

[a] Center for Electrochemical Science and Engineering, Department of Materials Science and Engineering, University of Virginia, Charlottesville, VA 22904, USA

Corresponding author: rgk6y@virginia.edu

2.9. Abstract

The use of reduced-order models for simulating potential, current density, and species distribution in an electrolyte are attractive due to the high computational costs required to solve the intricate set of highly nonlinear partial differential equations and boundary conditions characteristic of electrochemistry problems. In Part I of this work, it was shown that the loss in accuracy of the reduced-order models is small in high supporting electrolyte concentrations, and there was substantial savings in computational time. The analysis is extended to lower supporting electrolyte concentrations. The most reduced-order modeling approach performs poorly in low supporting electrolyte to electrochemically active species (SER) ratios. The modified Laplace approach improves the solution by updating the electrolyte conductivity at each time step, but the errors can be still significant in low SER ratios due to the absence of the diffusion potential term in the calculations.

Keywords: Modeling, Nernst-Planck equation, Laplace equation, Finite element method, Galvanic cell

2.10. Introduction

As described in Part 1 [110], the accessibility of commercially available physics-based FEM models has increased dramatically in the past two decades. Electrochemical systems, including those related to corrosion, are particularly well suited for the FEM approach as the governing equations are well known, and there is substantial literature on the topic [64,69,84,88,90,96,97,104,111,112]. This accessibility promises to allow more researchers to use these tools to model corrosion and electrochemical systems in which the distribution of potential, current density and species concentration is important in determining the initiation and progression of different forms of corrosion, for example.

The Nernst-Planck approach captures the three forms of mass transport that can occur in solution: migration, diffusion, and convection. In many cases, the convection term is ignored as either the system does not involve fluid flow or it is deemed too difficult computationally. By combining the Nernst-Planck equation with mass conservation, flux equations for each species of interest can be developed, leading to a

system of partial differential equations. However, an additional equation is needed that involves the potential in order to make the system of equations solvable. As pointed out in Part I [110], there are several approaches to determining the potential, each with its own level of rigor.

Although the highest level of rigor would seem to be critical, there can be very, very high computational costs that accompany such a choice. In some cases, the computational costs can be such that convergence to a solution is not possible, even with supercomputers. Thus reduced-order approaches have become very popular choices for modeling electrochemical systems [62,69,72,84,86–88,92,97,111]. However, few guidelines have been given regarding what the costs in accuracy are with the various reduced-order approaches and how that accuracy may be affected by system variables such as electrolyte concentration. In Part I [110], it was shown that for modest to high electrolyte concentrations, reduced-order approaches to the governing equations for potential produce results very close to those calculated with the most rigorous approach. The required ratio of supporting electrolyte to electrochemically reactive species (SER) of ca. 50 would indicate that in many, if not most, corrosion systems, reduced-order models would provide sufficient accuracy for most purposes. In this paper, the analysis is extended to lower SER to determine how the error increases in low conductivity environments.

For more details on the overarching problem with the selection of governing equations, the reduced-order approaches, the description of the model system studied, and the results for systems of high SER, please see Part I [110]. This manuscript focuses on systems with SER < 10.

2.11. Model description

The different governing equations (**NPP**, **NPE**, **Lvk**, and **Lk**) were used to calculate the potential, current density, and species distributions resulting from the galvanic coupling of two metals in a simple, 2D geometry. The concentration of the supporting electrolyte, NaCl, was varied from 10 to 0.1 mM. **Figure 2.1** (a) shows the geometry used in the work. The 10 mm scribe is centered in the geometry and lies within the two 5 mm portions of the MgRP-coated panel. At the scribe, hydrogen evolution reaction (HER) occurs. At the coating and the cut edges, anodic dissolution of Mg occurs. Details about the governing equations and boundary conditions can be found in Part I [110].

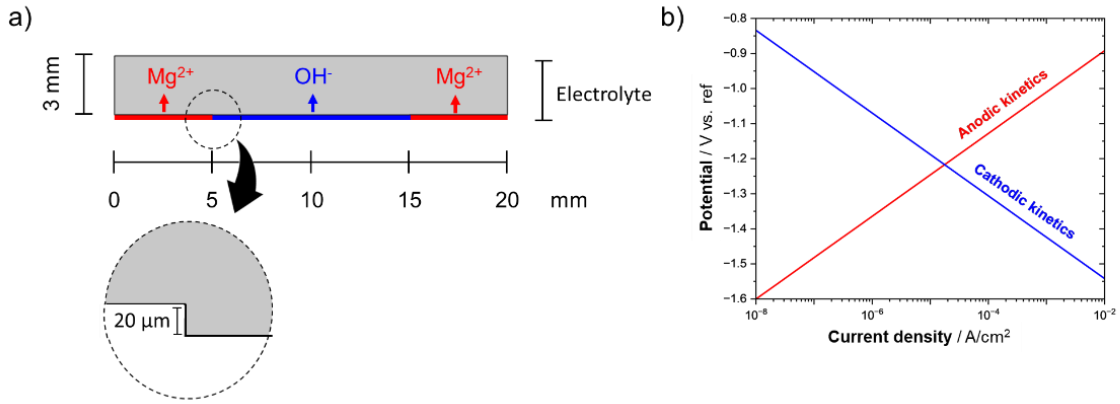

Figure 2.18. (a) Geometry utilized in the model; (b) Boundary conditions at the electrode/electrolyte interface: Tafel kinetics are used to describe the electrochemical behavior of the anode and cathode.

The model solved for the concentration of five species: Mg^{2+}, OH^-, H^+, Na^+, and Cl^-. The species diffusivities were acquired utilizing OLI Studios (v. 11), calculated for [NaCl] = 0.1 M at 25 ˚C and 1 atm. The diffusivities are shown in **Table 2.4**.

The model is developed under the following assumptions of quiescent electrolyte: that is, there is no forced or natural convection (the electrolyte layer is thinner than the diffusion layer), and infinite dilution: there is no interaction between the ions, apart from that necessary to maintain electroneutrality (in the **NPP** and **NPE** approaches).

Table 2.4. Parameters utilized in the model.

Parameter	Parameter description	Value	Reference
$\mathbf{D_{Na^+}}$	Diffusion coefficient of Na^+	$1.18x10^{-9}$ m^2/s	OLI Studios (v. 11)
$\mathbf{D_{Cl^-}}$	Diffusion coefficient of Cl^-	$1.75x10^{-9}$ m^2/s	OLI Studios (v. 11)
$\mathbf{D_{H^+}}$	Diffusion coefficient of H^+	$9.30\ x10^{-9}$ m^2/s	OLI Studios (v. 11)
$\mathbf{D_{OH^-}}$	Diffusion coefficient of OH^-	$5.22\ x10^{-9}$ m^2/s	OLI Studios (v. 11)
$\mathbf{D_{Mg^{2+}}}$	Diffusion coefficient of Mg^{2+}	$0.72\ x10^{-9}$ m^2/s	OLI Studios (v. 11)
$\boldsymbol{i_0}$	Exchange current density of the anodic and cathodic reaction	10^{-8} A/cm^2	Arbitrarily chosen
$\mathbf{E_{0,\ cathodic}}$	Reversible potential of the cathodic reaction	-0.346 V vs. ref	Arbitrarily chosen
$\mathbf{E_{0,\ anodic}}$	Reversible potential of anodic reaction	-1.60 V vs. ref	Arbitrarily chosen
B	Tafel slope of the anodic and cathodic dissolution	-118 mV	Arbitrarily chosen
k	Sink term reaction rate constant	$3.7\ m^6/(s{\cdot}mol^2)$	[87]
$\mathbf{k_{sp,\ app}}$	Apparent solubility product of $Mg(OH)_2$	$4.12x10^{-12}$ mol^3/dm^9	OLI Studios (v. 11)

2.11.1. Description of the cases evaluated

The goal of this work is to compare the solutions obtained with the most general model (**NPP**) to the most reduced-order model (**Lk**) under lower suppoting electrolyte (SE) concentrations. The models were performed for 0.01, 0.1, and 1 M NaCl in three different cases. In Case I, homogeneous reactions were not considered. Thus, the electrolyte composition changed due to the electrochemical reactions, and the minor species accumulated with time in the closed system. In Case II, homogeneous reactions were considered. In Case III, the models were performed with and without homogeneous reactions, but the diffusivities of all ions were equal to 10^{-9} m^2/s.

2.12. Results

2.12.1. Comparison between the computational time of each calculation method

Table 2.5 shows the computational time required by each calculation method in the various NaCl concentration for Case I and Case II. The computational time was generally inversely correlated to the number of simplifications of each approach: **Lk** was the fastest to compute, followed by **Lvk**, **NPE,** and **NPP**, in increasing order. The **NPP** approach took up to ca. 9 times longer to compute in comparison to the

Lk approach. The **Lvk** approach took about twice the time to compute compared to **Lk**. In comparison to **NPE**, **NPP** took up to 3 times longer. The addition of homogeneous reactions considerably increased the computational time, especially at high NaCl concentrations. Increasing the NaCl concentration from 1 to 10 mM led to a 10-fold increase in the computational time.

Table 2.5. Comparison between the computational time of the different governing equations

		Computational time / s		
	NaCl concentration / mM	0.1	1	10
Case I	Lk	15	13	13
	Lvk	28	26	27
	NPE	41	37	30
	NPP	68	75	87
Case II	Lk	25	60	766
	Lvk	50	76	310
	NPE	127	283	4800
	NPP	218	415	6105

2.12.2. Comparison between Nernst-Planck-Poisson and Nernst-Planck solved with electroneutrality

The solutions obtained by solving the Nernst-Planck equations utilizing the electroneutrality condition (**NPE**) yielded results that were identical or nearly identical to the results obtained by solving for the charge conservation utilizing Poisson's equation (**NPP). Figure 2.19**(a)-(d) compare the results of selected variables calculated with the **NPE** and **NPP** approach for a case in which the concentration of the supporting electrolyte, NaCl, was 0.1 mM. **Figure 2.19** (a) shows the potential transient at the center of the cathode. **Figure 2.19** (b) and (c) show the potential and current density distribution along the electrodes after 7200 s of simulation. **Figure 2.19** (d) shows the Na^+ concentration profile adjacent to the electrode/electrolyte interface after 7200 s of simulation. There is a negligible difference between the solutions. Even the concentration of the make-up ion, which is artificially calculated using the **NPE** approach, was nearly identical in both approaches. The largest difference between the [Na^+] found among all the cases modeled was less than 0.01% .

Figure 2.20 (a) shows the summation of the product of the concentration of each species and its charge adjacent to the electrode/electrolyte interface. The **NPE** method enforces electroneutrality, so the sum of the product of the concentration of each species and its charge is necessarily nearly zero (10^{-19} equiv/dm^3) – any non-zero value falls within the error tolerance for the model convergence. The **NPP**

approach allows for charge separation, as charge conservation is solved by Poisson's equation and not by enforcing electroneutrality. However, because of the length scale of the geometry studied, the electrolyte is electroneutral, as shown in **Figure 2.20** (a). There is a minute excess charge separation (10^{-9} equiv/dm^3) at the anode and cathode point of contact that can be neglected. **Figure 2.20** (b) shows the charge density in the electrolyte calculated by the **NPP** method. Again, the calculation shows a small charge density at the anode and cathode point of contact – ca. 10^{-9} C/m^2. Although small, the charge density found was 2 order of magnitude higher than in the 10 mM NaCl concentration reported in Part I [110].

Because of the similarity between the results obtained by the **NPP** and **NPE** approaches, the Laplace (**Lk**) and pseudo-Laplace (**Lvk**) approaches are only compared to the **NPP** approach unless otherwise noted.

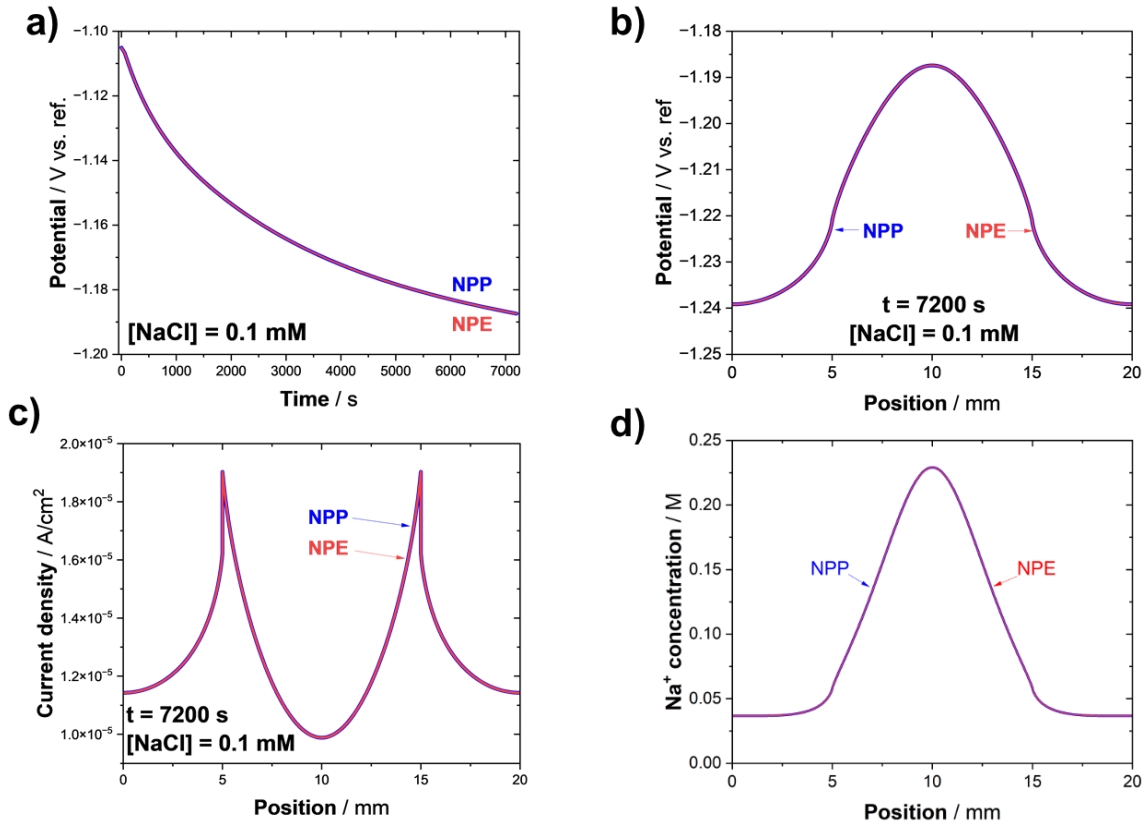

Figure 2.19. Solutions obtained by the **NPP** and **NPE** method utilizing Na^+ as the make-up ion. (a) Potential transient at x = 10 mm (middle of the cathode); Potential (b), current density (c), and Na^+ concentration profiles near the electrode/electrolyte interface after 7200 s.

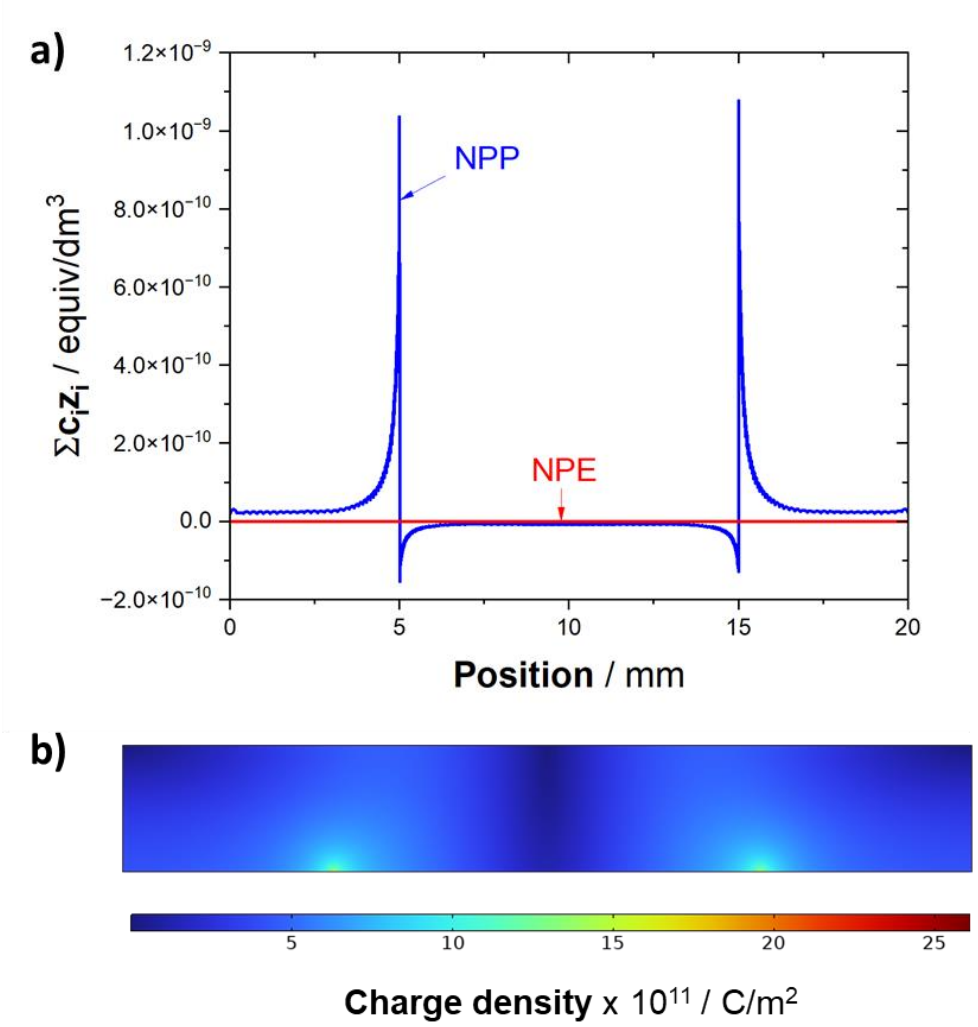

Figure 2.20. The charge density calculated by the summation of the product of each species concentration and their respective charge adjacent to the electrode/electrolyte interface calculated with **NPP** and **NPE** (a) and through the electrolyte, calculated with **NPP**.

2.12.3. Comparison between the approaches in the absence of homogenous reactions (Case I)

The aim of the following sections is to compare the results for selected variables obtained using the simplified approaches, **Lk** and **Lvk**, to the most general method, **NPP,** as a function of supporting electrolyte concentration. All the transients presented were calculated at the midpoint of the cathode (x = 10 mm), and the positional distributions were calculated at/near the electrode/electrolyte interface (y = 0 mm) after 7200 s of simulation. Firstly, the impact of the NaCl concentration on the potential, current density, and species distributions calculated by the **NPP** approach are briefly reported. Then, the impact of the NaCl concentration on the differences between the calculation methods is described.

2.12.3.1. Potential, current density, and electrolyte conductivity transients with NPP

Figure 2.20 shows the potential (a), current density (b), and the electrolyte conductivity (κ) normalized by its initial value (c) at the center of the cathode (x = 10 mm) as a function of time at varying NaCl concentrations calculated by the **Lk**, **Lvk,** and **NPP** methods.

The potential and current density decrease with time in the middle of the cathode, and the electrolyte conductivity increases with time due to the generation of ionic species by the interfacial reactions. The degree to which the potential, current density, and electrolyte conductivity change decreases as the concentration of the supporting electrolyte (NaCl) increases. In the lowest NaCl considered (0.1 mM), the conductivity has a 20-fold increase after 7200 s. The potential decreases 82 mV, starting at -1.105 V and falling to -1.187 V after 7200 s. As the potential at the cathode decreases, the current density decreases (the absolute value of the cathodic current density increases) from -1.98×10^{-6} to 9.88×10^{-6} A/cm^2. As the concentration of NaCl increases, the potential and current density at t = 0 s decrease. The temporal change of the variables is smaller; in the 1 mM case, the potential decreases by 22 mV, the current density by 4.3×10^{-6} A/cm^2, and the electrolyte conductivity has a 4-fold increase. For the 10 mM case, the potential decreases by 1.9 mV, the current density by 0.72×10^{-6} A/cm^{2,} and the conductivity has a 1.44-fold increase.

The potential and current density calculated by the **Lk** approach do not vary with time, as the electrolyte conductivity is constant and equal to the electrolyte conductivity at t = 0 s at their respective compositions. Thus, the **Lk** solution deviates from the **NPP** with time. The **Lvk** method is in closer agreement with the **NPP** solutions. In these NaCl concentrations, the **Lvk** approach underestimates the potential and current density at the center of the cathode, and it overestimates the electrolyte conductivity in the middle of the cathode. The discrepancy between **Lvk** and the **NPP** solutions generally increases with time.

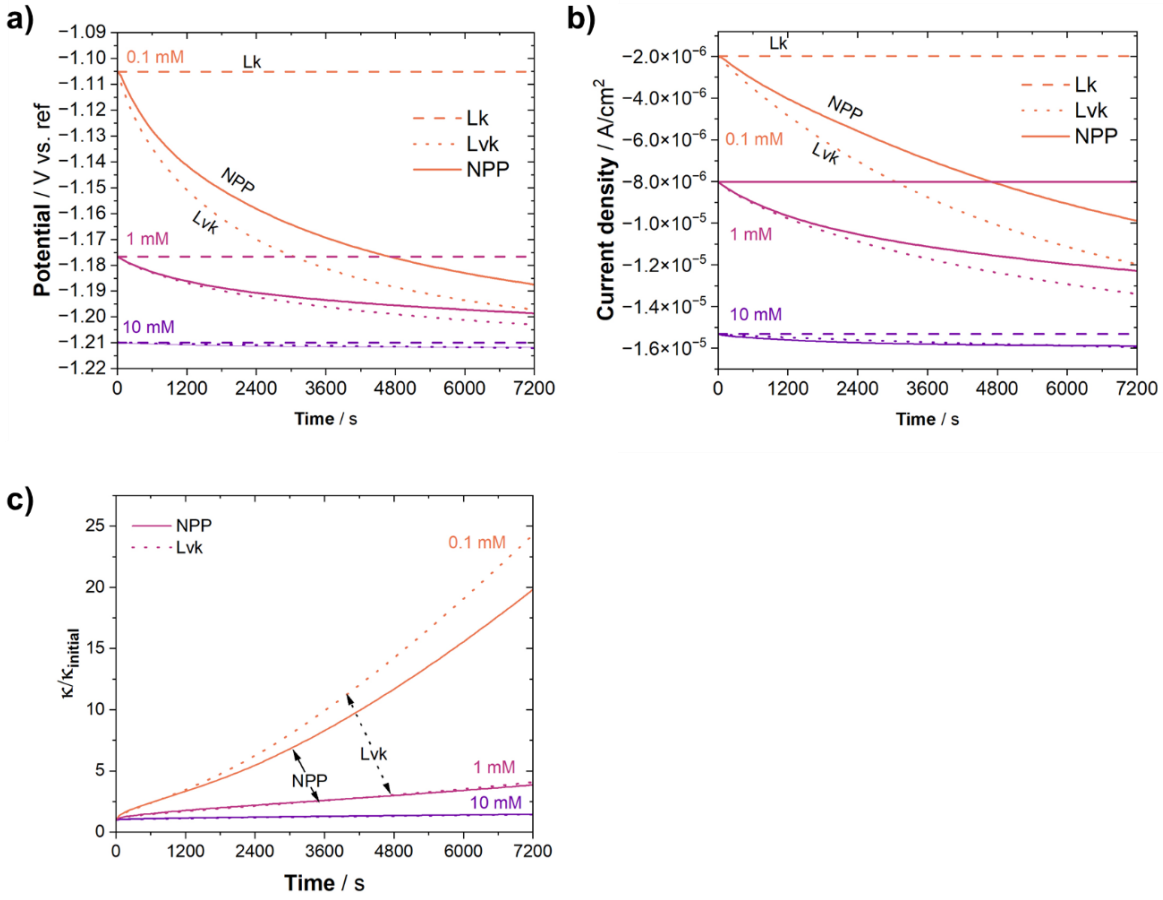

Figure 2.21. Potential and current density transients at the center of the cathode calculated by the Lk, Lvk, and NPP for varying NaCl concentrations: (a) potential transient for 0.1, 1, and 10 mM NaCl; (b) current density transient for 0.1, 1, and 10 mM NaCl.

2.12.3.2. Potential, current density, and electrolyte conductivity distributions near the electrode/electrolyte interface after 7200 s for Lk and Lvk vs. NPP

Figure 2.22 shows the potential at the electrodes as a function of position adjacent to the electrode/electrolyte interface (y = 0 mm) after 7200 s calculated by the different methods for varying NaCl concentrations. The y-axis scale changes for each NaCl concentration to better observe the differences between the calculation methods for each case.

The potential difference across the electrodes increases as the concentration of NaCl decreases. As a result, the potential in the middle of the cathode increases with decreasing NaCl concentration, while the potential at the edges of the anode decreases with decreasing NaCl concentration. At the lowest NaCl concentration, the **NPP** solution calculates an ohmic drop of 52 mV (**Figure 2.22** (c1)), whereas the ohmic drop decreases to 14 mV in the 10 mM NaCl case (**Figure 2.22** (a1)).

Figure 2.22 (a2), (b2), and (c2) display the absolute value of the current density as a function of position after 7200 s. The current density is the highest at the point of contact between the anode and the cathode, and it decreases with distance from the point of contact due to the resistance to the current flow in the solution. As the NaCl concentration increases and the electrolyte becomes more conductive, the absolute value of the current density increases and becomes more uniform across the electrodes.

The potential and current density distributions calculated by the **Lk** approach are significantly different than the solutions provided by the **NPP** method in the lower NaCl concentrations considered in this work compared to the results shown in Part I [110]. The **Lk** approach significantly overestimates the potential difference across the electrodes. The deviation in potential increases with the distance from the point of contact between the anode and cathode. As a result of the lower ohmic drop, the current density distribution is less uniform – the current density is high at the junction between the anode and the cathode and steeply decreases with increasing distance from the junction. As the concentration of the supporting electrolyte decreases, the discrepancies between the solutions obtained by the different methods increase. For the [NaCl] = 0.1 mM, the **Lk** calculates a 200 mV difference between the edges of the anode and the center of the cathode, whereas the potential difference calculated by **NPP** is 52 mV.

The **Lvk** solutions are in better agreement with the **NPP** method. In the [NaCl] = 10 mM case, the **Lvk** and **NPP** solutions are similar. Differently from the **Lk** approach, the **Lvk** method calculates a lower ohmic drop across the electrodes for [NaCl] = 0.1 and 1 mM, in comparison with the **NPP** approach. As a result, the current densities are higher throughout the electrodes.

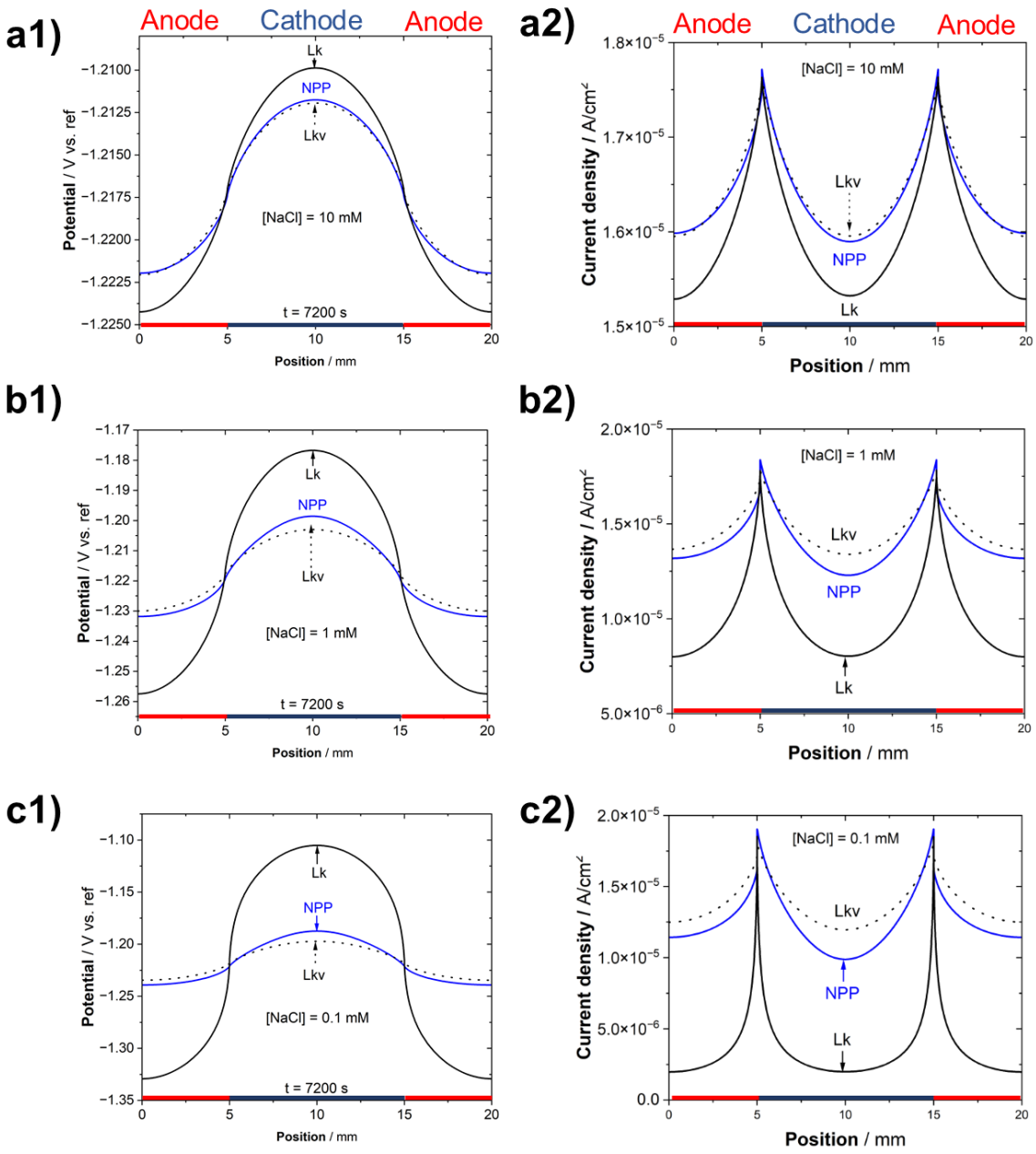

Figure 2.22. Potential and the absolute value of current density as a function of position after 7200 s obtained by the different calculation methods (**NPP**, **Lvk**, and **Lk**) for varying supporting electrolyte concentration (NaCl): a1-2) 10 mM; b1-2) 1 mM; c1-2) 0.1 mM; Please note that the potential and current density scale on the y-axis changes for each [NaCl].

Figure 2.23 shows electrolyte conductivity profile at t = 7200 s normalized by the initial electrolyte conductivity calculated by the **NPP** and **Lvk** approaches. In the **Lk** approach, the conductivity is uniform and constant, so the ratio is 1 for all cases.

For the 0.1 mM NaCl case, the conductivity increased substantially after 7200 s, as also observed in **Figure 2.21** (c). In addition to the temporal variation, the electrolyte conductivity varied considerably in space: at the anodes, the electrolyte conductivity is ca. 2 times higher than at the cathode. As the NaCl concentration increases, the electrolyte conductivity is more uniform with position and time. The **Lvk** approach captures the spatiotemporal changes in the electrolyte conductivity, but it deviates from the **NPP** solution: it underestimates the conductivity near the anodes and overestimates the conductivity near the cathode.

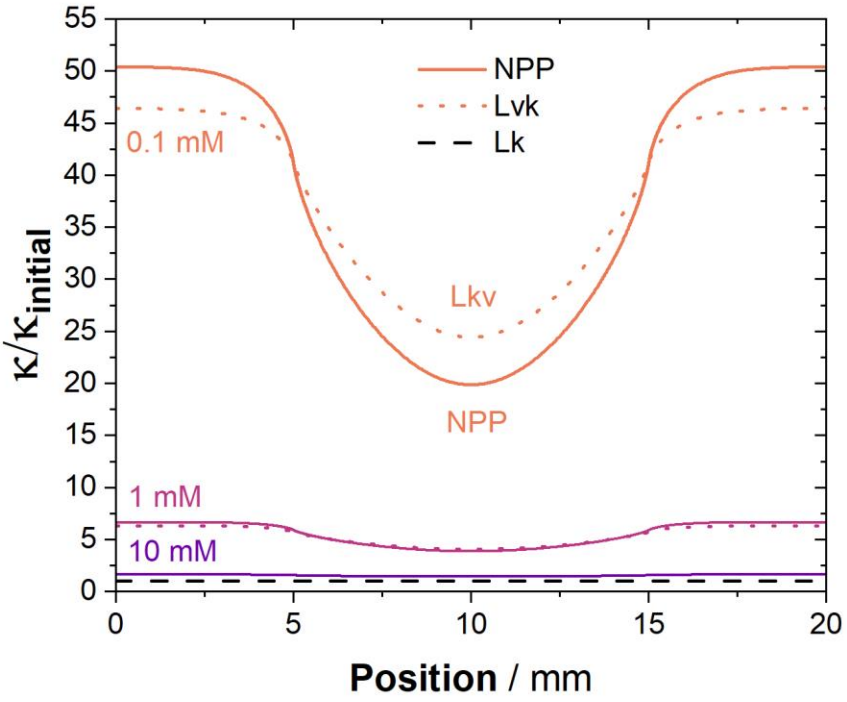

Figure 2.23. Ratio between the electrolyte conductivity at t = 7200 s and the initial electrolyte conductivity calculated by the **NPP** and **Lvk** approaches.

2.12.3.3. Species transient and profile

This section presents the results comparing the concentration of the species (Na^+, Cl^-, Mg^{2+}, H^+, and OH^-) as a function of time and position calculated with the different methods. For the **Lk** and **Lvk** methods, the transport by migration and diffusion and the production of the reacting species (Mg^{2+} and OH^-) via electrochemical reactions were calculated by coupling the Transport of Diluted Species and the Secondary Current Density modules of COMSOL. The rate of production of Mg^{2+} and OH^- were calculated using the solved current density through Faraday's law. The potential distribution calculation is decoupled from the transport of species – the potential gradient calculated using Laplace's equation is applied to solve for the

migration term in the transport of species. In the **Lvk** method, the computed concentrations are used in the Secondary Current Distribution module to update the local electrolyte conductivity using Equation 1:

$$\kappa = \mathrm{F}^2 \sum_{i} z_i^2 u_i c_i \qquad (1)$$

where F is the Faraday's constant, $z_i$is the charge number of species i, $u_i$is the mobility of species i, and c_i is the concentration of species i. The species mobility was calculated using the Nernst-Einstein relation.

Reacting species

Figure 2.24 shows the concentration transient of Mg^{2+} and OH^- (at the center of the cathode (x = 10 mm) for NaCl concentrations varying from 0.1 to 10 mM. The Mg^{2+} and OH^- concentrations increase as the electrochemical reactions occurring at the electrodes progress.The **Lk** approach overestimates the concentration of Mg^{2+} and underestimates the concentration of OH^- at the center of the cathode. The rate at which the Mg^{2+} concentration increases is faster in the **Lk** approach, while the rate at which the OH^- concentration increases is slower. As a result, the deviation from the **NPP** approach increases as time progresses.

In accordance with the results shown in the previous sections, the **Lvk** method has a better agreement with the **NPP** approach. For all cases, the **Lvk** solution is closer to the **NPP** solution than the **Lk** solution. In the lowest NaCl concentration, the Mg^{2+} concentration calculated by the **Lvk** is in a very good agreement with the **NPP** approach, although the concentration is slightly overestimated. The OH^- concentration is overestimated to a greater extent. For the [NaCl] = 10 mM, the **Lvk** method overestimates the concentration of Mg^{2+} and underestimates the concentration of OH^- at the center of the cathode.

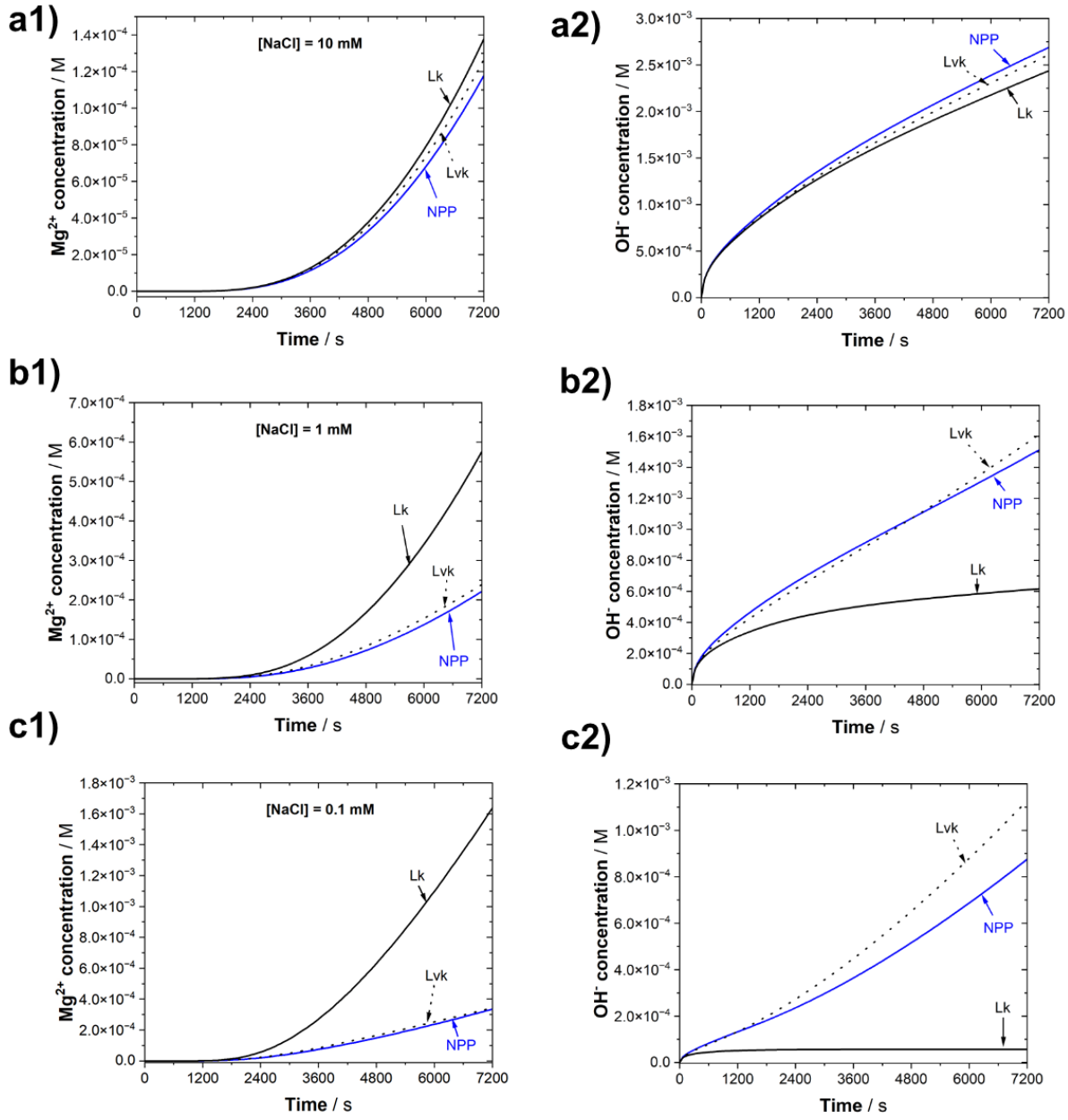

Figure 2.24. Transient of Mg^{2+} ((a1) to (e1)) and OH^- ((a2) to (e2)) in the middle of the cathode (x = 10 mm) calculated by the **Lk**, **Lvk**, and **NPP** methods in varying NaCl concentrations: (a) 10 mM, (b) 1 mM, and (c) 0.1 mM.

The concentration profiles of Mg^{2+} and OH^- near the electrode/electrolyte interface after 7200 s are displayed in **Figure 2.25**. In the **NPP** approach, the concentration of Mg^{2+} decreases with position away from the edge of anodes towards the center of the cathodes for all NaCl concentrations. The OH^- concentration profile also displays a minimum at the center of the cathode for the [NaCl] = 0.1 and 1 mM,

but the profile changes at the NaCl concentration of 10 mM – the OH^- concentration is lower near the anodes and higher near the cathode.

The species distributions calculated by the **Lk** approach are remarkably different (qualitatively and quantitatively) than those obtained by the **NPP** and **Lvk** methods for the [NaCl] = 0.1 mM (**Figure 2.25** (c1-2)) and 1 mM (**Figure 2.25** (b1-2)). The Mg^{2+} concentration profile calculated by the **Lk** approach displays an opposite behavior compared to the other approaches: its concentration is higher above the cathode and lower above the anode (**Figure 2.25** (c1)). For a [NaCl] = 1 mM, the $[Mg^{2+}]$ increases as it approaches the cathode, reaching a maximum near the interface between the anode and cathode. At the center of the cathode, $[Mg^{2+}]$ reaches a minimum (**Figure 2.25** (b1)). The **Lk** approach also underestimates the concentration of OH^- at the cathode and overestimates it at the anodes.

Again, the **Lvk** method displayed better agreement with the **NPP** approach. For the [NaCl] = 0.1 and 1 mM, **Lvk** calculates a higher Mg^{2+} concentration at the anodes. The deviation from the **NPP** approach decreases at the cathode, and the Mg^{2+} concentration calculated by the **Lvk** approach is closest to that calculated by the **NPP** approach at the center of the cathode. Additionally, the **Lvk** approach calculates a more uniform OH^- profile; at the anodes, the OH concentration is underestimated, and at the center of the cathode, it is overestimated. In the 10 mM NaCl case, the reduced-order approaches agreed better with the **NPP** solution.

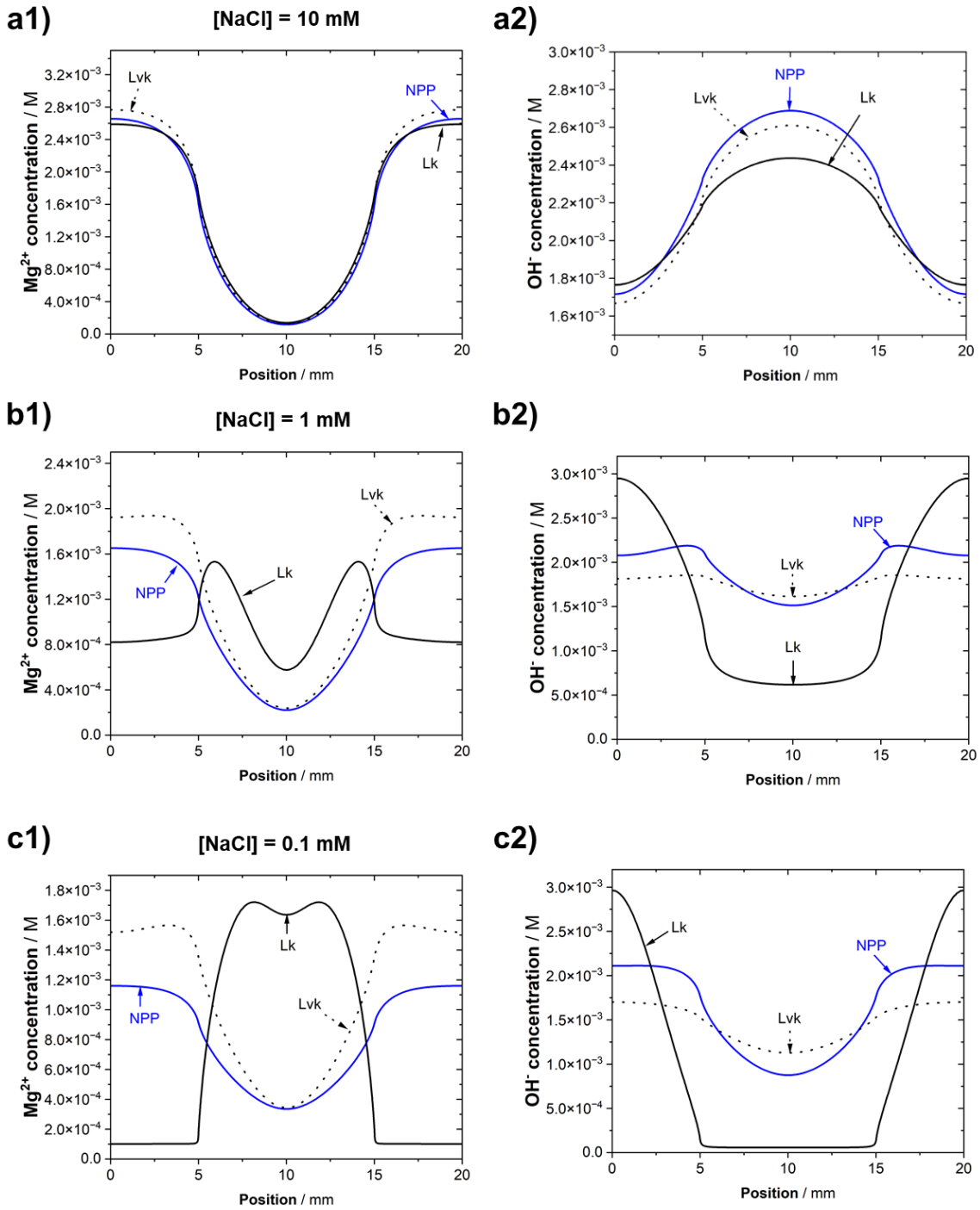

Figure 2.25. Concentration profile of the electrochemically active species adjacent to the electrode/electrolyte interface after 7200 s in Case I for the NaCl concentrations of 10 mM (a1 and a2), 1 mM (b1 and b2), and 0.1 mM (c1 and c2).

Supporting electrolyte species

Figure 2.26 shows the Na^+ and Cl^- concentration profiles after 7200 s adjacent to the electrode/electrolyte interface. The Cl^- concentration is higher at the anodes and decreases with distance away from the anode, displaying a minimum at the center of the cathode. The Na^+ concentration profile is the opposite – it has a maximum at the center of the cathode and a minimum at the edges of the anode. As the NaCl concentration decreases, the distribution of the Na^+ and Cl^- ions becomes less uniform.

In all NaCl concentrations, the **Lk** approach overestimates the Cl^- concentration at the edges of the anodes and the Na^+ concentration at the center of the cathode. In the 0.1 and 1 mM NaCl cases, the discrepancy between the **Lk** and **NPP** solutions is more significant; the concentration profiles predicted by **Lk** are more non-uniform. Consistent with previous results, the **Lvk** solution is closer to **NPP**. The concentrations of Na^+ and Cl^- calculated by the **Lvk** are more similar to **NPP** at the cathode than at the anode. At the anodes, the concentration of Cl^- is slightly underestimated, and the concentration of Na^+ is slightly overestimated.

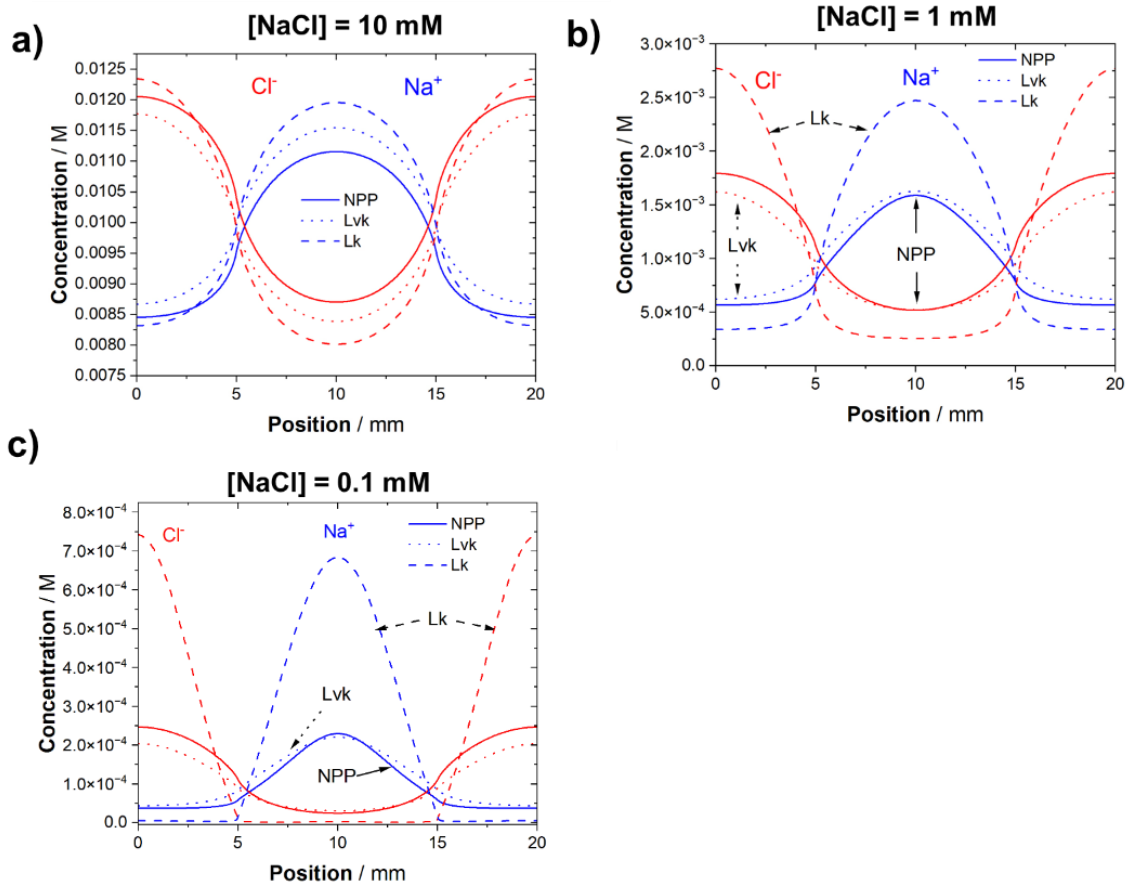

Figure 2.26. Distribution of Na^+ and Cl^- near the electrode/electrolyte interface for varying NaCl concentrations calculated by the **Lk**, **Lvk**, and **NPP** methods: (a) 1000 mM, (b) 100 mM, (c), 10 mM, (d) 1 mM, and (e) 0.1 mM.

2.12.4. Case II: the addition of homogeneous reactions in the electrolyte

The results shown above were obtained without considering any homogeneous reactions occurring in the electrolyte. In the absence of homogeneous reactions, the concentration of the species originating from the electrochemical reactions (Mg^{2+} and OH^-) would increase indefinitely because of their accumulation in the closed system. However, in most systems relevant to corrosion, corrosion products, such as hydroxides and oxides, will precipitate after a solubility limit is reached, saturating the solution. The homogeneous reactions will change the local composition of the electrolyte, impacting the electrolyte conductivity, potential, and current density distributions.

2.12.4.1. Impact of homogeneous reactions on the potential, current density, and species concentration calculated by the NPP method

Figure 2.27 shows the potential, current density, reacting ions concentration, and electrolyte conductivity transients calculated at the center of the cathode obtained in Case I (dashed lines) and Case II (solid lines) for a NaCl concentration of 0.1 mM with the **NPP** approach. The potential and current density transient obtained in Case II are in agreement with Case I until 540 s, after which the potential decrease and current density increase are slower in Case II (**Figure 2.27** (a)). After 7200 s, the potential is higher in Case II, and the absolute value of the cathodic current density is lower. The concentration of Mg^{2+} and OH^- also are in agreement in the first 540 s, after which their concentrations deviate from Case I. The rate at which the concentration of Mg^{2+} and OH^- increases decelerates after ca. 3600 s. In fact, the concentration of Mg^{2+} starts to slightly decreases (**Figure 2.27** (b)).

Figure 2.27 (c) shows the electrolyte conductivity transient at the center of the cathode for the NaCl concentrations of 0.1, 1, and 10 mM. Initially, the calculated conductivities are equivalent in Case I and Case II. As the simulation progresses, the electrolyte conductivity calculated in Case II diverges from the one calculated in Case I, and the rise of the electrolyte conductivity with time becomes slower. At the end of the simulation (t = 7200 s), the electrolyte conductivity is lower in Case II compared to Case I. The difference between the final electrolyte conductivities calculated in Case I and Case II decreases as the NaCl concentration increases. In the lowest NaCl concentration, the final electrolyte conductivity calculated in Case II is ca. 2.5 lower than in Case I.

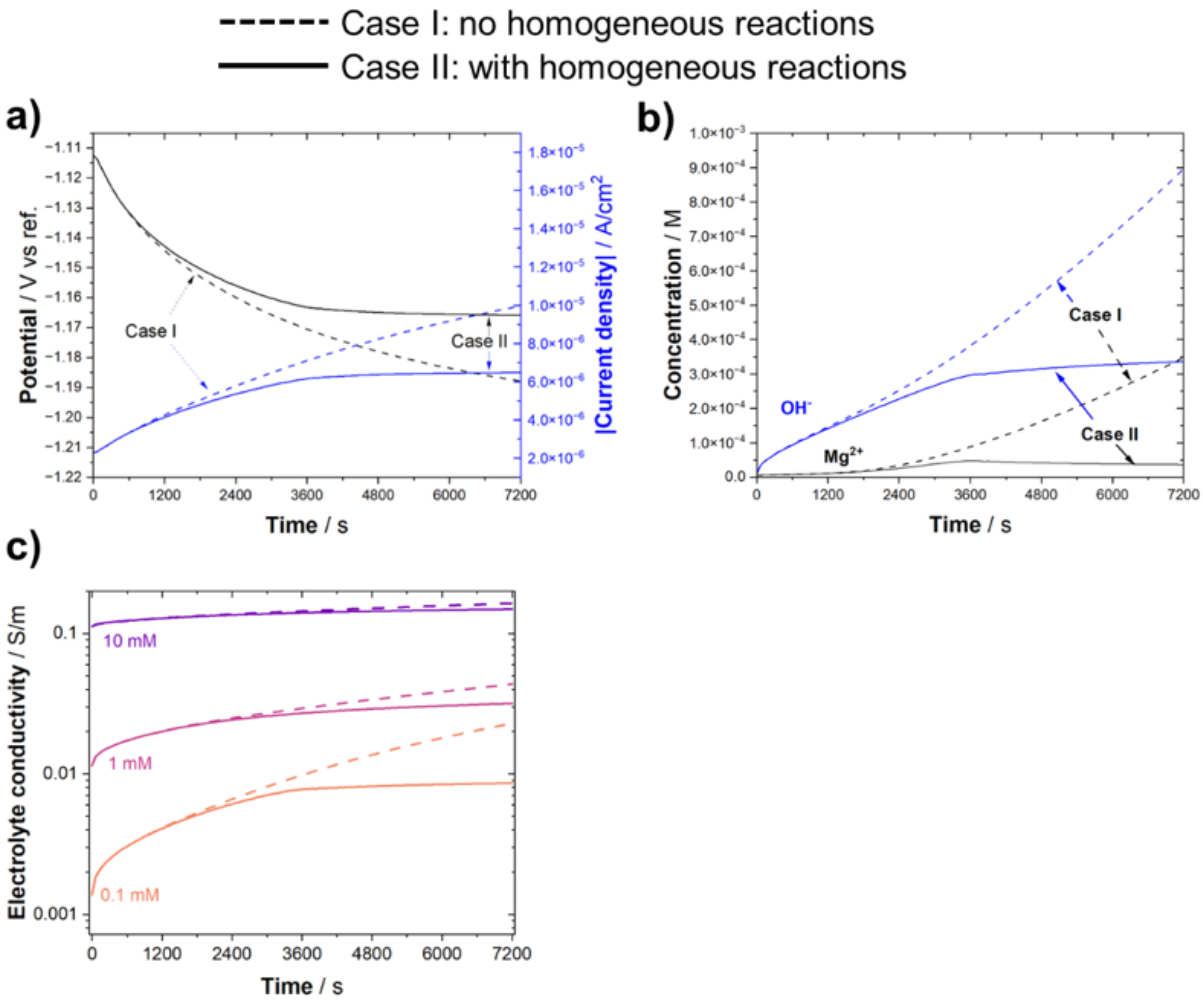

Figure 2.27. Comparison between the transients at the center of the cathode in Case I and Case II calculated using the **NPP** method. In (a), the potential and current density are shown for NaCl concentration of 0.1 mM. In (b), the Mg^{2+} and OH^- concentrations are shown. In (c), the electrolyte conductivity for the NaCl concentrations of 0.1, 1, and 10 mM is shown.

Figure 2.28 compares the potential, species concentration, and electrolyte conductivity profiles near the electrode/electrolyte interface after 7200 s obtained in Case I and Case II. In Case II, a higher potential difference across the anode and cathode was calculated (51.8 mV in Case I and 105 mV in Case II), as illustrated in **Figure 2.28** (a). The concentration of Mg^{2+} and OH^- are lower (**Figure 2.28** (b)), and the latter exhibits an opposite profile – in Case I, the concentration of OH^- is high at the anodes and decreases as the position approximates the center of the cathode, where it displays a minimum concentration; in Case II, the OH^- concentration minimum is at the edges of the anode. The addition of homogeneous reactions also influenced the distribution of the supporting electrolyte species. As shown in

Figure 2.28 (c)**,** the concentration of Na^+ and Cl^- are less uniform in Case II, and the concentration of Cl^- is higher near the anodes, and the Na^+ is higher near the cathode in Case II.

The ratio between the electrolyte conductivity at t = 7200 s and the initial electrolyte conductivity as a function of position obtained in Case I and II in the 0.1 mM NaCl case are demonstrated in **Figure 2.28** (d). With the addition of homogeneous reactions, the increase in the electrolyte conductivity was much smaller. After 7200 s, there was a 5-fold increase in the electrolyte conductivity in Case II, as compared to a 25-50-fold observed in Case I. Additionally, the electrolyte conductivity profile was more uniform in Case II, as the electrolyte conductivities at the anode and cathode are much closer in value.

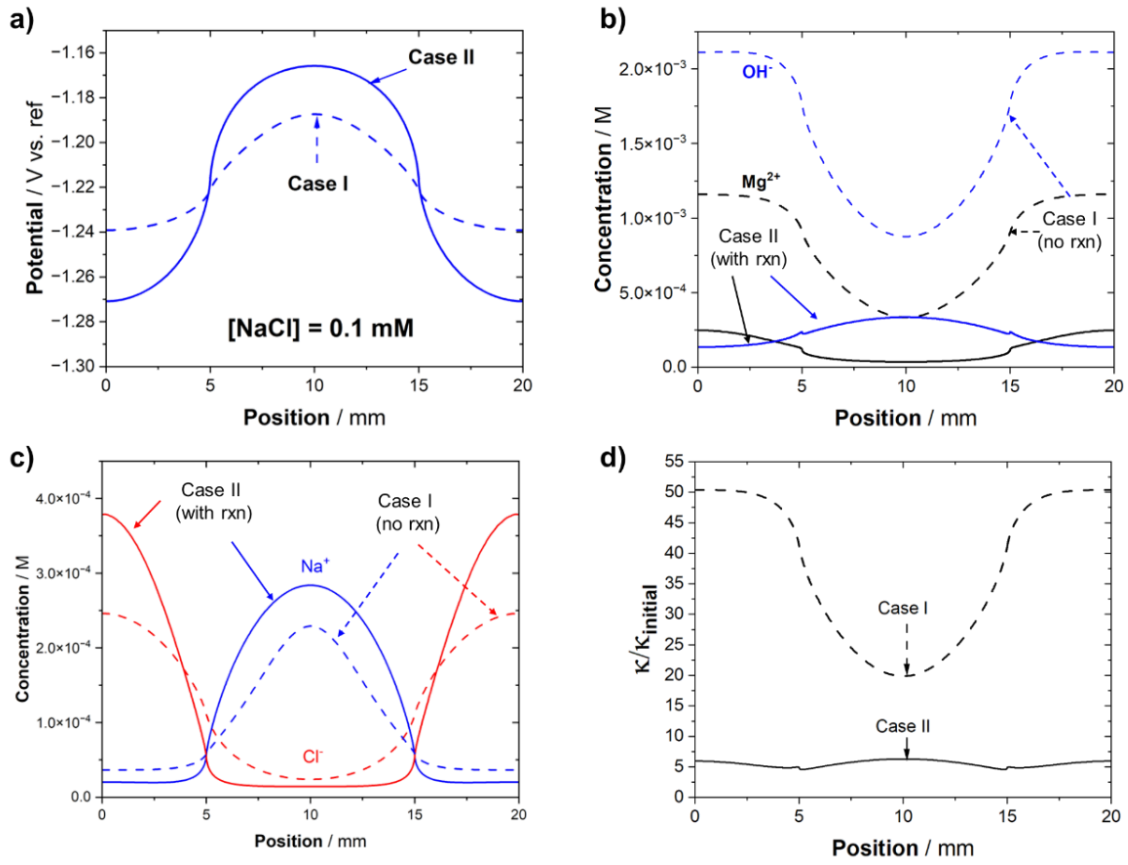

Figure 2.28. The impact of the addition of homogeneous reactions on the potential, species, and electrolyte conductivity profiles for a NaCl concentration of 0.1 mM at t = 7200 s: (a) potential distribution; (b) concentration of Mg^{2+} and OH^- species; (c) concentration of Na^+ and Cl species; (d) electrolyte conductivity normalized by its value at t = 0 s.

To visualize the impact of the addition of homogeneous reactions and of the supporting electrolyte concentration on the electrolyte inhomogeneity, **Figure 2.29** (a) and (b) show the ratio between the local electrolyte conductivity and the minimum conductivity adjacent to the electrode/electrolyte interface at t =

7200 s, calculated by the **NPP** approach for [NaCl] = 0.1, 1, and 10 mM (Figure 2.29 (a)) and [NaCl] = 100 and 1000 mM (**Figure 2.29** (b)) for Cases I and II. In Part I of this work, the results obtained in these higher NaCl concentrations are discussed [110].

With the exception of the 0.1 mM NaCl concentration, the addition of homogeneous reactions increased the non-uniformity of the electrolyte conductivity, as there is a higher difference between the maximum and minimum electrolyte conductivity at the boundary of the electrodes. In Case II, a minimum in the electrolyte conductivity is observed near the anode and cathode junction, whereas the minimum is observed in the middle of the cathode in Case I. The increase in the supporting electrolyte concentration decreases the non-uniformity, and lower κ/κ_{min} ratios are observed.

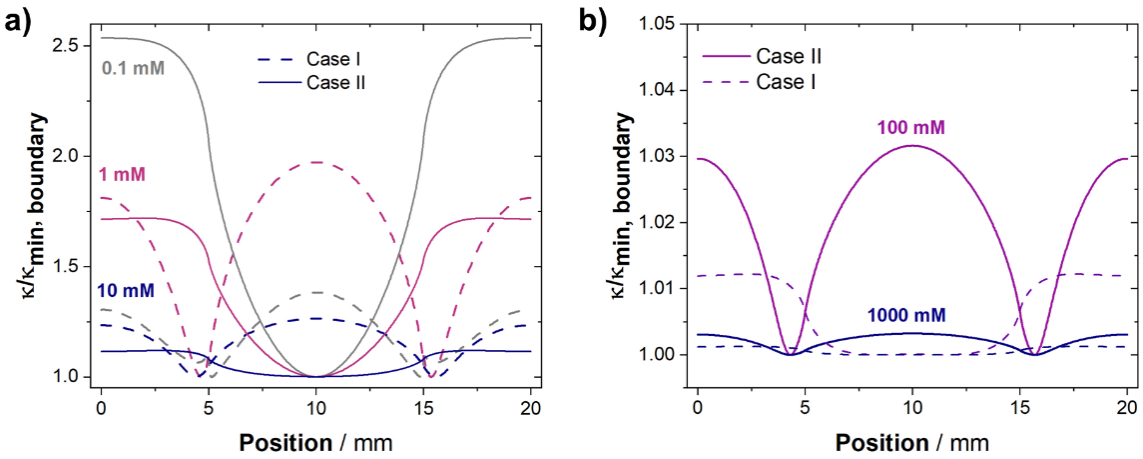

Figure 2.29. The ratio between the local electrolyte conductivity at the electrode boundary and the minimum electrolyte conductivity displayed at the boundary for the supporting electrolyte concentrations varying from 0.1 to 10 mM (a), and 100 and 1000 mM (b).

2.12.4.2. Comparison between the calculation methods in the calculated potential with reactions in Case II

This section shows the results obtained by the different calculation methods in the case in which the homogeneous reactions are added. The potential, current density, and species concentration profiles adjacent to the electrode/electrolyte interface after 7200 s are compared.

Potential and current density profiles after 7200 s

Figure 2.30 (a1), (b1), and (c1) show the potential and the absolute value of the current density profiles calculated by the different methods. As observed in Case I, the **Lk** method overestimates the potential difference across the electrodes. As a result, the potential at the edges of the anodes is

underestimated, and it is overestimated at the center of the cathode. Accordingly, the current densities are also underestimated, as shown in **Figure 2.30** (a2), (b2), and (c2). The **Lvk** approach is in better agreement with the **NPP** approach. Contrarily to the trend observed in Case I, the **Lvk** approach calculated a slightly higher potential difference across the electrodes, resulting in slightly underestimated current densities. The **Lvk** solutions are closer to those obtained by **NPP** than by **Lk** in the NaCl concentrations of 0.1 and 1 mM. Interestingly, the deviation of the **Lvk** solution in comparison to **NPP** is smaller at the 0.1 mM NaCl concentration, in comparison to the 1 mM NaCl case. For the 10 mM NaCl, the **Lvk** solution is more similar to that of **Lk**.

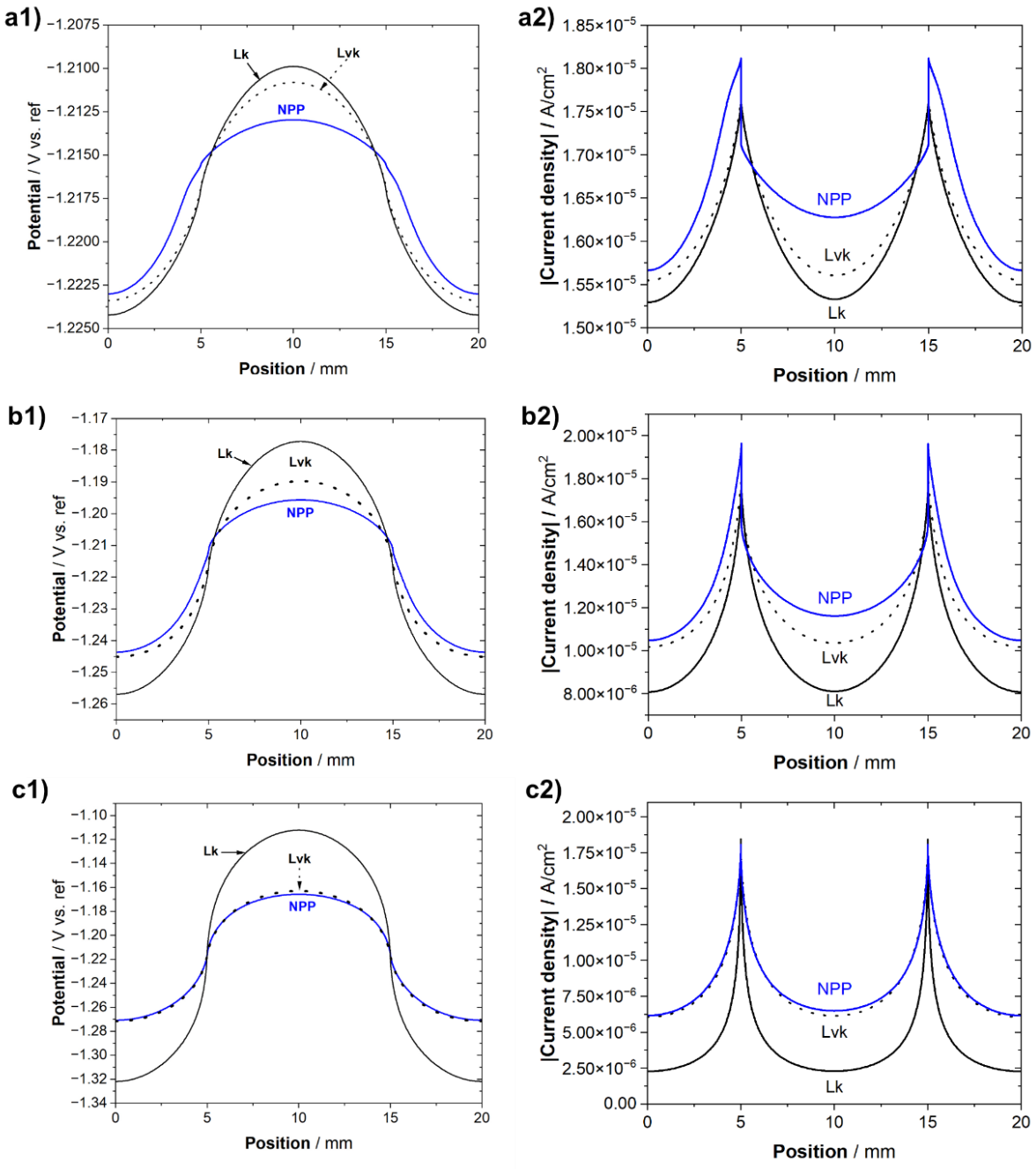

Figure 2.30. Potential (a1, b1, c1) and the absolute value of current density (a2, b2, c2) after 7200 s calculated by the different methods in Case II for the different NaCl concentrations: 10 mM (a), 1 mM (b), and 0.1 mM (c). Note that the scale changes in each NaCl concentration to better observe the differences between the solutions obtained by the calculation methods.

2.12.4.3. Reacting species distribution adjacent to the electrode/electrolyte interface after 7200s

Figure 2.31 illustrates the concentration of the reacting species near the electrode/electrolyte interface calculated by the different methods with the addition of homogeneous reactions for the NaCl concentrations of 10 mM (**Figure 2.31** (a1) and (a2)), 1 mM (**Figure 2.31** (b1) and (b2)), and 0.1 mM (**Figure 2.31** (c1) and (c2)).

As observed in Case I, the decrease in the supporting electrolyte concentration leads to large deviations in the solutions obtained by **Lk**. In the 10 mM NaCl case, the Mg^{2+} and OH^- are in good agreement across the electrodes, except at the edges of the anode for the Mg^{2+} species (which is slightly overestimated by 0.02 mM, a 1% difference) and the center of the cathode for the OH^- species (at which is underestimated by 0.24 mM, a 12% difference). Interestingly, there are higher discrepancies in the calculation of the OH^- species. Decreasing the NaCl concentration to 1 mM, the described differences in the Mg^{2+} and OH^- are exacerbated. The OH^- concentration is underestimated by 0.53 mM (a difference of 53%), and the Mg^{2+} is now underestimated by 0.36 mM (a difference of 37%).

In the 0.1 mM NaCl concentration (**Figure 2.31** c1 and c2), **Lk** significantly deviates from the **NPP** approach**.** As observed in Case I, there are qualitative and quantitative differences between the concentration profiles. The shape of the concentration profiles is the opposite of that calculated by the **NPP** approach. The **Lk** approach calculates the maximum of the Mg^{2+} concentration at the center of the cathode and the OH^- maximum at the anodes. The Mg^{2+} concentration at the cathode is overestimated by1.1 mM, representing a 3000% difference. The OH^- at the anode is also overestimated by 1.1 mM, representing a 785% difference.

The **Lvk** approach performs better. The deviations in the concentrations are higher at the edges of the anode and center of the cathode, as observed with the **Lk** solution. The OH^- concentration is also underestimated at the center of the cathode. However, the Mg^{2+} concentration is slightly overestimated at the edges of the anode. As observed in the potential and current density profiles, the **Lvk** solutions are closer to **NPP** in the 0.1 mM NaCl case in comparison to the 1 mM NaCl case.

The concentrations of the major species, Na^+ and Cl^-, calculated in Case II are shown in **Figure S4**, in the Supplementary Information.

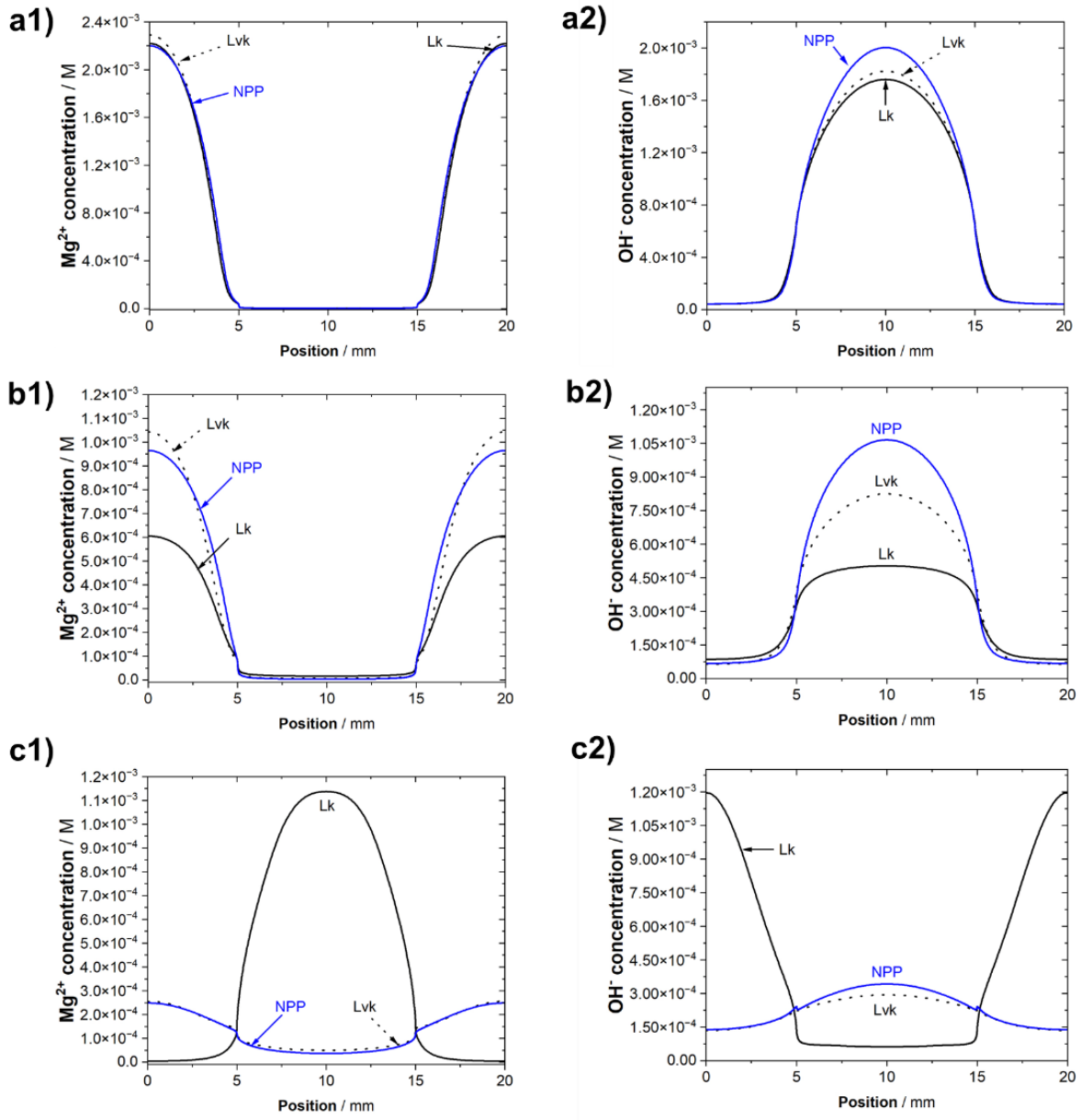

Figure 2.31. Concentration profile of the electrochemically active species (Mg^{2+} and OH^-) calculated by **NPP**, **Lvk**, and **Lk** methods for the supporting electrolyte concentrations of 10 mM (a1 and a1), 1 mM (b1 and b2), and 0.1 mM (c1 and c2).

2.12.4.4. Case III: comparison between the calculation methods for a case in which the diffusivities of all the ionic species are equal

In this section, the results between the different modeling approaches are compared in a case in which the diffusivities of all the ions were equivalent and equal to 10^{-9} m^2/s for a NaCl concentration of 0.1 mM and with the addition of homogeneous reactions. **Figure 2.32** shows the potential (a), current density

(b), Na^+ concentration (c), and Cl^- concentration (d) adjacent to the electrode/electrolyte interface after 7200 s. As shown in Part I of this work [110], for the case in which all ions have the same diffusivities, there are no differences between the **NPP** and **Lvk** calculation methods. The observation is extended to a case in which the supporting electrolyte concentration is 0.1 mM. The solution provided by the **Lk** method deviates from the **NPP** solution.

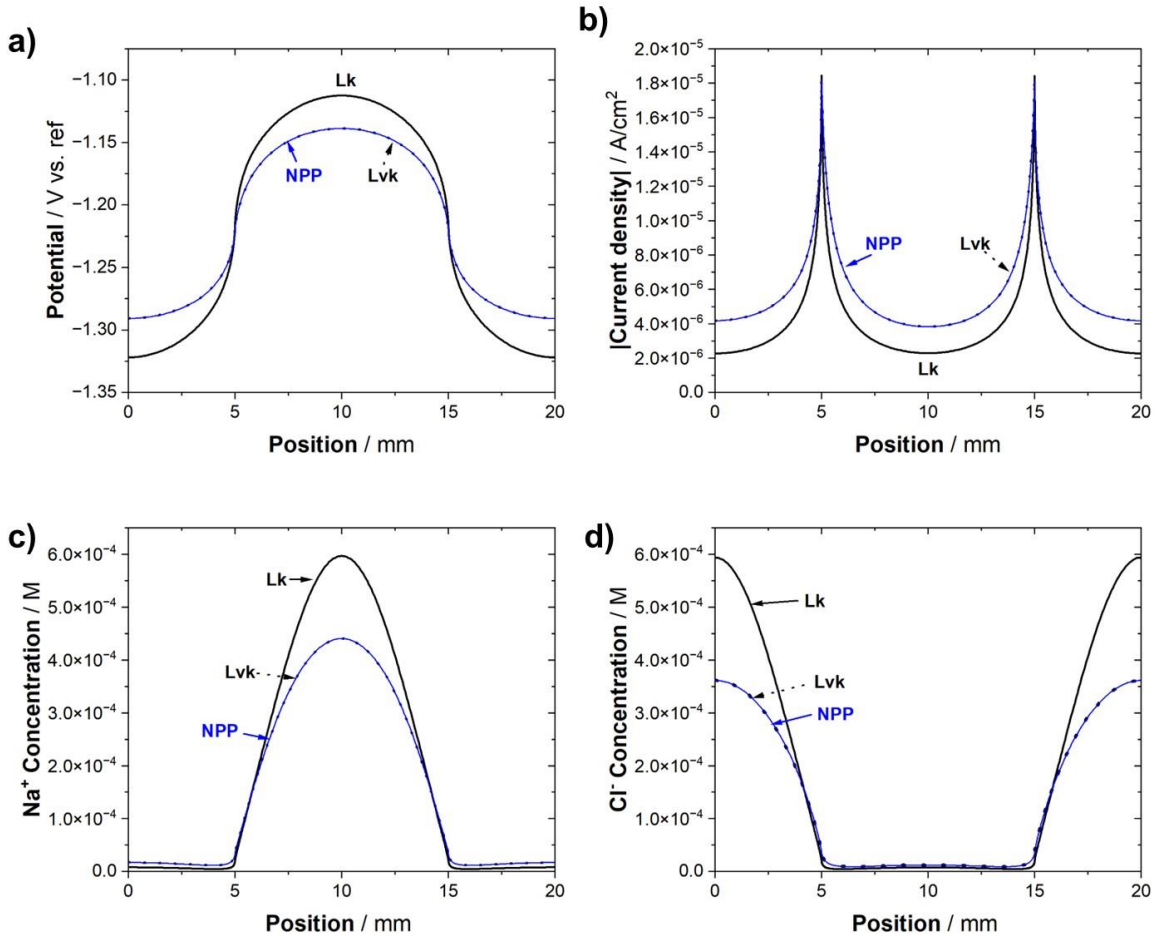

Figure 2.32. Comparison between the potential (a), current density (b), Na^+, and Cl^- concentration profiles adjacent to the electrode/electrolyte interface after 7200 s obtained in Case III calculated with the different methods.

2.12.5. Electroneutrality

In the reduced-order approaches, the equations describing charge and mass are partially uncoupled as Laplace is used to solving for charge conservation, and Fick's second law with the addition of a reaction term is used to solve for mass conservation. Even though the equations are coupled through the migration (**Lk and Lvk**), and conductivity terms (**Lvk**), mass conservation does not imply charge conservation. The diffusion potential term that prevents the charge separation of ions of different diffusivities is not taken into

account. To verify the impact of the decoupling of the two equations on charge conservation, the charge density ($\Sigma z_i c_i$) was calculated for the reduced-order approaches. The results are shown for the supporting electrolyte concentrations considered in Part I (10, 100, and 1000 mM) and II (0.1, 1, 10 mM) of this work.

2.12.5.1. Case I

Figure 2.33 (a) and (b) shows the charge density near the electrolyte/electrolyte interface after 7200 s resulting from the **Lk** and **Lvk** calculations in the range of NaCl concentrations of 0.1 to 10 mM (a), and 100 to 1000 mM (b). In the lower NaCl concentrations, the **Lk** approach calculates a net negative charge near the anode and a net positive charge near the cathode. The highest charge density is found at the edges of the anode and center of the cathode, reaching a net negative charge equivalent to 4 mM at the anode and a net positive charge equivalent to $4x10^{-3}$ equiv/dm^3 in the 0.1 and 1 mM NaCl cases. The increase in the NaCl concentration leads to a decrease in the charge density adjacent to the electrode/electrolyte interface. The charge density resulting from the **Lvk** calculations is lower than those from **Lk**. The **Lvk** approach calculated charge densities up to $2x10^{-3}$ equiv/dm^3 adjacent to the electrode/electrolyte interface, but lower than $1x10^{-3}$ equiv/dm^3 for most positions. In contrast to **Lk**, the **Lvk** approach calculates a net positive charge at the anodes and a net negative charge at the cathodes for the NaCl concentrations of 0.1 and 1 mM. For the 10 mM case, the **Lvk** approach calculates a net positive charge near both the anode and cathode. In the NaCl concentrations of 100 and 1000 mM, the charge density resulting from the **Lk** and **Lvk** approaches are similar, and both approaches calculate a net positive charge adjacent to the electrode/electrolyte interface boundary.

The false-color plots shown in **Figure 2.33** (c) and (d) show the distribution of the charge density across the electrolyte after 7200 s calculated by the **Lvk** approach for [NaCl] = 0.1 mM (a) and 1000 mM (b). The arrows in the figure show the direction of the total flux (diffusion and migration) of Mg^{2+} (white arrows) and OH^- (black arrows). In the lower NaCl concentration, a positive charge density is observed near the anode surface, and a net negative charge is seen at the cathode surface. Further away from the electrode/electrolyte interface and near the top boundary of the electrolyte, the magnitude charge density decreases. In contrast, in the [NaCl] = 1000 mM, there is a positive net charge across the anode and the cathode. At the top of the electrolyte, there is a net negative charge at the corners. The integration of the charge density over the entire electrolyte area yields zero for both reduced-order approaches.

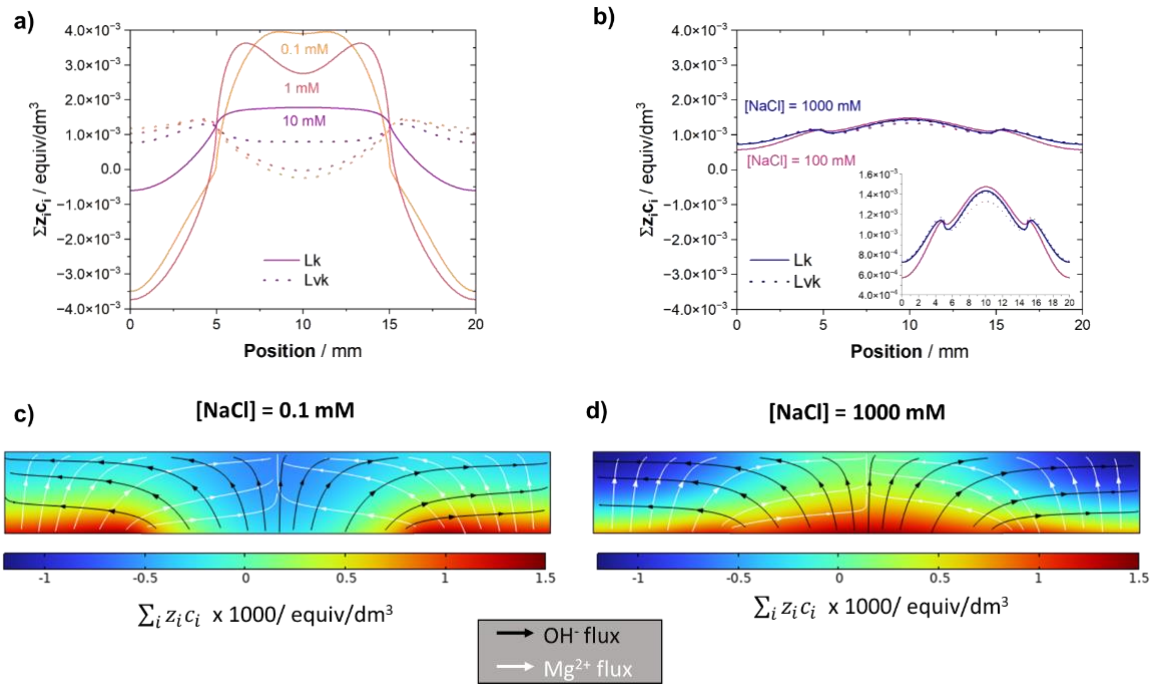

Figure 2.33. Charge density as a function of position after 7200 s. In (a) and (b), the charge density near the electrode/electrolyte interface calculated by the **Lk** and **Lvk** approaches in the NaCl concentrations of 0.1, 1, 10 mM (a), and 100 and 1000 mM (b) is shown. The charge density in the entire electrolyte and the lines of total Mg^{2+} and OH^- calculated by the Lvk approach are shown for the NaCl concentration of 0.1 mM (c), and 1000 mM (d).

2.12.5.2. Case II

With the exception of the lowest NaCl concentration (0.1 mM), the charge density near the electrode/electrolyte interface was higher in Case II in comparison to Case I. **Figure 2.34** (a) shows the charge density near the electrode/electrolyte interface resulting from the **Lvk** approach calculations for a NaCl concentration of 0.1 and 1000 mM. In the lower concentration, the charge density in Case II was smaller than in Case I. However, at the highest concentration, the charge density near the electrode/electrolyte interface was higher in Case II. Near the anode and cathode junction, the reduced-order approach calculated a net negative charge. The charge density increases with increasing the distance from the junction, and it reaches a net positive charge. The charge density reaches a maximum at the center of the cathode.

The distribution of the charge density across the electrolyte in Case I and II are seen in **Figure 2.34** (b). In Case II, the magnitude of the charge density is higher in the entirety of the electrolyte, and it is highest near the electrode/electrolyte interface boundary. Contrarily to Case I, the increase in the electrolyte concentration increases with increasing NaCl concentration in Case II, as observed in **Figure 2.34** (c). In

Figure 2.34 (d), the charge density at the center of the cathode obtained in each NaCl concentration is plotted against the ratio between the diffusion potential and the total potential gradient. There is a linear relationship between the magnitude of the charge density and the proportion of the potential gradient that is due to the diffusion term in the potential distribution calculation.

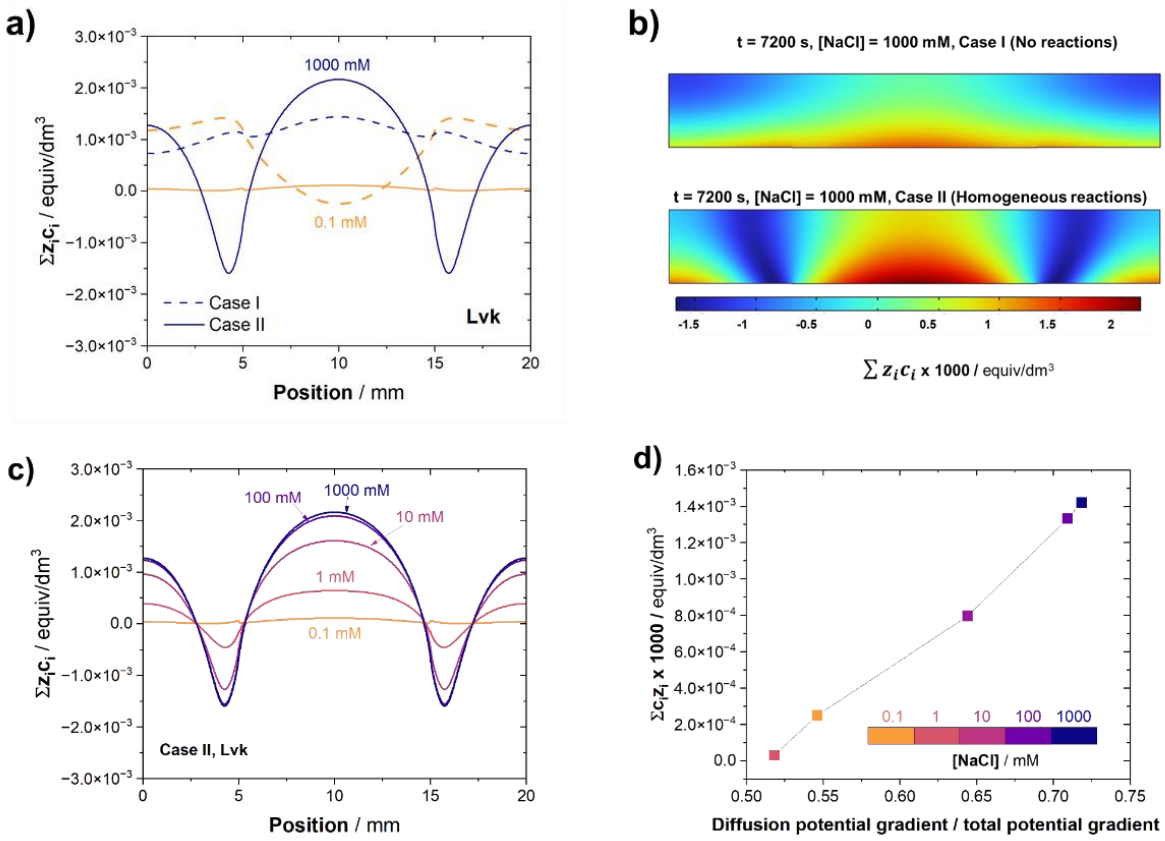

Figure 2.34. (a) Comparison between the charge density resulting from Lvk calculations for Case I and Case II at the NaCl concentrations of 0.1 and 1000 mM. (b) Charge density as a function of position in the electrolyte in Case I (top figure) and Case II (bottom figure) for a NaCl concentration of 1000 mM. (c) Charge density near the electrode/electrolyte interface as a function of NaCl concentration resulting from **Lvk** calculations. (d) Relationship between charge density and the ratio between the diffusion potential gradient bt the total potential gradient calculated in Case II.

2.12.5.3. Case III

Figure 2.35 shows the charge density resulting from the **Lk** and **Lvk** approaches in Case III, in which the model was performed for a condition in which all ions had the same diffusivities for a [NaCl] = 0.1 mM. In such conditions, there is a zero net charge density resulting from the **Lvk** approach, whereas

the **Lk** approach still results in a net charge, as observed in Cases I and II. The magnitude of the charge density is slightly smaller than in the other cases for **Lk**.

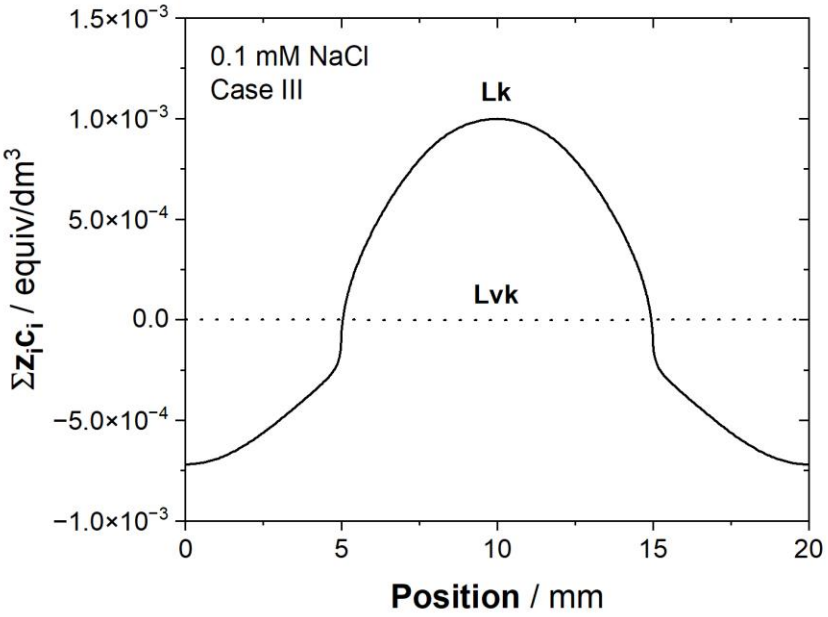

Figure 2.35. Charge density calculated by the **Lk** and **Lvk** approaches in Case III for a [NaCl] = 0.1 mM.

2.12.6. Lvk and Lk errors as a function of the ratio between the supporting electrolyte and the reacting species

The errors associated with the reduced-order approaches were estimated by comparing the value of selected variables, such as potential, current density, and concentration of Mg^{2+} and OH^- against those obtained with the **NPP** approach. The values were obtained at the center of the cathode after the 7200 s of simulation time. The errors were plotted against the ratio between the inert, supporting electrolyte species and the reacting species (SER). The ratio was obtained by summing the average of each species (Na^+ and Cl^- for the inert species, and Mg^{2+}, OH^-, and H^+ for the reacting species). The results from Part I ([NaCl] = 10, 100, and 1000 mM) and Part II ([NaCl] = 0.1, 1, and 10 mM) of this work are combined in **Figure 2.36**.

Figure 2.36 (a) and **Figure 2.36** (b) show the percentage of the error of the current density, OH^- and Mg^{2+} concentrations resulting from the **Lk** and **Lvk** approaches in Case I and II, respectively. **Figure 2.36** (c) shows the magnitude of the difference between potential calculated at the center of the cathode using the reduced-order approaches against **NPP** after 7200 s as a function of the SER. In all cases, the **Lvk** approach yielded smaller errors. The percent error associated with the Mg^{2+} at the center of the cathode was higher than that of the other variables for all cases. However, the errors associated with Mg^{2+} at the center

of the cathode in Case II should be analyzed with caution in the higher SER. The addition of the sink term decreased considerably the concentration of Mg^{2+} at the center of the cathode. At the higher SER ratios, the concentration of Mg^{2+} were in the order of magnitude of 0.1 μM.

As shown in Part I of this work, the error decreases considerably as the ratio between the inert species over the reacting species increases. However, in Case II (**Figure 2.36** (b)), the error slightly increases even with an increase in SER in the lower range of the ratio. The differences between the errors of the **Lk** and **Lvk** approaches decrease with increasing SER. In Case II, the ratio above which the difference between **Lk** and **Lvk** approaches are minimal is lower than in Case I.

For the same SER ratio, the errors calculated in Case II are higher than in Case I, with the exception of the Lvk case in the lower range of the inert-to-reactive species ratio, as shown in **Figure 2.36** (d). In Case III, the error associated with the **Lk** approach is smaller for the same inert-to-reactive species ratio. In higher *SER*, the error in Case III is significantly smaller than in the other cases. As a reminder, **Lvk** method yielded results virtually identical to the **NPP** approach in Case III.

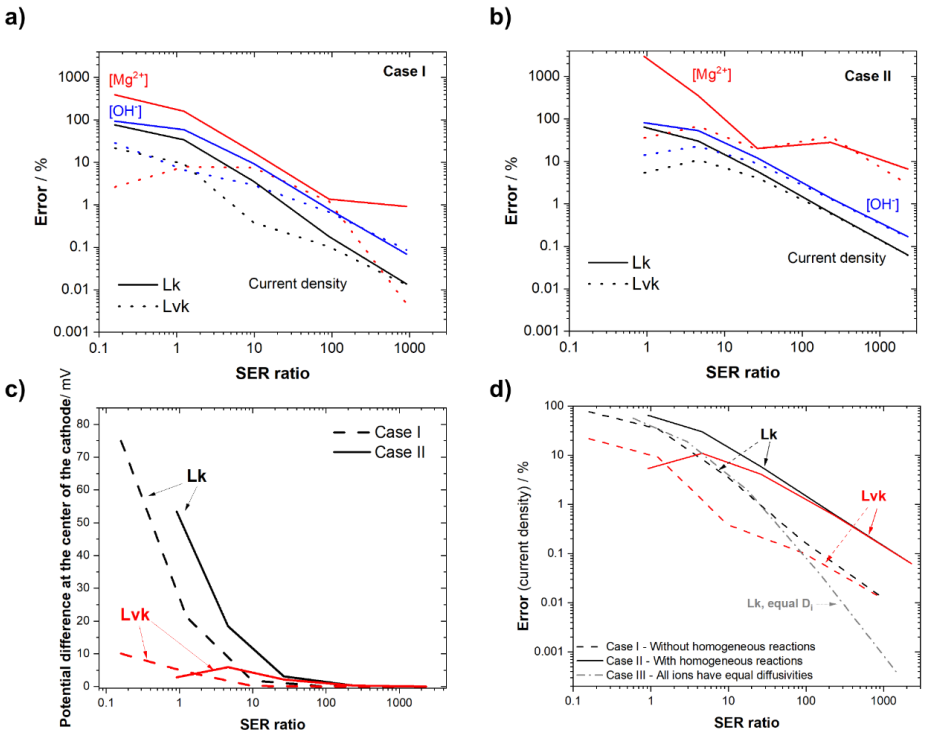

Figure 2.36. Errors resulting from the reduced-order modeling approaches as a function of the ratio between the inert/ supporting electrolyte species and the reacting species for Case I (a) and Case II (b). In (c), the potential difference calculated at the center of the cathode resulting from Lk and Lvk are shown for Case I and Case II. In (d), the Case I, Case II, and Case III are compared by the error calculated by the current density at the center of the cathode after 7200 s.

2.13. Discussion

As discussed in Part 1 [110], the accuracy with which numerical models describe electrochemical phenomena depends not only on the governing equations used but also (and sometimes more importantly) on the accuracy of the properties of the solution and the electrodes of interest (i.e., boundary conditions at the electrode/electrolyte interface). In Part 1 we showed that one could use reduced-order governing equations to calculate potential, current density, and species spatiotemporal distributions with high accuracy under conditions in which the ratio of supporting electrolyte ions to reactive ions is sufficiently high (a minimum ratio of between 5 and 100, depending on the details). In Part 2, we extend that analysis to lower supporting electrolyte ratios. Such ratios can occur in dilute environments or in concentrated environments in which the reactive species are present at high concentrations.

To orient the reader, this section first discusses the two most accurate governing equations, **NPE** and **NPP**, showing that they result in virtually identical results even at low supporting electrolyte ratios, but with **NPP** taking up to 3x longer to converge. Next, the impact of the relative concentration of non-reactive species to reactive species is defining in determining the amount of error introduced in the potential and current density distributions by using reduced-order governing equations (i.e., **Lvk** and **Lk**). That analysis informs a discussion of the relative importance of the migration and diffusion terms on the potential distribution. The impacts of homogeneous reactions which create sinks for species, such as precipitation reactions, on the error in the solutions from the reduced-order governing equations are then discussed. The analysis is then extended to address the relative importance of diffusion and migration errors. Finally, the issue of local and global charge balance and the dependence on differences in ionic diffusion coefficients in the electrolyte is addressed.

2.13.1. Nernst-Planck solved with the electroneutrality condition using the method of elimination is a robust approach for the studied system

As in Part 1, the solutions obtained with the **NPP** method were in excellent agreement with the **NPE** solutions, the latter being the gold standard governing equation. The largest net charge density at any position calculated by the **NPP** approach was $3x10^{-16}$ C/mm^2 for the 0.1 mM NaCl case, as compared to $8x10^{-19}$ C/mm^2 for the 1000 mM NaCl case [110]. In the 0.1 mM NaCl case, the difference in the total charge associated with the separation of the cations and anions summed to $1x10^{-12}$ M. Thus, electroneutrality is an appropriate assumption for the length scales of the problem considered and very likely would be for a wide range of corrosion phenomena of interest.

The implementation of the **NPE** method via the method of elimination is a robust approach to solving for the electroneutrality even at low electrolyte concentrations. Although the concentration of the make-up ion is artificially calculated by the electroneutrality condition, the difference in the concentration

of the Na^+ (the chosen make-up ion for **NPE**) calculated using **NPP,** and that calculated using **NPE** was 0.06%. It has been previously reported that there may be significant discrepancies in modeling results when utilizing different make-up ions [2]. Those errors were not observed in the present work, when either Na^+ or Cl^- were used as make-up ions for all cases modeled. Error! Reference source not found.(a) shows the [Na^+] and [Cl^-] calculated with the **NPE** method using Na^+ and Cl^- as make-up ions in Case II. There was a negligible difference between the solutions.

As discussed in Part I, there were discrepancies in the **NPE** results performed using different make-up ions if the electrolyte was not initially charge balanced. Such conditions can occur as a result of adjustments in the species intial concentrations so that they satisfy equilibrium constants to aid model convergence, for example. We showed an example in which the **NPE** approach was applied using different make-up ions for a case in which the electrolyte was not initially charge balanced, and there was a surplus of 0.7 mM of cations in a 1000 mM NaCl solution.

The **NPE** calculations were performed for the same initial electrolyte unbalanced, but in a NaCl concentration of 0.1 mM.

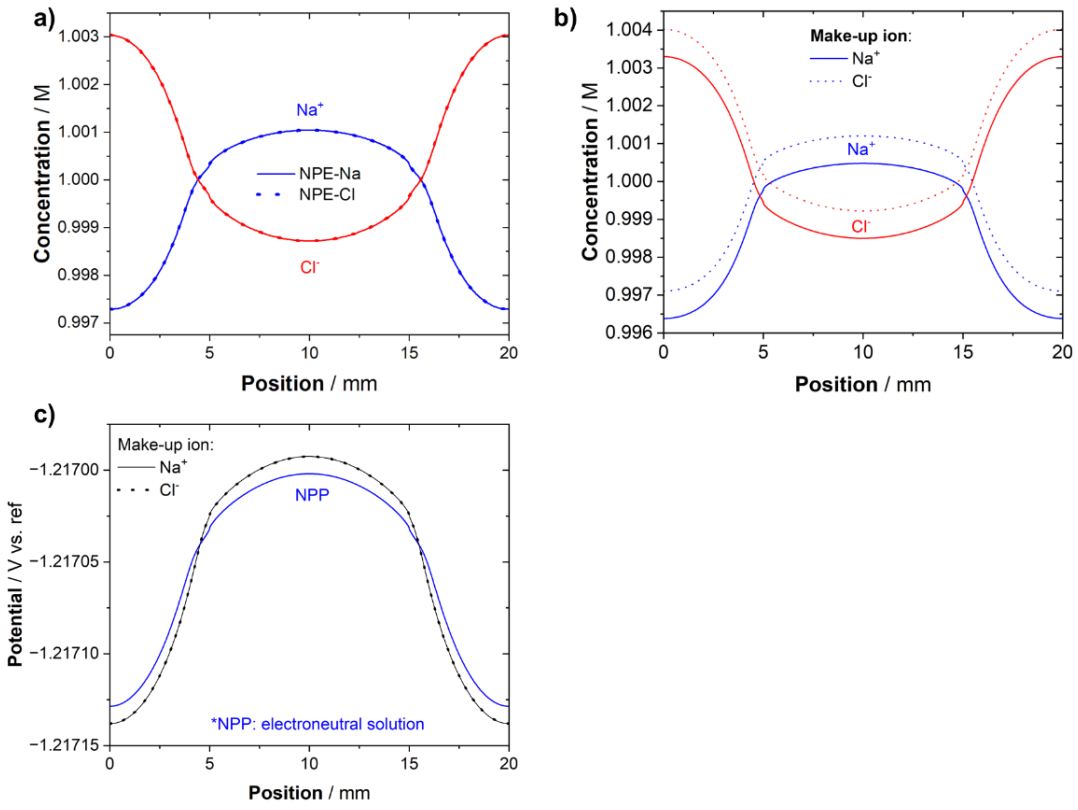

Figure 2.17. Impact of the make-up ion on the species concentration and potential distributions. In (a), the concentration profiles of Na+ and Cl- obtained when using either Na+ (NPE-Na) or Cl- (NPE-Cl) as the make-up ions in Case II for a NaCl **concentration** of 1 M **are** shown. The

concentration profiles of Na+ and Cl- (b) and the potential distribution at the electrodes (c) obtained using NPE-Na and $^{NPE\text{-}Cl}$ are shown for a case in which the electrolyte is not electroneutral at t = 0s.

Table 2.6 shows the initial concentrations of the ions in the unbalanced electrolyte, and **Figure 2.37**(b)-(e) compares the solutions obtained when using either Na^+ (**NPE-Na**) or Cl^- (**NPE-Cl**) as the make-up ion.

Figure 2.37 (b) shows the Na^+ and Cl^- concentrations calculated by **NPE-Na** and **NPE-Cl** methods for a 0.1 mM NaCl case. The **NPE-Na** method calculates a negative concentration of Na^+, as the amount of cations needed to be removed to balance the initial positive charge density is higher than the NaCl concentration. If Cl^- is used, a surplus of Cl^- is calculated. **Figure 2.37** (c) displays the discrepancies in the potential distributions obtained by **NPE-Na** and **NPE-Cl** for the [NaCl] = 0.1 mM case and the potential distribution obtained via **NPP** for the case in which the electrolyte was charge-balanced. Unlike the 1 M NaCl case discussed in Part 1, in the 10^{-4} M case, the discrepancies between the potentials calculated using either Na^+ or Cl^- as make-up ions are more noticeable. The potential distribution calculated by **NPE-Cl** was in closer agreement with the charge-balanced **NPP** solution than the **NPE-Na**.

Upon analyzing the results reported by Gagnon et al. [2], it was observed that the only case in which discrepancies between results obtained by different make-up ions were found was the only case in which the electrolyte was not initially electroneutral. Prior to performing the potential, current density, and species distribution calculations, the electrolyte composition was determined by a separate initial step in which ionic dissociation and equilibrium reactions were used to determine the initial species concentrations. The electrolyte composition resulting from this initial step was not charge-balanced, and it had an excess of $1.7x10^{-4}$ mol/m^3 cations. Albeit small, the excess charge can explain the discrepancies and convergence problems observed by the authors.

As discussed in Part 1, **NPE** artificially calculates the concentration of the make-up ion to satisfy the electroneutrality condition, so it does not necessarily respect mass conservation. Any charge imbalance in the electrolyte is solved artificially by imposing a concentration on a selected species, even if that results in a negative species concentration. The imposition of charge conservation by the Poisson equation prevents the **NPP** method from converging at the first time step.

The water autoionization reaction adds difficulties to the calculations: not only does it introduce numerical stiffness, but it also creates charge conservation issues. In the view of electroneutrality, if an electrolyte has, for example, a pH = 10, then it needs the presence of another cation to balance the surplus charge of -10^{-4} M of OH^-. Finding the ions and reaction parameters that satisfy the electroneutrality is not as straightforward as one would think. In lower supporting electrolyte concentrations, small errors in the kinetic and thermodynamic parameters of the homogeneous reactions can prevent **NPP** from solving or

lead to significant differences in the **NPE** solutions depending on the make-up ion of choice. For example, if we were to use the solubility product constant of $Mg(OH)_2$ in seawater reported in the literature (Ksp = $4.5x10^{-10}$) [113] and repeated the same process to calculate Mg^{2+} initial concentration for a pH = 10, the charge imbalance would increase to $4.5x10^{-2}$ M, resulting in an addition or removal of $8.99x10^{-2}$ M of Cl^- or Na^+, respectively. In the 0.1 mM NaCl case, that concentration alteration represents almost 900x the NaCl concentration. In reality, electroneutrality dictates that other species must be present in the electrolyte at such conditions.

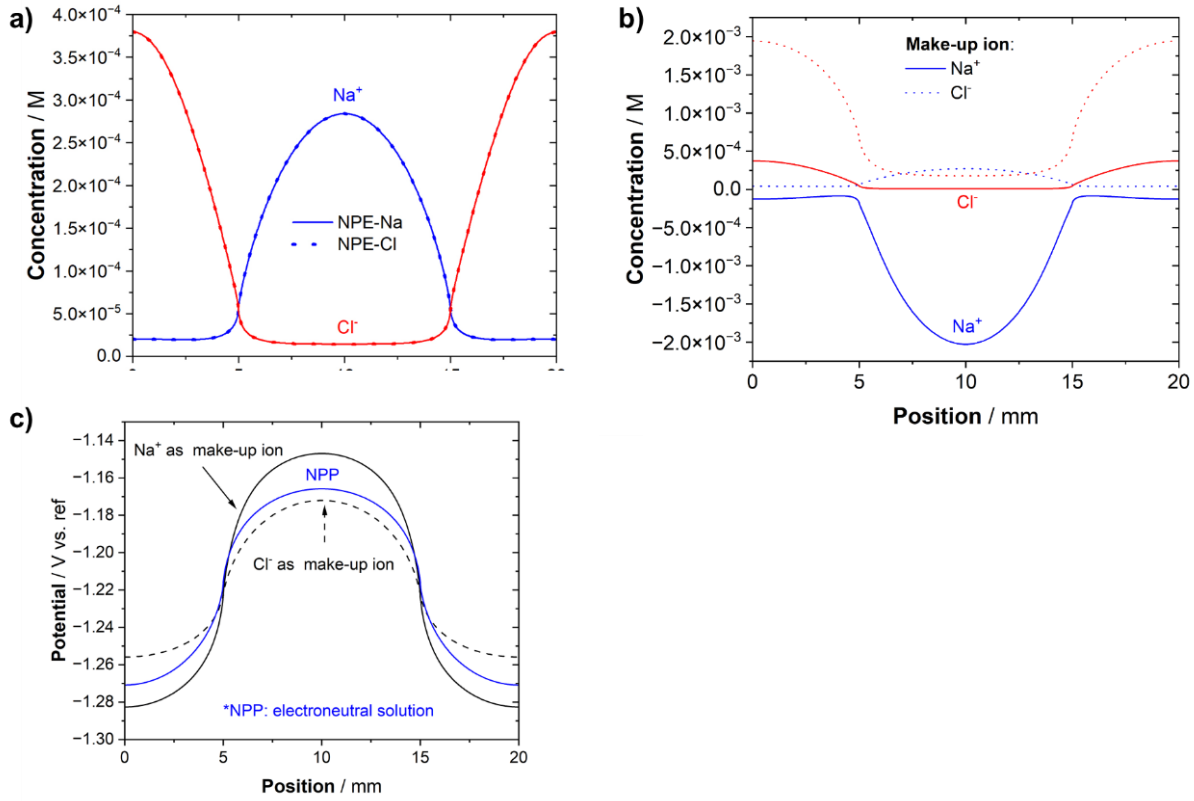

Figure 2.37. Impact of the make-up ion on the species concentration and potential distributions. In (a), the Na^+ and Cl^- concentrations calculated using the **NPE** method using either Na^+ (NPE-Na) or Cl^- (NPE-Cl) as make-up ions for an initially electroneutral electrolyte is shown. In (b) and (c), the NPE-Na and NPE-Cl calculations are compared for a case in which the electrolyte is not electroneutral at t = 0 s: the resulting Na^+ and Cl^- concentration profiles are shown in (b), and the potential distribution is shown in (c).

Table 2.6. Initial concentration of the ionic species and the product of the their concentration and their respective charge number used in a case in which the electrolyte was not electroneutral at t = 0 s.

Species	Initial concentration / M	$z_i c_i$ / equiv/dm^3
Mg^{2+}	4.2×10^{-4}	8.24×10^{-4}
Na^+	1.0×10^{-4}[a]	1×10^{-4}
Cl^-	1.0×10^{-4}[b]	-1×10^{-4}
H^+	1.0×10^{-10}	1×10^{-9}
OH^-	1.0×10^{-4}	-1×10^{-4}
	$\sum z_i c_i$	7.24×10^{-4}

a. Initial concentration of Na^+ when Cl^- is used as the make-up ion

b. Initial concentration of Cl^- when Na^+ is used as the make-up ion

2.13.2. The reduced-order approaches perform poorly in electrolytes with low ionic concentrations, but Lvk substantially improves the solutions while still saving computational time

The reduction in computation time using either the **Lvk** or **Lk** as governing equations relative to the **NPE** and **NPP** governing equations is substantial, a factor of up to 10x. As shown in Part 1, for electrolytes of sufficiently high conductivity, the loss of accuracy of potential, current density, and species concentration distributions is negligible. However, at lower electrolyte concentrations, the errors in the two reduced-order approaches increase substantially. As shown in **Figure 2.36**, for SER ratios less than 10, the **Lk** method has errors > 3% in the current density, with the error increasing to 40% at a 1:1 ratio for Case 1, in which no homogeneous reactions are considered. The **Lvk** method performs better, decreasing the error in current density to 0.4% at a ratio of 10:1, and to 10% at a ratio of 1:1.

The addition of homogeneous reactions also led to increased errors for the same SER ratio. For the **Lk** method, the error in Case II increases to ca.15% for a SER ratio of 10, and to ca. 60% for a SER ratio of 1. For the **Lvk** method, the error in current density in Case II increases to 7% for a *SER* ratio of 10 and *decreases* to 6% for a SER ratio of 1.

As can be seen Part 1, there are negligible differences between the methods in the distribution of the potential, current density, and species concentration after 7200 s for ratios of 100 or more for Case 1 when [NaCl] ≥ 100 mM. Considerable differences arise when the supporting electrolyte concentration is decreased to a ratio of < 1 (1 mM) with errors as high as nearly 100% for the **Lk** approach at a ratio of 0.1 (i.e., the reactive species are the dominant species). Importantly, even under those conditions, the **Lvk** approach has an error of <30%. It is important to put in perspective the magnitude of these errors in

comparison to the impact of the boundary conditions on the potential, current density, and species distributions. The typical exponential behavior of the relationship between the rate of electrochemical reactions with the overpotential will cause a much larger impact on the results for small discrepancies in the reaction parameters (*e.g.*, Tafel slopes), so even at those concentration ratios, the use of **Lvk** approach might be a valuable option for a reasonably good estimation of the distributions while saving computational time and power.

In this model, convection effects are neglected. Forced convection can decrease the concentration gradients and homogenize the solution. In such cases, the Laplace approach might yield better results. Current density distributions obtained by Laplace and Nernst-Planck equations have been compared to experimental current density distributions measured by SVET [84]. It was shown that, although less rigorous, the current density distributions calculated using the Laplace approach agreed better with the experimental results.

2.13.3. The relative importance of the migration and diffusion terms and the impact of homogeneous reactions

In the view of electroneutrality, the governing equation solving the charge conservation can be described by Equation 2 [54]:

$$\nabla \cdot F \sum_{i} z_i D_i \nabla c_i + \nabla \cdot \nabla \Phi F^2 \sum_{i} z_i^2 u_i c_i = 0 \qquad (2)$$

In the **Lvk** approach, electrolyte conductivity is calculated at each time step, but the diffusion potential term (the first term of the left side of Equation 1) is neglected. As discussed in Part I of this work [110], the errors observed in the **Lvk** are solely due to the negligence of the diffusion potential term on the calculation of the charge conservation. Indeed, when solving for the potential, current density, and species distributions in a case in which the ions had equivalent diffusivities (Case III), the **Lvk** and **NPP** methods yielded virtually identical solutions. In such cases, the diffusion potential term is zero in the view of electroneutrality, as the diffusion potential is the driving force that prevents the separation of charge of ions of different diffusivities.

The comparison between the errors obtained with the **Lk** and **Lvk** methods, together with the error of the **Lk** approach in Case III, allows for the understanding of the relative importance of the diffusion (first term of Equation 1) and migration (second term of Equation 1) on the potential, current density, and species distribution calculations. In low SER ratios, the migration term has a higher contribution to the error of the **Lk** approach, as evidenced by the higher discrepancies between the errors of **Lk** and **Lvk** approaches and by the similarity between the **Lk** errors calculated in Case III and Case I in low SER. In higher SER ratios, the diffusion potential term has a higher contribution to the error of the reduced-order approaches. This is

evidenced by the similarity between the **Lk** and **Lvk** solutions in higher SER ratios and by the discrepancy between the **Lk** error calculated in Case I and Case III – the errors of Case III, in which there is no diffusion potential, are significantly smaller in high SER ratios.

The addition of the sink term and the equilibrium between H^+ and OH^- species increased the errors associated with the reduced-order approaches for the same supporting electrolyte to minor species ratio, with the exception of the lowest NaCl concentration of 0.1 mM, as illustrated in **Figure 2.36** (b-d). Most of the increase in error can be attributed to the absence of the diffusion term on the potential calculation, which increased with the addition of the homogeneous reactions, as indicated by the following observations: i. in Case III, in which there is no diffusion potential as the ions have equivalent diffusivities, but the homogeneous reactions are included, the error of the **Lk** approach in low SER ratios is very similar to the **Lk** error in Case I, in which no reactions are included; ii. the **Lk** and **Lvk** solutions are more similar in the higher SER ratios in Case II.

As discussed in Part I [110], the sink term increased the non-uniformity of the Mg^{2+} and OH^- concentration profiles. As these species have the most discrepant diffusivities and are the electrochemically active species that cause changes in the electrolyte conductivity, the increased non-uniformity in their concentration profiles causes both non-uniformities in the electrolyte conductivity, and higher diffusion potential gradients. The higher electrolyte inhomogeneity is sufficient to explain the increased error of the **Lk** approach, as the calculations are performed assuming a uniform conductivity across the electrolyte. The increase in the diffusion potential term led to an increased error of the **Lvk** approach. The relationship between the errors obtained in Case I and Case II, and the relationship between the errors at varying NaCl concentrations can then be correlated to the non-uniformity of the electrolyte after 7200 s, which can be observed in **Figure 2.29**.

Differently from the other NaCl concentrations, the addition of homogeneous reactions decreased the error of the **Lvk** in the lowest NaCl concentration of 0.1 mM in comparison to Case I. The sink term limited the increase in the electrolyte conductivity caused by the production of the electrochemically active species (Mg^{2+} and OH^-). After 7200 s, the overall increase in the electrolyte conductivity is lessened, and the electrolyte conductivity adjacent to the electrode/electrolyte interface is more homogeneous, as observed in **Figure 2.29** (a). In Case I, the average concentration of the minor species is ca. 7 times higher than that of the supporting electrolyte after 7200 s. As a result, the electrolyte conductivity varied significantly with time and position: it increased by a 30-fold factor, and it was 2.5 x higher at the anode compared to the cathode after 7200 s. Because most of the diffusion potential arises from the unbalanced transport of the Mg^{2+} and OH^-, the diffusion potential term is high in cases in which most of the electrolyte is composed of these species, and they carry most of the current. The higher migration fluxes of Mg^{2+} and OH^- and their discrepant transport properties lead to a higher diffusion term. The sink term increased the

ratio of the supporting electrolyte and minor species concentration, as the sink term removed the Mg^{2+} and OH^-. As a result, the variation of the conductivity with position and time is attenuated (the average electrolyte conductivity had a 5-fold increase, and the highest difference between the maximum and minimum electrolyte conductivity with the position was 30%), and the diffusion potential term is also decreased.

Further increasing the NaCl concentration, the addition of the sink term increased the non-uniformity of the Mg^{2+} and OH^- distributions and consequent electrolyte conductivity in comparison to Case I, which led to an increase in the error. As observed in **Figure 2.29**, there is a higher electrolyte conductivity variation with the position in Case II for NaCl concentrations higher than 0.1 mM. The vigorous reaction sink term near the positions in which the anode and cathode are closer (where there is a higher production of Mg^{2+} and OH^-) decreases the local electrolyte conductivity due to the removal of Mg^{2+} and OH^- and the inhomogeneity of their distributions leads to higher diffusion potentials.

2.13.4. Electroneutrality

The diffusion potential term is the driving force that prevents the separation of charge resulting from the different transport properties of the ions. In the reduced-order approaches, this term is neglected, as the charge conservation equations are partially uncoupled from the mass conservation equations (that is, the model does not "know" that the ions are the charges in the electrolyte to be solved).

Because the electrochemical and homogeneous reactions are charge-balanced, the overall charge of the system is conserved – the summation of the product of the average species concentration and the respective charge of each species is zero. However, locally, electroneutrality is not obeyed, and a net charge is observed. The charge density is then a measure of error associated with decoupling the charge and mass conservation equations, and the magnitude of the charge density in comparison to the characteristic concentration of the species indicates the importance of the error in the species distribution calculations.

The charge density calculated by **Lk** is higher than that calculated by **Lvk**, as it does not account for temporal and positional changes in the electrolyte conductivity, besides neglecting the diffusion potential term.

Table 2.7 shows the diffusivities of the ions considered in the model and the ratio between their diffusivities. H^+ is the ion whose diffusivity most diverges from the others, followed by OH^-. For the system investigated, however, the concentration of H^+ was significantly lower than the other ions, while OH^- was a predominant species in lower NaCl concentrations. Thus, it is expected that much of the charge separation is due to the faster transport of OH^- in comparison with the other ions. The combination of cation and anion with the highest ratio was Mg^{2+} and OH^-; OH^- is 7.25 times faster than Mg^{2+}. In the absence of homogeneous reactions, the distribution of the charge imbalance is related to the transport of Mg^{2+} and OH^-. In the cases

in which migration of Mg^{2+} and OH^- was substantial (e.g., [NaCl] = 0.1 mM), the highest charge imbalances are located near the electrode/electrolyte interface, as observed in **Figure 2.33** (c). At the anodes, a positive charge is calculated due to the sluggish transport of Mg^{2+}. At the cathode, positive and negative charges are calculated, which can be associated with the combination of the fast transport of OH^- away from the cathode, and a sluggish migration of Mg^{2+} to the cathode, yielding a negative charge. In high SER ratios, cases in which Na^+ and Cl^- are the main current carriers, diffusion is the main transport mechanism of Mg^{2+} and OH^-, whose fluxes are oriented from the electrodes to the bulk of the electrolyte, as observed **in Figure 2.33** (d). Because OH^- is faster, a negative charge is observed at the top corners of the electrolyte, the direction to which OH^- diffuses, and a positive charge is observed near the electrode/electrolyte interface, resulting from the combination of the fast OH^- and sluggish Mg^{2+} diffusion.

The addition of the sink term created a higher charge imbalance. The charge imbalance was proportional to the rate of the sink reaction. The higher the current densities, the higher the production rate of the Mg^{2+} and OH^- species and, accordingly, the higher rate of the sink reaction if the conditions for the precipitation were met (solubility product being reached). Thus, a higher charge imbalance is observed where the anode and cathode are in proximity, and it increases with increasing NaCl. As a result, most of the charge density is located adjacent to the electrode/electrolyte interface, as observed in **Figure 2.34** (b). The magnitude of the charge density at the center of the cathode obtained by the **Lvk** increases linearly with the ratio between the diffusion potential over the total potential gradient, as observed in **Figure 2.34** (d).

The ionic charge density in the electrolyte calculated by the **Lvk** approach sheds light on how the diffusion potential acts. By comparing the results between **NPP** and **Lvk**, it is possible to see the impact of the charge imbalance on the potential, current density, and species distributions. In the absence of reactions, the diffusion potential acted to increase the migration of anions to the anodes, slow down the migration of anions away from the cathode and increase the migration of the sluggish cations to the center of the cathode in the lower NaCl concentrations. In 0.1 mM NaCl, these effects can be seen by: (i) the lower potentials calculated at the anodes and higher potentials at the cathodes; (ii) the higher electrolyte conductivity near the anodes; (iii) lower electrolyte conductivity near the cathode; (iv) the higher anion concentrations at the anodes; (v) higher cation concentrations at the cathodes calculated by **NPP**, observed in Figure 2.6 and Figure 2.23**.**

For the higher NaCl concentration, in which the positive charge is concentrated near the electrode/electrolyte interface, and the negative charge is concentrated at the top corners of the electrolyte, the diffusion potential acted to increase the concentration of anions near the electrode/electrolyte interface, and the concentration of cations at the top of the electrolyte. The conductivity near the electrode/electrolyte interface is increased, lowering the ohmic drop across the electrodes.

In the case in which all diffusion coefficients are equal, **Lvk** predicted electroneutrality, as shown in Figure 2.35 and there were negligible differences between **NPP** and **Lvk** solutions. **Lk**, on the other hand, calculated an excess charge; the local variations in the electrolyte conductivity are important to guarantee electroneutrality.

Table 2.7. Diffusion coefficients of the ions and their ratios (10^9 m^2/s)

		Diffusivity / 10^9 m^2/s				
		0.72	**1.18**	**1.75**	**5.33**	**9.30**
		$D_{Mg^{2+}}$	**D_{Na^+}**	**D_{Cl^-}**	**D_{OH^-}**	**D_{H^+}**
0.72	**$D_{Mg^{2+}}$**	1.00	0.61	0.41	0.14	0.08
1.18	**D_{Na^+}**	1.64	1.00	0.67	0.22	0.13
1.75	**D_{Cl^-}**	2.43	1.48	1.00	0.33	0.19
5.22	**D_{OH^-}**	7.25	4.42	2.98	1.00	0.56
9.30	**D_{H^+}**	12.92	7.88	5.31	1.74	1.00

2.13.5. There are competing effects when increasing the supporting electrolyte concentration for a galvanic system

The increase in the supporting electrolyte concentration did not necessarily decreased the error of the reduced-order approaches in low SER ratios. To explain the observed behavior, the authors will reference the expressions describing the current density and potential gradient and rationale delineated by Newman [54]. In the absence of the convection term (and in the assumption of electroneutrality), the electrolyte current density in the electrolyte can be expressed by Equation 3:

$$\boldsymbol{i} = -F^2 \nabla\varphi \sum z_i^2 i_i c_i - F \sum z_i D_i \nabla c_i \tag{3}$$

The electrolyte conductivity is described by Equation 3:

$$\kappa = F^2 \sum z_i^2 i_i c_i \tag{4}$$

Rearranging the terms in Equation 2 and using κ to represent the electrolyte conductivity we obtain Equation 4:

$$\nabla\varphi = -\frac{\boldsymbol{i}}{\kappa} - \frac{F}{\kappa} \sum z_i D_i \nabla c_i \tag{5}$$

In the reduced-order approaches, the second term on the right side of the Equation 4 is neglected; in addition, in the **Lk** approach, κ term is constant, and its value is only given by the concentration of the supporting electrolyte.

The increase in the supporting electrolyte concentration increases κ, and decreases the contribution of the electrochemically active species to the electrolyte conductivity. Thus, in the absence of other effects,

the increase in the supporting electrolyte concentration decreases the error associated with both reduced-order approaches, as the electrochemically active species contribute less to the electrolyte conductivity, and the magnitude of the diffusion potential term decreases (as it is divided by κ). However, this is only true if the increase in the supporting electrolyte concentration does not impact the other terms in Equation 4.

In a galvanic system, the increase in the electrolyte conductivity also leads to an increase in the current density, which leads to a higher production of the electrochemically active species, which can then have a higher participation in the electrolyte conductivity (the SER ratio decreases). Additionally, the increase in the production rate of the electrochemically active species can increase their concentration gradient, which can increase the second term of Equation 4.

In Case II, the increase in the supporting electrolyte concentration from 0.1 to 1 mM caused an increase in the error of the **Lvk** approach. The increase in the electrolyte conductivity led to an increased polarization of the electrodes (increased galvanic interaction), which led to an increase in the current densities. Thus, the production rates of Mg^{2+} and OH^- were higher, causing an increase in the rate of the sink reactions. The higher error indicates a rise in the magnitude of the diffusion potential term: the increase in the concentration gradients caused by the increase in the electrolyte conductivity overwhelmed the decrease in the overall term (as it is divided by κ). Further increasing the supporting electrolyte concentration from 1 to 1000 mM, the error of the **Lvk** approach decreased with the increase in the supporting electrolyte concentration.

The increase in the local charge unbalance calculated adjacent to the electrode/electrolyte interface in Case II indicate that contribution of the diffusion potential term to the distributions increases with increasing supporting electrolyte concentration. However, the increase in the electrolyte conductivity in these higher supporting electrolyte concentrations overwhelms the increase in the concentration gradient term (second term of Equaiton 4), so the overall term was smaller.

The analysis of the impact of the supporting electrolyte concentration on the validity of the assumptions of the reduced-order models is not straightforward, as the interdependency between the variables convolute the analysis. By analyzing Equation 5, one might conclude that the higher the conductivity, the lower the contribution of both terms to the potential. However, in a galvanic system, the higher the conductivity, the higher the current density, which leads to a decrease in SER, and to larger concentration gradients, so each case should be considered on its own merits, but the process described herein provides the framework to perform the analyses.

2.14. Conclusions

This work extends that of Part 1 [110] to electrolytes of lower ionic strength. As was the case in the higher ionic strength solutions in Part 1, the use of **NPE** using the method of elimination results in solutions that are as accurate as those using **NPP** but with a much lower computational cost. The error in current density at the center of the geometry serves as a measure of discrepancies between **NPP** and **Lk** and **Lvk**. In the absence of homogeneous reactions that involve a sink term, **Lk** has a 4% error at a ratio between the supporting electrolyte and the minor species of 10, with that error rising to 10% at a ratio of four, and over 30% at a ratio of one. The **Lvk** method performs substantially better in this case, reaching a 4% error at a ratio of four, and 25% at a ratio of 0.2.

- The addition of homogeneous reactions with a sink term degrades the accuracy of both Laplace-based methods. At the lower supporting electrolyte concentrations, these homogeneous reactions have a large impact than observed in Part 1 for higher supporting electrolyte concentrations. Specifically, the **Lk** has a 4% error at a ratio of ~35, rising to 30% at a ratio of four. The **Lvk** method offers a more limited improvement as compared to Case I.
- The source of the differences between **Lvk** and **NPP** is the differences in the diffusion coefficients of the different species. **NPP** is able to handle these differences without the loss of electroneutrality, whereas **Lvk** created results that were different from **NPP** unless the diffusivities of all the species were the same, as shown in Case III.

Because of the strong interdependency between the potential, current density, and species distribution, the conclusions made herein are applied to the specific system investigated. Changes in the electrochemical kinetics of the materials, ions of interest, and geometry may result in different quantitative conclusions regarding the minimal supporting electrolyte-to-reactive species ratio (SER) required to obtain the desired accuracy. However, qualitatively, the conclusions can be generalized to other systems. At these low SER, if accurate results in current density or species concentrations (i.e., less than ~25% error) are required, then the **NPP** or **NPE** method should be used.

2.15. Acknowledgments

Financial support from the SERDP program through the Office of Naval Research (C. Sanders) via Contract N00173-19-1-G011 as well as the DOD Corrosion Program Office through the US Air Force Academy via Contract FA7000-18-2-0006 is gratefully acknowledged.

2.16. Supplementary Information

A Comparison of FEM Results from the Use of Different Governing Equations in a Galvanic Cell

C. V. Moraes and R. G. Kelly

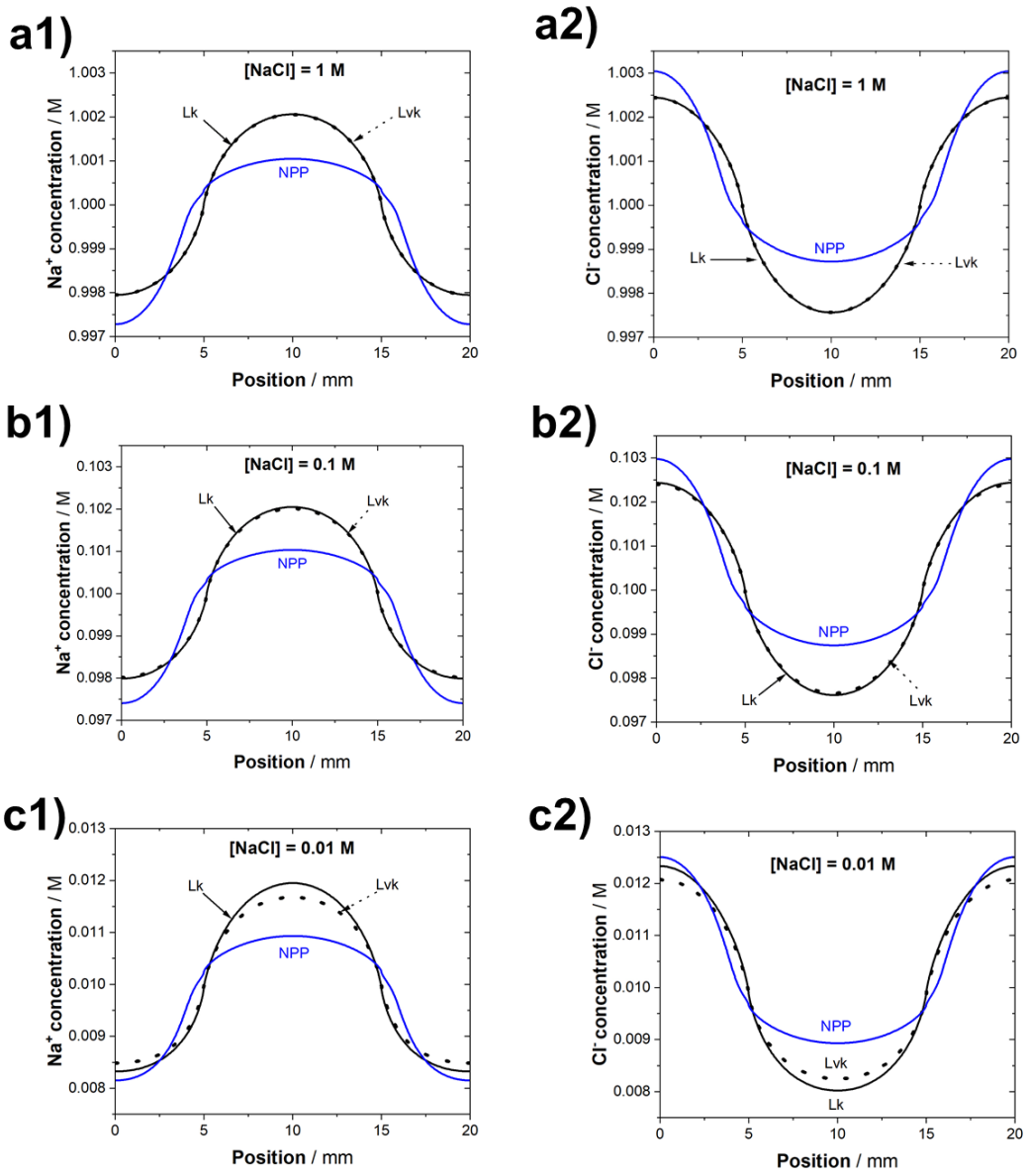

Figure S1. Na^+ and Cl^- concentration profiles after 7200 s obtained at the NaCl concentrations of 1 M (a1 and a2), 0.1 M (b1 and b2), and 0.01 M (c1 and c2) calculated by the different approaches in Case II.

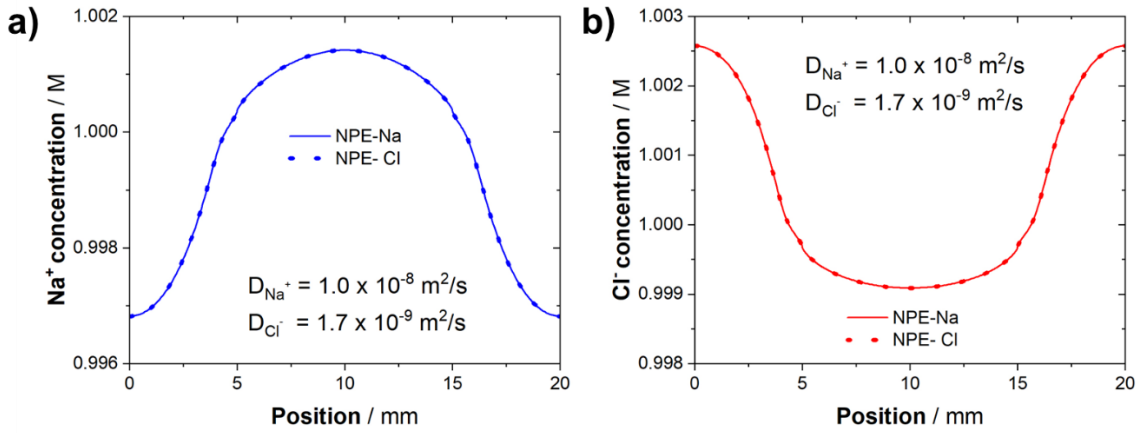

Figure S2. Na^+ (a) and Cl^- (b) concentration profile after 7200 s using the **NPE** approach using either Na^+ or Cl^- as make-up ions (**NPE-Na** and **NPE-Cl**, respectively), for a case in which their diffusivities are significantly different ($1.0x10^{-8}$ m^2/s for Na^+ and $1.7x10^{-9}$ m^2/s for Cl^-).

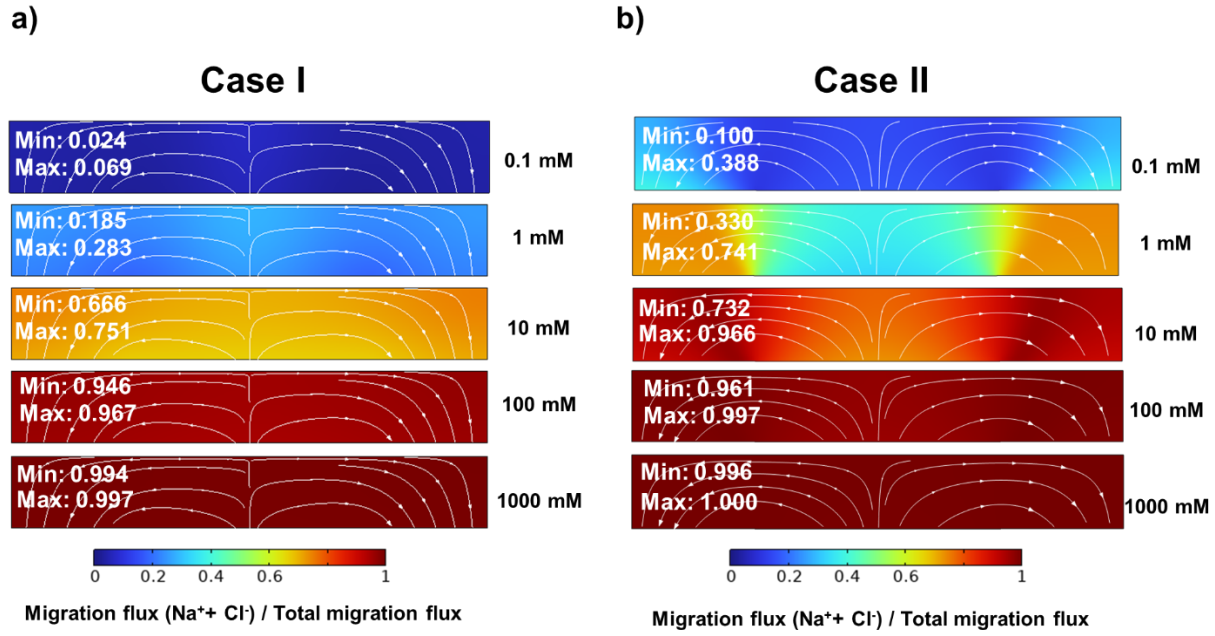

Figure S3. Ratio between the migration flux of the Na^+ and Cl^- species over the sum of the migration fluxes of all species in the electrolyte at the different NaCl concentrations for Case I (a) and Case II (b).

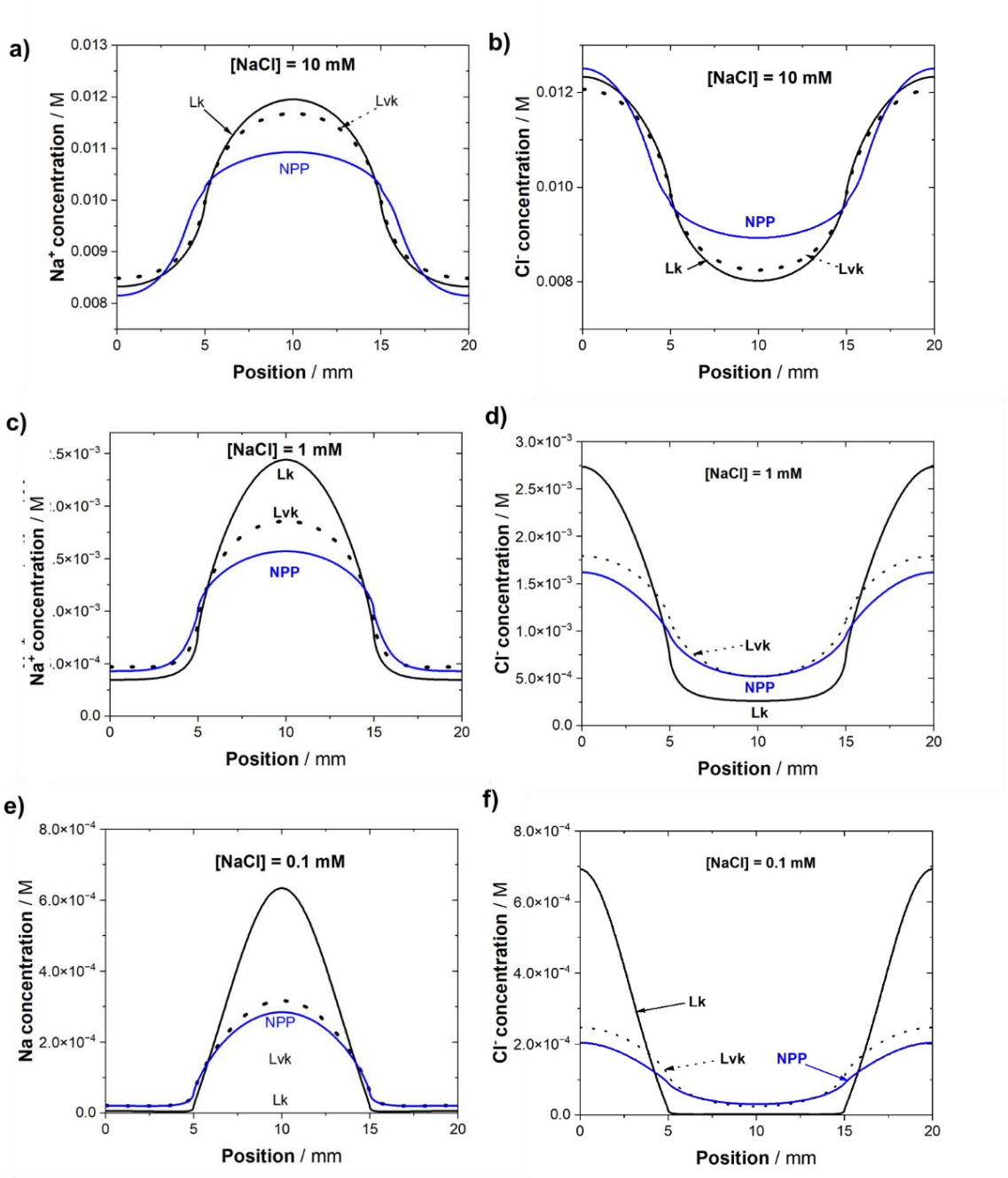

Figure S4. Na^+ and Cl^- concentration profiles after 7200 s obtained at the NaCl concentrations of 10 mM (a1 and a2), 1 mM (b1 and b2), and 0.1 mM (c1 and c2) calculated by the different approaches in Case II.

Chapter 3. Application of the Laplace Equation to Model the Galvanic Coupling of Al alloys

In this Chapter, the suitability of the Laplace approach in predicting current density distributions between an AA7050 and SS316 galvanic couple under solution of relatively lower conductivity was tested. The work was performed in collaboration with other researchers and it is shown below in its original form.

Application of Finite Element Modeling to Macro-Galvanic Coupling of AA7050 and SS316: Validation Using the Scanning Vibrating Electrode Technique

U. Charles-Granville*, R. S. Marshall*, C. V. Moraes*, C. F. Glover, J. R. Scully, R. G. Kelly

* Equal contribution

Center for Electrochemical Science and Engineering,

Department of Materials Science and Engineering,

University of Virginia, Charlottesville, VA 22904

3.1. Abstract

The scanning vibrating electrode technique (SVET) was utilized to experimentally validate the applicability of finite element modeling (FEM) in simulating macro-galvanic-induced corrosion of AA7050 coupled to SS316, in environments representative of the boldly exposed surface of an actual fastener couple. The FEM boundary conditions were modified from the SVET environments in which the AA7050-SS316 couple sample was initially exposed, in order to better represent the steady-state corroding surface of the localized corrosion-prone AA7050. Better agreements between the SVET-derived data and the model in the case of macro-galvanic coupling behavior were achieved for near-neutral conditions, compared to acidic conditions. The current density at the electrode/electrolyte interface was determined with the validated model. In addition, the percent difference between the measured current density at the SVET probe height and that at the electrode surface was observed to scale with the magnitude of current density at the electrode surface, with the largest discrepancy seen at the galvanic couple interface. Plausible reasons for the deviation of the model predictions from the SVET-derived data are discussed.

3.2. Introduction

Precipitation-strengthened Al alloys such as those belonging to the 2XXX and 7XXX series are the preferred materials for the construction of light-weight aerospace vehicles.[114] Despite their superior mechanical properties, these high-strength Al alloys pose a huge challenge in weldability. Because they are precipitation-strengthened, the use of traditional welding techniques to join them often leaves undesirable weld joints with deteriorated properties due to weld porosity and weld cracking during solidification.[115]

As an alternative, high-strength, noble fasteners such as stainless steels (SS) are often used in joining the Al alloy (AA) parts in aerospace structures. In natural corrosive environments, macro-galvanic interactions between the more noble fastener and the AA, in addition to the micro-galvanic coupling within the base AA microstructure,[116] can exacerbate localized corrosion of the Al-based structures.[117–124]

Many studies of galvanic corrosion processes on Al alloys have utilized a number of experimental techniques, including the zero resistance ammeter (ZRA) technique, the coupled microelectrode array (CMEA), and the scanning vibrating electrode technique (SVET).[124–133] The ZRA technique conducted on planar coupled electrodes enables the simultaneous measurements of global galvanic potentials and coupling currents. In this configuration, spatial resolution of localized corrosion processes occurring on the AA cannot be captured; only global current measurements are possible. In this context, the CMEA coupled with the ZRA allows the interrogation of in-situ local electrochemical processes occurring on individual microelectrodes by mapping the local current density distributions as a function of spatial location and time. In the case of AA7XXX, one can monitor the transition of initial anodes to cathodes which could signify dealloying of Al_2CuMg and/or Cu replating.[124,128] That said, some of the limitations of the CMEA are the intricacy of constructing the arrays, the use of surrogate materials as opposed to plate or sheet products used in aerospace construction, as well as the need for controlling specific geometric parameters such as anode-to-cathode ratio and electrode spacing.

The primary benefit of using the SVET to investigate galvanically-induced corrosion is that it enables the spatial and temporal resolution of the electrochemical behavior from the macro-galvanic couple (between SS and AA, in this instance) and localized behavior as a result of the micro-galvanic coupling on the same surface. The evolution of local net anodic and cathodic activity can be mapped, enabling the magnitude of currents to be monitored as a function of time. This distinction between the two types of corrosion occurring in this system cannot be achieved with bulk electrochemical techniques. Although the SVET provides a good representation of the localized corrosion processes occurring *in-situ* on an electrode surface with no perturbation from the test itself, the results should be used with caution.[134] The SVET measures the dominant reaction or net current and detects current based on the potential gradient. It also does not account for local variations in conductivity that may occur at the electrode surface as a result of corrosion processes, and is disrupted by hydrogen bubbles.[135] The SVET measurements are not taken at the electrode surface but at a specific height above the electrode surface, typically ~ 50-150 μm.[130,136–139] As such, the calculated currents are typically an underestimation of the actual values at the electrode surface.[134] One way to bridge this gap is to utilize finite element modeling (FEM) in conjunction with the SVET. If the FEM simulations can be reasonably validated by the SVET at a specified probe height, then one can utilize the FEM to predict current density distributions at the electrode surface as well as quantify the underestimation of the electrode surface current density as a function of SVET probe height.

A number of studies have employed the SVET to validate FEM simulations using the Laplace,[140–142] Laplace and Fick's second law,[138,143,144] and Nernst-Planck[140,143,145,146] as governing equations. The Laplace equation assumes that the solution is homogeneously mixed such that the diffusive and convective transport of species can be ignored, allowing the solution to be treated as an ohmic resistor, which makes the model less complex.[147] The Laplace approach can be supplemented with transport equations for cases in which kinetics of the electrodes are dependent on the concentration of species present in the electrolyte, that either do not considerably carry the current (minor species) or that do not have charge (e.g., O_2). This approach has been widely used to model the mixed charge-transfer and diffusion-controlled kinetics of the oxygen reduction reaction (ORR).[138,143,144]

The Nernst-Planck equation is more robust in considering concentration gradients of all ionic species in the electrolyte, yet computationally demanding in terms of complexity and execution time.[147] Thébault et al.[143] demonstrated that the locally-induced convection from the vibrating probe tip during SVET measurements homogenizes the electrolyte, thus, eliminating any concentration and conductivity gradients. This natural outcome makes the SVET an ideal experimental technique to compare with a Laplacian model.

When solving for the variables that describe corrosion phenomena in FEM with any of the governing equations above, it is common to use a scaffolding approach to determine the correct boundary conditions by starting with simplifying assumptions and working towards a more realistic scenario.[141,148–150] As noted previously, computational results depend highly on the choice of boundary conditions, which are also dependent on a variety of environmental factors.[147]

The aforementioned studies demonstrate the viability of the SVET for modeling galvanic corrosion processes and, to the best of the authors' knowledge, no studies in the available literature have combined these techniques with a focus on AA-SS galvanically-coupled systems.

The objective of this work is to utilize the SVET to validate the FEM-based Laplacian model in predicting macro-galvanic current distributions on an AA7050-SS316 couple in simulated environments representative of near-neutral and acidic corrosive conditions. The geometry of the AA7050-SS316 couple mimics the boldly exposed surface of an actual fastener couple.

As with all models, the choice of the input boundary conditions is crucial to the accuracy and reliability of the model as a predictive tool, especially for conditions that are experimentally difficult or impractical to investigate. Emphasis is made on the choice of boundary conditions as well as the adjustments made in an attempt to correctly represent the conditions being simulated. The sources of the discrepancies observed between the SVET and modeling results are discussed. The results of this study are intended to add to the knowledge base of the applicability of FEM to the simulation of galvanic corrosion phenomena.

3.3. Methods

3.3.1. SVET Measurements

The AA7050-SS316 couple was constructed by inserting a short rod of SS316 onto an AA7050 plate with the dimensions as shown in **Figure 3.1** (a). The SS316 rod was flush-mounted so that the transverse cross-section produces a circular disk in the plane of the plate. The anode-to-cathode area ratio was ~ 7:1. No intentional crevice gap was created. The structure was encapsulated in epoxy with an internal Ni wire electrical connection. Immediately preceding each experiment, the sample was wet-ground successively from 400 grit to a surface finish of 1200 grit with SiC paper, rinsed with deionized water, and dried with clean compressed air. A Biologic SP™ instrument was utilized for the SVET measurements. The scans were conducted on an area of ~ 7.5 mm x 7.5 mm within the exposed bare area of the couple surface in each case, under freely corroding conditions. For each experiment, the exposed couple surface was fully immersed (i.e., water layer thickness ≥ 1000 μm) in an electrolyte bath containing aqueous 1 mM NaCl electrolyte at the relevant pH. The choice of 1 mM NaCl was made based on the resolution limitations of the SVET as signal-to-noise ratios decrease with increasing solution conductivity.[134] Experiments were conducted at the electrolyte's natural pH of 5.8 and at pH 3 (adjusted with HCl) to simulate normal rainy conditions and acid rain conditions, respectively.

An additional experiment was conducted on a 200 μm Au point current source that was used to determine the change in the SVET-derived current density as a function of the SVET probe height from the electrode surface. Two current values of 5 μA and 25 μA were applied separately to the Au point current source. The experiments were conducted in 1 mM NaCl at its natural pH of 5.8, for consistency with the galvanic coupling experiment.

The vibrating SVET probe consisted of a platinum probe with a diameter specified by the manufacturer as between 5 and 50 μm. The probe was positioned vertically and scanned at a constant height of 100 μm above the experimental area with a peak-to-peak amplitude of 30 μm and a frequency of 80 Hz. The peak-to-peak SVET voltage signal (V_{pp}) is related to the current flux density along the axis of probe vibration (j_z) by:

$$V_{pp} = j_z \left(\frac{A_{pp}}{\kappa}\right) \quad (1)$$

where κ is solution conductivity and A_{pp} is the peak-to-peak amplitude of vibration of the SVET probe, such that a quantity $G = \kappa/A_{pp}$ may be defined as the SVET calibration factor.

SVET calibration was carried out galvanostatically using the point current source technique described above, where a graphite counter electrode was held ~ 8 cm away from the Au point current source, and the setup can be found elsewhere.[151],[152] Samples were scanned immediately following immersion

and continuously thereafter for a period of 24 h. The total number of measurement points in each scan was ~ 5776, and the time taken for each measurement was ~ 0.12 s, for a full scan duration of ~ 12 min. There was no wait time between measurements. SVET j_z distributions were plotted using Surfer 8™ by Golden Software.

3.3.2. Electrochemical Measurements

Cathodic and anodic potentiodynamic polarization curves were generated on SS316 and AA7050, respectively, to serve as input boundary conditions for the model. Experiments were conducted on separate SS316 and AA7050 specimens in a standard three-electrode flat cell configuration, in the same environments used for the SVET measurements, under quiescent conditions. HCl was used to adjust the pH. Two concentrations of $AlCl_3$, 0.003 mM and 0.3 mM, were added to the cathodic scans while maintaining the total chloride concentration of 1 mM. The pH in both $AlCl_3$ containing solutions was not controlled but was measured to be 5 and 3.6 for the low and high concentrations, respectively. The scans were conducted after a 30-min full immersion exposure at open circuit and at a scan rate of 0.5 mV/s.

3.4. Model Description

3.4.1. Governing equation and boundary conditions

COMSOL Multiphysics® software (v. 5.6) was used to solve the partial differential equations by the finite element method. Laplace equation (Equation 2) was used to solve for the potential distribution in the electrolyte domain:

$$\nabla^2 \varphi = 0 \tag{2}$$

where φ is the electrolyte potential. By using Laplace as the governing equation, the electrolyte is assumed to be well-mixed (i.e., there is a negligible concentration gradient of the ionic species); hence, electrolyte is assumed to behave as a homogeneous ohmic conductor with a constant conductivity. Thus, the electrolyte current density could be solved using Ohm's law:

$$i = \kappa_i \nabla \varphi \tag{3}$$

where κ_i corresponds to the conductivity of the solution i. For each case investigated, the conductivities were adjusted according to the solution in which the measurements were performed. **Table 3.1** shows the conductivity of the solutions considered in this work, which were calculated using OLI™ Studio Analyzer 10.1 (from OLI Systems, NJ). In all scenarios tested, the conservation of charge (i.e., $I_a = I_c$, with I_a being the total anodic current and I_c being the total cathodic current) was verified.

The assumption of a well-mixed electrolyte to model SVET measurements is reasonable, as the convection induced by the microelectrode vibrations homogenizes the electrolyte, reducing any concentration gradients.[143]

In an additional model, Al^{3+} production and transport were calculated. Fick's second law was used to solve for the concentration distribution through space and time:

$$\nabla^2 c_{Al^{3+}} = 0 \quad (4)$$

Note that, even though Al^{3+} is a charged species that can carry current, it was assumed that Na^+, Cl^-, and H^+ were the main species that carried current.

The model was built using a 3D geometry. The dimensions of the sample on which the SVET was performed were used to build the geometry, as shown in **Figure 3.1** (b).

3.4.2. Boundary conditions

As illustrated by **Figure 3.1** (c), at the upper (xy), left (yz), and right (xz) boundaries, which represent the air/solution interface (z = water layer thickness), Neumann boundary conditions were applied (i.e., no current flux). At the lower boundary, the electrochemical kinetics of SS316 and AA7050 were defined using different approaches. In the first approach, piecewise interpolations of the full immersion potentiodynamic polarization scans were used as boundary conditions. In a second approach, a limiting current density corresponding to the diffusion-limited oxygen reduction reaction (ORR) current density was imposed. In a third approach, the cathodic kinetics of SS316 were defined using an analytical expression:

$$i = \frac{i_{ct}}{1 + \left|\frac{i_{ct}}{i_{lim}}\right|} \quad (5)$$

$$i_{ct} = i_0 \cdot 10^{\frac{E-E_0}{b}} \quad (6)$$

where i_{ct} is the charge transfer-controlled portion of the current density, i_{lim} is the ORR limiting current density extracted from the cathodic polarization scans, i_0 is a pseudo-exchange current density, E is the applied potential, E_0 is the reversible potential, and b is a fitted Tafel slope. The pseudo-Tafel parameters were obtained by fitting Equation 6 to the cathodic polarization scans. The values of the parameters are displayed in **Table 3.1.**

Note that the edges of the sample (x = 0 and 8 mm) were the boundaries of the simulation, which simulates a condition in which the walls of the container in which the SVET was performed were exactly at the edges of the sample (**Figure 3.1**b and 3.1c). This modeling approach is common in literature, even if the sample is exposed to bulk immersion such as occurs during SVET.[138,140,145,153] However, the dimensions of the container in which the SVET was performed were much larger than the sample's dimensions.

For the case in which Al^{3+} concentration was calculated, Faraday's law was used to calculate the local flux of the Al^{3+} species being produced at the AA7050 electrode ($J_{Al^{3+}}$), with the assumption that the dissolution of the other alloying elements present in AA7050 (e.g., Zn, Mg) are negligible:

$$J_{Al^{3+}} = \frac{i_{local,AA7050}}{nF} \tag{7}$$

where n is the number of electrons transferred during the reaction, and F is Faraday's constant. Additionally, for the case in which Al^{3+} was considered, the geometry of the model was altered to match the total volume of the solution in which the SVET measurements were performed. Zero flux boundary conditions were imposed at the interfaces between electrolyte/air and at the walls of the container. Effects of natural convection were not taken into consideration.

3.4.3. Error calculations

When comparing experimental results against each other, such as calculating the conservation of electroneutrality between the experimentally-derived anodic and cathodic currents, or to quantify the difference between computational results, the percent difference was used (Equation 8).

$$\frac{ABS(x_1 - x_2)}{ABS\left(\frac{(x_1 + x_2)}{2}\right)} \times 100 \tag{8}$$

where ABS represents the absolute value, x_1 represents one experimental/computational datapoint, and x_2 represents another experimental/computational datapoint, respectively. However, when the computational and experimental current densities (or currents) were compared, the percent error was utilized (Equation 9).

$$\frac{ABS(i_{experiment} - i_{computational})}{ABS(i_{experiment})} \times 100 \tag{9}$$

In this way, the experimental results acted as a "baseline" with which to compare the computational data.

3.5. Results

3.5.1. Potentiodynamic Scans

Cathodic and anodic potentiodynamic scans (PDS) were plotted separately for clarity in **Figures 3.2**a and **3.2**b, respectively. Note that only cathodic reactions on the SS316 surface were considered in this work. The anodic passive current density of SS316 was calculated to be approximately three orders of

magnitude lower than the cathodic behavior of SS316 within the potential range of interest. This result justifies the assumption that anodic reactions occurring on the SS316 surface in the present system would be negligible.

In the pH 3 environment, cathodic kinetics on SS316 increased by at least two-fold compared to that at pH 5.8, which is consistent with what has been reported in the literature.[154,155] Additionally, it was observed that the cathodic kinetics increased with increasing Al^{3+} concentration while keeping the chloride concentration constant. Decreased amounts of Al^{3+} in solution exhibited a smaller effect, with a diffusion limiting current density visible and approximately equal to that observed in the pH 3 solution, where no additions of $AlCl_3$ were made. Both the change in pH and the addition of Al^{3+} had minimal impact on the open circuit potential (OCP) of the SS316. Concerning the cathodic scans on SS316 without the addition of Al^{3+}, there was a current wave at potentials between the charge-transfer regime and the diffusion limiting regime (**Figure 3.2**a). This cathodic peak was determined to be a transient and will be discussed in a later section.

All anodic curves were manually post-processed to correct for ohmic drop by first calculating the slope of the linear E vs. i plot to determine the ohmic (solution) resistance. The true potential was determined by subtracting the product of the current density and ohmic resistance, that is, the potential due to ohmic drop. To confirm the calculated solution resistance from post-processing, EIS was used to measure the actual resistance between the reference and working electrodes. Impedance at high frequencies performed in the same cell, assuming a Randles circuit, resulted in ohmic resistance values consistent with the manually calculated values as displayed in **Table 3.2.**

Conventional anodic polarization of AA7050 typically starts either at, or slightly below, the measured OCP before scanning to more positive potentials. In this study, scans were also conducted starting at a high potential and sweeping towards the OCP. This method captures the anodic kinetics and OCP while the surface is undergoing active localized corrosion, and is evident in the data presented in **Figure 3.2**b, where increased anodic kinetics and a suppressed OCP are observed in the 'high E to OCP' negative scans, relative to those observed for the positive 'OCP to high E' scans. Additionally, independent of scan direction, the OCP of the AA7050 in the pH 3 solution was found to be more negative than that observed in pH 5.8. When considering a steady-state model, the boundary conditions should also reflect steady-state corrosion while neglecting any passive breakdown initiation period that may occur during the initial immersion. Selecting a polarization curve that best describes the steady-state corroding surface requires careful consideration. This aspect of modeling will be discussed later.

3.5.2. SVET Current Density Distributions

Figures 3.3a and **3.3**b show the SVET-derived current density distribution maps obtained on the AA7050-SS316 couple in 1 mM NaCl at pH 5.8 and pH 3, respectively, after 24 h of immersion. Under pH 5.8 conditions (**Figure 3.3**a), localized anodic activity was observed in multiple locations on the AA7050 surface, indicative of pitting corrosion. It is noteworthy that these anodically activated regions on the AA7050 surface were not necessarily found to be adjacent to the SS316 cathode. Peak anodic and cathodic j_z values over the couple surface were ~ $\pm$ 10 μA/cm^2. Under pH 3 conditions (**Figure 3.3**b), increased cathodic current density over the SS316 (up to 50 μA/cm^2) facilitated the anodic activation of nearly the entire exposed surface of AA7050, with an anodic j_z maximum of ~ 30 μA/cm^2. The j_z distributions measured above the SS316 were up to five times greater than the values observed over SS316 under pH 5.8 conditions.

3.5.3. Comparison of the Global Current Density Distribution

Two steady-state finite element models were created, with input from PDS providing the boundary conditions. Each PDS was performed in an identical solution as that used for the SVET measurements. The global current density was calculated for each pH condition and compared with results measured from the SVET (**Figures 3.3**c and **3.3**d). At a distance of 100 μm above the surface, the SVET tip measures the electrolyte current density in the normal z-direction by oscillating $\pm$ 15 μm to calculate the potential difference. The resulting current density is important to distinguish from that on the electrode surface. Therefore, the z-component of the current density vector 100 μm above the surface was calculated computationally, unless otherwise specified.

To best compare the dynamic experimental data with the steady-state computational results, SVET experiments were conducted for 24 h. Area-averaged integrated current density vs. time plots were used to confirm that the system reached steady-state. Note that the bounds of the color-scale bar from the computational plots are consistent with that of the SVET data and that the pH 3 scenario bounds are not symmetric. Qualitatively, the models at both pH conditions capture the interface between the AA7050 panel and SS316 disk, with the same order of magnitude as was measured via SVET (**Figures 3.3**a to **3.3**d). That is, the model also predicted an increase in current density as the solution was changed from pH 5.8 to pH 3.

Figures 3.3e and 3f show the simulated potential distributions for the pH 5.8 and pH 3 conditions, respectively. For both pH cases, there was a small ohmic drop across the electrodes (6 mV for the pH 5.8 case, and 12 mV for the pH 3 case), and the couple potentials were closer to the non-polarizable AA7050 anode.

3.5.4. Comparison of the Current Density Line Profiles under pH 5.8 Conditions

Line scans taken across the center of the sample, as indicated by the black dashed lines in **Figures 3.3**a and **3.3**b, were compared between the SVET data and modeled results to facilitate a more rigorous interrogation of the current density distributions across the galvanic interface. Note that the SVET line scans contain small fluctuations rather than a completely smooth line, indicative of the local reaction transients taking place at the time of the scan or noise due to hydrogen bubbles, as seen in the 2D maps presented in **Figures 3.3**a and **3.3**b.

To compare the model with the SVET line scans, three boundary condition scenarios (as displayed in **Figure 3.4**a) were tested in 1 mM NaCl at its natural pH of 5.8:

1. Cathodic SS316 PDS and anodic AA7050 PDS (full PDS)
2. Cathodic SS316 PDS with i_{lim} imposed and anodic AA7050 PDS (PDS + i_{lim})
3. Cathodic SS316 i_{ct} fitting with i_{lim} imposed and anodic AA7050 PDS (i_{ct} + i_{lim})

In all scenarios, the modeled results show the electrolyte current density calculated at a height of 100 μm from the surface for consistency with the SVET-derived data.

For scenario 1 (full PDS), the evaluation largely overestimated both the anodic and cathodic currents when compared to those measured with the SVET (**Figure 3.4**b). Speculating that the overestimation may be due to the current wave between the charge-transfer and diffusion limiting current regime, a new model was created (scenario 2), strictly enforcing that the maximum current density was not greater than the diffusion limiting current density ($i_{lim,\ 5.8}$) reported in **Table 3.1** (**Figure 3.4**a). Although neglecting current densities greater than $i_{lim,5.8}$ neglected the HER as well as the cathodic current wave, the couple potential was positive enough such that the HER would not contribute in any way. Utilizing the new cathodic boundary condition (PDS + i_{lim}), the computational line scan of current density decreased to values closer to what was measured with the SVET (**Figure 3.4**b).

An additional method of selecting model boundary conditions involves the use of charge transfer-controlled kinetic parameters (scenario 3), which were extracted from the measured cathodic PDS (**Figure 3.4**a), and are documented in **Table 3.1**. These E-log(i) parameters generalize the cathodic behavior in the given environment, increasing the reproducibility of FEM, and were input as new cathodic boundary conditions (i_{ct} + i_{lim}) while the AA7050 anodic boundary condition remained the same. The resulting cathodic current density was increased slightly, while the anodic current remained nearly constant due to the much larger anodic surface area. Both boundary conditions including i_{lim} appeared to accurately capture the peak anodic behavior in the horizontal line scan, as well as the overall cathodic behavior seen in both horizontal and vertical line scans (**Figure 3.4**b).

To determine whether the observed cathodic current wave was a complexation of species, or a transient reaction, a potentiostatic hold was applied to SS316 at a value of -0.62 V vs. SCE for 24 h (**Figure**

3.5). During the hold, the current density decreased sharply before quickly stabilizing, indicating that a transient reaction may have occurred but would not be sustained nor representative of the long-term cathodic behavior of the SS316. The transient reaction was speculated to be the reduction of the native Fe^{3+} oxide to Fe^{2+}, which is consistent with the system E-pH region on the iron E-pH diagram, calculated using Medusa™ software. It is noted that the native oxide film on the SS316 was not reduced prior to performing the PDS.

3.5.5. Comparison of the Current Density Line Scans under pH 3 Conditions

A similar approach was employed to model the galvanic coupling between AA7050 and SS316 in the pH 3 solution, with the following boundary conditions tested, as displayed in **Figures 3.6**a and **6**c:

1. Cathodic SS316 i_{ct} fitting with i_{lim} imposed (1) and anodic AA7050 positive PDS, OCP to high E (2)
2. Cathodic SS316 with 0.003 mM $AlCl_3$ PDS (3) and anodic AA7050 positive PDS, OCP to high E (2)
3. Cathodic SS316 with 0.003 mM $AlCl_3$ PDS (3) and anodic AA7050 negative PDS, high E to OCP (4)
4. Cathodic SS316 with 0.3 mM $AlCl_3$ PDS (5) and anodic AA7050 negative PDS, high E to OCP (4)

Figure 3.6b shows current density line profiles calculated by the models and measured by the SVET, both at a distance of 100 μm above the electrode surface. The SVET-derived data were extracted from both the horizontal and vertical centerlines of the sample surface. Additionally, the plot shows an SVET-derived current density line profile where an average value has been applied for the cathodic portion. This corrects the asymmetry observed in the cathodic region and entailed averaging all cathodic current density data points except the first and last three, as they were approximately symmetric. The averaged value was plotted between the original, unaveraged cathodic data points.

In the first model scenario tested ((1) and (2) in **Figure 3.6**a), the cathodic kinetics on SS316 were implemented using fitted charge transfer-controlled kinetics with a limiting current density ($i_{lim,3}$ = 30 $\mu A/cm^2$), as this approach provided better agreement with the SVET-derived data from the experiments performed in the pH 5.8 solution. That is, the coupled SS316 cathode and AA7050 anode within the SVET were assumed to behave exactly as described by the polarization of the individual materials in the same solution and pH but with an imposed limiting current density. The model underestimated both anodic and cathodic current densities (line (1) + (2) in **Figure 3.6**b). The anodic current densities were underestimated by almost one order of magnitude, whereas the cathodic current densities were ca. 30% lower than the averaged cathodic current density. The strikingly different results obtained from the calculations indicated that the boundary conditions implemented at the SS316 and AA7050 surfaces did not represent the kinetics

of the coupled alloys after 24 h of exposure in the pH 3 solution. It was rationalized that the electrolyte chemistry after 24 h of exposure evolved due to the higher currents observed in the acidic solution; thus, the behavior of the alloys in the solution in which the SVET sample was initially exposed would not represent the kinetics after the 24 h exposure.

In an attempt to simulate a more representative electrolyte chemistry of the galvanic couple, new cathodic boundary conditions (scenario 2) were generated with a low concentration of Al^{3+} ((3) in **Figure 3.6**a). This modification was incorporated because the presence of Al^{3+} in the electrolyte (stemming from the oxidation of the AA7050 anode) could influence the electrochemical behavior of the SS316 cathode. However, the kinetics of the AA7050 anode were still assumed to behave as the conventional positive polarization of OCP to high E would predict (i.e., with a passive film present). Line (2) + (3) in **Figure 3.6**b shows the current density profile obtained when using this boundary condition, in comparison with the SVET-derived data. Utilizing faster cathodic kinetics in this modified model slightly increased the cathodic current densities; however, it still largely underestimated both the SVET-derived anodic and cathodic current densities.

Scenario 3 simulated a condition in which AA7050 was actively corroding, i.e., little to no passive film present. New anodic polarization scans were performed by starting the scan at a high E and sweeping down to the OCP, as described previously ((4) in **Figure 3.6**a). The results are shown in **Figure3.6**b (line (3) + (4)). The cathodic current densities calculated from the model correlated well to the averaged SVET-derived cathodic current densities. However, the anodic current densities were still underestimated. The total current density increased by a factor of 1.55, which is consistent with Mixed Potential Theory predictions (**Figure 3**.6a). Due to the smaller area, the current density on the SS316 is higher, so the 55% increase in the cathodic current density results in a higher increase than the anodic current density increase.

One last scenario was tested (scenario 4), in which the anodic kinetics were kept the same as the previous model in scenario 3 (i.e., where negative PDS were conducted from high E to the OCP), but the Al^{3+} concentration was increased on the cathodic boundaries from 0.003 mM $AlCl_3$ to 0.3 mM $AlCl_3$ ((5) in **Figure 3.6**c), to account for the increased dissolution of the AA7050 anode.

Evaluating the PDS data with both Al^{3+} concentrations, the higher Al^{3+} concentration resulted in faster cathodic kinetics (**Figure 3.6**c). This observation also translated to the model. **Figure 3.6**d shows line scans from the models using the two Al^{3+} concentrations as cathodic boundary conditions, in comparison to the SVET-derived data. The high Al^{3+} concentration resulted in anodic current densities that were in agreement with those measured with the SVET. However, the cathodic current densities were largely overestimated by approximately one order of magnitude.

3.5.6. Total Current Comparisons in pH 5.8 and pH 3 Environments

Although it was not possible to simulate the pitting events that occurred under pH 5.8 conditions with the modeling approach used in this work (**Figure 3.4**b), good comparisons were achieved when total currents were considered. **Figure 3.7**a compares the SVET-derived total currents with FEM results for pH 5.8 conditions assuming the horizontal line scan (with no apparent pitting events) was representative of the current distributions over the entire sample. The i_{ct} + i_{lim} fitted kinetics slightly overestimated the total anodic and cathodic currents by 0.13 μA. However, the same boundary conditions largely underpredicted the experimental data when the total currents derived from the global sample were analyzed (**Figure 3.7**c).

To better represent the high currents from the localized corrosion, the boundary conditions simulating an actively pitting surface over the entire AA7050 surface (i.e., negative anodic PDS from high E to OCP) with release and transport of a low concentration of Al^{3+} to the bulk solution, including over the SS316 (cathodic scan with the addition of 0.003 mM Al^{3+}) were utilized. A better agreement was attained for total currents, with 3% error between the computational and total anodic currents and 8.5% error between the computational and total cathodic currents (**Figure 3.7** c). Note that the percent difference between the global anodic and cathodic currents from the SVET was 5.5%.

For the pH 3 environment line profiles, the experimental anodic and cathodic current densities could only be replicated with separate models taking into account the two concentrations of Al^{3+} as cathodic boundary conditions (**Figure 3**.6d). When the total current was calculated, assuming that the line scan was representative of the entire system, a similar trend was observed (**Figure 3.7**b). When the low Al^{3+} concentration boundary conditions were used, the *cathodic* currents from the computational results had 7% error relative to the SVET measurements, while the *anodic* current was underestimated by 71%. However, when the higher Al^{3+} concentration boundary conditions were used, the computational *anodic* current had only 11% error when compared with the SVET-derived data, while the computational *cathodic* currents largely overestimated the experimental work by 291% (**Figure 3.7**b).

However, looking instead at the globally calculated SVET currents, there was a reasonable agreement with the high Al^{3+} concentration model (**Figure 3.7**d). That is, the model simulated with the boundary conditions of scenario 4 presented a better agreement with the global SVET currents. The computational anodic currents had 13% error in comparison to the SVET global anodic currents, whereas the computational cathodic currents had 26% error.

3.6. Discussion

3.6.1. Macro Galvanically-Driven Corrosion of AA7050 is Exacerbated in Acidic Conditions

The significant increase in SVET-derived j_z distributions over the surface of the AA7050-SS316 couple when fully immersed in pH 3 solution compared to those observed at pH 5.8 conditions was expected

due to the detrimental effect of acidic pH on galvanic corrosion of Al alloys. On the uncoupled AA7050, pH 3 is shown to increase anodic kinetics relative to the case at pH 5.8 (**Figure 3.2**b). This adverse effect of low pH is attributed to the uniform dissolution of the native oxide film in acidic conditions compared to the more localized attack of the protective oxide film in (near) neutral conditions.41–435 Coupling with SS316 exacerbates the attack on AA7050 because of the increased cathodic current available to sustain higher rates of Al dissolution (**Figure 3.2**a). The released Al^{3+} could transport from local anodic sites into the bulk solution, including over the SS316, leading to further increases in cathodic currents (**Figure 3.2**a). This phenomenon of Al^{3+} increasing cathodic kinetics on SS316 has been reported previously, and was determined to mainly impact the HER diffusion kinetics.[154,159] In the present work, this impact on the HER kinetics was evident on the cathodic scan carried out in 0.3 mM $AlCl_3$ (**Figure 3.2**a).

3.6.2. Choice of Computational Boundary Conditions to Best Represent Different Environments

Choosing boundary conditions within the model may seem as straightforward as conducting PDS in a replicate solution of the system of interest. However, this work has shown that there are two potential pitfalls that must be appreciated, 1) the time dependence of the PDS and 2) the effects of localized corrosion.

The PDS time-dependence was apparent during the cathodic scans. Although the model assumed steady-state, the PDS samples were exposed to the solution for 30 min at OCP with an additional 30 min of exposure during the scan, resulting in only 1 h of total exposure time. Therefore, the transient current wave was still observed (**Figure 3.2**a). The decay in current density during the potentiostatic hold (**Figure 3.5**) confirms that the cathodic current wave was a transient reaction that would not be present during longer times of exposure, such as with the 24 h SVET scan. Neglecting the cathodic current transient (i.e., using PDS + i_{lim}, and i_{ct} + i_{lim} boundary conditions) led to a better comparison between the model and SVET line scans in the pH 5.8 environment (**Figure 3.4**b). Transient reactions may be present during a fast-scan polarization experiment; however, if the goal is to represent a steady-state system such as the SVET after 24 h, then careful evaluation of the PDS must be conducted to determine that no transient reactions are present.

In aggressive environments, such as acidic conditions, it is necessary to ensure that the computational boundary conditions for a steady-state model represent an actively corroding system. In the current system, this was accomplished by modifying both the anodic and cathodic boundary conditions.

As stated previously, an acidic environment breaks down the native passive film of Al alloys. However, the anodic PDS in pH 3 solution that was scanned conventionally from OCP to high E was not able to capture the kinetics of the active system measured with the SVET (**Figure 3.6**b). The reason could either be due to the short exposure time of the PDS when immersed in the acidic condition, thereby not

allowing enough time for the passive film to dissolve, or due to the lack of extra polarization provided by the SS316 in the SVET galvanic couple. The latter is justified by the fact that the anodic polarization of AA7050, provided by galvanically coupling with the SS316, is greater in acidic conditions than in near-neutral conditions, as evident by the potential difference between the alloys (i.e., the driving force for galvanic coupling) in **Figure 3.3**e and **3.3**f. Performing the anodic polarization scan starting at a high E to OCP artificially ensured that the entire surface was active and uninhibited corrosion could occur (**Figure 3.2**b).

Concerning the cathodic kinetics, it is expected that there would be an increase in the concentration of Al^{3+} due to the relatively high anodic kinetics and the stability of the Al^{3+} species at pH 3.[160] Because it has been observed that Al^{3+} increases the cathodic kinetics on SS316,[154,159] two new cathodic PDS were conducted on SS316 (Figure 6c). The low Al^{3+} concentration, containing 1 mM NaCl + 0.003 mM $AlCl_3$, was estimated by calculating the total anodic charge from the SVET-derived current density measurements after 24 h, and then using Faraday's law to calculate the total amount of Al^{3+} produced, assuming that the dissolution of the other alloying elements present in AA7050 (e.g., Zn, Mg) to be negligible. The higher concentration of Al^{3+}, 0.3 mM attained with only $AlCl_3$, was determined to be the maximum amount of Al^{3+} possible while keeping the chloride concentration consistent with the other scenarios.

In order to verify if the Al^{3+} concentrations chosen to perform the new boundary conditions were appropriate and to calculate the Al^{3+} concentration at the surface of SS316 and AA7050, the production and transport of Al^{3+} were calculated in the model that simulated the galvanic coupling in the pH 3 solution, using the activated AA7050 PDS. **Figure 3.8** shows the simulated Al^{3+} concentration as a function of position and time. At the SS316 surface, the concentration ranged from 0.28 mM to 0.34 mM after 24 h. The method of calculating the Al^{3+} concentration by utilizing the total charge and dividing by the volume of the solution thereby underestimated the Al^{3+} concentration at the surface of SS316. It is noted that the model calculations were performed ignoring the convection caused by the vibration of the SVET probe. The forced convection decreases concentration gradients and homogenizes the solution. Thus, the concentration of the species at the electrode surface is also expected to change.

It is also worth noting that the assumption that Na^+, Cl^-, and H^+ are the only species carrying current might not be valid after 24 h as the concentration of Al^{3+} increases to values of the same order of magnitude as Na^+, Cl^-, and H^+. Thus, under this condition, the Nernst-Planck equation approach must be invoked. To maintain electroneutrality, it is likely that an increase in the local Cl^- and OH^- concentration would occur to compensate for the additional positive charge originating from the Al^{3+} production. Additionally, if the supporting electrolyte assumption is no longer valid, then local changes in the conductivity of the solution should be taken into consideration.

3.6.3. Discrepancies Between Model Predictions and SVET Measurements

Both vertical and horizontal SVET-derived line profiles were compared with the model in order to capture a good representation of the localized processes occurring on the AA7050 surface. The simulated galvanic coupling under pH 3 conditions presented higher discrepancies compared to those simulated for pH 5.8 conditions, when using the $i_{ct} + i_{lim}$ boundary conditions (**Figures 3.4**b and **6**b). Interestingly, the reverse situation was expected because the computational model, with the present homogenous assumptions, should better represent the case of pH 3 in which the oxide film was dissolved globally and more uniform corrosion was occurring, as opposed to the localized corrosion occurring in the pH 5.8 case. Furthermore, the SS316 cathodic current measured potentiostatically at pH 3 varied throughout the 24-h test, indicating that steady-state was not achieved (**Figure 3.5**), in contrast to the present assumption of a steady-state model. Considering the stability of the current measured by the potentiostatic hold at pH 5.8 and the relatively good comparison with computational results, it is conceivable that the system at pH 3 may not have reached steady-state within 24 h.

When quantifying the difference between the SVET and FEM calculated total currents, the percent error between the anodic and cathodic values was often asymmetric, which can be attributed to an asymmetry in the experimental anodic and cathodic currents. Within the model, the anodic and cathodic currents must be equal to preserve the conservation of charge. However, as visible in **Figure 3.7**b, the total anodic and cathodic currents obtained experimentally at pH 3 were not equal, with 111% difference (i.e., 4.8 μA). This situation would therefore be impossible for a singular model to capture, because the computational currents *have to be equal*. Speculations as to possible causes of the lack of electroneutrality in the experimental measurements are discussed in a later section.

Comparing the globally calculated total current over the entire sample, the experimental difference between anodic and cathodic currents was much lower (41%, 3.5 μA). Using boundary conditions with the high Al^{3+} concentration resulted in the best comparison with the experimental values (**Figure 3.7**d). Notably, the high concentration of Al^{3+} was also predicted to occur based on local flux predictions of the model (**Figure 3.8**).

It is suggested that another source of the discrepancies observed between the model predictions and the SVET measurements is the inhomogeneities of the anodic and cathodic kinetics of AA7050 and SS316 due to surface heterogeneity and/or changes in local chemistry. Indeed, the analysis of the current density maps in Figures 3a and 3b shows that the distributions are non-uniform. Localized “hot spots” of current density can be seen from the SVET in pH 5.8, where pits grew while the remaining AA7050 surface was either passive or catalytic to cathodic reactions (**Figure 3.3**a). In the pH 3 case, there were regions with significantly decreased anodic activities over the top half of the sample surface (**Figure 3.3**b). These regions

with lower current densities might correspond to locations with precipitated corrosion products. Such regions could include locations immediately adjacent to cathodic areas, where the local pH could be considerably higher. As a result, the bulk of the cathodic current that the SS316 supplies may support rapid dissolution of the remaining active areas on the AA7050.

Such localized distributions are not captured in the model, as the polarization scans performed on AA7050 represent averaged kinetics of the intermetallic particles and the matrix weight by their activity and area fractions. Thus, within the model, AA7050 was assumed to be homogeneous with the entire panel actively corroding. On a macroscale, this assumption is generally valid as the local cathodic and anodic regions average out, as noted when comparing the global total currents (**Figure 3.7**c and **7**d). One method of manually accounting for the local variations was conducted in the pH 3 horizontal line scan, where the cathodic currents were averaged to provide a better comparison with the homogenous model (**Figure 3.6**b). The peak cathodic current between the modeled scenario 3 and the averaged cathodic kinetics had 1% difference between them (**Figure 3.6**b).

The observations discussed above highlight the experimental complexities of non-steady-state, lack of charge conservation, and inhomogeneities in electrode surface conditions/chemistry. These complexities may shed light on the inability of the model to correctly estimate both the cathodic and anodic current densities with the same boundary conditions. This observation may be important, especially in systems in which the increased electrochemical activity leads to significant changes in the local electrolyte chemistry, which in turn can locally affect the electrochemical behavior of the electrode. That is, one portion of the sample in the pH 3 environment may be undergoing different rates than an adjacent portion, due to local changes in the electrolyte or at the electrode surface, making it difficult to predict computationally. For such cases, transient models that take into account the evolving electrolyte chemistry and its effect on the electrochemical behavior of the alloys can improve the predictability of the computational approach.[150]

3.6.4. Advantages of Combining the SVET and Computational Techniques

The advantages of combining SVET with FEM approaches have been discussed in the literature, and both techniques have been combined to investigate the galvanic coupling behavior between dissimilar alloys.[129,138,140,141,143–146,161] As stated previously, the SVET tip herein measured the potential difference at 85 μm and 115 μm over the entire surface. This potential difference allows for the calculation of the ionic current density (Equation 1), which is assumed to be at an average distance of 100 μm from the sample surface. One important aspect of modeling is the ability to calculate the current density at the electrode/electrolyte interface and also at any point within the electrolyte. Thus, once validated, the models

can be used to predict the current density at the electrode/electrolyte interface and better interpret the results obtained with SVET.

Recently, Saeedikhani et al.[138] compared SVET and modeling results performed on a scratched zinc-based coating applied to a steel substrate. Although a good agreement of electrolyte current density above the surface was observed between SVET and FEM, the current density at the electrode/electrolyte was underpredicted, especially within the scribed region. One of the major sources of the discrepancy was due to the geometry of the specimen, as the distance between the SVET probe and the electrode surface almost doubled (from 150 to 270 μm) as it moved from the Zn-coated steel surface to the scribed bare steel. In this work, however, a planar geometry was used to measure the galvanic current densities between AA7050 and SS316. Thus, the SVET probe height from the electrode surface was constant across the sample. Any local variation between the electrolyte current density and the interface current density could then be isolated and attributed to a non-geometric effect.

Figure 3.9a shows the calculated electrolyte current densities in the pH 5.8 environment at four heights: z = 0 (at the electrode/electrolyte interface), z = 85 μm, z = 100 μm, z = 115 μm. At the center of the SS316 electrode (x = 4 mm), a difference in current density of ca. 10% was observed between z = 0 and z = 100 μm. The difference in current density from 85 μm to 115 μm above the surface, which were the minimum and maximum distance of the SVET tip, respectively, was calculated. The value was negligible at 0.22 $\mu A/cm^2$, in the context of currents discussed in this work, with the peak cathodic current in pH 5.8 being 6 $\mu A/cm^2$ (**Figure 3.4**b).

Figure 9b shows the absolute and percent difference between the current density at the electrode surface and the electrolyte current density calculated at a distance of 100 μm above the surface as a function of position. Near the interface between AA7050 and SS316, there is a significant increase (200%) in the difference between the currents. Conversely, far from the coupled interface, the current densities difference is ca. 10%. The variation in the percent difference can be understood by **Figure 3.9**a, in which the current density at the electrode surface follows a step function, with the current densities immediately changing from anodic to cathodic. In contrast, the current density at 100 μm above the surface is a continuous function.

Looking instead at the distance from the electrode surface in the z-direction, the current density magnitude was seen to decrease linearly with a slope of -70 A/m^3 (**Figure 3.10**a). At the position of x = 1 mm above the AA7050 surface, the slope was decreased to -10 A/m^3. The comparison of the two slopes above indicates that lower current densities, as observed above the anodic region, decrease the degree of variation of current density with position from the electrode surface, due to ohmic drop. Indeed, the ratio between the slopes is the same as the ratio between the current densities at the surface of the electrode. Practically, this result indicates that in systems with low overall current densities, the height of the SVET

probe tip will not largely impact the results. However, in systems or locations with high current densities, the chosen height of the SVET probe tip can have a substantial effect on the measured results in comparison to the current densities occurring at the electrode surface.

This result is further demonstrated by the experimental data presented in Figure 10b, where the peak current was measured above a point current source with two applied current values over a range of SVET probe heights. The higher applied current ($i_{applied}$ = 25 μA) resulted in a faster decrease in SVET-derived current density as a function of probe height, i.e., a steeper slope, in comparison to the lower applied current ($i_{applied}$ = 5 μA). These results validate what was observed computationally in **Figure 3.10**a. Furthermore, Murer et al.[140] and Demeter et al.[162] also observed this inverse correlation between current density magnitude and probe height, both experimentally and computationally. Therefore, it is recommended that the SVET be conducted at several probe heights, although it does not completelyalleviate issues seen at the galvanic couple interface.

Visualization of the current density vectors in a planar view can improve the understanding of the variations observed between the current density at the electrode surface and at a specified distance within the electrolyte above the anode/cathode interface. **Figure 3.11**a shows the electrolyte current density lines and the magnitude of the electrolyte current density in the z-direction, represented by a color gradient from a "slice" of the geometry in the x-z plane at the center of the geometry, and **Figure 3.11**b shows the ratio between the z-component of the electrolyte current density and the magnitude of the electrolyte current density vector.

Note that the simulation used to determine the current density vectors in **Figure 3.11** was conducted in a geometry whose volume was equivalent to the volume of electrolyte used for the SVET experiments. Conventionally, computational works have kept the electrolyte *height* consistent with experimental conditions, but have not considered the effects of keeping the electrolyte *volume* the same.[138,140,145,153] This assumption does not affect the interface current densities, and it is computationally less expensive to mesh a smaller volumed domain. However, when considering current density in the electrolyte (i.e., above the electrode surface) or the concentration of ions, the volume of the electrolyte becomes more important. This distinguishing feature of the large-volume model can be seen by the current density vectors in **Figure 3.11**a, in that they continue past the edges of the galvanic couple.

As the SVET probe measures the potential difference between two points by oscillating in the z-direction, it is only able to "sense" the z-component of the electrolyte current density. As **Figure 3.11**a indicates, at regions further away from the boundary between the two electrodes (SS316 and AA7050) and from the edges of the AA7050 electrode, most of the magnitude of the current density vectors are composed by the z-component. However, near the boundary between the two electrodes and near the edges of the sample, the magnitude of the z-component of the electrolyte current density vector decreases significantly.

As the probe moves closer to the surface, the z-component of the current density vector increases, consistent with the negative slope observation in **Figure 3.10**. Interestingly, as **Figure 3.11**b shows, the z-component of the current density is small near the edge of the galvanic couple and at the edge of the sample, even at z = 0 μm, indicating an intrinsic limitation of the SVET technique in capturing the current densities at such locations by measuring the potential difference only in the z-direction.

Two important conclusions can be drawn from this analysis. First, increasing the spatial resolution of the SVET by decreasing the step-size in the x- and y-directions would not improve the underestimation of the current density at the electrode surface, as the current density measurement losses are purely based on the limitation of the distance between the probe and the electrode surface and the assumption that all current is in the z-direction. Second, even at locations very close to the surface, part of the current density would not be sensed, because of the direction of the current density vector near the galvanic couple and near the edges of the sample.

3.7. Limitations

3.7.1. Experimental Limitations

As mentioned previously, the choice of 1 mM NaCl used in this work was made based on the resolution limitations of the SVET. In real atmospheric environments, the NaCl concentration would be expected to equilibrate at ~ 600 mM at 98% relative humidity.[124] However, because the SVET signal-to-noise ratios decrease with increasing solution conductivity,[134] experiments conducted in 600 mM NaCl would be too noisy to allow extraction of any meaningful information. Therefore, with reasonable model validation with the SVET at low Cl^- concentrations, predictions could be made with the model for higher Cl^- concentrations scenarios.

Another limitation with the SVET is the frequent mismatch of the area-averaged integrated total anodic and cathodic currents, especially in non-steady state systems, which drift and exhibit transient reactions.[136,163,164] At any instant in time, the total anodic and cathodic currents in reality are equal in magnitude, so that the net current equals zero. A general rule of thumb for the SVET to be able to avoid this situation is that the measurement time be much less than the periodicity of transients or the time frame of drifts. The error depends on the magnitude and area of the current transient relative to the steady-state current and area. Regarding another issue, for the couple geometry utilized in this work, there was a slight overestimation of the total cathodic current, particularly for the pH 3 case, most likely due to edge effects. That is, the SVET misses the anodic activity in the vicinity of the edges of the AA7050 surface but captures the cathodic activity occurring over the entire SS316 surface located at the center of the structure.

3.7.2. Computational Limitations

One shortcoming of the model is readily apparent through its prediction of homogenous current density distributions in **Figures 3.3**c and **3.3**d, as opposed to the non-uniform distribution (with distance and time), which occurs experimentally (**Figure 3.3**a and **3.3**b). Additionally, because of the macroscale geometry in this work, the model cannot account for localized corrosion. Localized corrosion is an important form of corrosion that occurs on AA, especially when galvanically coupled with more noble alloys, such as SS, that can polarize the AA to potentials above critical potential thresholds for localized corrosion (e.g., pitting and repassivation potentials). It is acknowledged that in real service conditions, such localized hotspots as observed on the SVET-derived surface map for the pH 5.8 case may be important, as they could act as susceptible sites for fatigue crack nucleation.[165] Furthermore, the model is not able to capture the precipitation of any corrosion products, which may stifle the local anodic and cathodic reactions in some areas and cause a shift of those currents elsewhere. Notice that the white "halo" in the global current distributions is larger in the experimental maps than the computational model would predict (**Figures 3.3**b and **3.3**d). As the locations closest to the anode/cathode interface should have the highest currents, it follows that the precipitation of corrosion products would also be greatest in this area, leading to a corresponding decrease in current at longer times. As the present model cannot yet account for the corrosion product formation, the white "halo" is underpredicted. Recent work in the literature have utilized FEM to investigate the effects of corrosion products on micro- and macro-galvanic corrosion.[150,166–168] Understanding the complex precipitation reactions and how they may contribute in stifling localized corrosion, is an area of future work. In addition, sites with copper replating could switch their behavior from anodic to cathodic, which was not accounted for in the present model.

3.8. Conclusions

The scanning vibrating electrode technique (SVET) was utilized to experimentally validate the applicability of finite element modeling (FEM) in simulating macro-galvanic-induced corrosion of AA7050 coupled to SS316. The SVET and FEM both provided local current density distributions, which were then compared. The discrepancy between the two techniques was traced to several sources. However, once the correct boundary conditions were used to validate the model, both techniques were able to enhance each other, thereby providing valuable information otherwise unachievable. In summary, the following findings are highlighted:

- Methods are proposed to generate anodic and cathodic boundary conditions to represent a macro-scaled galvanic couple between AA7050 and SS316, with localized corrosion present. One method of including the accelerated kinetics present during localized corrosion while still assuming a homogenous surface condition was based on performing the anodic scans starting at a high potential

and decreasing it to OCP, in order to capture the behavior of a surface without the natural oxide present. Furthermore, the addition of Al^{3+} in the cathodic polarization scans led to better agreement between the total currents calculated with the model and measured with SVET.

- Although the computational model was not able to capture the localized corrosion events (as seen especially in the less aggressive pH 5.8 scenario), the *total anodic currents* in the overall macro-scale geometry, through using boundary conditions generated with the methods above, were found to have less than 13% error when compared with the global SVET currents, in both pH environments.
- The AA7050-SS316 galvanic couple in near-neutral solutions reached steady-state within 24 h, making computational validation through SVET less complicated. Better agreements regarding macro-galvanic couple behavior were achieved in pH 5.8 environment compared to pH 3 environment. However, the FEM method was not able to address corrosion at specific locations on the AA7050 in the pH 5.8 scenario where corrosion was localized.
- Electrolyte current densities measured by vibrating probe methods at a distance of 100 μm from the electrode surface can be significantly different from the actual current density at the electrode surface, and the difference depends on the position above the galvanic coupled surface. It was predicted that there was a 10% difference at locations far away from the galvanic couple interface. At the vicinity between the two electrodes, the difference was as high as 200%, corresponding to ca. 5 $\mu A/cm^2$.
- The linear dependence of current density on the SVET probe height from the electrode surface was found to scale directly with the current density magnitude. This result indicated that the underestimation of the SVET-derived data from the current density at the electrode surface is dependent on both the z-position and the spatial location on the galvanic couple and current density magnitude. That is, in systems or positions with high current densities or galvanic coupling currents, choosing the SVET probe tip height from the electrode surface can have a more significant impact on the results as opposed to lower current density systems, due to ohmic drop and the inability of the probe oscillation to capture components of the current that are parallel to the surface.

3.9. Acknowledgements

This work was supported by the Office of Naval Research (ONR) Grant N00014-14-1-0012 (W. Nickerson/A. Rahman), and via contract N00173-19-1-G011 (C. Sanders), as well as by the Department of Defense (DoD) Corrosion Program Office through the USA Air Force Academy via contract FA7000-18-2-0006. In addition, support was also provided by the NASA Virginia Space Grant Consortium through a Graduate Research Fellowship.

3.10. List of Tables

Table 3.1. Parameters used in the FEM.

Parameter	Description	Value
$\mathbf{i_{0,5.8}}$	Pseudo-exchange current density for ORR kinetics in pH 5.8	4 x 10^{-11} (A/cm^2)
$\boldsymbol{b_{c,5.8}}$	Fitted cathodic Tafel slope in pH 5.8	-0.193 (V) 95%CI (-0.194, -0.191)
$\mathbf{E_{eq,5.8}}$	Equilibrium potential of the cathode in pH 5.8	0.573 (V)
$\mathbf{i_{lim,5.8}}$	Diffusion limited current density in pH 5.8	1.2 x 10^{-5} (A/cm^2)
$\boldsymbol{\kappa_{5.8}}$	Conductivity in 0.001M NaCl, pH 5.8	0.0188 (S/m)
$\mathbf{i_{0,3}}$	Pseudo-exchange current density for ORR kinetics in pH 3	5 x 10^{-13} (A/cm^2)
$\boldsymbol{b_{c,3}}$	Fitted cathodic Tafel slope in pH 3	-0.181 (V) 95%CI (-0.182, -0.180)
$\mathbf{E_{eq,3}}$	Equilibrium potential of the cathode in pH 3	0.809 (V)
$\mathbf{i_{lim,3}}$	Diffusion limited current density in pH 3	3 x 10^{-5} (A/cm^2)
$\boldsymbol{\kappa_3}$	Conductivity in 0.001M NaCl, pH 3	0.0767 (S/m)

Table 3.2. Ohmic resistance values used for iR correction of anodic polarization curves.

Description of Technique	Description of Solution	$\mathbf{R_{ohmic}}$ ($\mathbf{\Omega \cdot cm^2}$)
EIS	1 mM NaCl, pH 5.8	5750
Manual correction	1 mM NaCl, pH 5.8, OCP to high E positive scan	7221
Manual correction	1 mM NaCl, pH 5.8, high E to OCP negative scan	5246
EIS	1 mM NaCl, pH 3	3541
Manual correction	1 mM NaCl, pH 3, OCP to high E positive scan	3368
Manual correction	1 mM NaCl, pH 3, high E to OCP negative scan	2467

3.11. List of Figures

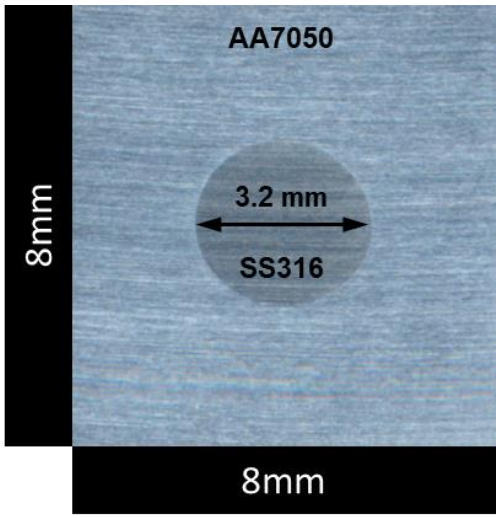

(a)

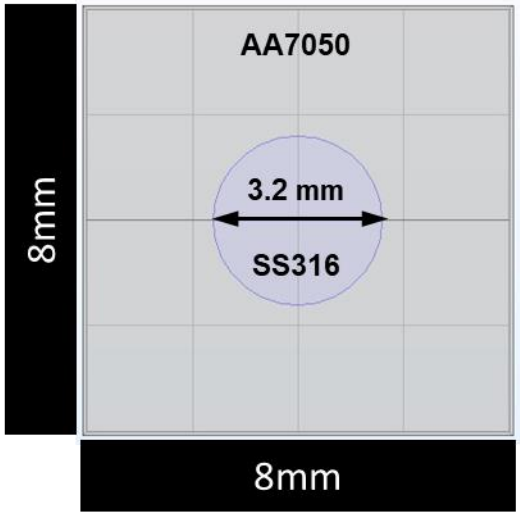

(b)

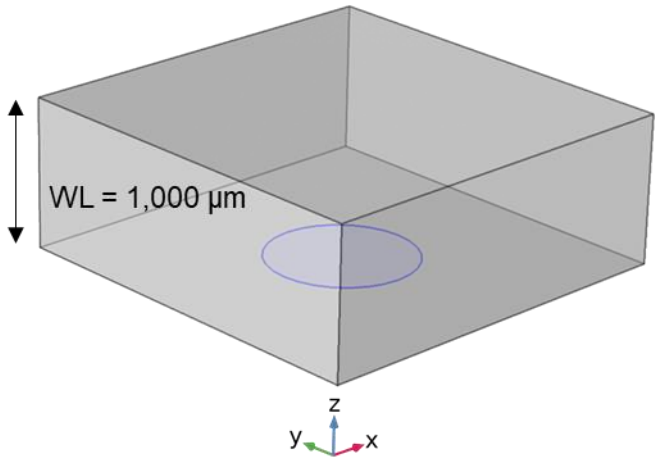

(c)

Figure 3.1. Geometry of the AA7050-SS316 couple used for (a) SVET experiments and (b) FEM; (c) xy, yz, and xz boundaries representing the air/solution interface in (b) with z = water layer thickness of 1000 µm.

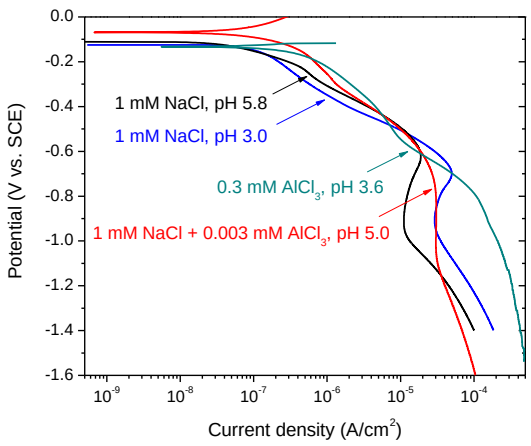

(a)

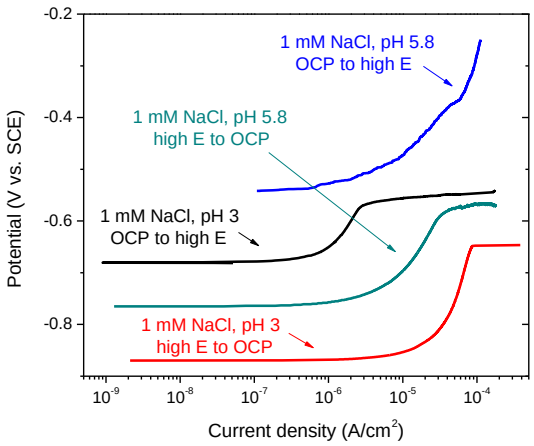

(b)

Figure 3.2. Potentiodynamic polarization scans used as input boundary conditions for the model; (a) cathodic scans on SS316, and (b) anodic scans on AA7050, corrected for ohmic drop.

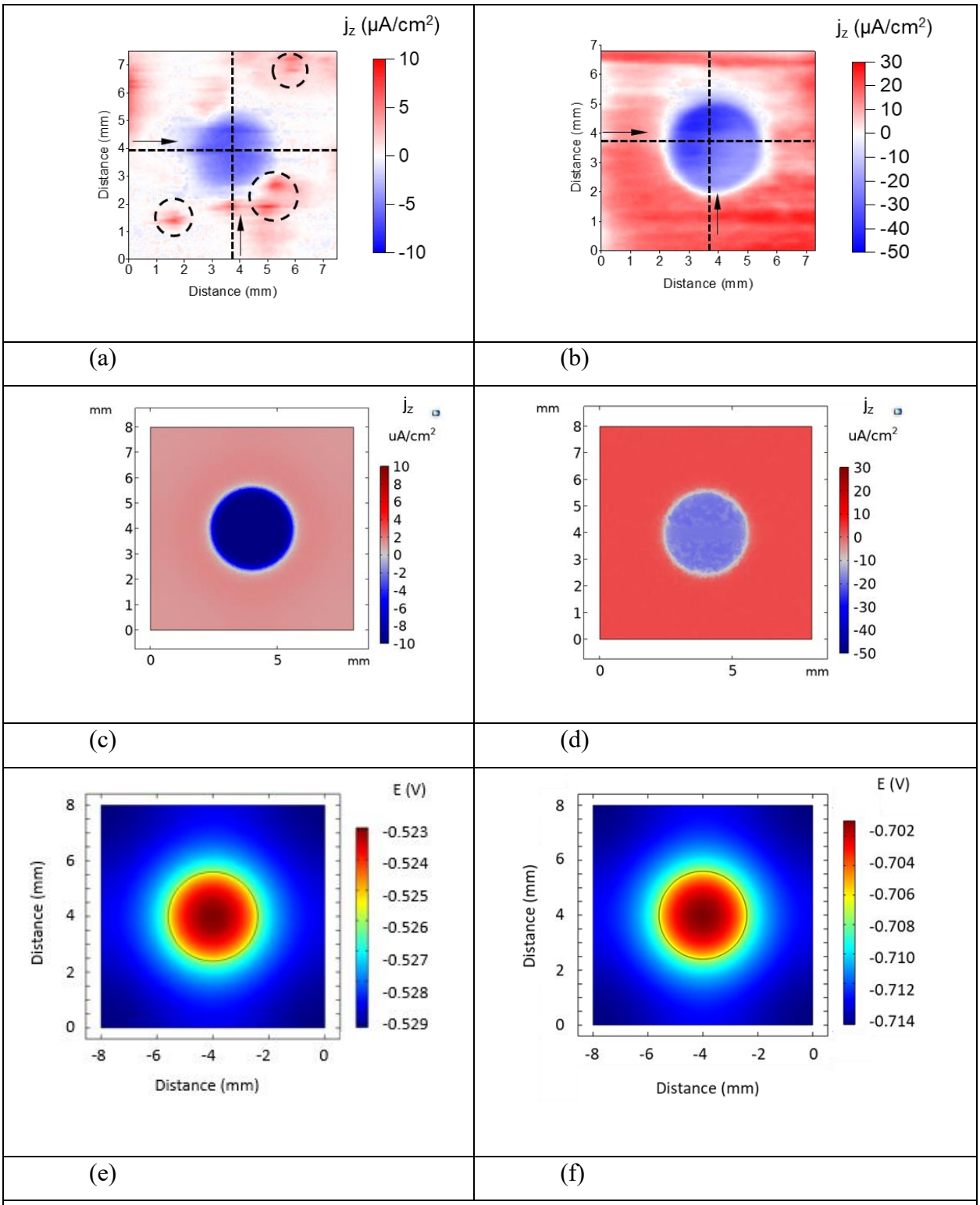

Figure 3.3. SVET-derived 24 h surface maps (a) and (b), corresponding FEM results (c) and (d) showing current density distributions above a freely-corroding AA7050-SS316 couple immersed in 1 mM NaCl at pH 5.8 and pH 3, respectively. Note that the color bar in each pH

scenario is consistent. Current density distributions were taken at a distance of 100 µm above the electrode surface, in each case. Dashed lines in (a) and (b) show the location of vertical and horizontal line profiles taken. Dashed circles in (a) show some regions with localized corrosion activity. Potential distributions (e) and (f) corresponding to FEM current density maps (c) and (d), respectively.

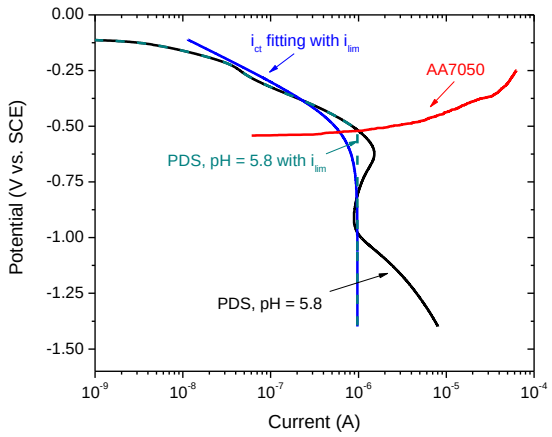

(a)

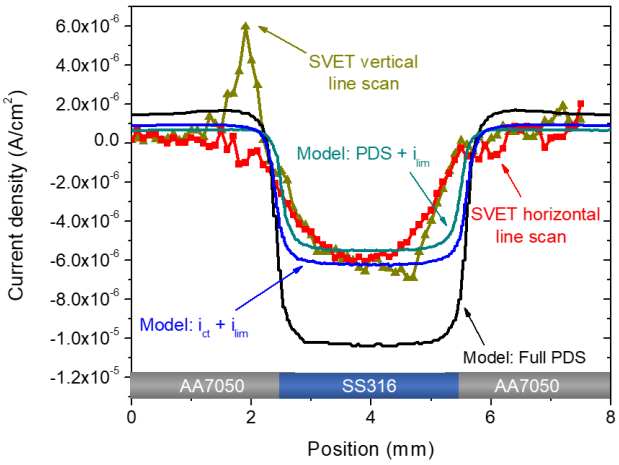

(b)

Figure 3.4. (a) Anodic and cathodic boundary conditions used within the model, scaled to correct for cathode:anode area differences; (b) comparison of the SVET current density line profiles with three computational models for pH 5.8 conditions. The current density line profiles were taken at a distance of 100 µm above the electrode surface, in each case. The notation "full PDS" in (b) indicates the black and red curves in (a) were used as boundary conditions. Correspondingly, "PDS + i_{lim}" in (b) indicates the dashed teal and red curves in (a) were used. Lastly, "i_{ct} + i_{lim}" in (b) indicates the blue and red curves in (a) were used as boundary conditions.

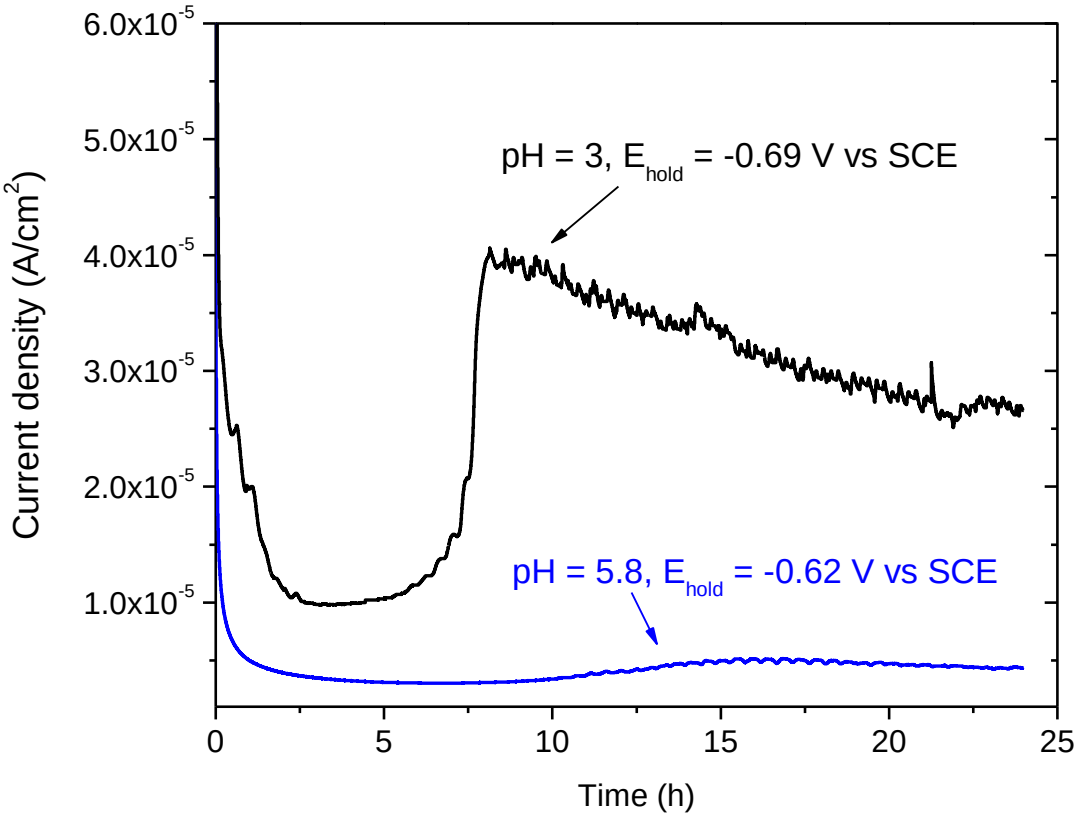

Figure 3.5. 24-h potentiostatic tests on SS316 in 1 mM NaCl at pH 5.8 and pH 3. Potentials were held at the values corresponding to the peak current waves observed on the respective cathodic polarization curves displayed in Figure 2a.

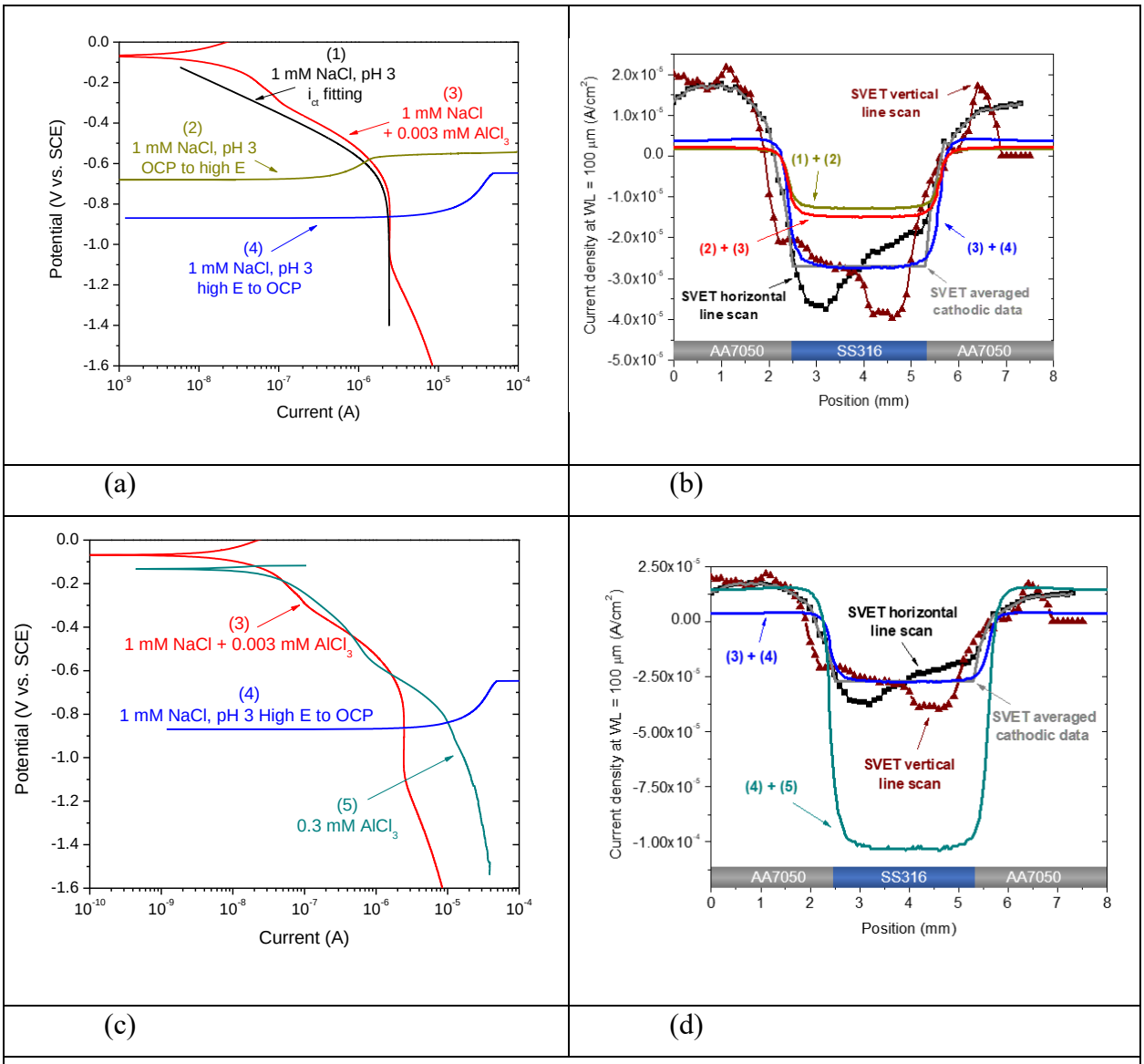

Figure 3.6. (a) and (c) Anodic and cathodic boundary conditions used within the model, scaled to correct for cathode:anode area differences, and (b) and (d) comparison of the SVET current density line profiles with 4 computational models, for pH 3 conditions. The current density line profiles were taken at a distance of 100 µm above the electrode surface, in each case. Numerical values in (b) and (d) represent the solutions in (a) and (c), with (1) = cathodic analytically-fitted charge transfer-controlled PDS on SS316 in 1 mM NaCl at pH 3, (2) = anodic PDS on AA7050 in 1 mM NaCl at pH 3 scanned in the positive direction from the OCP to high E, (3) = cathodic PDS on SS316 in 1 mM NaCl + 0.003 mM $AlCl_3$, (4) = anodic PDS on AA7050 in 1 mM NaCl at pH 3 scanned in the negative direction from high E to the OCP, (5) = cathodic PDS on SS316 in 0.3 mM $AlCl_3$.

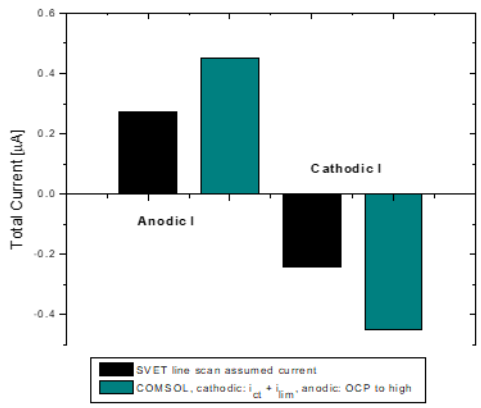

(a)

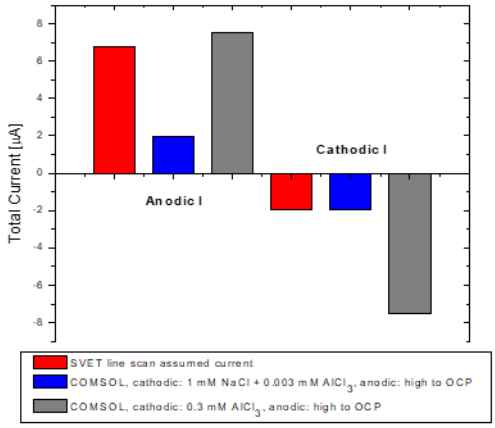

(b)

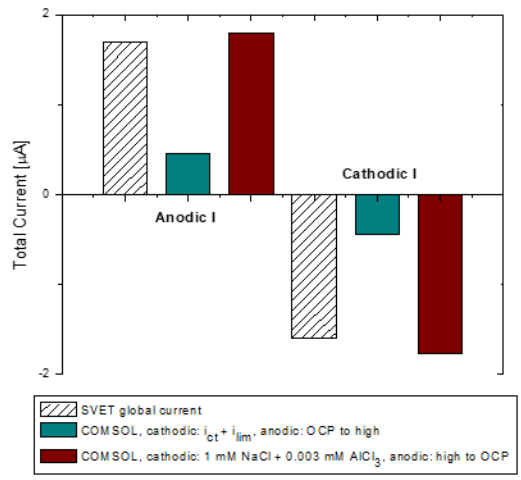

(c)

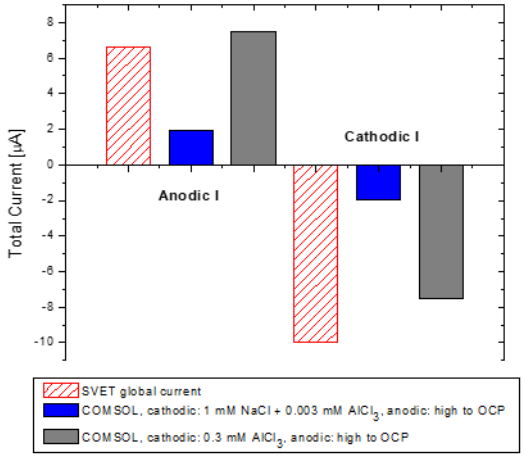

(d)

Figure 3.7. Computational and SVET-derived total currents assumed only from the line profiles under (a) pH 5.8 and (b) pH 3 conditions; area-averaged integrated total currents calculated over the entire AA7050-SS316 couple surface under (c) pH 5.8 and (d) pH 3 conditions. Both the computational and SVET-derived total currents in each pH case, were calculated from the current density distributions taken at a distance of 100 μm above the electrode surface.

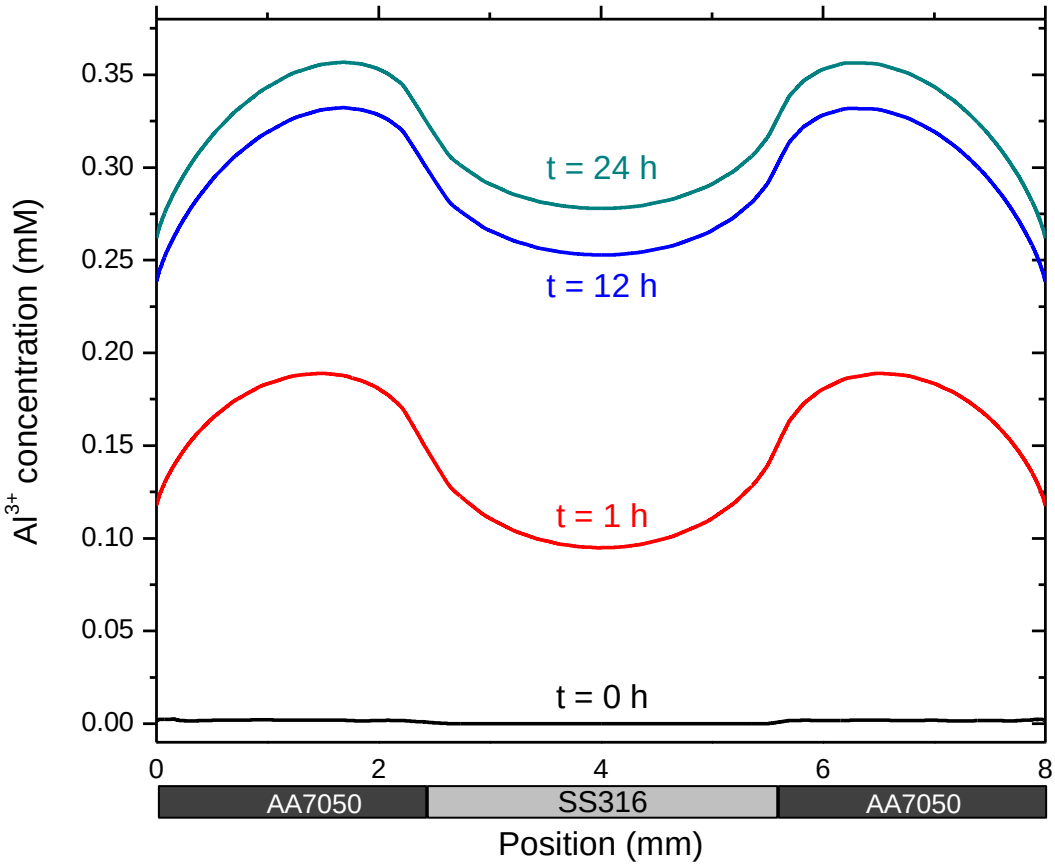

Figure 3.8. Simulated spatial distribution of the Al^{3+} concentration at different times at the centerline of the geometry.

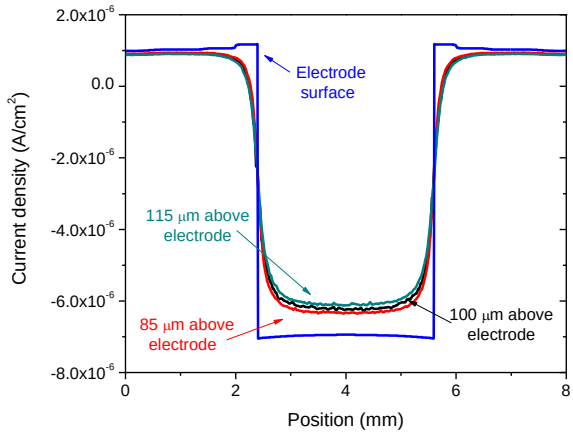

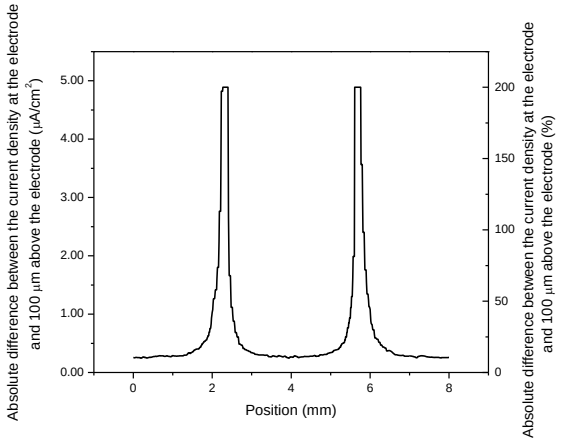

(a) (b)

Figure 3.9. (a) Computationally-derived current densities along horizontal line scan at various distances from the electrode surface; (b) absolute and percent difference between current density at the electrode surface vs. at 100 μm above the electrode surface, as a function of the x-axis position.

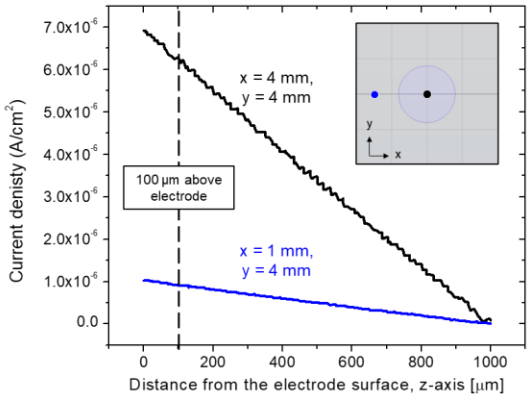

(a)

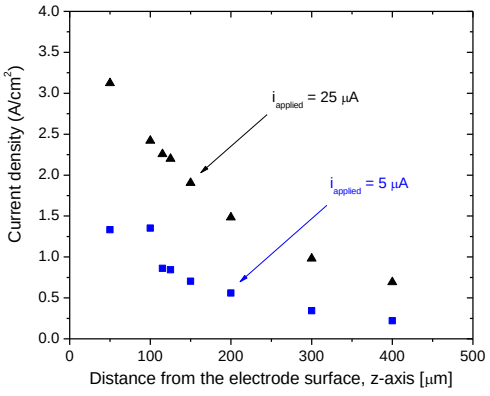

(b)

Figure 3.10 (a) Computationally-derived linear relationship of current density with distance from the electrode surface to the top of the electrolyte, along the z-axis; (b) SVET-derived point source data, with measured current density as a function of SVET probe height, with two applied current values. Inset in (a) represents the x-y view of sample surface, and the points chosen to measure current density along the z-axis.

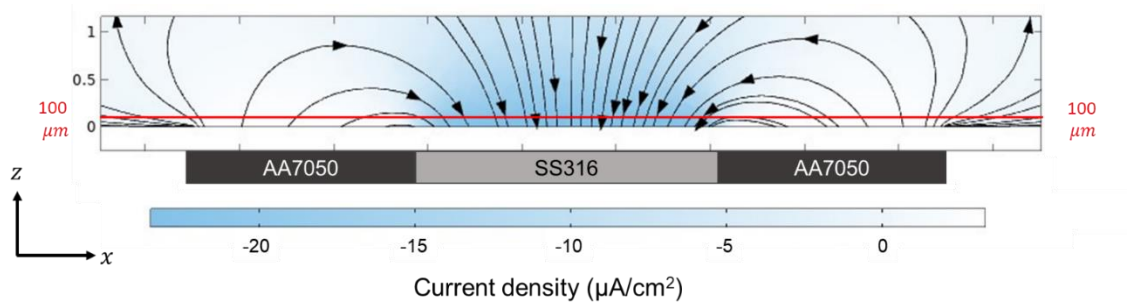

(a)

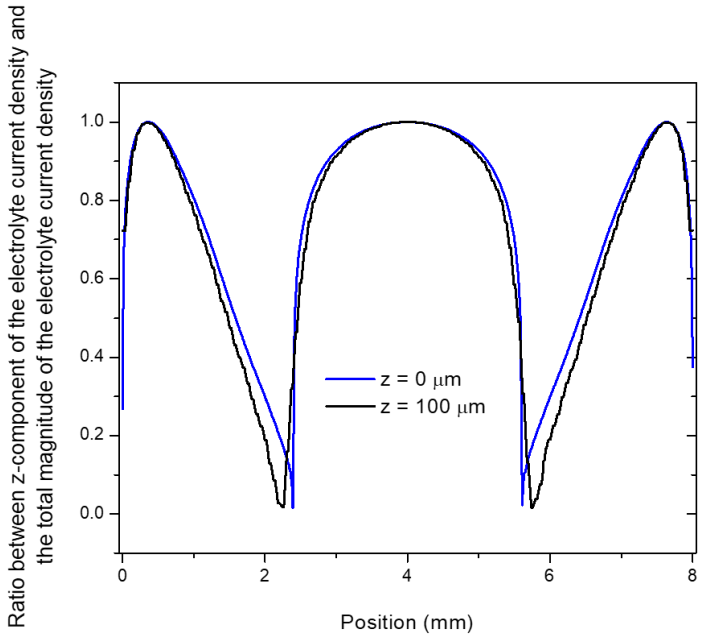

(b)

Figure 3.11. (a) Electrolyte current density lines and the magnitude of the electrolyte current density in the z-direction represented by a color gradient at the x-z plane at the center of the geometry. The red line indicates the distance between the SVET probe and the electrode used in this work; (b) ratio between the z-component of the current density and the magnitude of the current density vector at different electrolyte heights (0 and 100 μm).

Chapter 4. Finite element modeling of chemical and electrochemical protection mechanisms offered by Mg-based organic coatings to AA2024-T351

C.V. Moraes [a], R.J. Santucci Jr. [b], J.R. Scully [a], and R.G. Kelly [a]

[a] Center for Electrochemical Science and Engineering, Department of Materials Science and Engineering, University of Virginia, Charlottesville, VA

[b] United States Naval Academy, Annapolis, MD

Corresponding author: rgk6y@virginia.edu

The majority of this work has been published (DOI 10.1149/1945-7111/abfab8). Unpublished data and analysis are added to the chapter. **Figure 4.11** and **Figure 4.15** show the unpublished data.

4.1. Abstract

A finite element model of the protection mechanisms offered by Mg-based organic coatings was developed. The model predicted the change in the corrosion potential of AA2024-T351 as a function of pH, water layer thickness, and the inhibition of oxygen reduction reaction. The pH in the solution was calculated taking into account Mg dissolution, precipitation of $Mg(OH)_2$, Al dissolution, and hydrolysis of Al^{3+} ions. The predicted critical pH value at which the corrosion potential of AA2024-T351 sharply decreases to values below pitting and pit repassivation potentials under full immersion conditions was in accordance with experimental observations. A limiting water layer thickness below which the pH-induced pit repassivation mechanism is not predicted to occur was calculated. Cathodic protection offered by Mg-rich primers was modeled as a function of coating resistance, water layer thickness, and electrolyte chemistry. The magnitude of the resistance of the film in which Mg pigments are embedded mitigates the extent of the cathodic protection. The change in local pH due to corrosion reactions affects the galvanic potentials obtained. The framework developed can be used to help identify chemical inhibitors that can operate by the chemical protection mode described in this work.

4.2. Introduction

High-strength Al alloys such as AA2024-T351 require corrosion protection systems when used in aircraft structures due to their susceptibility to localized corrosion. The corrosion protection systems typically involve surface treatments, primers with inhibiting pigments, and topcoats. These corrosion protection systems can protect the substrate via different protection mechanisms, such as barrier protection, chemical inhibition, and cathodic protection [21]. Barrier protection is commonly provided by organic coatings, which impede aggressive species from reaching the substrate and provide high resistance to ionic movement, mitigating the charge transfer between anodic and cathodic sites. Chemical inhibition is

provided by pigments that inhibit electrochemical reactions occurring at the substrate, lowering the corrosion rate of the metal. Cathodic protection is provided by the incorporation of metallic pigments that are electrochemically more active than the substrate. The less noble metal polarizes the substrate to potentials where its corrosion rate is significantly reduced and/or to potentials below some critical threshold. Maintaining the coupled potential below pitting and repassivation potentials or the corrosion potential of secondary phases can prevent pitting damage and/or other localized corrosion phenomena, such as intergranular corrosion and intergranular stress corrosion cracking [25,169,170]. In corrosion protection systems commonly used, surface treatments promote adhesion between the metal and the organic layer and can also offer corrosion protection by containing inhibitors that dissolve into local coating defects [171]. Primers with inhibiting pigments grant active corrosion protection either by releasing pigments that inhibit corrosion or by serving as sacrificial anodes, thus providing cathodic protection. In addition, primers can provide additional adhesion to the topcoat [172]. The topcoat is composed of a polymer that provides barrier against corrosive species and protects the coating from UV exposure.

Historically, aerospace Al alloys have been protected by chromate-based coating systems. Cr(VI) compounds form an insoluble, protective film composed of chromium oxide (Cr_2O_3 or $Cr(OH)_3$) that adheres well to aluminum [171,173]. However, Cr(VI) has carcinogenic effects; thus, environmental regulations are restricting its use [19], stimulating the research in alternative corrosion protection technologies. In this context, Nanna and Bierwagen [174] developed Mg-rich primers (MgRP) to protect aerospace Al alloys. Its function is analogous to the sacrificial cathodic protection provided by zinc-rich primer to steels. The Mg metallic pigments, being more anodic than Al, serve as sacrificial anodes, providing cathodic protection and polarizing Al to potentials below its pitting and repassivation potentials. Since their conception, many studies have investigated the performance of MgRP [20,23,25,27,175–185]. In earlier studies, two mechanisms of protection were observed – the cathodic polarization of Al alloy substrates provided by the Mg sacrificial anodes and the barrier protection provided by the precipitation of magnesium compounds. The ability of Mg to polarize Al to more negative potentials, below pitting and repassivation potentials, prevents pit nucleation and growth of existing pits [20,180,183]. Additionally, magnesium compounds, such as $Mg(OH)_2$ and $MgCO_3$, can precipitate on the surface of the substrate, forming a protective film that can provide barrier protection [20]. $Mg(OH)_2$ precipitates at cathodic sites, where the pH is alkaline. Depending on the partial pressure of CO_2, $Mg(OH)_2$ can be converted to $MgCO_3$, which forms a uniform and compact layer [182,186]. Recent development of stability diagrams has allowed rationalization of the observation of magnesium carbonate compounds in field exposure [187,188].

Recently, an additional chemical protection mechanism offered by Mg-rich primers has been proposed [24]. Field and laboratory exposures comparing two Mg-based primers, MgRP and MgO-rich primers (MgORP), showed comparable protection efficiency [25,179]. A decrease in the open circuit

potential (OCP) of an AA2024 coated with MgORP was observed, even though MgO does not galvanically couple with the AA2024 substrate as Mg^{2+} is already in its highest oxidized state [25,178]. Because MgORP does not provide galvanic protection, another protection mechanism was rationalized, in which products of Mg-based dissolution, in addition to its precipitation compounds, play a role. Santucci and Scully [24] investigated the mechanism of OCP decrease by analyzing the effect of the solution chemistry on the kinetics of the electrochemical reactions occurring at AA2024, and a pH-induced electrode potential control mechanism was postulated. As the dissolution of MgO produces $Mg^{2+}$and OH^-, the solution pH increases. The higher alkalinity causes an increase in the passive current density of Al due to the easier dissolution of Al_2O_3 at higher pH [39,189]. According to mixed potential theory, the cathodic current density increases to match the higher anodic (passive) current density. The main cathodic reaction occurring at AA2024 at pH 7 is the oxygen reduction reaction (ORR), which has a mixed diffusion control and charge transfer control. At a sufficiently high pH, the passive current density surpasses the diffusion-limited ORR current density, and hydrogen evolution reaction (HER) becomes the primary cathodic reaction occurring at AA2024, shifting the corrosion potential to more negative values. The pH at which this corrosion potential decrease occurs was termed critical pH (pH_{crit}). The feasibility of the pH-induced potential control mechanism was tested experimentally by measuring the open circuit potential of AA2024 as a function of pH in a full immersion cell in 0.9 M NaCl. A sharp OCP drop from -0.6 V vs. SCE to -1.1 V vs. SCE was observed at a pH value of 9.86. This newly established OCP lies below the pitting and repassivation potentials of the alloy in this altered solution chemistry (ca. -0.7 V vs. SCE and -0.9 V vs. SCE, respectively) [24]. This decrease in potential effectively stifles any localized corrosion that occurs and is termed “pit repassivation” in this study. In addition to the OCP depression, the pH rise and the presence of aqueous Mg^{2+} in the solution lead to the precipitation of $Mg(OH)_2$ on the cathodic sites [179]. The beneficial effect of the $Mg(OH)_2$ is two-fold: it can prevent pH from rising to values in which caustic dissolution/attack is too severe, and the precipitated film can increase the pitting potential and decrease the passive current density as well as the cathodic kinetics of the reactions occurring at AA2024, reducing its corrosion rate [24].

The same mechanism can occur in a MgRP-coated AA2024 system, as the electrochemical dissolution of Mg provides the same products as the chemical dissolution of MgO. Consequently, MgRP may still offer protection even when the pigments are not able to provide cathodic protection, i.e., after the Mg pigments are oxidized and/or when there is a high ohmic resistance between the pigments and the substrate. After the pigments are depleted, precipitated $Mg(OH)_2$ can lower cathodic kinetics and maintain the local pH sufficiently high (above pH_{crit}) [24]. For the cases in which galvanic coupling between the pigments and substrate is not established, release of Mg^{2+} and OH^- from self-corroding Mg pigments could potentially provide the chemical protection mechanism described.

Most aerospace structures are exposed to atmospheric conditions in which a thin electrolyte layer forms. The diffusion-limited ORR current density is higher for thinner electrolyte films due to the faster transport of O_2 from the liquid/air interface to the surface of the metal [62]. Thus, the chemical protection mechanism described herein is affected by atmospheric conditions, and it is expected that a higher pH would be necessary to induce the OCP suppression of AA2024 than that needed in quiescent bulk solution. Understanding how corrosion protection modes are influenced by the details of atmospheric exposures is important to the design of effective corrosion protection systems. Hence, the goal of the present work is to develop a model that describes the different protection mechanism provided by Mg-based rich primers with the objective of understanding how variables such as water layer thickness, chemical reactions occurring in the electrolyte, solubility product of the inhibitor, and coating properties influence these protection mechanisms.

In this work, finite element modeling was utilized to model three modes of corrosion protection: pH-induced electrode potential control, cathodic protection by Mg as a sacrificial anode, and barrier protection provided by a simple resistive layer. The corrosion potential of AA2024 was calculated considering the dependence of the kinetics of the electrochemical reactions on the solution chemistry. The effectiveness of the chemical protection mechanism under atmospheric conditions was investigated. The electrochemical protection mechanism that MgRP can offer – cathodic protection via sacrificial anode dissolution - was also investigated. Finite element modeling has been performed to assess the galvanic throwing power of a MgRP protecting an AA2024 [74]. The effect of polymer resistance over Mg, electrolyte chemistry and thickness, and Mg depletion (based on anode-to-cathode ratio) on the galvanic throwing power was assessed. The magnitude and distribution of cathodic and anodic current densities predicted by the model were in accordance with measurements performed in microelectrode galvanic arrays on the coupled Mg and AA2024 electrodes reported in a separate study [23]. However, the previous model did not account for the evolving electrolyte chemistry due to the electrochemical reactions occurring at the electrode. Thus, in this work, the galvanic coupling between Mg and AA2024 was calculated considering the effect of pH on the electrochemical kinetics of AA2024. In a first approach, the potential distribution in steady-state condition was calculated in order to compare the results with previous work and validate the AA2024 boundary conditions used. Then, the effect of the evolving electrolyte chemistry – mainly pH change – on the galvanic potential obtained was investigated. Ultimately, this model was built to provide a better understanding of the different protection mechanisms provided by Mg-based rich primers and serve as a framework for the study of new coating systems.

4.3. Model description

The model simulated a scribed AA2024 panel coated with a Mg-based rich primer exposed to 0.9 M NaCl solution (initial pH=7). The concentration of 0.9 M NaCl solution was chosen based on the standard used for laboratory accelerated lifecycle test, ASTM B117 [190]. Calculations were made for an open system considering an oxygen partial pressure of 0.21 atm. A two-dimensional geometry was used, similar to that previously utilized by King *et al.* [74]. **Figure 4.1** shows a schematic drawing of the 2D geometry and the four cases studied in the model. In Case I, depicted in **Figure 4.1**a, the change in electrolyte composition was only a result of the dissolution of Mg particles from the MgRP – that is, species released from cathodic and anodic reactions occurring at AA2024 were not taken into account. pH-dependent electrochemical boundary conditions were defined on AA2024 [24], and the corrosion potential of AA2024 was calculated in the evolving electrolyte chemistry. In Case II, schematized in **Figure 4.1**b, the corrosion products of Al and their subsequent homogeneous reactions (mononuclear Al^{3+} species hydrolysis) were included in addition to the Mg-based dissolution from the primer. The hydrolysis reactions considered in the model are shown in Appendix A. The production rate of the ionic species was calculated by Faraday's law (treating pure Al as a proxy for AA2024), using the local current densities from the partial reactions occurring on the AA2024 electrode. Thus, in this case, the electrolyte chemistry changes with both Mg and Al dissolution. Cases I and II, therefore, simulate the chemical protection mechanism that is offered by MgRP, when the Mg particles are electrically isolated from AA2024, and they are dissolving via self-corrosion. Such isolation is known to occur when certain pretreatments are used which produce highly electrically resistive layers [23]. Cases I and II can also be applied to simulate the protection provided MgORP, as its chemical dissolution provides the same products as Mg electrochemical dissolution and in the same ratio (*i.e.*, 1:2 ratio of Mg^{2+} and OH^-).

Cases III and IV simulated the cathodic protection provided by a MgRP, thus the galvanic coupling between AA2024 and Mg in the primer was considered. In Case III (**Figure 4.1**c), the electrolyte chemistry was assumed constant, and the steady-state potential and current distributions between AA2024 and Mg were calculated. The results extend previous work [74] and demonstrate that when the Mg particles are in electrical contact with AA2024, the surrounding AA2024 is rapidly polarized to more negative potentials even in thin water layers. However, depending on the polymer resistance in which the Mg particles are embedded, or the resistance of the topcoat covering the primer layer, or of the surface pretreatment, the Mg pigments may not be able to polarize AA2024 to potentials negative enough to prevent pitting events. In the last case (Case IV, **Figure 4.1**d), the effect of the evolving electrolyte chemistry was included in the galvanic coupling model. The effect of the electrolyte chemistry on the electrochemical kinetics of AA2024 and, therefore, on the galvanic couple established between AA2024 and Mg was considered. The potential

profiles were compared to the repassivation potentials (E_{RP}) of AA2024 measured in alkaline solutions of similar chemistry [24].

Even though AA2024 has a complex, heterogeneous microstructure, in which intermetallic particles have their distinct electrochemical characteristics, the model simulated the macroscopic behavior of AA2024 in different solutions. Indeed, the electrochemical kinetics were described using potentiodynamic polarization measurements that were performed on a macroscopic scale (electrode surface = 0.785 cm^2). Thus, the kinetics used in the model represent an averaged kinetics of the microconstituents and of the matrix weighted by the reactivity and area fractions. The reader is referred to other work where individual phases were tested in $Mg(OH)_2$ [24].

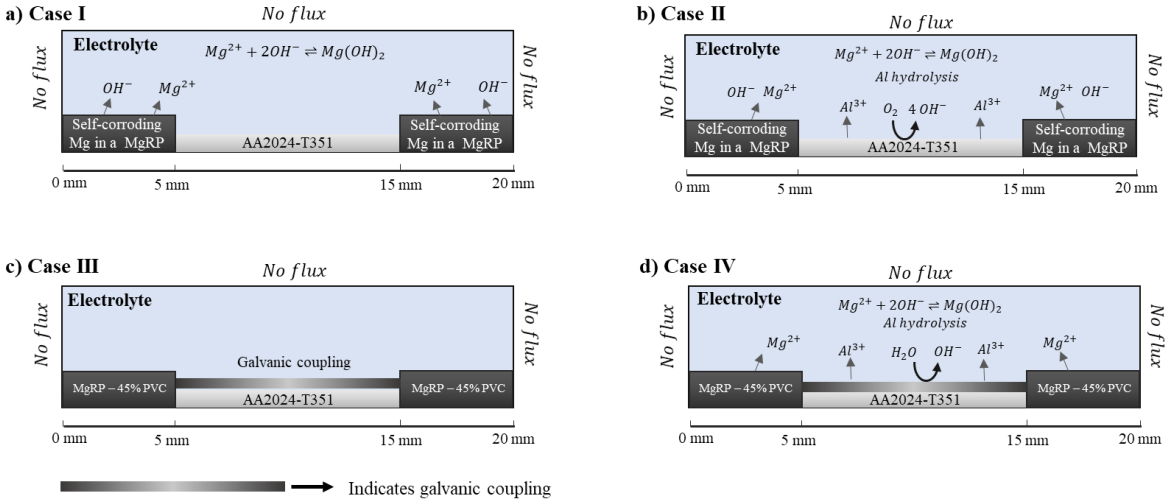

Figure 4.1. Schematic drawing of the 2D geometry used in the model, where a coated substrate with a scribe is represented. The four different cases studied are illustrated: a) Case I: the change in electrolyte composition was only a result of the Mg-based dissolution; b) Case II: the AA2024 corrosion products and their subsequent homogeneous reactions (mononuclear Al3+ species hydrolysis) were included in addition to the Mg-based dissolution; c) Case III: simulation of galvanic protection in which the electrolyte chemistry was assumed constant, and the semi-steady-state potential and current distributions between AA2024 and Mg were calculated, and d) Case IV: electrolyte chemistry evolution included in the galvanic coupling model. Note that the drawing is not to scale.

4.3.1. Approach to calculation and governing equations

The Laplace equation was used as the governing equation to solve for the potential distribution under the assumptions of electroneutrality and near-constant electrolyte composition (Equation 1).

$$\nabla^2 \varphi = 0 \qquad [1]$$

where φ is the electrolyte potential.

Due to the high conductivity of the 0.9 M NaCl solution (ca. 8 S/m), the compositional changes of the electrolyte as a result of Mg dissolution and hydrolysis were assumed to negligibly affect the conductivity of the solution (σ_l). Thus, σ_l was assumed constant. If it is also assumed that diffusion adds a negligible contribution to the current, then the Laplace equation can be used. Species transport was decoupled from the current distribution model: Ohm's law (Equation 2) was used to solve for the electrolyte current density, and the Laplace equation was used to solve for potential distribution. The ionic transport of minor species was solved independently. This approach was used to overcome some of the difficulties associated with solving the Nernst-Planck equations with electroneutrality: the larger computational power needed and the discrepancies in modeling results found depending on the choice of the make-up ion used to solve the electroneutrality equation [55,56].

$$i = -\sigma_l \nabla \varphi \qquad [2]$$

Charge conservation in the domain demands that the sum of the currents in the electrodes equals zero. Thus, mixed potential theory is implicit in the calculation of the corrosion potential of AA2024 for Cases I and II. For Cases I, II, and IV, the local solution composition was calculated at each time step based upon the products of cathodic and anodic reactions and the hydrolysis of the metal ions. The diffusion coefficients for the various species are shown in **Table 4.2** in Appendix A.

4.3.2. Electrochemical and chemical reactions

The release rate of Mg^{2+} from the MgRP for Cases I and II was based on the work of Lin *et al.* [191], in which the progression of Mg oxidation was measured via H_2 collection in 0.18 M NaCl [1]. From the rate of H_2 production arising from the cathodic reaction (i.e., water reduction), the rate of OH^- and Mg^{2+} production was calculated accordingly. Importantly, this H_2 collection technique monitors all of the charge associated with the paired Mg oxidation/H_2 evolution whether the cathodic reaction occurs locally on the Mg pigment or remotely on a cathodically polarized AA2024 substrate. Either mode of H_2/OH^- production will be efficacious to the protection mechanism explored herein. In the electrolyte, $Mg(OH)_2$ precipitation was considered:

$$Mg^{2+} + 2OH^- \rightleftharpoons Mg(OH)_2 \qquad [I]$$

The rate of $Mg(OH)_2$ precipitation was defined using a step function to ensure the reaction would only occur after the saturation was reached, as shown in Equation 3 [192,193]:

$$r_{Mg(OH)_2} = k(c_{Mg^{2+}} c_{OH^-}^2 - K_{SP}) \cdot H(x) \qquad [3]$$

[1] The hydrogen collection experiment was conducted on a 70 μm-thick MgRP of PVC = 40% coated on an AA2024. The exposed area of the coated sample was 9 cm^2.

where k is the reaction rate constant, $K_{SP}$is the apparent solubility product constant for $Mg(OH)_2$, and $H(x)$ is a Heaviside function:

$$H(x) = \begin{cases} 0, x \leq 0 \\ 1, x > 0 \end{cases} \quad [4]$$

where x defines the solubility limit as follows:

$$x = \frac{c_{Mg^{2+}} c_{OH^-}^2}{K_{SP}} - 1 \quad [5]$$

Note that the difference between the thermodynamic K_{sp} and the apparent K_{sp} is that the thermodynamic solubility product is defined assuming that the activity coefficient is equal to 1 at infinite dilution, whereas the apparent solubility product is defined assuming that the activity coefficient is equal to 1 at the ionic strength of the experimental medium [194].

The water dissociation reaction was also included in the model:

$$H_2O \rightleftharpoons H^+ + OH^- \quad [II]$$

For Cases II and IV, the production rate of Al^{3+} and OH^- were calculated according to Faraday's law. The hydrolysis reactions of Al^{3+} species included in the model are shown in Appendix A. The reaction rate constants of all the homogeneous reactions considered in this work are shown in **Table 4.3** in Appendix A.

4.3.3. Electrochemical boundary conditions

The boundary conditions at the electrode/electrolyte interface at the scribe (AA2024) were defined by distinct half-cell electrochemical reactions. Cathodic and anodic partial reactions were described analytically using experimental and theoretical parameters [24].

Many dissolution reactions do not follow standard kinetic expressions, or the values needed to fit the behavior are incompatible with mechanistic interpretation. For the purposes of this work, accurately capturing the phenomenology of the kinetics, i.e., the current-voltage relationships, is both necessary and sufficient to provide the boundary conditions for the model. The kinetics of hydrogen evolution reaction (HER) were defined using pseudo-Tafel expression (Equation 6):

$$i_i = i_{0,i} \cdot 10^{\frac{\eta_i}{A_i}} \quad [6]$$

where $i_{0,i}$ is the pseudo-exchange current density in reaction i, η_i is the overpotential in reaction i, A_i is the pseudo-Tafel slope of reaction i. The overpotential of the reaction is defined as:

$$\eta_i = E - E_{0,i} \quad [7]$$

where E is the local potential and $E_{0,i}$ is the pseudo-reversible potential. The kinetics of Al active dissolution and passive behavior, oxygen reduction reaction (ORR), and pitting were each fitted respectively to Equation 8:

$$i = \frac{i_i}{1 + \left|\frac{i_i}{i_{lim}}\right|} \quad [8]$$

where i_i is the Tafel expression shown in Equation 6 and i_{lim} is the limiting current density that describes the Al passive behavior and the diffusion-limited kinetics of ORR. A limiting current density was also used to fit the pitting kinetics to facilitate the convergence of the model. The parameters $E_{0,i}$ A_i, and $i_{0,i}$ were determined by fitting experimental data.

For cases III and IV, in which galvanic coupling between AA2024 and Mg particles in the MgRP is considered, Mg electrochemical kinetics were defined with a Tafel expression, where the parameters A, i_0, and E_0 parameters were derived from experimental data and acquired from previous work [74]. The exchange current density for the Mg dissolution was multiplied by a PVC of 45%, assuming that the fraction of the exposed area that is Mg is equal to its volume fraction. To model the polymer-coated Mg particles in the primer, a source of potential drop, interpreting a resistive film with 0 thickness, was added across the MgRP/electrolyte and MgRP/AA2024 boundaries. This source of potential drop was also considered at the MgRP/AA2024 boundary because the Mg particles at the edge of the scribe dissolve quickly, so, effectively, the remaining Mg particles are further from the cut edge and covered with the polymer. This approach was utilized in previous modeling work [74]. The calculation of the potential and current density distribution was performed in two different scenarios. In one case, the oxygen reduction reaction kinetics on AA2024 were constant with respect to the water layer thickness. In another case, the impact of the water layer thickness on the oxygen reduction reaction kinetics was taken into account utilizing the relationship obtained via RDE analysis and the Koutecky-Levich approach.

Note that in Cases I and II, the release rate of Mg^{2+} from a MgRP was used to model the rate of Mg^{2+} introduction into the thin water layer because there was no galvanic interaction considered. Hence, no net current flows between the MgRP and the substrate. In Case III, the electrochemical kinetics are used to inform the calculation of the current distribution because there is a net current, and hence ohmic drop. In Case IV, the Mg^{2+} production rate is calculated from the electrochemical kinetics using Faraday's law.

Table 4.4 in Appendix A summarizes the parameters used to define the boundary conditions at the electrode-electrolyte interface.

Anodic potentiodynamic scans and potentiostatic holds were conducted in AA2024 in deaerated 0.9 M NaCl solution in a pH range of 9.00 to 12.25 to define an expression for the passive current density as a function of pH. It was assumed that the same expressions were valid for pH values outside the range

tested – from 6 to 14. Different expressions were obtained depending on the method (*i.e.*, potentiodynamic vs. potentiostatic) and whether the solution was buffered. The unbuffered solutions were prepared with incremental additions of NaOH to adjust the pH. The buffered solutions were prepared with sodium borate or phosphate salts near 0.01 M concentrations. The experimental procedure is described elsewhere [24]. For the potentiostatically-determined expressions, the steady-state current (current measured over the last hour of a three-hour hold) was recorded as a function of pH. For the potentiodynamically-determined expressions, the average current density in the passive region, between -0.8 to -0.65 V vs. SCE, was recorded as a function of pH. Then, a linear fit of the log of the current density versus pH was performed. The resulting expressions are shown in **Table 4.1.**

The diffusion-limited current density of oxygen reduction was determined as a function of water layer (*WL*) thickness utilizing a rotating disk electrode (RDE) configuration at rotation speeds of 100, 200, 400, 800, 1600, and 3200 rotations per minute on AA2024-T351. A Koutecky-Levich framework assuming mixed activation and mass transport control was used to define the dependence of the limiting current density (i_d) on the diffusional boundary layer thickness (δ). The *WL* thickness was assumed to be equal to δ for *WL* thickness less than the natural convection boundary layer. The value of the natural convection boundary layer was calculated by fitting a linear function to data from rotating disk experiments [24] and following the procedure described by Liu *et al.* [62] – plotting the current density vs. $1/\delta$ and solving for the i_d obtained experimentally in quiescent, full immersion conditions.

COMSOL Multiphysics (ver. 5.5) was utilized to perform the finite element analysis calculations. At the top, left, and right boundaries of the water layer domain in **Figure 4.1**, Neumann boundary conditions were applied, where the normal flux of all species was set to zero ($\boldsymbol{n} \cdot N_i = 0$). The Transport of Dilute Species and the Secondary Current Distribution interfaces of the Electrochemistry Module were used.

Table 4.1. Passive current density as a function of pH determined by different methods in different solutions.

	Unbuffered solution	**Buffered solution**
Potentiodynamic	$\log i_{pass} = 0.979 * pH - 14.741$	$\log i_{pass} = 0.464 * pH - 8.526$
Potentiostatic	$\log i_{pass} = 1.111 * pH - 16.490$	$\log i_{pass} = 0.387 * pH - 8.042$

4.4. Results

The results are organized into eight sections. In the first section, results from sensitivity analyses performed on the parameters chosen for the electrochemical boundary conditions are presented to assess the importance of the current-pH behavior on the potential transient. Then, a comparison of the model

results with experimental data is demonstrated to validate the model. The results of the investigation on the effect of thickness of the *WL*, K_{sp}, Al corrosion products and the simulation of the electrochemical protection mode are subsequently presented.

4.4.1. Abstraction of electrochemical boundary conditions pH dependence and sensitivity analysis

The expressions defining the passive current density as a function of pH were abstracted from the potentiodynamic scans and potentiostatic holds performed in deaerated 0.9 M NaCl solution adjusted to pH 9, 10, 11.5, and 12.25 in buffered and unbuffered solutions [24]. **Table 4.1** shows the expressions obtained for the passive current density as a function of each method in unbuffered and buffered solutions.

The cathodic polarization curves generated using the RDE at six rotation speeds were analyzed using the Khoutecky-Levich method as described to extract the dependence of the diffusion-limited current density [24]. The RDE data points were fitted to a power-law function, and the resulting equation is shown in Equation 9.

$$i_{d,ORR} = 0.01125 * \delta^{-0.8473} \, [A/\mathrm{cm}^2] \quad [9]$$

Using the method described by Liu [62], a value of 3,860 micrometers was obtained for the natural convection-controlled boundary layer thickness, δ_{nc}. For WL thicknesses less than δ_{nc}, Equation 9 was used to determine the $i_{d,ORR}$.

Sensitivity analyses were performed to assess the effects of the different expressions for the passive current density as a function of pH. As stated before, the dependence of AA2024 passive current density on pH can be described by different expressions determined by the solution composition and the experimental procedure used to measure the polarization data. The model was implemented for each of the four expressions of passive current density found in the previous study [24], and **Figure 4.2**(a) shows the corrosion potential transients obtained for each expression. For all cases, a starting pH of 7 was used. Although qualitatively similar, the details of the potential transient change significantly depending on whether an unbuffered or buffered solution was used. For the buffered solutions, the corrosion potential decreases more quickly – 3 s for the potentiodynamically-determined expression and 8 s for the potentiostatically-determined equation. For the unbuffered solutions, the corrosion potential drop occurs after approximately 420 s for the potentiodynamically-determined expression and 1080 s for the potentiostatically-determined equation.

Figure 4.2b shows the calculated pH_{crit} versus *WL* for each case. The pH_{crit} was calculated by solving for pH at which the equality in Equation 10 is obtained:

$$i_{d,ORR} = i_{pass} \quad [10]$$

for *WL* ranging from 1 µm to 3000 µm. For *WL* thicker than 100 µm, the pH_{crit} obtained in buffered solutions is lower than that obtained in unbuffered solutions because i_{pass} was significantly higher in buffered solutions. That said, there is a limiting *WL* thickness below which the pH_{crit} in buffered solution surpasses the pH_{crit} in unbuffered solutions. The limiting *WL* for the potentiostatically-obtained i_{pass} is approximately 100 µm and the limiting *WL* for the potentiodynamically-obtained i_{pass} is approximately 15 µm for buffered solutions. It is important to stress that these expressions were measured in the pH range of 9 to 12.25. Thus, we are assuming that these expressions will hold for pH values outside this range, as stated in the model description section.

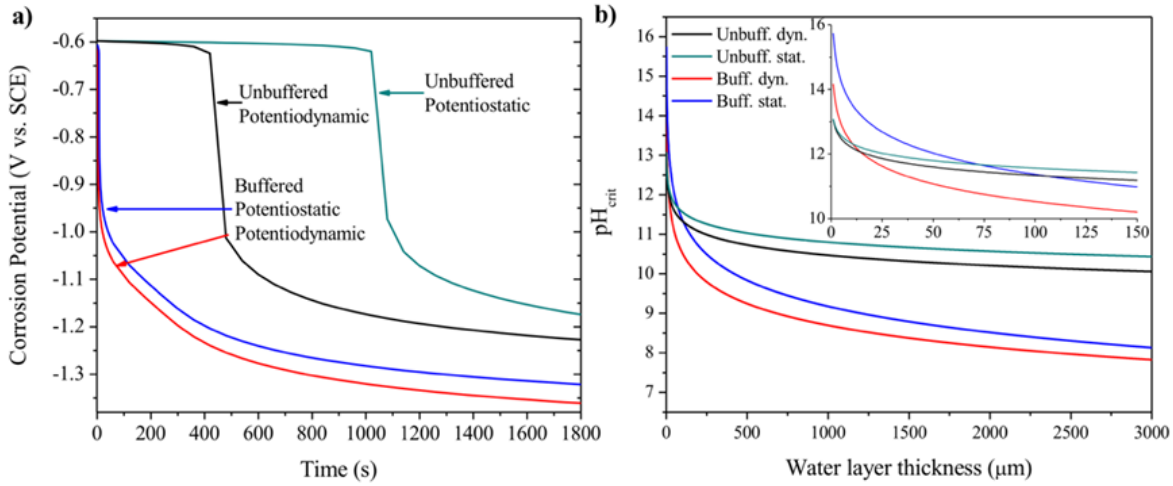

Figure 4.2. (a) Corrosion potential transients obtained in the middle of the scribe (10 mm) when performing the model with different expressions for the AA2024 passive current density as a function of pH (**Table 4.1**) and (b) pH_{crit} as a function of WL obtained for the different passive current density expressions.

4.4.2. Verification of the model

The model implementation was first verified by comparing AA2024 OCP measured in a full immersion cell in a 0.9 M NaCl unbuffered solution at various pH values to the corrosion potentials calculated in the model. Figure 3.3a shows experimental OCP observations measured as a function of pH [24] and the corrosion potential as a function of pH obtained from the model. Experimentally, a value of 9.86 for the pH_{crit} was determined. The expression for i_{pass} as a function of pH obtained

potentiodynamically was found to best capture the potential versus pH trend observed experimentally in unbuffered solution. Further explorations on the effect of other parameters investigated in this study were evaluated using the i_{pass} expression obtained from the potentiodynamic tests performed in unbuffered solutions unless otherwise noted.

One of the advantages of modeling electrochemical systems is the ability to calculate the current density of specific half-cell reactions, parameters that cannot be measured experimentally. Figure 3.3b shows the transients with time of the corrosion potential and the current densities of the anodic kinetics simulated in a full immersion condition for Case I. As the potential falls below and thus deviates from the pitting potential, the current density that represents pitting kinetics decreases substantially, while the passive current density increases more slowly. After the pitting current density is suppressed, the anodic current that remains is the passive current density. At all times, mixed potential theory requires that the total cathodic current equal the total anodic current. At early times (i.e., t < 420 s), the cathodic current is dominated by the ORR, whereas at times greater than 420 s, the cathodic current is dominated by the HER. Note that the pitting current density is normalized by the total area of the AA2024 electrode. Hence relatively small current densities are obtained, although it should be understood that the local pitting current densities are orders of magnitude higher due to the small area of the pits.

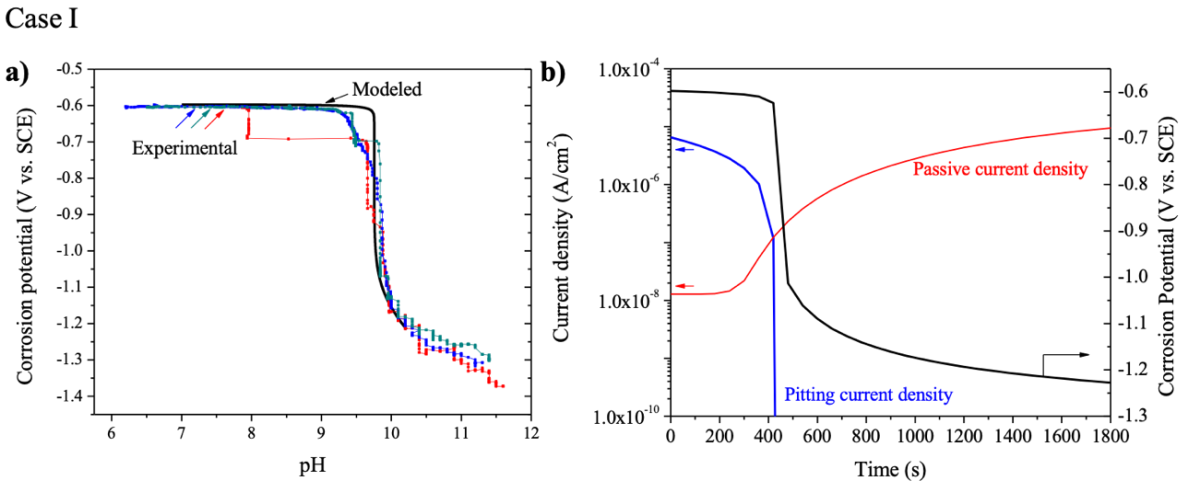

Figure 4.3. (a) Comparison between the measured and simulated corrosion potential as a function of pH for AA2024-T3 in 0.9 M NaCl. (b) The current density transient that represents the pitting kinetics, the passive current density transient, and corrosion potential transient in the middle of the scribe (10 mm) in a 6000 µm WL obtained for Case I. Note that it was possible to calculate separately what we refer to as the pitting current density, as pitting kinetics was defined as a separate half-cell reaction occurring over the surface of AA2024.

4.4.3. The effect of *WL* thickness on the pit repassivation

The effect of the *WL* thickness on the viability of the pH-induced pit repassivation was investigated, as the *WL* thickness significantly affects the diffusion-limited kinetics of the oxygen reduction reaction, affecting the value pH_{crit} [62]. The corrosion potential transient for different *WL* thicknesses is shown in **Figure 4.4** a shows the corrosion potential transient in atmospheric conditions, in a *WL* range in which the diffusion-limited kinetics of ORR is affected by the thickness of the film. **Figure 4.4**b shows the corrosion potential transient in a *WL* range above the natural convection *WL* (3860 μm) – that is, in a range where the diffusion-limited current density of ORR is constant. As the *WL* thins from 3000 μm to 300 μm, the time at which pit repassivation occurs – the time when the corrosion potential rapidly falls - increases. For 200 and 100 μm *WL*, pit repassivation does not occur at all, and the potential remains at the same potential as the initial corrosion potential of AA2024, signifying continued localized corrosion. **Figure 4.4**c shows the pH transient in the middle of the scribe for selected *WL* thicknesses (100, 200, 500, and 1000 μm). The pH transient is slightly affected by the thickness of the *WL*.

Figure 4.5a shows the critical time (time at which the corrosion potential shifts to more negative values) as a function of *WL* for a wider range of thicknesses, and **Figure 4.5**b shows the pH_{crit} versus *WL*. In **Figure 4.5b**, the pH_{crit} was calculated separately by solving Equation 10 for *WL* ranging from 1 μm to 3000 μm.

It can be seen that the pH_{crit} increases as the *WL* becomes thinner. At a 100 μm thickness, *WL*, pH_{crit} is 11.94. However, this pH cannot be achieved because the precipitation of $Mg(OH)_2$ limits the pH rise. For all *WL* thicknesses tested, the pH reached an equilibrium value of around 10.98, based on a K_{sp} of $4.5 \cdot 10^{-10}$, as found in the literature [195]. Under these conditions of thin *WL*, pit repassivation is not predicted to occur by pH-induced pit repassivation facilitated by Mg-based dissolution.

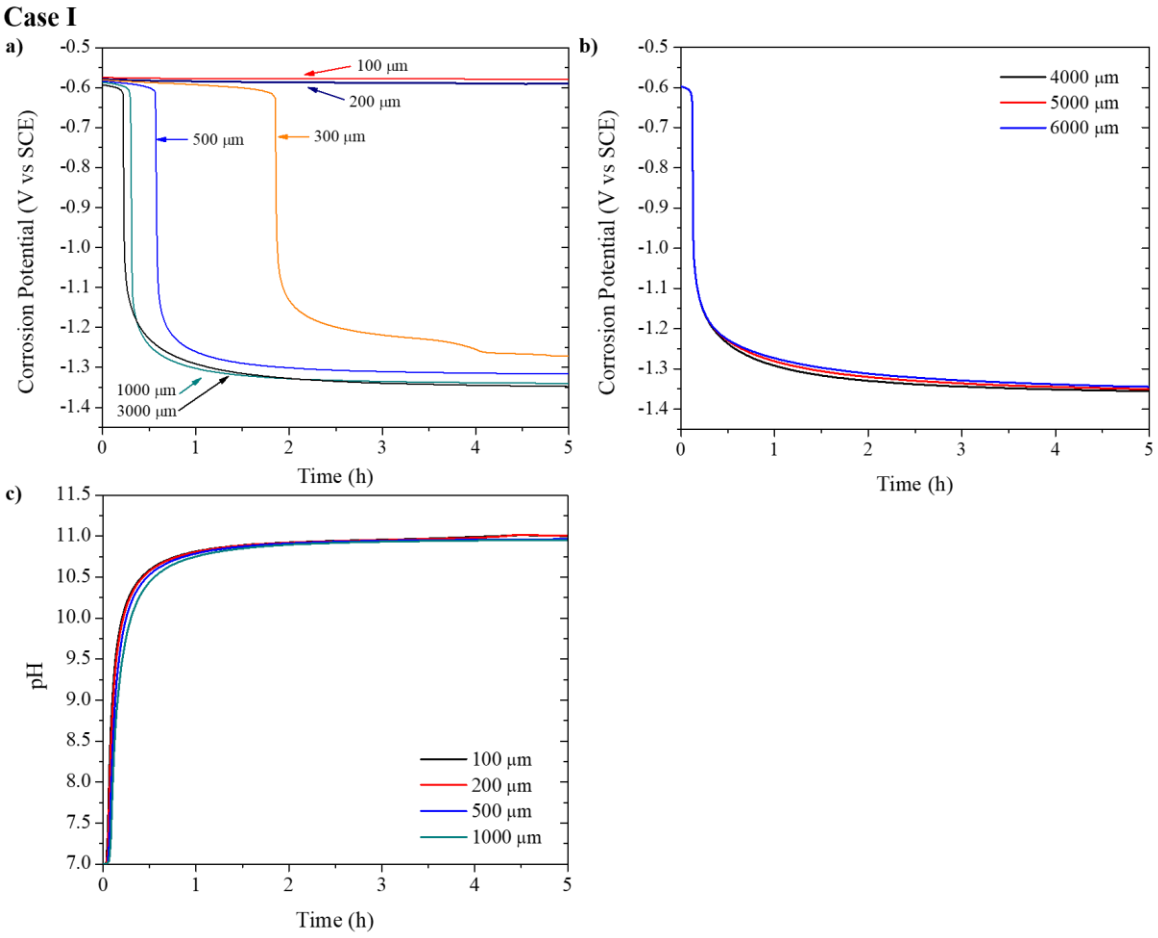

Figure 4.4. a) Corrosion potential transient at the center of the scribe for different *WL* thicknesses in atmospheric conditions after 5 hours of exposure; b) corrosion potential transient at the center of the scribe in full immersion with varying electrolyte thickness; c) pH transient in the middle of the scribe (10 mm) for *WL*= 100, 200, 500, and 1000 µm.

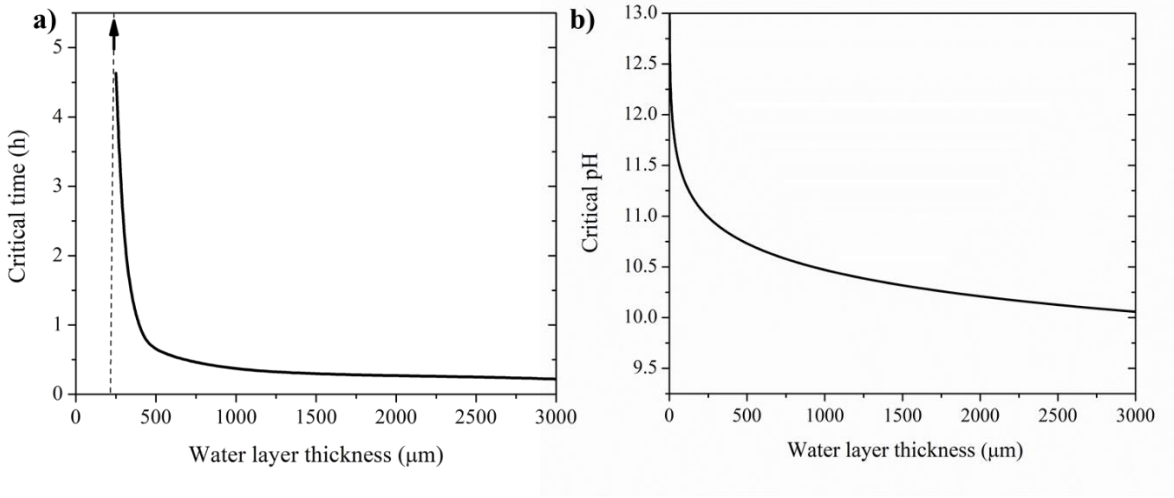

Figure 4.5. Critical time (a) and critical pH obtained from the model (marks) and calculated by solving Equation 10 for pH (line) (b) versus *WL* thickness.

4.4.4. The effect of solubility product on the pit repassivation

The precipitation of $Mg(OH)_2$ limits the pH rise, which is beneficial to prevent alkaline corrosion of the Al alloy substrate. However, at the same time, the precipitation limits the pit repassivation mechanism in thinner electrolyte layers. In an effort to explore other inhibitors that could act via pH-induced pit repassivation, the K_{sp} was varied. The aim was to define a range of K_{sp} values of oxides/hydroxides that would allow the pit repassivation to occur at thin electrolyte films.

Figure 4.6 shows the potential and pH transients for apparent K_{sp} ranging from $4.5 \cdot 10^{-10}$ to $4.5 \cdot 10^{-6}$ simulated for a 6000 μm *WL* (**Figure 4.6**a and **Figure 4.6**b), and a 25 μm thick *WL* (**Figure 4.6**c and **Figure 4.6**b-d). The corrosion potential reaches more negative values with the increase in the solubility product because the pH reached in the solution increases as the hypothetical oxide/hydroxide product becomes more soluble. For K_{sp} values from $4.5 \cdot 10^{-10}$ to $4.5 \cdot 10^{-8}$, the pH reached after 5 h of simulation increases from 10.83 to 11.43. For K_{sp} ranging from $4.5 \cdot 10^{-8}$ to $4.5 \cdot 10^{-6}$, the pH transient did not change with increasing K_{sp}. The corrosion potential after 5 h of simulation decreased from -1.35 to -1.46 V vs. SCE with increasing K_{sp}. The corrosion potential transient did not change with K_{sp} for K_{sp} values larger than $4.5 \cdot 10^{-8}$. The K_{sp}, however, did not affect the time at which the pit repassivation occurs.

In a 25 μm thick *WL*, however, the opportunity for pit repassivation depends strongly on the K_{sp}. For the K_{sp} values of $4.5 \cdot 10^{-10}$, $4.5 \cdot 10^{-9}$, and $4.5 \cdot 10^{-8}$, pit repassivation does not occur because the hypothetical oxide/hydroxide product precipitates and the solution pH remains below pH_{crit}. At higher K_{sp} (i.e., higher solubility), the solution pH can surpass pH_{crit} before precipitation takes place and pit repassivation occurs.

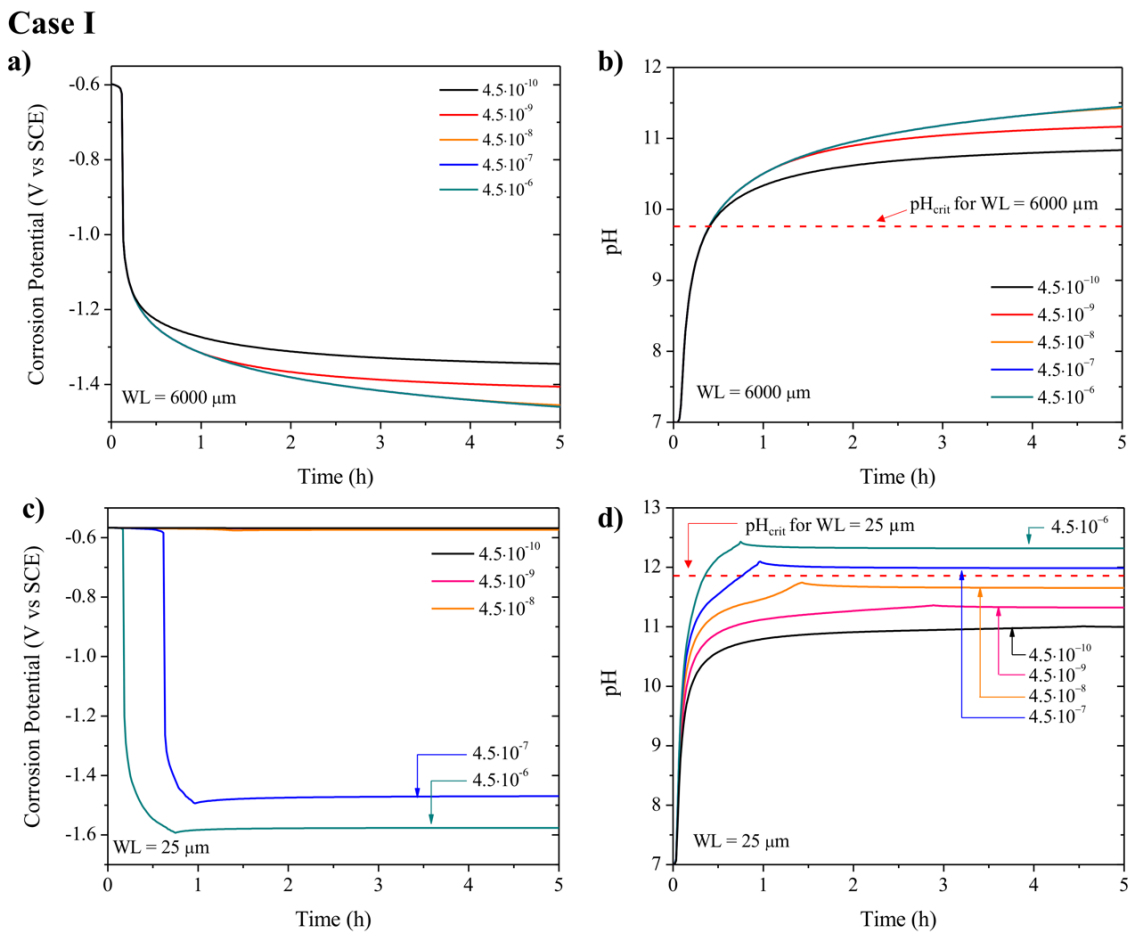

Figure 4.6. Potential (a) and pH (b) transient calculated using different K_{sp} values at a *WL* of 6000 µm; Potential (c) and pH (d) transient calculated using different K_{sp} values at a *WL* thickness of 25 µm.

4.4.5. The effect of oxygen reduction reaction inhibition

The results so far did not include the barrier effect that the $Mg(OH)_2$ film can cause when precipitated over the corroding scribe. It has been shown that the cathodic kinetics on AA2024 are reduced when there is a $Mg(OH)_2$ film over the surface [24]. This inhibiting effect was accounted for in a simplified manner. Instead of modeling the barrier effect considering the thickness of the film formed and its resistivity on the rate of the electrochemical reactions occurring on the electrode, the effective ORR limiting current density (i_{ORR}) was decreased at the time and locations where the solubility product was reached. The extent of ORR inhibition necessary for the pit repassivation mechanism to occur at a *WL* = 100 µm was calculated. **Figure 4.7**a shows the corrosion potential transient at a 100 µm *WL* obtained when i_{ORR} is reduced by 50, 55%, and 90% in respect to the i_{ORR} value obtained at a 100 µm *WL*. The corrosion potential decreased for the case in which i_{ORR} is reduced by at least 55%. For the case in which i_{ORR} is reduced by 55%, the

corrosion potential decreased to -1.25 V vs. SCE. In the case in which a reduction of 90% was considered, the corrosion potential decreased to a value of -1.36 V vs. SCE. **Figure 4.7**b shows the pH_{crit} for pit repassivation calculated for ORR current densities determined by Equation 10 and the pH_{crit} for pit repassivation calculated for ORR current densities reduced by 55% and 90% in respect to the current densities determined by Equation 9. The pH value reached at steady-state is also shown. The *WL* thickness value at which the pH_{crit} and the pH at equilibrium curves meet determines the critical *WL* thickness below which the pit repassivation mechanism is not predicted to occur. For the case in which the i_{ORR} can be reduced by 55%, the critical *WL* is 100 µm. For the case in which the $i_{ORR}$is reduced by 90%, the critical *WL* is approximately 17 µm.

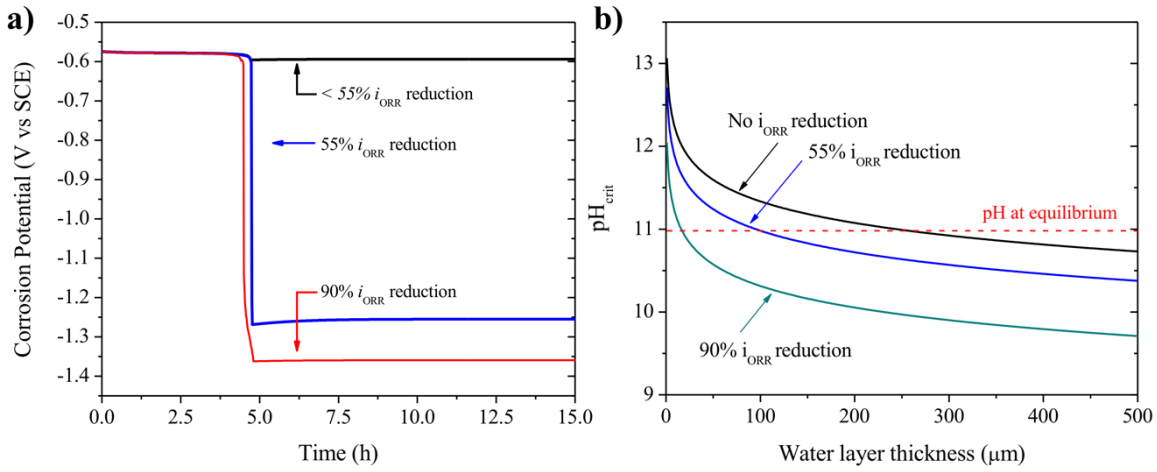

Figure 4.7. a) Corrosion potential transient obtained when reduction the ORR current density by less than 55%, 55%, and 90% at a *WL* = 100 µm. b) Critical pH for pit repassivation calculated for ORR current densities determined in AA20234 by RDE measurements and for ORR current densities reduced by 55% and by 90%. The pH that stabilizes in the solution after $Mg(OH)_2$ precipitates $Mg(OH)_2$ is shown to delimit the *WL* below which the pit repassivation process is not predicted to occur for each of the cases.

4.4.6. Case II: the effect of Aluminum corrosion products on the chemistry of the electrolyte

In the results reported above, only species from Mg dissolution were considered; species from the anodic and cathodic reactions occurring on the AA2024 were not included. To investigate the effects of these reactions on the electrolyte chemistry and on the ability of the Mg-based dissolution of raising the solution pH above pH_{crit}, Al corrosion products and the subsequent hydrolysis reactions of the metallic ions were included. The production rates of Al^{3+} and OH^- were calculated according to Faraday's law, using the anodic and cathodic local current densities. Hydrolysis of Al^{3+} was also accounted for using the reactions

in Appendix A. **Figure 4.8** shows the pH transient obtained when simulating the electrolyte chemistry evolution considering only the corrosion products of Al and the subsequent hydrolysis reactions – that is, without Mg-based dissolution. The pH decreased from the initial solution pH (=7) to a pH = 6.77 in 500 s, then it slowly increased to a pH value of 6.85.

Figure 4.9 displays the corrosion potential **(Figure 4.9**a) and pH transients (**Figure 4.9**b) obtained for Cases I and II. The addition of the Al corrosion products and Al^{3+} hydrolysis increased the time of pit repassivation from 434 s to 960 s, as Figure 9a evidences. **Figure 4.9**b shows the pH profile over the scratch at 434 s (critical time of Case I). In Case I, 33% of the scribe surface pH is above pH_{crit} at the critical time, while in Case II, 8% of the surface pH is above pH_{crit}.

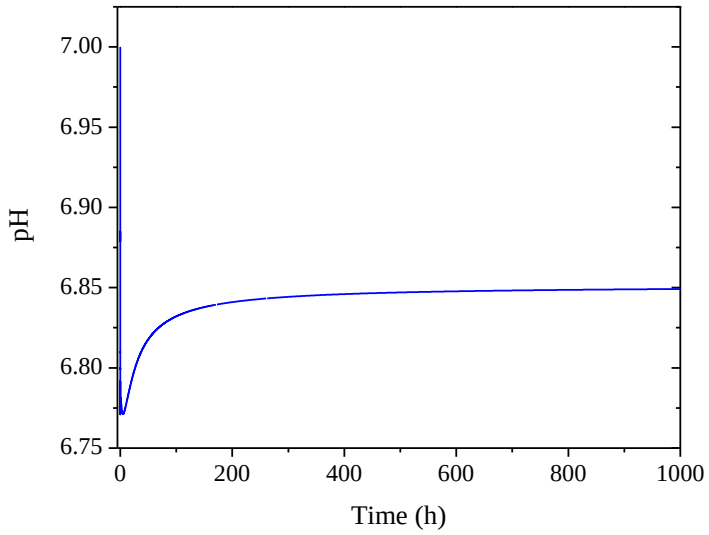

Figure 4.8. pH transient in the middle of the scribe as a result of the cathodic and anodic reactions occurring on Al and the subsequent hydrolysis of Al^{3+} species.

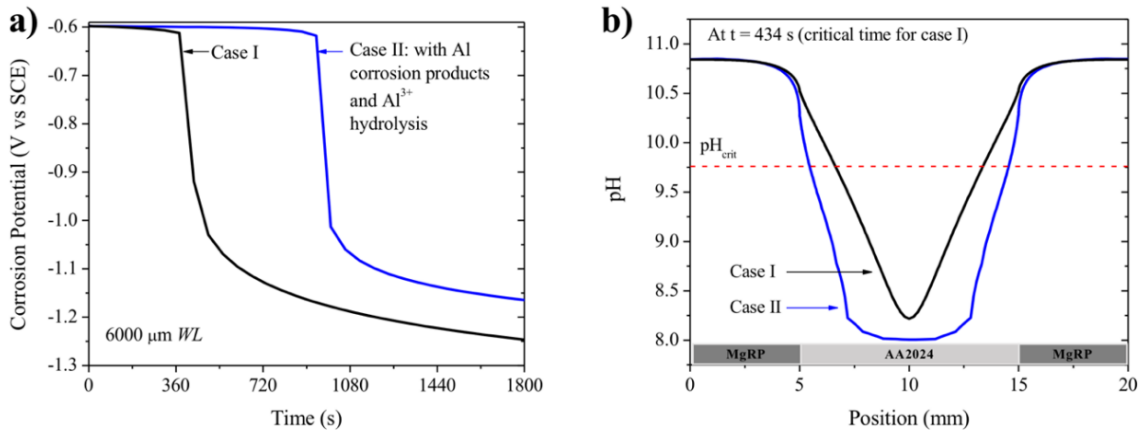

Figure 4.9. Potential (a) and pH transient (b) of Cases I and II obtained for a *WL*=6000 µm. In Case I, the species production from the electrochemical reactions occurring at AA2024 are not considered, and the only source of OH^- is from the constant dissolution of Mg- or MgO-rich primer. In Case II, the production of Al^{3+} and OH^- from the electrochemical reactions occurring at AA2024 are considered, as well as the hydrolysis reactions of the Al species.

4.4.7. Case III: potential distribution of the Mg/AA2024 galvanic couple

This section presents the results that were obtained when the galvanic coupling between AA2024 and Mg is considered without chemical effects. For this case, species production by the electrochemical reactions was not considered, and only the potential and current distributions resulting from the galvanic coupling of the two metals were calculated under fixed chemical conditions. This simplified approach was used to investigate the effect of coating resistance and water layer thickness on the galvanic protection mechanism separately and to compare the current model with the previously developed model [74]. In addition, the effect of the faster ORR kinetics in thinner electrolyte layers on the potential distribution was investigated.

Figure 4.10 shows the potential distribution established between AA2024 and Mg, and the open circuit potentials (OCP) of both metals, measured in a 0.9 M NaCl solution, pH = 7 [24] for two different cases: a) AA2024 is in contact with bare Mg for different *WL* thicknesses (**Figure 4.10**a); b) AA2024 is in contact with Mg coated with a 0-thickness resistive polymer with resistances of 0.1 and 10 $\Omega \cdot m^2$ (**Figure 4.10** b). The impact of the water layer thickness on the ORR was not taken into account in **Figure 4.10**. In the former case, the mixed potential reached in AA2024 in nearly steady-state ranged from -1.52 V vs. SCE, at the point closest to Mg, to -1.40 V vs. SCE, in the middle of the scribe for a 6000 µm *WL*. For thinner *WL* (25 µm), the calculated potential in the middle of the scribe was -1.17 V vs. SCE.

The potential established between Mg coated with a film of resistances 0.1 and 10 $\Omega \cdot m^2$, and AA2024 was nearly constant, as **Figure 4.10**b shows. With a 0.1 $\Omega \cdot m^2$ resistance over Mg, the calculated galvanic potential was -1.2 V vs. SCE, which lies below the repassivation potential. Increasing the resistance to 10 $\Omega \cdot m^2$, the potential established was -0.88 V vs. SCE, which is more positive than the AA2024 repassivation potential. **Figure 4.10**c shows a 2-D section through a galvanic potential surface, in which the galvanic potential established in the middle of the scribe is shown as a function of *WL* thickness and film resistance. Film resistance has a greater impact on the galvanic potential established in the middle of the scribe. For relatively small changes in the film resistance, there is a relatively large change in the potential established. For resistances above approximately 9 $\Omega \cdot m^2$, the potential in the center of the scribe lies above the repassivation potential. The repassivation potential referenced in this work was measured in different alkaline solutions, and experimental details can be found in [24].

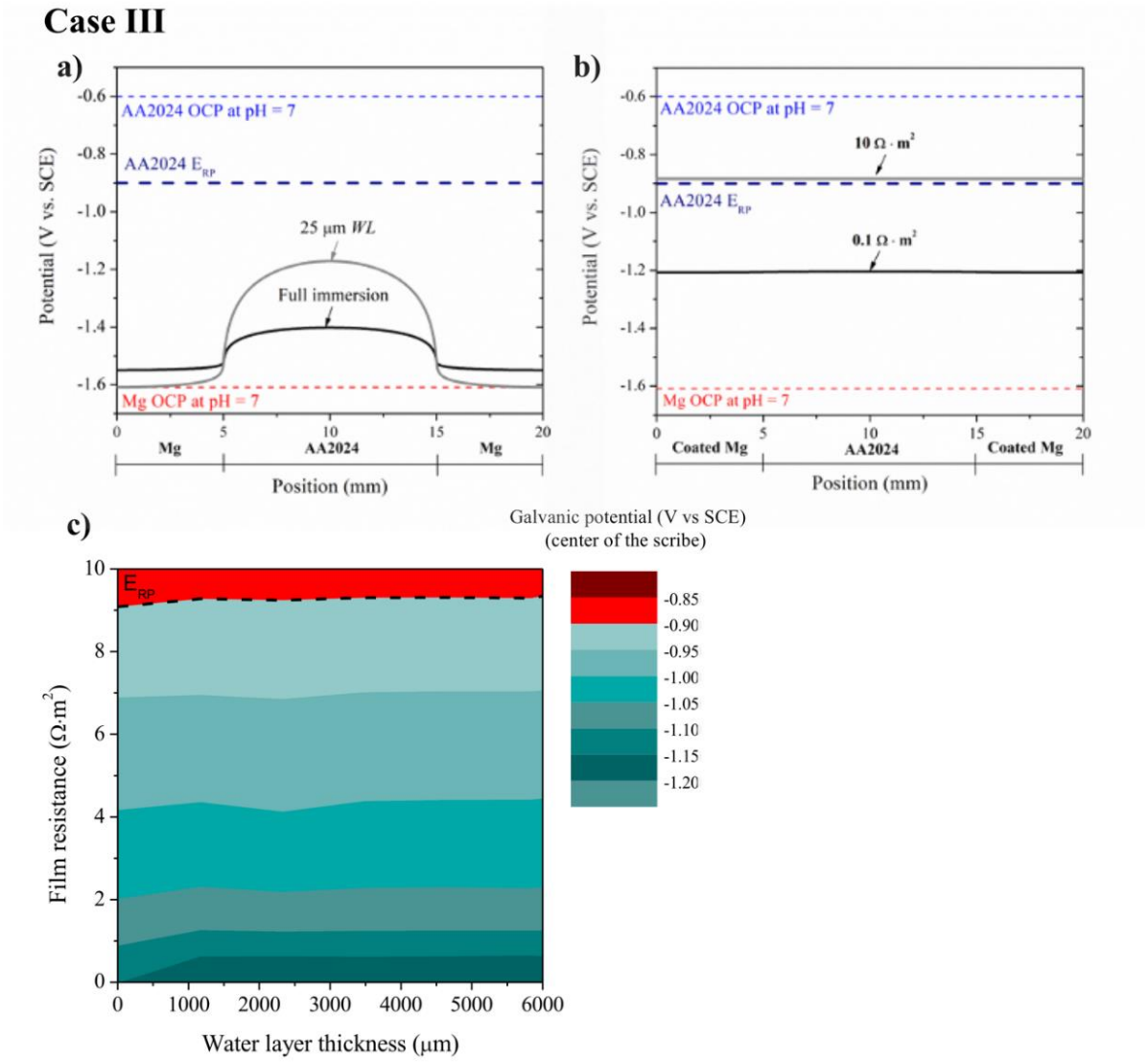

Figure 4.10. Potential distribution for Mg/AA2024 galvanic couple and OCP of Mg and AA2024 in a 0.9 M NaCl solution of pH = 7. At the bottom of the figure, the location of each electrode is indicated. In (a), the potential distribution for different water layer thicknesses (25 and 6000 μm) between bare Mg and AA2024 is shown. In (b), the potential distribution established between a coated Mg with different film resistances (0.1 and 10 $\Omega \cdot m^2$) and AA2024 is shown. In (c), the contour plot shows the potentials established in the center of the scribe at different *WL* thickness and film resistances.

Figure 4.11 shows the potential distribution obtained for the cases in which the ORR kinetics used was obtained in full immersion conditions and for the ORR kinetics in thin films simulated by RDE experiments calculated for a water layer thickness of 100 and 15 μm. There is not much difference between the potential distribution obtained under 100 μm. The galvanic potential obtained for the full immersion

ORR kinetics case was slightly lower at the center of the scribe. However, under a 15 μm water layer, the difference in the galvanic potential is significant. Without considering the impact of water layer thickness on the ORR kinetics, Mg is able to polarize the 10 mm AA2024 scribe to a potential down to ca. -1.15 V vs. SCE. However, if the thin film ORR kinetics are considered, the potential at the center of the scribe is at the AA2024 corrosion potential.

Figure 4.11 (b) shows the difference between the galvanic potential at the center of the scribe (x = 10 mm, 5 mm way from Mg) calculated for a full immersion and thin film ORR kinetics. The difference in potential increases with the decrease in the water layer thickness. For water layers thicker than 100 μm, the difference between the potentials is less than 10 mV. For water layers thinner than 35 μm, however, the difference in the galvanic potentials is over 100 mV. **Figure 4.11** (c) shows the potential distribution as a function of water layer thickness obtained for the case in which the ORR kinetics in thin film is modeled. The potential at the Mg is not much affected by the change in the water layer thickness, although it does slightly decrease with the increase in the water layer thickness. For the *WL* thicker than 25 μm, the potential at the AA2024 scribe is lowered below its repassivation potential. If the criterion for protection is the polarization below the repassivation potential, then the galvanic throwing power of Mg extends the 10 mm scribe. However, for a 15 μm thick *WL*, the coupled potential sharply increases with increasing distance from Mg until and AA2024 and Mg are essentially uncoupled. Only 3.2 mm of the 10 mm scribe are below the repassivation potential under the 15 μm *WL*.

Figure 4.11 (d) shows the 2-D section through the galvanic potential surface, in which the galvanic potential established in the middle of the scribe is shown as a function of *WL* thickness and film resistance for the case in which the ORR kinetics in thin films is taken into account. The resistance above which the coupled potential increases to potentials higher than the repassivation potential decreases as the water layer thickness decreases. Under *WL* thinner than ca. 25 μm, the galvanic potential established is higher than the repassivation potential for the entire range of polymer resistances tested.

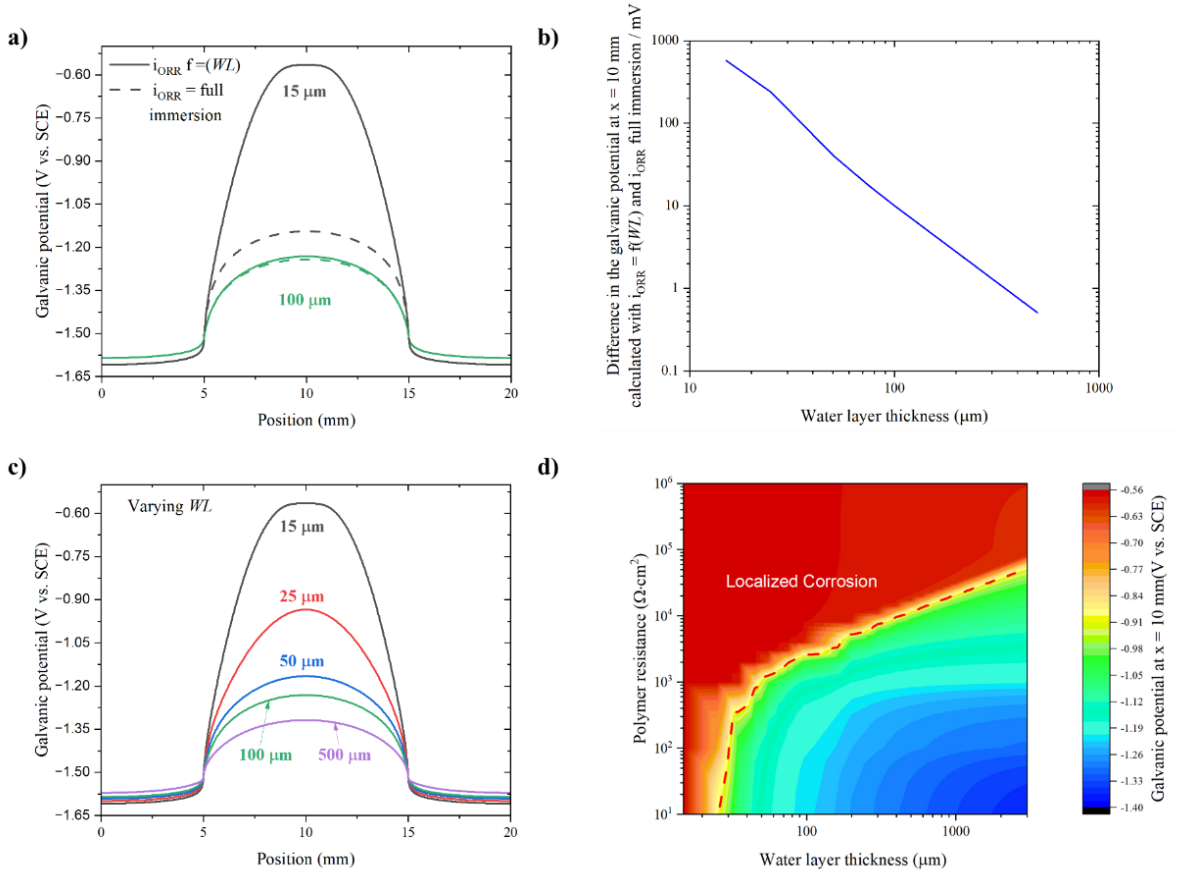

Figure 4.11. Impact of the ORR kinetics on the potential distribution between Mg and AA2024. In (a) the dashed lines show the potential distribution obtained for a constant ORR kinetics obtained in full immersion; the solid lines show the potential distribution obtained for simulated ORR kinetics in thin films. In (b), the difference between the galvanic potential at the center of the scribe (x = 10 mm) obtained for the two different cases is shown. In (c), the potential distribution obtained for different water layer thicknesses considering the respective ORR kinetics. In (d), the updated heat map showing the combined effect of water layer thickness and polymer resistance on the coupled potential of AA2024 at 5 mm away from Mg, in the case in which the ORR kinetics in thin film is accounted for.

4.4.8. Case IV: galvanic protection in an evolving electrolyte chemistry

The combined action of both electrolyte composition change (from the Mg and AA2024 electrochemical reactions) and galvanic protection was considered. **Figure 4.12**a shows the potential distribution at different times obtained for Mg and AA2024 when considering the electrolyte composition change over time and a 10 $\Omega \cdot m^2$ film resistance over Mg in a WL = 6000 µm, in comparison to the corrosion

potential calculated in Case II. The potential at the center of the scribe is instantly polarized to -0.94 V vs. SCE. The galvanic potential decreases to -1.25 after 1 h of simulation, reaching more cathodic values than Case II (-1.18 V vs. SCE). **Figure 4.12**b shows the pH transient for Cases II and IV. With galvanic coupling, the pH rises faster and reaches more alkaline values than the case in which galvanic coupling is not considered.

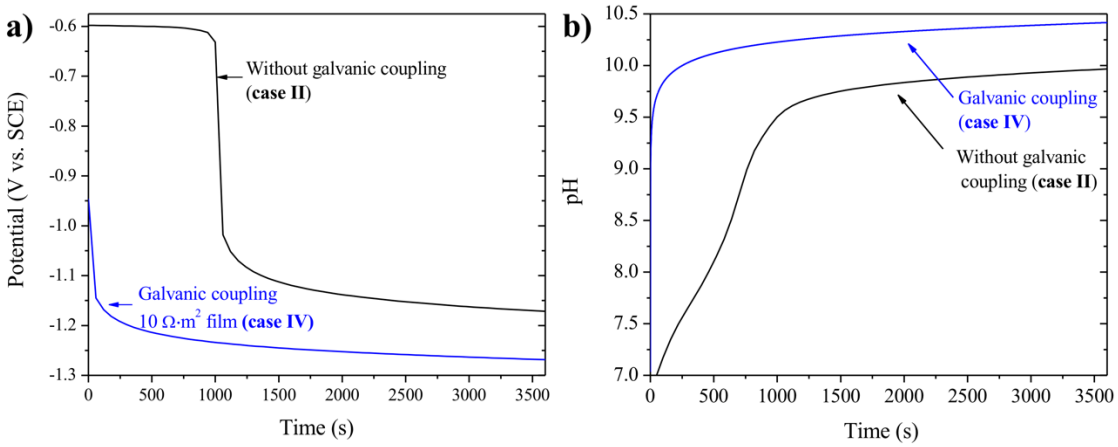

Figure 4.12. Potential and pH results obtained when the electrolyte composition changes over time in a 6000 µm *WL* for Cases II and IV (with and without galvanic coupling). In (a), the potential distribution between Mg and AA2024 obtained at t = 0 h and at t = 1 h is shown; pH transient is shown in (b).

4.5. Discussion

The model framework described in this work was developed to simulate the different protection mechanisms that a Mg-based rich primer can offer to AA2024. First, the abstraction of the electrochemical kinetics and their dependence on pH are described. Then, the validation of the model framework with experimental results is discussed. The concept of pH-induced electrode potential [24] was successfully reproduced computationally. The importance of the electrochemical boundary conditions that describe the kinetic anodic behavior of AA2024 is also discussed. The effect of water layer thickness and K_{sp} on the efficacy of the chemical inhibition via pH-induced pit repassivation was examined. The viability of the pit repassivation mechanism described herein is strongly determined by the water layer thickness. The mitigation of the limitation of this pit repassivation mechanism is granted by the selection of an inhibitor with higher K_{sp} and by the ability of the precipitated compound to inhibit the oxygen reduction reaction. Additionally, galvanic coupling between Mg and AA2024 is simulated, and a brief discussion on the

galvanic protection that MgRP can provide is presented. Lastly, the model limitations are considered, and potential model enhancements are suggested.

4.5.1. Model framework and its validation with experimental results

The calculated corrosion potential of AA2024 as a function of pH was compared with OCP measurements taken at different pH values. The model captures the influence of pH on the corrosion potential of AA2024 in full immersion conditions, which indicates that the boundary conditions implemented at the electrodes are adequate.

It is important to note that the predicted pH_{crit} is dependent on the passive current density expression as a function of pH, as evidenced in the results shown in **Figure 4.2**. The passive current density expression depends on both the extent of buffering in the solution in which the measurement was taken and the electrochemical method used to determine it. Higher anodic current densities were observed in buffered solutions, which resulted in a lower pH_{crit}, because only a smaller increment in pH was necessary for the anodic current density to surpass the diffusion limited ORR current density. The higher anodic current density obtained for the buffered solution was attributed to the presence of complexation agents like borate and phosphate that affect Al dissolution rate [24]. The following analyses are based on the results obtained when using the passive current density expression obtained potentiodynamically in unbuffered solutions. However, it is important to remember that quantitatively but not qualitatively, different results would have been obtained using different boundary conditions.

4.5.2. pH-induced potential control mechanism viability is dependent on water layer thickness

The viability of a protection mechanism based on the pH-induced potential control in atmospheric conditions strongly depends on the chemistry of the electrolyte. As explained by Santucci and Scully [24], the corrosion potential of AA2024 decreases to values well below its pitting potential when the passive current density exceeds the ORR diffusion-limited current density. The passive current density of Al increases as the solution becomes more alkaline due to increased solubility of the oxide film, and there is a critical pH at which the passive current density overcomes ORR diffusion-limited current density. When the passive current density exceeds the ORR diffusion-limited current density, mixed potential theory demands that the corrosion potential fall to the potential at which the hydrogen evolution reaction current density equals the passive current density. This corrosion potential is well below the pitting and repassivation potentials of AA2024; thus, any active localized corrosion is expected to stop. In a Mg^{2+}-containing solution, the precipitation and deposition of a $Mg(OH)_2$ film at cathodic sites prevent the pH from rising to values at which Al actively corrodes. At the same time, once it is deposited, it can keep the

local pH sufficiently high so that the corrosion potential remains below the repassivation potential even after Mg-based pigment is depleted.

The important role that *WL* has on the viability of the pit repassivation mechanism is due to its strong effect on the diffusion-limited current density of ORR. Because the diffusion-limited current density increases as the water layer becomes thinner, the passive current density must increase accordingly for the pit repassivation to occur, as discussed above. Thus, thinner electrolyte films require higher pH_{crit} to cause pit repassivation. The time required to reach the pH_{crit} also increases with decreasing *WL* thickness, following the behavior of the pH_{crit} vs. *WL* thickness. In the absence of other effects, there is critical *WL* below which pit repassivation will not occur because the solution is not able to reach the pH_{crit} as dictated by the K_{sp} of the precipitating phase. This critical *WL* will depend on the electrolyte chemistry, as different chemistries will impact the pH of the solution and the kinetics of the electrochemical reactions.

Figure 4.13a shows the pH transient for different *WL* thicknesses and indicates the pH_{crit} and the pH at which precipitation occurs. In a full immersion condition, the Mg^{2+} concentration does not reach the solubility limit, and $Mg(OH)_2$ does not precipitate, so the pH keeps rising, as OH^- is produced at a constant rate. The solution reaches the pH_{crit}, and pit repassivation occurs. At a 500 µm *WL*, Mg^{2+} reaches the solubility limit at a pH of 10.98, which is higher than the pH_{crit} at this *WL* (10.73). Thus, pit repassivation occurs. At a 25 µm *WL*, precipitation occurs at a pH lower than the pH_{crit} (11.85), and pit repassivation cannot occur. At this point, any additional Mg^{2+} and OH^- will simply form additional amounts of $Mg(OH)_2$, and the Mg^{2+} concentration and pH will remain constant, despite the continuous production of Mg^{2+} and OH^- by the anodic and cathodic reactions. **Figure 4.13**b shows pH_{crit} and the pH at saturation versus *WL* thickness. The pH_{crit} and pH at saturation lines cross at a *WL* = 257 µm. According to **Figure 4.13**b, it is expected that the pit repassivation would not occur at *WL* < 257 µm, because the pH at which precipitation occurs is lower than pH_{crit}, explaining the sharp transition in the corrosion potential behavior between the 200 and 300 µm *WL*, shown in **Figure 4.4a**.

The degree of supersaturation required for precipitation will also influence the critical *WL* thickness. **Figure 4.13**c shows the critical water layer thicknesses obtained for different amounts of supersaturation. Increasing supersaturation leads to a slightly lower critical *WL*, with a difference of 75 µm (250 vs. 175 µm) between a supersaturation of 1 and 3.4.

The addition of the electrochemical reactions occurring at AA2024 and subsequent Al^{3+} hydrolysis significantly changed the time at which pit repassivation occurs. Due to the equilibrium among the Al ion hydrolysis products, some of the produced OH^- will subsequently complex with Al^{3+}, thereby tempering the extent of alkalization. The number of OH^- anions that will complex with the Al^{3+} cation is a function of pH, which dictates whether there will be net acidification or net alkalization. As **Figure 4.8** shows, there is a net acidification of the solution for the self-corrosion of Al, and the pH decreases to 6.85. With OH^-

originating from Mg dissolution, the solution pH still increases when taking into account Al^{3+} hydrolysis reactions, but it does so at a slower rate. It is important to note that the Mg dissolution rate used in the model is based on the dissolution rate of a MgRP measured by Lin *et al.* [191]. Thus, the predicted transients would change depending on the type of pigment (Mg or MgO), pigment volume concentration, electrolyte chemistry, and other variables that can affect the electrochemical or chemical dissolution rates of the pigments.

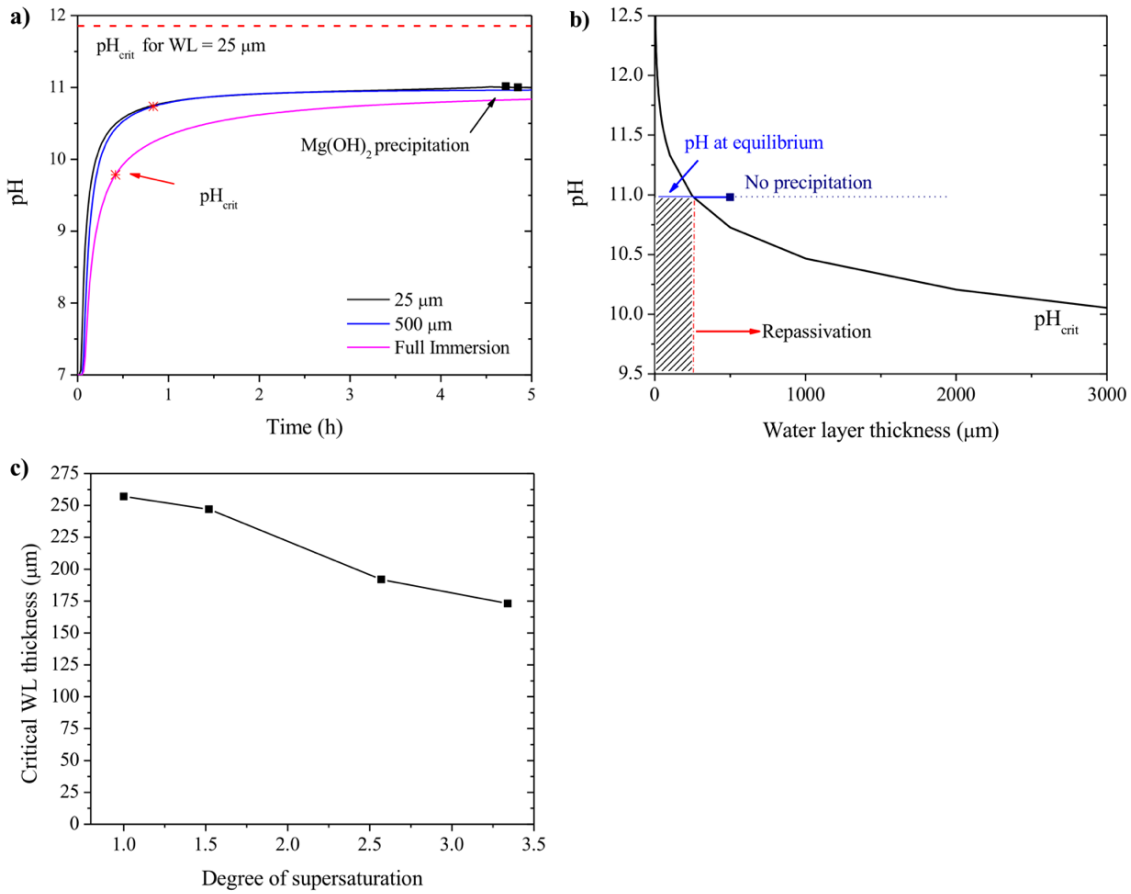

Figure 4.13. a) pH transient for different water layer thicknesses. The red asterisk indicates pH_{crit}, and the black square marks the pH at which $Mg(OH)_2$ precipitation occurs. The dashed line indicates the pH_{crit} at a *WL*=25 µm b) pH_{crit} and pH at saturation versus water layer thickness. The hatched area indicates the water layer thicknesses in which the pit repassivation mechanism does not occur; c) critical water layer thickness below which the pit repassivation mechanism is not predicted to take place as a function of supersaturation of Mg^{2+}.

4.5.3. K_{sp} as a critical parameter for protection via pH-induced potential control mechanism

The increase in the apparent K_{sp} makes the pH-induced potential control mechanism feasible at thinner *WL*, because the solution can reach higher pH values. **Figure 4.14** shows the limiting *WL* below which the pit repassivation mechanism explained herein cannot take place for each K_{sp} tested. For example, an inhibitor whose hydroxide has a K_{sp} in the order of magnitude of 10^{-7} or higher is needed to provide pit repassivation in *WL* of 20 µm, in the absence of other effects. The pH_{crit} of such thin *WL* is above 11.9. Inhibitors that can increase the solution pH up to such values and, at the same time, buffer the solution at this targeted pH would provide protection against localized corrosion of an AA2024 over a wide range of atmospheric conditions. However, at such high pH, caustic attack can be excessive. Mokaddem et al. studied the Al dissolution rate of AA2024 as a function of pH and found that at a pH of 11.83 the dissolution rate of Al was 2.9 A/cm^2 after 5 min in 0.5 M NaCl solution [196]. This result indicates this mechanism alone may be limited to thicker *WL*, where the pH_{crit} is not high enough to cause an intense caustic dissolution.

Another potential problem with higher K_{sp} values is the coating blistering effect that more soluble inhibitors can cause. A correlation between the solubility of the inhibitor with blistering and extent of delaminated area has been observed, due to an osmotic mechanism associated with pigment leaching and water absorption [197]. Sinko investigated the blistering effect for a range of solubility of inhibitor pigments and observed severe blistering for inhibitors with saturated concentration above $2.8 \cdot 10^{-1}$ M for dry, solvent-based, medium oil alkyd primers [197]. However, for the range of K_{sp} investigated, the saturated concentration of the inhibitor is still significantly below this threshold value observed by Sinko. For the highest K_{sp} value tested, the concentration at saturation found was $4.83 \cdot 10^{-3}$ M for Mg^{2+} and $2.08 \cdot 10^{-2}$ for OH^-. At a solubility in this order of magnitude, Sinko did not observe blistering effect after 117 h of immersion.

The satisfactory protective performance of MgO-rich primers observed in atmospheric field exposures and the results shown in this work suggest that ORR inhibition plays an important role in the chemical protection mechanism provided by Mg-based rich primers [179,187]. The inhibition of ORR decreases the pH_{crit} for pit repassivation, enabling the pH-induced mechanism at thinner electrolyte layers. When taking into consideration the barrier effect that the precipitated film may cause, a higher solubility would be disadvantageous. Therefore, the selection of an inhibitor that provides these modes of protection combined should consider both the extent of ORR inhibition and the pigment solubility. The combined effect of the ORR inhibition and pH_{crit} on the pH-induced pit repassivation mechanism can be seen **in Figure 4.15**, which shows the extent in which ORR needs to be inhibited in order for the pH-induced pit repassivation mechanism to occur above the specified pH_{crit} as a function of *WL* thickness. For example, to

decrease the pH_{crit} to 9 at a *WL* = 15 µm, ORR would need to be 1000 x slower (ORR kinetics is multiplied by a factor of 10^{-3}).

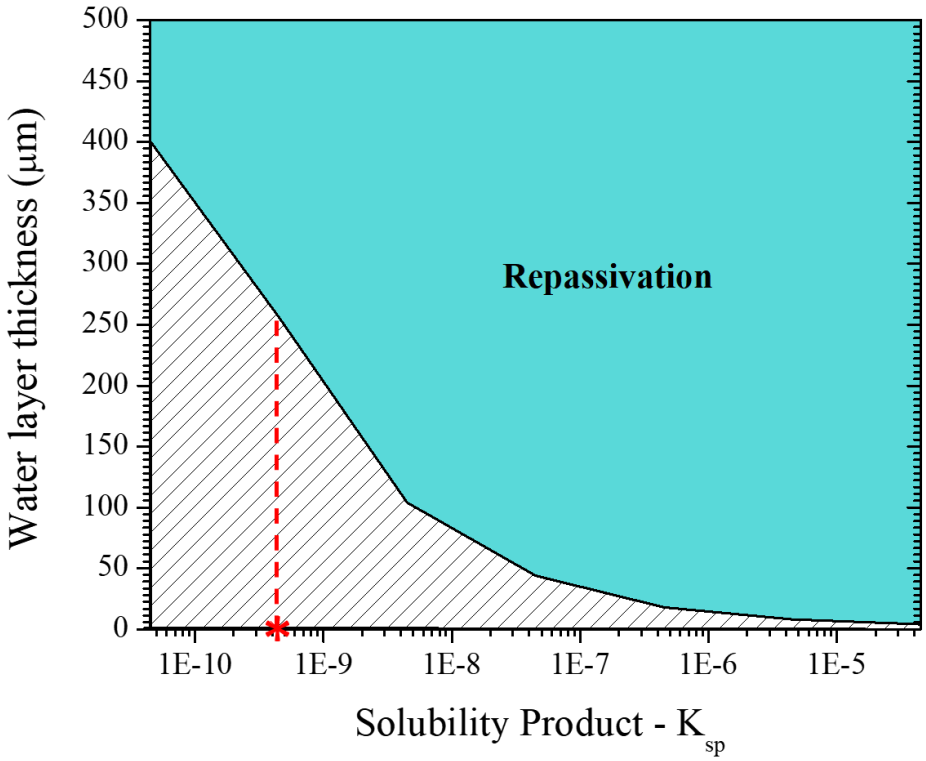

Figure 4.14. Threshold of *WL* where AA2024 can be protected by the pH-induced potential control mechanism for different K_{sp}. The asterisk indicates the K_{sp} value of $Mg(OH)_2$ in seawater [195].

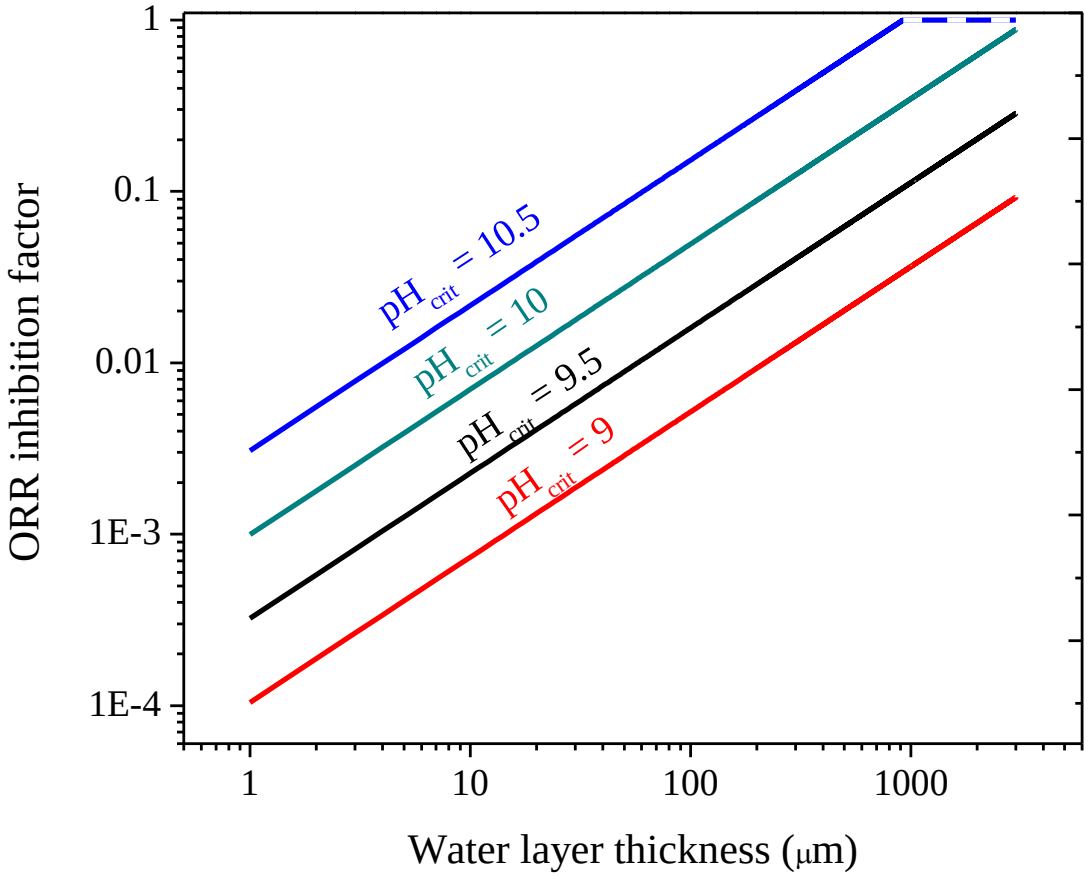

Figure 4.15. Relationship between the extent of ORR inhibition needed for the feasibility of the pH-induced pit repassivation mechanism to occur at the specified pH_{crit} as a function of water layer thickness.

4.5.4. Polarization of AA2024 by Mg pigments in electrical contact

The results obtained when using Laplace equation to model the galvanic coupling between Mg and AA2024 agree with experimental and computational work conducted previously. Kannan *et al.* conducted EIS measurements of an AA2024 coated with MgRP without a topcoat in full immersion conditions, and they reported that the system initially exhibited potentials close to -1.4 vs. SCE and that it stabilized at -1.2 V after 12 h. In the model, AA2024 was polarized to -1.4 V vs. SCE for the case that simulated the galvanic coupling of bare Mg in contact with AA2024 and to -1.2 V vs. SCE for the case where Mg was coated with a 0.1 $\Omega \cdot m^2$ resistive coating. It would seem that at early times, the bare Mg on the surface of the coating is sufficient to polarize the AA2024 to a very negative potential, but once the freely available Mg has

dissolved, the resistance of the surrounding polymer film and topcoat limits the polarization. In a previous FEA work performed to predict galvanic couple current and potential distribution between Mg and AA2024 [74], the potential distribution the authors found is similar to what was found in this work. However, because the authors of the previous work performed the simulations in thinner water layers, there is a higher ohmic drop between the electrodes.

Based on the polarization curves of AA2024 and Mg published by King et al. [74], mixed potential theory demonstrates that the galvanic coupling potential between AA2024 and Mg in a 1:1 anode to cathode ratio will be -1.5 V vs. SCE in the absence of ohmic drop. In the model developed in this work, the same galvanic potential was found at the points closest to Mg for the case where there was no resistive layer on Mg, as shown in **Figure 4.10**. The agreement between the galvanic potentials obtained in the model and by those determined by applying mixed potential theory to the experimental polarization curves of Mg and AA2024 indicates that the boundary conditions chosen for AA2024 are adequate. The large polarization of the AA2024 results from the combination of the fast anodic reaction rate of Mg and the slow cathodic reaction rate of AA2024 [20]. It should be noted that if Al alloys are polarized to potentials as negative as -1.5 V vs. SCE, cathodic corrosion can occur [39,175,198]. Due to the high currents in the case of bare Mg connected to AA2024, there is a large ohmic drop of up to 395 mV for the 25 μm water layer. Nonetheless, even the center of the scribe is polarized well below the repassivation potential, which is the criterion used for pit repassivation.

The low potential and low polarizability of Mg drive the Mg/AA2024 coupled potential to potentials at which HER is the dominant cathodic reaction. As such, the diffusion-limited ORR current density was not expected to have much influence on the potential and current density distribution between Mg and AA2024. However, if the ionic resistance between AA2024 and Mg increases sufficiently, then AA2024 might be in a potential where ORR is dominant. The thinning of the water layer will compound two effects that could lead to an increase in the coupled potential. The decrease in the area ratio will increase the resistance to the passage of current, increasing the ohmic drop. At the same time, the thinning of the water layer will increase the diffusion-limited current density of ORR, further increasing the ohmic drop. The results shown in **Figure 4.11** indicate that the ORR kinetics influence the galvanic coupling between AA2024 and Mg in *WL* thinner than 100 μm. Below 100 μm, the difference between the coupled potentials in the middle of the scribe calculated with and without the *WL* thickness dependence of the ORR kinetics steeply increases with the decrease in the *WL* thickness.

The addition of a 0.1 $\Omega \cdot m^2$ (10^3 $\Omega \cdot cm^2$) resistive layer over Mg changed the galvanic potential in the center of the scribe to -1.2 V vs. SCE. In contrast to the case where there was no resistance, the maximum difference between the potentials at the center of the scribe and the interface between the Mg and 2024 was

only 3.5 mV, indicating that the ohmic drop at the electrolyte is negligible compared to the ohmic drop caused by the resistive film over Mg. With a 10 $\Omega \cdot m^2$ (10^5 $\Omega \cdot cm^2$) film resistance, Mg is not able to polarize AA2024 below the pit repassivation potential, indicating that pitting events might occur. Such film resistances are easily obtained with standard organic coatings [23,175].

If the fast ORR kinetics in thin films is considered, then the resistance above which the center of the scribe is not polarized below the repassivation potential decreases with decreasing *WL* thickness. From 3000 to ca. 60 µm, the critical resistance decreases 16 Ohm·cm^2 per 1 µm decrease in *WL*. Below 60 µm, the decrease is steeper – ca. 40 Ohm·cm^2 per 1 µm decrease in *WL*. Below a *WL* of ca. 20 µm, the potential at the center of the scribe is not polarized below the repassivation potential, even in the absence of a resistance mediating the galvanic coupling between Mg and AA2024.

The role of resistive coatings in corrosion protection is important and has been discussed elsewhere [23]. In many cases, they are considered to function as barriers to the ingress of water and damaging species while also creating pathways of high ionic resistance, limiting the interactions of anodic and cathodic sites, thus suppressing corrosion. In the case of metal-rich primers, however, the resistive nature of the organic portion of a coating system restricts the ability of the pigment to protect the substrate galvanically but also limits self-corrosion of MgRP [23,199]. The results of **Figure 4.10** and **Figure 4.11** put this consideration into context; for the Mg-rich primers considered here, a coating resistivity of greater than 9 ohm-m^2 (9 x 10^4 ohm-cm^2) is sufficient to prevent polarization of the AA2024-T3 to below its repassivation potential, making it susceptible to localized corrosion. That said, by having the pH-induced potential change mechanism active, the self-dissolution of the Mg in the outer portion of the primer and its transport to the exposed AA2024-T3 is sufficient to repassivate the AA2024-T3 quite quickly. As the coating resistance degrades, the galvanic protection can become more important, particularly if the outer portions of the coating become exhausted in Mg and the precipitated $Mg(OH)_2$ is either removed or converted to a less protective form. This type of "defense in depth" and "condition-based activation" of different protection mechanisms may be responsible for the outstanding performance observed with Mg-rich primers during field exposures [25,179,187].

4.5.5. Model limitations

This section addresses some limitations of the model developed in this work. The use of the Laplace equation as the governing equation of the model can be justified considering that the electrolyte conductivity remains effectively constant throughout the simulation. Although there will be a local variation in the electrolyte composition because of Mg dissolution and accompanying cathodic reactions, the concentration of Mg^{2+} and OH^- are more than an order of magnitude lower than the constant concentration of NaCl (0.9 M), even in the case of the thinnest *WL* considered (20 µm), where the highest concentration

of Mg^{2+} is reached ($4 \cdot 10^{-4}$ M). Thus, the conductivity is not considerably affected, it can be considered to be constant throughout the volume, and the electrolyte can be considered to be an ohmic conductor – a requirement for the applicability of the Laplace equation. Although they do not contribute substantially to the current, the minor species and their transport are important in the phenomena of interest. Thus, considering their transport by diffusion is appropriate in the absence of forced convection. In essence, the model classifies species into two categories: (a) those that carry current (i.e., Cl^- and Na^+) and those that only react (i.e., Mg^{2+}, OH^-, Al^{3+}, H^+). Other species emanating from the dissolution of the AA2024-T3 (i.e., Mg^{2+}, Zn^{2+}, and Cu^{2+}) are not considered in this model, although all can have effects on aluminum dissolution and/or ORR [58,200].

The description of the dissolution rate of Mg in a MgRP is another simplification of the model. In this work, a constant dissolution rate based on the work of Lin *et al.* [191] was used. In their work, Lin *et al.* estimated the oxidation rate of Mg pigments by measuring the volume of H_2 generated from a MgRP coated AA2024 sample immersed in 0.18 M NaCl. Even though the volume of H_2 collected did not increase linearly with time, a constant dissolution flux was assumed to simplify the model. Additionally, the AA2024 electrode boundary conditions of the model described herein were defined using experimental data acquired in 0.9 M NaCl. The rate of Mg corrosion is dependent on NaCl concentration [201], so the rate of MgRP dissolution is expected to be higher in the conditions studied herein.

The explicit effect of $Mg(OH)_2$ film on the cathodic reactions was not taken into account. Instead, the inhibiting effect caused by the $Mg(OH)_2$ film was considered through a conceptual inhibition efficiency factor (**Figure 4.7**). The implementation of the deposition of $Mg(OH)_2$ can provide information about the thickness of the film formed, providing insights on the extent of barrier protection and cathodic inhibition that the film can offer. The model also does not consider the possible change in the electrochemical kinetics in AA2024 that may occur due to Cu-enrichment. The enrichment of Cu on the surface of AA2024 due to cathodic corrosion around Cu-bearing intermetallic particles causes an increase in the cathodic kinetics, which could further limit the *WL* range in which the pH-induced pit repassivation mechanism occurs [61,202–204].

Additionally, the effect of dissolved atmospheric carbon dioxide was not considered. Dissolved CO_2 undergoes equilibrium reactions in water, forming carbonic acid and acidifying the solution, which can hinder the pH-induced pit repassivation. On the other hand, in the presence of CO_2, $Mg(OH)_2$ reacts with dissolved CO_2 to form $MgCO_3$, which provides a more uniform and compact barrier layer than $Mg(OH)_2$, inhibiting anodic and cathodic reactions occurring at the substrate [186,205,206]. It is noted that the dissolution of $MgCO_3$ also acts to increase $[Mg^{2+}]$ and $[OH^-]$, albeit in a different manner than $Mg/MgO/Mg(OH)_2$. Nonetheless, there has been observed the absence of $MgCO_3$ corrosion product after the exposure of MgRP under salt spray test (ASTM B117), in contrast to outdoor field exposure, which was

attributed to the lower concentration and reduced solubility of CO_2 in the salt spray chamber [186]. Thus, the framework developed herein can be applied to predict and evaluate the performance of MgRP in such accelerated testing environments.

The work described assumes a constant chloride concentration (0.9 M), and thus, a constant relative humidity (RH) of ~97%. Differences in *WL* correspond to differences in the loading density of the salt. In practice, decreases in *WL* are more often due to decreases in RH during a diurnal cycle. Under these conditions, the concentration of NaCl increases. As the Cl^- concentration rises, the Al passive current density may also increase, and the solubility and diffusivity of oxygen decrease. Both effects would make pH-induced pit repassivation more tenable, and they could be the reason that scratches in MgRP-coated 2024-T3 are so well protected when exposed to marine atmospheres. Although the increased chloride during drying will decrease the pitting and repassivation potentials, the corrosion potential of 2024 for pH values above pH_{crit} is still lower than the pitting and pit repassivation potentials at higher chloride concentrations.

Future work will explore the impact of these simplifications and assumptions listed above. A sensitivity analysis of laboratory and field relevant parameters can be conducted to determine which aspects of the developed model need further development and which are currently satisfactory. Ample observations of the behavior of Mg-pigmented primer systems in laboratory and field exposure testing exist in the literature and can be used to inform this sensitivity analysis and compare against model results. For example, *WL* thickness was shown to act as an operational threshold for the efficacy of this mode of protection, whereas field-returned coupons have shown satisfactory protection for exposures in which the *WL* thickness is suspected to reach quite low values [25,179].

4.6. Conclusions

In this work, a framework for the modeling of chemical and electrochemical protection mechanisms provided by Mg-based primers was developed. Chemical-dependent electrochemical kinetics were used to describe AA2024 transient behavior in evolving electrolyte chemistry, and model results were compared to experimental data to validate the boundary conditions. The effect of water layer thickness, solubility product, ORR inhibition, and film resistance on the chemical and electrochemical protection mechanisms were investigated. In summary, the following important findings were reported:

- The pH required to induce pit repassivation of AA2024-T3 (pH_{crit}) increases with decreasing water layer thickness due to the increased diffusion-limited current density for ORR, requiring a higher passive current density, which occurs at higher pH.
- In the absence of other effects, there is a limiting water layer thickness (257 μm) below which the pH-induced pit repassivation is not expected to take place in 0.9 M NaCl for Mg-based dissolution

protection of AA2024 because the precipitation of $Mg(OH)_2$ impedes the solution from reaching the pH_{crit}.

- If Mg-products such as $Mg(OH)_2$ can mildly inhibit ORR, then the pH-induced potential control mechanism is feasible in thin water layers. This mechanism is also feasible if the complexation of Al^{3+} increases i_{pass} beyond that needed.
- The solubility product can be the basis for the selection of inhibitors that operate via the pH-induced potential control mechanism.
- Cathodic protection of bare AA2024 from Mg pigments is substantial but is mitigated by the presence of resistive effects of organic coatings. In fact, even coating resistances that are often considered indicative of failed coatings ($<10^5$ ohm-cm^2) are sufficient to prevent the pigment from polarizing scribe-exposed AA2024-T3 below its pit repassivation potential.
- The pH-induced pit repassivation may serve as an initial mode of protection in the case of a resistive film, with the galvanic protection mode becoming more important as the coating degrades and galvanic coupling is enabled.

The model developed in this work can be used to help the selection of inhibitors that can operate by the chemical and electrochemical protection mechanisms, and by the interaction between the two mechanisms.

4.7. Acknowledgments

Financial support from the SERDP program through the Office of Naval Research (C. Sanders) via Contract N00173-19-1-G011 as well as the DOD Corrosion Program Office through the US Air Force Academy via Contract FA7000-18-2-0006 is gratefully acknowledged.

4.8. Appendix A

Table 4.2. Diffusion coefficient and charge number of the species considered in the simulation.

Species	Diffusion coefficient ($\cdot 10^9$ m^2s^{-1})	Ref.
H^+	9.31	[109]
OH^-	5.27	[109]
Mg^{2+}	0.76	[193]
Al^{3+}	0.54	[109]
$AlOH^{2+}$	0.54	[109]
$Al(OH)_2^{1+}$	0.54	[109]
$Al(OH)_3$	0.54	[109]
$Al(OH)_4^-$	0.54	Assumed

The equilibrium of the Al^{3+} mononuclear species was described by the hydrolysis reactions as shown in the expressions below:

$$Al^{+3} + H_2O \rightleftharpoons Al(OH)^{2+} + H^+ \quad \text{[I]}$$

$$Al(OH)^{2+} + H_2O \rightleftharpoons Al(OH)_2^{1+} + H^+ \quad \text{[II]}$$

$$Al(OH)_2^{1+} + H_2O \rightleftharpoons Al(OH)_3 + H^+ \quad \text{[III]}$$

$$Al(OH)_3 + H_2O \rightleftharpoons Al(OH)_4^- + H^+ \quad \text{[IV]}$$

The reactions V-VII were defined kinetically as forward and backward reactions. The kinetic parameters were found in the literature [109], and the backward reaction rate constants were adapted by equaling the quotient between the forward and backward rate constants to the equilibrium constants reported in [207]. Unfortunately, it was not possible to find kinetic data for the reaction VIII; the reaction was defined as an equilibrium reaction, and the equilibrium constant was calculated from equilibrium constants found in [207] . The dissolution and hydrolysis of the other alloying elements present in AA2024 were not included in the model.

Table 4.3. Reaction parameters utilized in the simulation.

Homogeneous reactions	Reaction parameters		Ref.
I	$\boldsymbol{k = 3.7}\ (m^6 mol^{-2} s^{-1})$[a]	$\boldsymbol{k_{sp}} = 0.45\ (mol^3 m^{-9})$	[208]
II	$\boldsymbol{K_w} = 10^{-14}$		[109]
V	$k_{forward} = 4.2 \cdot 10^4 (s^{-1})$	$k_{backward} = 4.6 \cdot 10^6 (m^3 mol^{-1} s^{-1})$	[109]
VI	$k_{forward} = 4.2 \cdot 10^4 (s^{-1})$	$k_{backward} = 3.6 \cdot 10^6 (m^3 mol^{-1} s^{-1})$	[109]
VII	$k_{forward} = 5.6 \cdot 10^4 (s^{-1})$	$k_{backward} = 2.8 \cdot 10^6 (m^3 mol^{-1} s^{-1})$	[109]
VIII	$\mathbf{K} = 10^{-8}$		[207][b]

[a] Adjusted to a degree of supersaturation of approximately 2.

[b] Calculated from equilibrium constants reported in [207].

Table 4.4. Parameters used to define electrode reactions kinetics.

	$\boldsymbol{A}$ (m$\boldsymbol{V}$ $\boldsymbol{/decade}$)	$\boldsymbol{i_0}(\boldsymbol{A}/\boldsymbol{cm^2})$	$\boldsymbol{E_0}$ ($\boldsymbol{V_{SCE}}$)	$\boldsymbol{i_{lim}}$
Al active and passive dissolution [a]	300	0.1	-1.8	$i_{pass} = 10^{0.979 * pH - 14.741}$
Pitting	15	10^{-8}	-0.7	
ORR	-118	10^{-4}	E_r= 0.99 -0.059*pH	$i_{d,ORR} = 0.01125 * \delta^{-0.8473}$.
HER	-118	10^{-8}	E_r=-0.24 -0.059*pH	
Mg active dissolution	18.4	$1.8 \cdot 10^{-5}$	-1.6	

[a] A limiting current density was applied to Al active dissolution to describe the passive behavior.

Chapter 5. Applications of the chemistry-dependent boundary conditions in the study of corrosion and protection mechanisms of Al alloys

5.1. General introduction

The applicability of the reduced-order modeling approach used to develop models that simulate the interdependency between the electrochemical reactions and solution chemistry is demonstrated. The chapter is divided in three parts. In Part I, the chemistry-dependent boundary conditions are expanded to include the impact of Cl^- concentration. The impact of the Cl^- concentration on the pH-induced potential control mechanism is evaluated. The hypothesis that the increase in Cl^- concentration leads to a decrease in the critical pH above which there is a large shift in the corrosion potential of AA2024 is tested. In Part II, an experimental approach is developed to validate the modeling approach used to calculate the impact of an ohmic resistance on the galvanic coupling of Mg and AA2024. The conditions under which chemical-dependent boundary conditions are necessary to describe experimental observations are discussed. In Part III, the applicability of the pH-dependent anodic kinetics to model the phenomenon of cathodic polarization, in which Al dissolution occurs under cathodic polarization, is tested by the comparison between modeling results and data available in the literature. The use of FEM framework to understand the polarization behavior of pure Al obtained via voltammetry is briefly demonstrated.

Part I. The impact of Cl^- on the pH-induced pit repassivation mechanism

5.2. Introduction

In Chapter 4, a comprehensive framework was developed to model the cathodic and chemical protection mechanisms offered by Mg-based rich primers to Al alloys [87]. The pH-induced pit repassivation mechanism described by Santucci and Scully was modeled [24]. The mechanism is based on the decrease in the corrosion potential of AA2024-T351 to potentials below the repassivation potential, stifling pit nucleation and growth, by increasing the solution pH above a critical value. The sharp decrease in the corrosion potential at the critical pH (pH_{crit}) was explained by the mixed potential theory. The increase in the solution pH from neutral to more alkaline values causes an increase in the passive current density of Al [24]. When the passive current density surpasses the diffusion-limited ORR, then the corrosion potential sharply decreases to potentials at which HER is operative and can supply the necessary cathodic current to balance the surplus of the anodic current caused by the pH increase, so charge conservation is maintained. Essentially, the corrosion behavior of the Al alloy would change from localized to uniform corrosion, with the cost of an increased rate of uniform dissolution. Localized corrosion is more difficult to detect, and the high rates of dissolution in a small, undetectable area can lead to sudden, unpredicted catastrophic failures.

The model was able to capture the critical pH above which the corrosion potential of AA2024 sharply decreases. The framework was utilized to test the impact environmental variables on the viability of the mechanism under atmospheric environments. According to the calculations, the model predicted that the pH-induced pit repassivation mechanism would not be viable below a critical water layer thickness, due to the combination of the increased ORR kinetics in thin films, which leads to an increase in the pH_{crit}, and the solubility limit of the corrosion products, which buffers the solution to pH values below the pH_{crit}. Besides, the anodic current densities at such high pH would be prohibitively high. However, if the effect of these precipitation products on the inhibition of the cathodic kinetics is taken into account, the mechanism becomes more attenable under thin electrolytes.

The model was performed utilizing data obtained in 0.9 M NaCl solution, typically used in accelerated corrosion tests. In atmospheric environments, however, the electrolyte concentration varies significantly under wetting and drying events in a diurnal cycle. In such cases, Cl^- concentration can exhibit a wide range of values [209]. The concentration of Cl^- can impact both anodic and cathodic kinetics [85,210–215]. In neutral NaCl solutions, the oxygen reduction reaction (ORR) is the main cathodic reactions occurring on AA2024-T3. At the corrosion potential of AA2024-T3, ORR is under mixed charge- and diffusion-controlled kinetics. The diffusion-limited current density of ORR depends on the concentration of dissolved O_2 in the bulk electrolyte, on the diffusivity of O_2 in the solution, and on the thickness of the diffusion layer. For a planar electrode and assuming one-dimensional diffusion, the theoretical diffusion-limited ORR current density can be expressed as a function of O_2 diffusivity (D_{O_2}), bulk concentration ($c_{O_2,bulk}$), and thickness of the diffusional boundary layer (δ) by Equation 1, assuming that the reaction is fast, such that O_2 is readily consumed at the surface and its concentration zero:

$$i_{lim} = \frac{nFD_{O_2}c_{O_2,bulk}}{\delta} \quad (1)$$

where n is the number of electrons transferred during the electrochemical reaction and F is the Faraday's constant.

The concentration of dissolved O_2 and its diffusivity decreases as the concentration of NaCl increases [85]. Thus, the increase in the concentration of NaCl decreases the rate of the diffusion-limited ORR. If the charge-transfer controlled ORR kinetics on the Al alloy is not affected by the Cl^- concentration, then it can be hypothesized that the ORR kinetics will be slower in increasing Cl^- concentration at open circuit potential.

The influence of Cl^- on the localized corrosion of Al alloys has been extensively studied, and reviews are available [211,216]. Aggressive anions, such as Cl^-, adsorb on and interact with the oxide film, causing the breakdown of the passive film [216]. With the increase in the Cl^- concentration, the passive alloys are more susceptible to pitting corrosion. Because in aerated, neutral electrolytes, the corrosion

potential of Al alloys is usually at or near the pitting potential, previous work focused on evaluating the impact of Cl^- on the pitting and repassivation potentials. The effect of Cl^- on the anodic dissolution rate of Al is less reported. In acidic or neutral environments, it has been reported that Cl^- increases the anodic dissolution of Al [210], by either the participation of Cl^- ions in the metal dissolution reaction, or by the incorporation of Cl- into the oxide film and consequent generation of additional charge carriers. In alkaline media, however, Pyun et al. reported that Cl^- reduced the anodic dissolution rate of pure aluminum in the passive region range, which they attributed to the precipitation of $Al(OH)_2Cl$ and $Al(OH)Cl_2$ compounds that provided an additional mild barrier protection [217].

In view of the pH-induced potential control mechanism discussed in Chapter 4, the influence of NaCl concentration on both cathodic and anodic will cause a shift in the critical pH, above which the corrosion potential of AA2024 sharply decreases. From the cathodic kinetics perspective, the decrease in the diffusion-limited current density of ORR in increasing NaCl concentrations should decrease the pH_{crit}, if the relationship between the passive current density and pH remains constant in the various NaCl solutions. From the anodic kinetics perspective, if the passive current density increases in increasing Cl^- concentration, then the pH_{crit} should also decrease. However, the increase in the passive current density with Cl^- concentration was reported in acidic and neutral media, whereas in alkaline media, the opposite relationship was found. Thus, from the anodic kinetics perspective, it is unclear whether the increase in Cl^- would decrease or increase the pH_{crit}.

The objective of Part I of this Chapter is to investigate the impact of Cl^- on the pH-induced potential control mechanism and extend the model developed in Part I to various NaCl concentrations. Anodic and cathodic polarization scans were performed in unbuffered solutions of varying NaCl concentrations (0.01, 0.1, 0.9, 2, and 5 M) in a pH range of 6 to 11.5. The relationship between the passive current density and pH for the various NaCl concentrations was determined. The anodic and cathodic kinetic parameters obtained were applied to the framework described in Chapter 4, which was used to model the corrosion potential behavior of AA2024 as a function of pH under the varying NaCl concentrations.

5.3. Methodology

5.3.1. Potentiodynamic polarization scans in deaerated solutions

The potentiodynamic scans were performed in deaerated solutions to better observe the passive region of the Al alloy, as O_2 shifts the corrosion potential to more positive values, at which the passive behavior is not observed. The deaerated anodic potentiodynamic scans in varying pH were performed in NaCl solutions of different concentrations (0.01, 0.1, 0.9, 2, and 5 M). The pH was adjusted using NaOH prior to performing the voltammetry. The solutions were prepared using 18.2 MΩ-cm deionized water and

reagent-grade NaCl and NaOH. A deaeration setup was assembled to allow for the solution and electrochemical cell deaeration prior to performing the scans. N_2 flowed into the solution container and the cell for 30 min. After 30 min, the cell was filled by the deaerated solution using N_2 pressure. A conventional three-electrode cell was used with a Ag/AgCl reference electrode and a Pt counter electrode.

The potentiodynamic scans were performed at a scan rate of 1 mV/s after 5 min at the open circuit potential. The ohmic drop was compensated while performing the scan by using the impedance in high frequencies measured prior the polarization. The scan was reversed after the anodic current density reached 0.785 mA (1 mA/cm^2) and terminated 20 mV below the initial measured open circuit potential. The AA2024 coupons were ground to a 4000 grit paper, cleaned with deionized water and dried using pressurized air prior performing the technique.

5.3.2. Open-circuit potential (OCP) measurements at varying pH

The AA2024 OCP was measured as a function of solution pH for NaCl solutions of varying concentrations (0.01, 0.1, 0.9, 2, 5 M). The procedure described by Santucci was applied [24]. The AA2024 was exposed to the solutions in a horizontal electrochemical cell. The open-circuit potential was measured using a Ag/AgCl reference electrode. The pH of the solution was measured using a pH electrode. While performing the OCP measurements, the pH of the solution was varied by adding aliquots of NaOH diluted in NaCl solutions of concentrations equivalent to those used in the test. The OCP measurements and the measured pH were recorded.

5.3.3. Description of the finite element models

The framework described in Chapter 3 and in [87] was used to simulate the corrosion behavior of AA2024 in an evolving electrolyte solution resulting from the self-corrosion of Mg and the Al alloy. A few details are described below.

5.3.3.1. Model geometry

Figure 5.1 (a) shows a schematic illustration of the model geometry, along with a brief description of the boundary conditions and the homogeneous reactions occurring in the electrolyte. In **Figure 5.1** (b), the boundaries and their respect boundary conditions are shown.

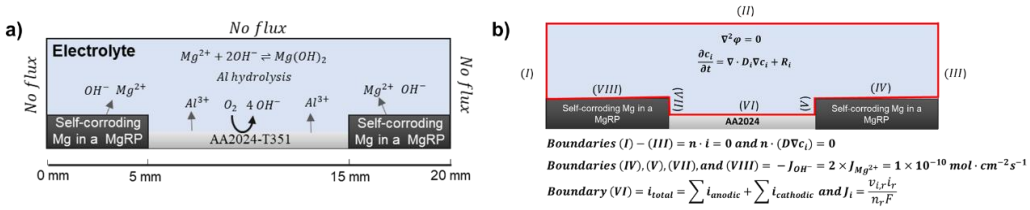

Figure 5.1. (a) Schematic illustration of the model simulating the electrolyte chemistry considering the electrochemical reactions at the electrode and chemical reactions in the bulk of the electrolyte considered in the model; (b) Governing equations and boundary conditions applied to the model that simulates the Mg-rich primer-coated AA2024 damaged with a scribe.

5.3.3.2. Governing equations

As described in Chapter 4, the Laplace equation was used to solve for the charge conservation in the electrolyte, assuming a constant and uniform electrolyte conductivity. The transport of the minor, electrochemically active species was modeled using Fick's second law, with the addition of the reaction terms. As discussed in Chapter 2, for cases in which the supporting electrolyte concentration is orders of magnitude higher than the minor species, the minor species contribution to the migration fluxes is negligible and they are mainly transported by diffusion. In these cases, the error associated with the simplified Laplace approach supplemented by the transport of minor species is negligible.

5.3.3.3. Boundary conditions

As described in Chapter 4, the corrosion behavior of AA2024 was modeled by defining separate anodic and cathodic half-cell reactions kinetics representative of pitting and passive kinetics, ORR and HER. Mixed potential theory is implied in the model, as it solves for charge conservation using the Laplace equation. Thus, if various half-cell reactions are used to define the electrochemical reactions occurring at a boundary, the model will calculate the condition in which the sum of the currents is zero: the conditions at the corrosion potential. If there are no other electrodes and the electrolyte composition is homogeneous, there will not be a distribution of potential and current density, and the model will calculate the corrosion potential and corrosion current density of a uniformly corroding metal. The electrochemical kinetic parameters were obtained from the literature and abstracted from the potentiodynamic polarization scans obtained in the different NaCl solutions.

Anodic kinetics

Figure 5.2 (a) shows examples of the PDS performed on AA2024 in the deaerated solutions of varying pH. The different kinetic behaviors – the passive dissolution and the fast dissolution above the

breakdown/pitting potential (here referred to as "pitting" kinetics) were implemented in the model by defining two separate anodic electrochemical reactions, as schematized in **Figure 5.2** (a).

The pitting kinetics was defined with using Equation 2, where E_0 was dependent on the Cl^- concentration according to Equation 3, obtained by linear regression of the averaged E_{pit} observed in each of the NaCl solutions, shown in the Results section:

$$i = i_0 10^{\frac{E-E_0}{B}} \tag{2}$$

where i_0 is a pseudo-exchange current density, E is the potential at the electrode, and B is a pseudo-Tafel slope.

$$E_{pit} = -0.5833 - 0.107\left(\frac{[Cl^-]}{c_{ref}}\right), \qquad r^2 = 0.99 \tag{3}$$

The active/passive dissolution was modeled using a Butler-Volmer equation (Equation 4) limited by an imposed limiting current density. The resulting boundary condition is described by Equation 5. The reversible potential was defined according to the reversible potential of Al/Al^{3+} (E_0 = -1.859 V vs. Ag/AgCl) obtained from Pourbaix [1].

$$i_{BV} = i_0\left(e^{\frac{\alpha_a F(E-E_0)}{RT}} - e^{\frac{-\alpha_c F(E-E_0)}{RT}}\right) \tag{4}$$

where α_a is the anodic charge transfer coefficient, F is the Faraday's constant, R is the universal gas constant, T is temperature, and α_c is the cathodic charge transifer coefficient. α_a and α_c were defined arbitrarily as 0.5.

$$i = \frac{i}{1 + \left|\frac{i}{i_{BV}}\right|} \tag{5}$$

To model the passive dissolution, a limiting current density was imposed. The limiting current density was expressed as a function of pH, according to the expressions shown in **Table 5.1.** These expressions were obtained from measurements in alkaline media, and they were assumed to be valid in the pH range of 9 to 14.

Cathodic kinetics

ORR and HER kinetics were defined utilizing Tafel expressions, and their Tafel slopes were assumed as -118 mV/decade. The reversible potential for ORR and HER were defined using the Nernst equation. The exchange current densities of ORR and HER in Al were assumed equal and they were obtained from Trasatti [218]. The diffusion-limited ORR kinetics was simplified by imposing a limiting current density with empirically determined values extracted at -0.95 V vs. Ag/AgCl from the cathodic

voltammetry as schematized in **Figure 5.2** (b). The resulting boundary condition is described by Equation 5.

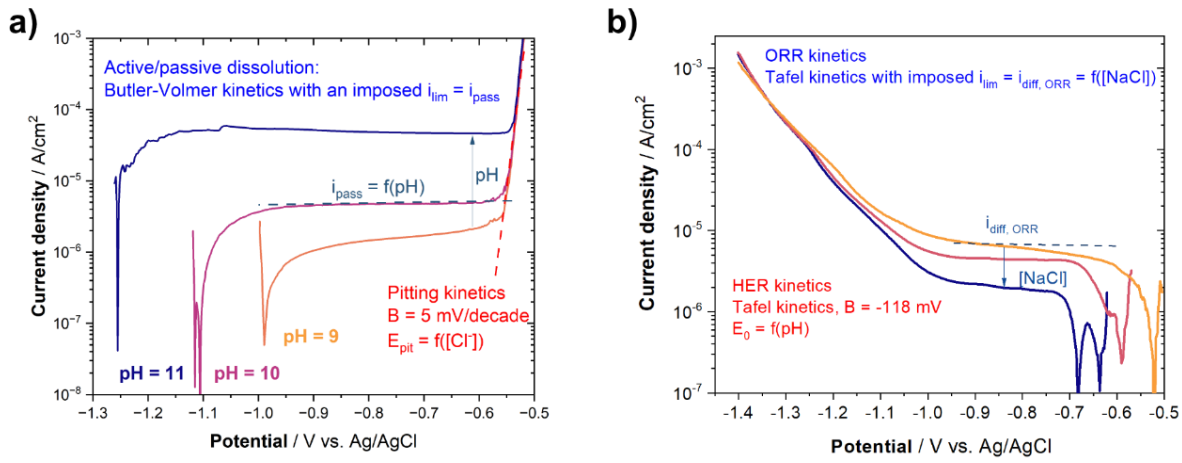

Figure 5.2. Schematic representation of the method for determining the boundary conditions, which consisted of defining anodic and cathodic half-cell reactions whose kinetic parameters were defined using theoretical and measured values from the literature [1,218], and extracted from the potentiodynamic polarization scans. In (a), anodic potentiodynamic scans and the two different anodic kinetics are shown. In (b), cathodic potentiodynamic scans and the two different cathodic kinetics included in the model are shown.

It is acknowledged that the electrochemical behavior of a heterogeneous alloy is complex, as it depends on the electrochemical kinetics of all the phases that constitute the alloy. In Al-Cu-Mg alloys, such as AA2024, for example, the cathodic reactions take place mostly on Cu-rich phases. Thus, cathodic kinetics will depend on the Cu coverage, which is known to increase due to selective dissolution of Al and Mg, and Cu replating [61]. As the length scales of the model are much larger than the length scales of the IMP, the framework models the average kinetics of the alloy. Indeed, the potentiodynamic polarizations were performed in the "bulk" alloy, and the observed kinetics is a result of the contribution of each phase averaged by their relative area ratios. The complications arising from the changes in the surface composition of AA2024 in alkaline media will be discussed in the Chapter.

5.3.3.4. Spatiotemporal distribution of species in the electrolyte

The spatiotemporal distributions of minor species $(Al^{3+}, Al(OH)^{2+}, Al(OH)_2^+, Al(OH)_3, Al(OH)_4^-, Mg^{2+}, OH^-, H^+)$ were calculated. The flux of $Al^{3+}$and OH^- was calculated by Faraday's law, using the local cathodic and anodic current densities at the Al

boundary. The release of Mg^{2+} and OH^- resulting from either the self-corrosion of Mg, or from the dissolution of MgO pigments was modeled by a constant flux, as described in Chapter 4. The precipitation of $Mg(OH)_2$ was modeled using a sink term, also described in Chapter 4. The equilibrium between the Al ionic species was modeled using reaction rate constants found in the literature. The details can be found in Chapter 4 and in Appendix A.

5.4. Results

5.4.1. Impact of Cl^- and pH on the anodic behavior of AA2024

Figure 5.3 shows the single-cycle potentiodynamic scans of AA2024 performed in deaerated solutions of varying NaCl concentrations and pH of ca. 6 (**Figure 5.3** (a)), 9 (**Figure 5.3** (b)), 9.5 (**Figure 5.3** (c)), 10 (**Figure 5.3** (d)), and 11 (**Figure 5.3** (e)), and 11.5 (**Figure 5.3** (f)) . The single-cycle potentiodynamic scans were performed to obtain the relationship between the passive current density and pH for varying NaCl concentrations.

Before commenting on the PDS results, the characteristics of the current density/potential relationship observed in the single-cycle potentiodynamic scan are briefly described. The single-cycle voltammetry performed in deaerated NaCl solutions shows the different anodic kinetic behavior of AA2024. In the forward scan, it is possible to see the passive region, where the increase in potential does not lead to a significant increase in the current. In alkaline solutions, the current is practically constant and independent of potential below the pitting potential. The passive region is delimited by a sharp transition in the current density/potential behavior when the potential becomes more positive than the pitting potential (E_{pit}), above which there is a rapid increase in the current density. Upon scan reversal, there is a hysteresis behavior in the current/potential curve; in all measurements performed, the current density was higher in the reverse scan compared to the forward scan. Further decreasing the potential led to a sharp decrease in the current density. The potential at which the forward and the reverse scans intersect is generally defined as the repassivation potential (E_{rp}), below which pits repassivate and localized corrosion is stifled [9].

5.4.2. Impact of Cl^- concentration on the passive dissolution of AA2024

In the deaerated scans, the corrosion potential of AA2024 was lower than the pitting potential, so it is possible to observe the anodic dissolution in the passive region. In near-neutral solutions (**Figure 5.3** (a)), the current densities in potentials lower than the breakdown potential are lower in comparison to the more alkaline pH. In the 0.01 M curve, the corrosion potential is very near or at the breakdown potential, so it is not possible to see the passive region. The discrepant behavior could be due to an inefficient deaeration prior to performing the test. The current densities measured in the potentials lower than the breakdown potential increase with the increase in pH. For pH > 9, the potential window in which the passive

behavior is observed is higher, due to the lower corrosion potentials and the current density does not vary with potential.

The relationship between Cl- concentration and the passive current density was not clear. In the near neutral solution, the current densities in the passive region seem to increase in the with the increase in the NaCl concentration for 0.1, 2, and 5 M. However, the current densities are higher in the 0.9 M solution. In pH 9, the passive current density in 0.1 M was lower, but increasing the NaCl concentration from 0.9 to 5 M did not significantly impact its value. In pH 9.5, the current density in the 0.01 and 0.1 M are lower than in 2 M. In pH 10, the passive current densities measured in 0.01 M was clearly lower than those measured in 5 M NaCl, but between 0.1 and 2 M, the NaCl concentration did not impact the passive dissolution rate. In pH 11, the passive current densities were similar in value for all the NaCl solutions, but the rate in 0.9 M NaCl was slightly higher than in the other solutions. In pH = 11.5, the passive current density increased from 0.01 M to 2 M. However, in 5 M, an anodic current peak is present, followed by a decrease in the current density with the potential increase, before the breakdown occurs. The anodic current density peak was only clearly observed in the 5 M NaCl solution; in the 2 M NaCl solution, the current density also slightly decreases with the increase in the potential.

Figure 5.4 (a) shows the passive current density as a function of pH extracted from the PDS at -700 mV vs. Ag/AgCl for the solutions of pH > 9. The values shown in the near neutral pH region were obtained via Tafel extrapolation. The relationship between the passive current density and pH is steeper at pH > 9, above which there is approximately a linear relationship between the log of the current density and pH. Below pH = 9, the passive current density does not change significantly with pH. Similar results have been reported [2]. The lower passive current densities in pH < 9, and the lower dependence with pH are in agreement with the range of stability of Al_2O_3 [[1,2].

Figure 5.4 (b) shows the passive current densities data points as a function of pH for pH > 9, along with the linear regression fits of the log of the passive current density as a function of pH **Table 5.1** shows the expressions resulting from the linear regressions and their respective r^2. These expressions were used as part of the boundary conditions of the AA2024, except for the 0.9 M NaCl case, in which the expression obtained by Santucci was used [24].

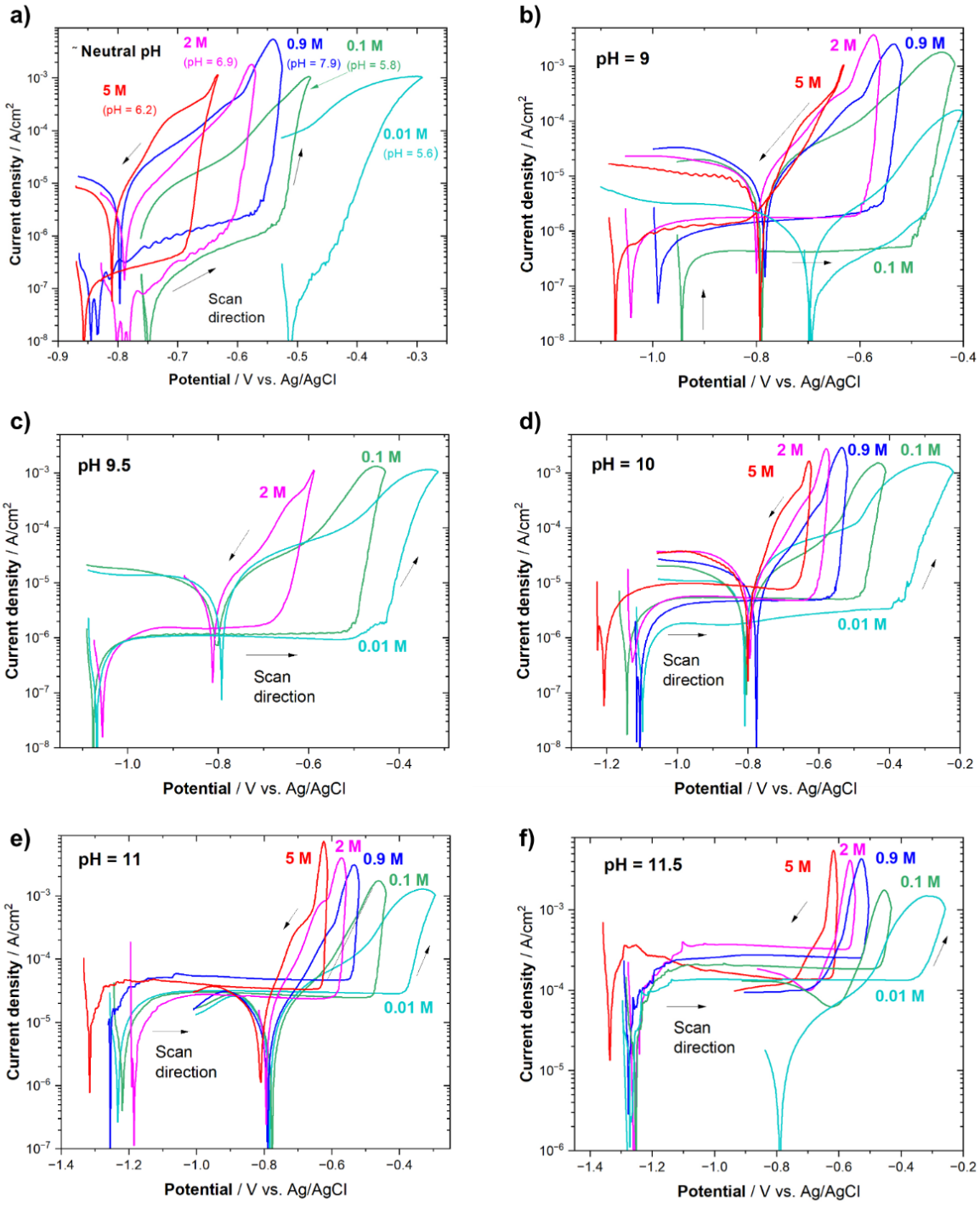

Figure 5.3. Potentiodynamic scans of AA2024 in NaCl solutions of concentrations varying from 0.01 to 5 M in various pH: (a) 6, (b) 9, (c) 9.5, (d) 10, (e) 11, (d) 12.5.

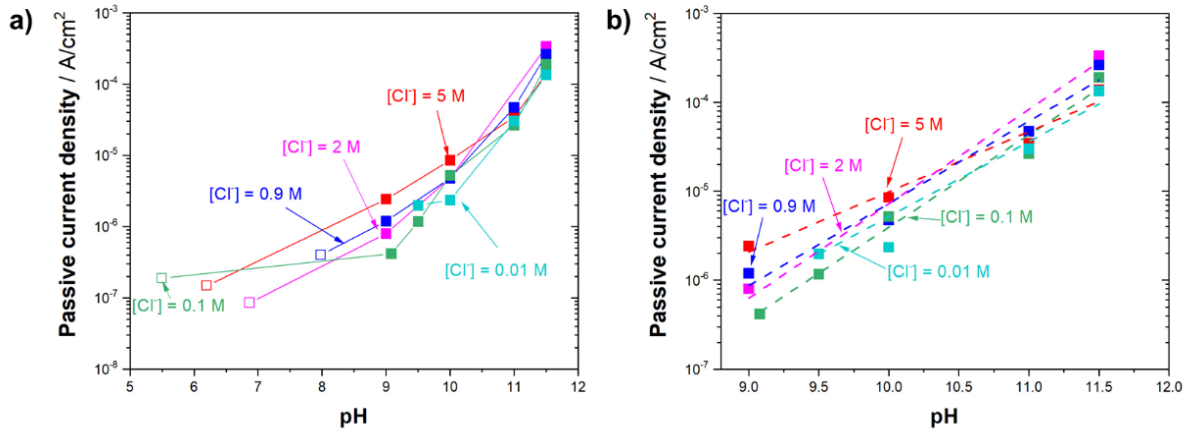

Figure 5.4. (a) Experimental values of passive current density as a function of pH; (b) Experimental values of the passive current density and the line describing the linear relationship between the log of the passive current density and pH obtained by linear regression for pH ≥ 9.

Table 5.1. Expressions of the passive current density as a function of pH for the different NaCl concentrations obtained via linear regression.

[NaCl] / M	Passive current density = f(pH)	r^2
0.01	$Log(i_{pass}) = -14.96 + 0.95xpH$	0.96
0.1	$Log(i_{pass}) = -15.78 + 1.04xpH$	0.98
0.9	$Log(i_{pass}) = -14.38 + 0.92xpH$	0.97
2	$Log(i_{pass}) = -15.77 + 1.06xpH$	0.99
5	$Log(i_{pass}) = -11.77 + 0.68xpH$	0.97

5.4.3. Impact of Cl^- and pH on the pitting and repassivation potentials

There is a clear difference between the E_{pit} obtained in the different NaCl solutions of varying concentrations. **Figure 5.5** (a) shows the E_{pit} as a function of NaCl concentration obtained at the different pH. The E_{pit} decreases linearly with the log of Cl^- concentration with an average slope of -106 mV, similar to those reported for pure Al and Al alloys [2,203,213]. The decrease in the pitting potential with Cl^- concentration indicates the well-known increased pitting corrosion susceptibility in higher Cl- concentrations. The dependence of E_{pit} with pH is much weaker, but E_{pit} seems to slightly increase with increasing pH. Nevertheless, the dependence of pH was neglected in the model, and the expression obtained by linear regression of the averaged values of E_{pit} in each NaCl solution was used as part of the boundary conditions in the model. The resulting linear fit is shown in **Figure 5.5** (a) by the black dotted line and Equation 3, shown in the Section 5.2.3, displays the resulting expression.

Figure 5.5 (b) shows the repassivation potential as a function of NaCl concentration. Although the parameter was not used in the model, the relationship between E_{rp} and Cl^- and pH are shown. The E_{rp} was dependent on the solution pH, and the dependence was stronger in solutions of lower NaCl concentration. The E_{rp} was higher in higher pH, although the difference was more significant in the solutions of pH 11 and 11.5. In these more alkaline solutions, the Cl- concentration also had a higher impact in the E_{rp}. In the pH = 11.5 solution, the repassivation potential decreased with increasing Cl^- concentration in the entire range of Cl^- concentrations tested. In the pH = 11 solution, the repassivation potential seemed to only depend on pH for Cl^-concentrations higher than 0.9 M. it decreased with increasing Cl^- concentration. For the solutions of pH < 11, the concentration of Cl^- did not seem to significantly affect the E_{rp}.

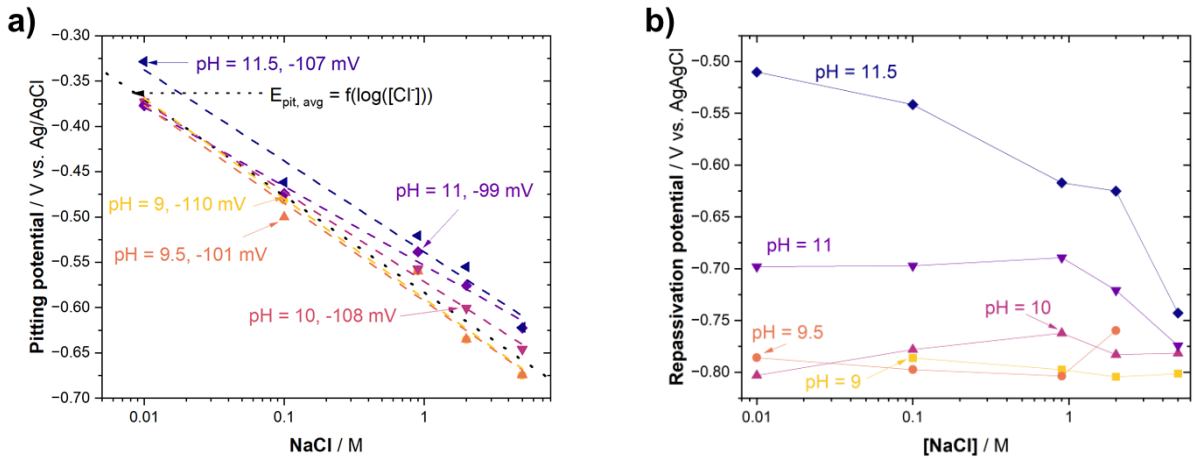

Figure 5.5. Pitting (a) and repassivation (b) potentials as a function of NaCl concentration obtained in the solutions of varying pH values.

5.4.4. Cathodic behavior of AA2024 in varying NaCl concentrations

Figure 5.6 (a) shows the cathodic potentiodynamic scans performed on AA2024 in aerated NaCl solutions of various concentrations. The pH of the solutions was not adjusted, so the solutions are slightly acidic (pH ≈ 5.5) at the beginning of the scan. The corrosion potential of AA2024 in the aerated solutions decrease as the NaCl concentration increases. In the PDS performed in the NaCl ranging from 0.01 to 2 M, it is possible to see a region in which the cathodic current density is almost invariant with the potential (between ca. 100 mV below the corrosion potential to ca. -1 V vs. Ag/AgCl), which can be attributed to the diffusion-limited ORR kinetics. Because the corrosion potential of AA2024 in 5 M is lower, the range of potential in which this behavior is observed is narrower.

There was not a significant difference between the cathodic current densities obtained in 0.01 and 0.1 M. However, increasing the NaCl concentration from 0.1 M to 5 M, it is possible to see a decrease in

the current densities in the potentials higher than -1.2 V vs Ag/AgCl. For potentials lower than -1.2 V vs. Ag/AgCl, there was not much difference between the current densities measured in the different solutions, with the exception of the current densities measured in the 5 M NaCl solution. In the 5 M NaCl solution, the current density is lower than in the other NaCl solutions for the entire range of the cathodic potentials. The current densities measured in 0.01 M also show a slight deviation from the others at high cathodic overpotentials.

Figure 5.6 (b) shows the approximate ORR limiting current densities, extracted at -0.95 V vs. Ag/AgCl. The limiting current densities measured in the 0.01 and 0.1 M NaCl solution are almost identical. For [NaCl] > 0.1 M, a decrease in limiting current density was observed. The cathodic current density at -0.95 V vs. Ag/AgCl is 6 times lower in 5 M NaCl in comparison to 0.01 M.

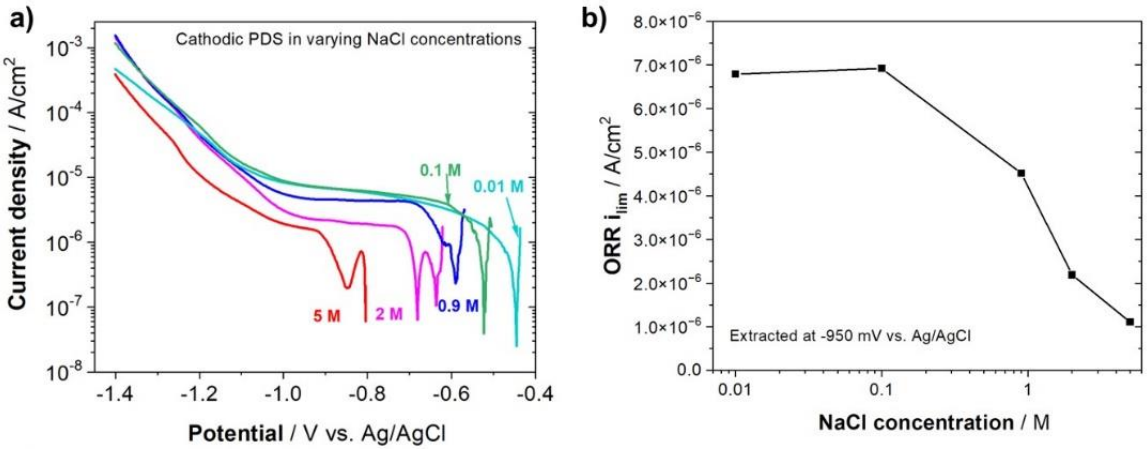

Figure 5.6. (a) Cathodic PDS performed on AA2024 in neutral, naturally aerated NaCl solutions of concentrations of 0.01, 0.1, 0.9, 2, and 5 M; (b) current density extracted at -950 mV vs. Ag/AgCl as a function of NaCl.

5.4.5. Modeling the corrosion potential of AA2024 as a function of pH

The corrosion potential of AA2024 was modeled for each NaCl solution for pH varying from 7 to 11.5. The difference between the boundary conditions of each NaCl concentration was in the relationship between passive current density and pH, shown in **Table 5.1**, and the limiting current density of ORR. The model was performed in steady-state, and the pH was a controlled variable that was applied to the entire electrolyte.

Figure 5.7 (a) shows corrosion potential as a function of pH predicted by the model for the various NaCl solutions. At neutral and mild alkaline solutions, the corrosion potential of AA2024 is constant, and it increases with decreasing NaCl concentration, as observed in the experimental cathodic PDS shown in

Figure 5.6 (a). The corrosion potential decreased sharply when the pH surpassed a critical value, the pH_{crit}, as discussed in Chapter 4 and in [24,219]. For pH > pH_{crit}, the corrosion potential decreased steadily with the increase in pH, and the differences between the corrosion potentials calculated for the varying NaCl concentrations decreased.

The predicted pH_{crit} decreased with increasing Cl^- concentration. The relationship between pH_{crit} and the NaCl concentration is shown in **Figure 5.7**(b).

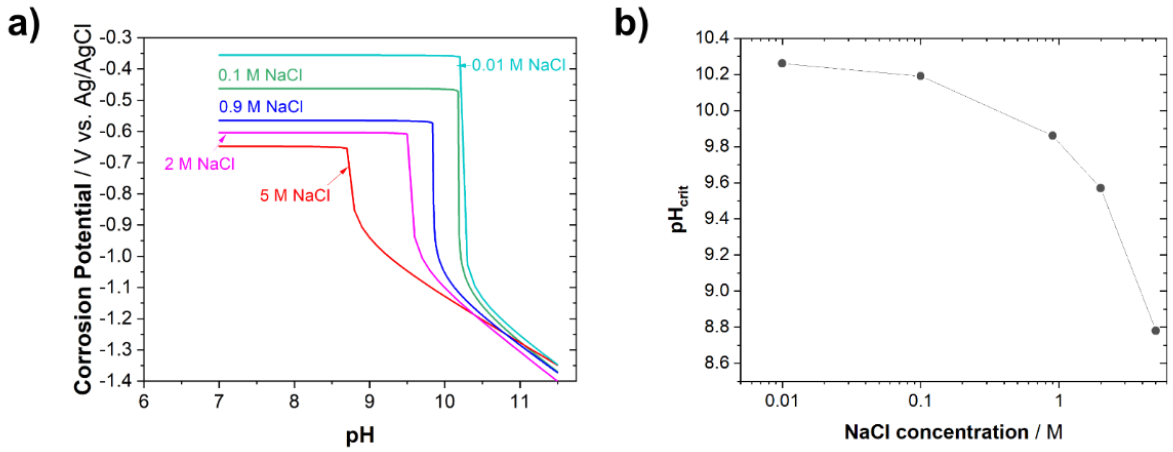

Figure 5.7. (a) AA2024 corrosion potential as a function of pH predicted by the model for the different NaCl concentrations; (b) pH_{crit} for the pH-induced pit repassivation as a function of NaCl concentration.

5.4.6. Experimental determination of pH_{crit} by OCP measurements with incremental additions of NaOH

Figure 5.8 shows the corrosion potential (E_{corr}) measurements obtained in the various NaCl solutions obtained as a function of pH, which was increased during the measurements by additions of NaOH diluted in NaCl solutions. In all solutions, the E_{corr} decreased sharply when the pH surpasses a critical pH. Further increasing the pH, the E_{corr} decreases steadily with increasing pH. In pH < pH_{crit}, the E_{corr} of AA2024 is nearly constant for the NaCl concentrations below 5 M. In 5 M, the E_{corr} fluctuates in almost 200 mV in near neutral solutions before it sharply decreases at pH > pH_{crit}. As a note, the E_{corr} measurements obtained by the additions of NaOH were performed up to a pH of 9.3 for the 5 M NaCl case. For higher pH, the E_{corr} shown were obtained prior to performing the anodic scans, and they are indicated with asterisks. Because these were obtained in deaerated solutions, they could be lower than those in aerated solutions. However, because in these higher pH the corrosion potential is low and the main cathodic reaction is HER, a small difference in the E_{corr} is expected.

The pH at which the E_{corr} shift occurs decreases as the concentration of NaCl decreases. The pH_{crit} found for each NaCl is approximately 8.65, 9.40, 9.86, 10.00, and 10.20 for the NaCl solutions of 5, 2, 0.9, 0.1, and 0.01 M, respectively.

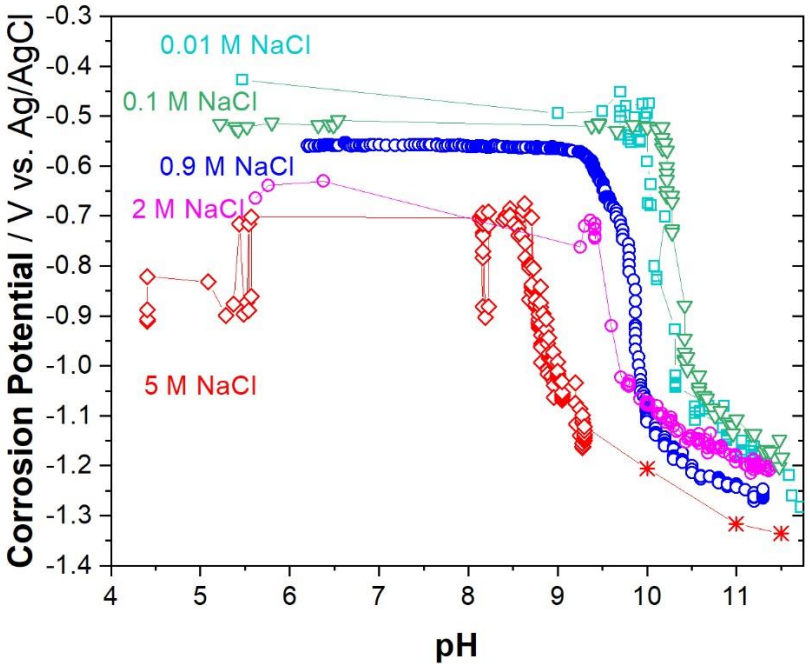

Figure 5.8. Open circuit potential measurements of AA2024 in the various NaCl solutions as a function pH obtained by incremental additions of NaOH.

5.4.7. Comparison between modeled and experimental corrosion potentials

Figure 5.9 (a)-(e) displays the modeled and experimentally-determined corrosion potential as a function of pH for the different NaCl concentrations. The model captures well the overall behavior: below the pH_{crit}, the AA2024 corrosion potential does not depend on pH, and it remains near the pitting potential. Above the pH_{crit}, the corrosion potential decreases steadily with increasing pH. However, there are discrepancies between the modeled and measured corrosion potentials. In near neutral solutions, the model overestimated the corrosion potential for most of the NaCl concentrations. In the more alkaline solutions, the model underestimated the corrosion potential obtained in the [NaCl] ≤ 2 M; for [NaCl] = 5 M, the model overestimated the corrosion potential for 9≤ pH < 11.5.

The pH at which the sharp transition in the corrosion potential, however, agrees with the experimental measurements, as demonstrated in **Figure 5.9** (f), which shows the modeled pH_{crit} as a function of the pH_{crit} obtained experimentally. The model overestimated the pH_{crit} for [NaCl] = 0.01, 0.1, and 2 M.

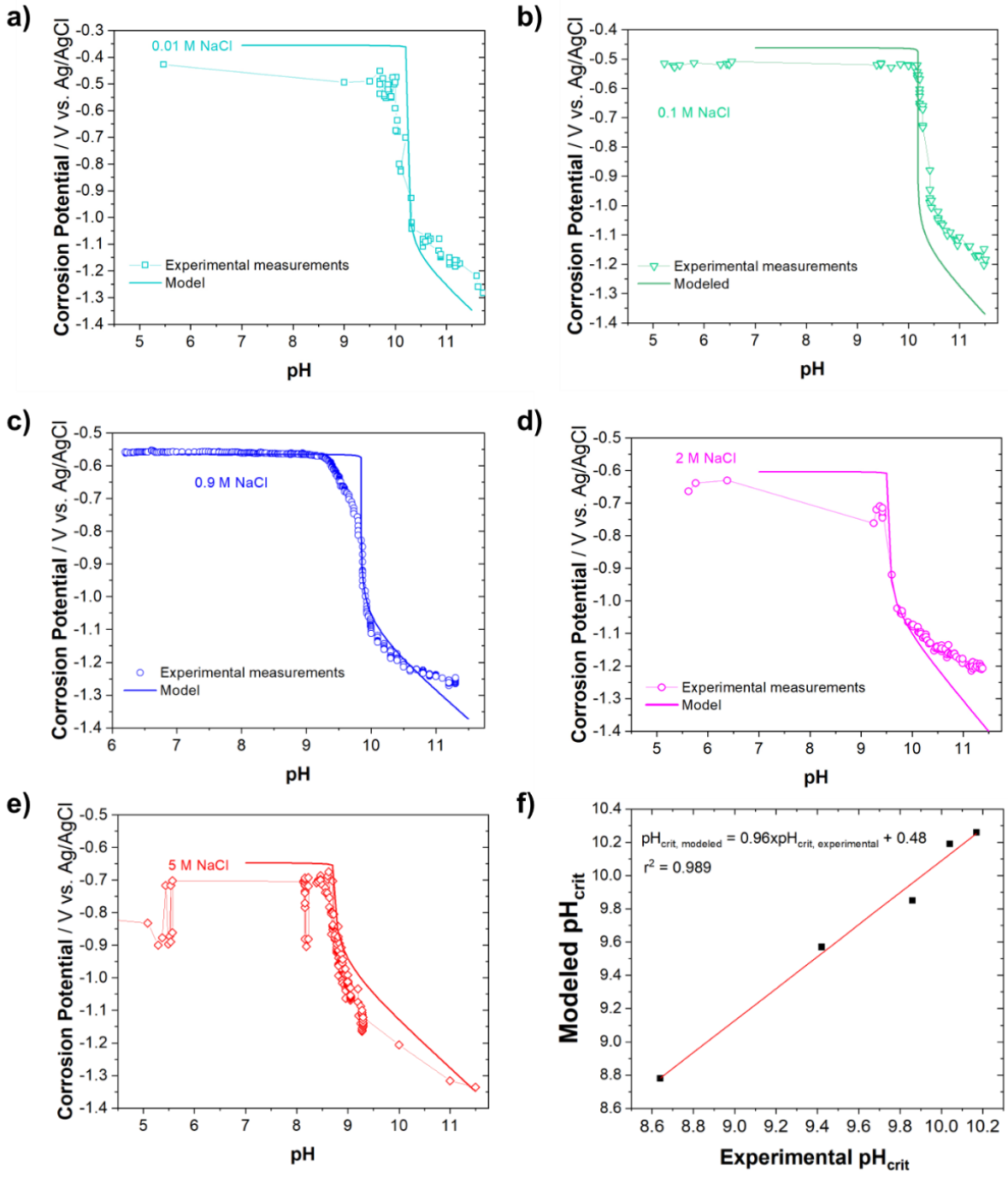

Figure 5.9. Modeled and experimental AA2024 corrosion potential as a function of pH for the NaCl concentrations of 0.01 M (a), 0.1 M (b), 0.9 M (c), 2 M (d), and 5 M (e). In (f), the modeled and experimental pH_{crit} are compared.

5.4.8. Modeling the transient behavior of the electrolyte chemistry and electrochemical behavior of AA2024 in the presence of a Mg-rich primer in the case of a high resistance between the Mg pigment and AA2024

In the former section, the model was performed for a situation in which the pH was an independent, controlled variable that was applied in the entire electrolyte. The objective of the calculations was to verify the model's capability of capturing the dependence of the AA2024 corrosion potential on pH. In the following sections, the species production from the cathodic and anodic reactions, and the homogeneous reactions occurring in the electrolyte are taken into account. The mass conservation equations are solved considering the transport of the minor species by diffusion and the sink/production terms due to the homogeneous reactions. First, the model is used to predict the pH at the surface of the Al alloy as a result of the electrochemical reactions occurring at the open circuit potential, and the equilibrium reactions between the Al species. Then, the flux of Mg^{2+} and OH^-, arising from the self-corrosion of metallic Mg pigments, or by the dissolution of MgO pigments, is included. First, the transients of solution pH and AA2024 corrosion potential is calculated for a case in which the Al species hydrolysis are not taken into account, and the change in the electrolyte chemistry is only due to the dissolution of the Mg pigments. Then, the impact of the Al hydrolysis on the solution chemistry and subsequent impact on the corrosion potential is assessed.

The goal of the model was to calculate how long it would take for the corrosion potential of AA2024 to decrease to potentials below the repassivation potential, so that localized corrosion events are stifled, for a scribe of 10 mm under a 3000 μm thick electrolyte film. The influence of the different anodic and cathodic kinetics in the varying Cl^- concentration on the pH and corrosion potential transients was assessed.

5.4.8.1. Prediction of solution pH as a result of Al uniform corrosion

Figure 5.10 (a) and (b) show the pH transient adjacent to the electrode/electrolyte interface as a result of the electrochemical reactions occurring on the Al surface at open circuit potential for an initial pH = 7. The calculated pH is a result of the production of Al^{3+} species by the anodic reactions and subsequent hydrolysis, the production of OH^- by the cathodic reactions, and the equilibrium between the H^+ and OH^- species. In **Figure 5.10** (a), the pH transients calculated for the different [NaCl] are shown. In less than 1 h, the pH reaches a steady-state, decreasing from the initial value of 7 to ca. 6.4, in all cases. There are differences among the pH values in the first few seconds. For the solutions obtained for [NaCl] = 0.01, 0.1, and 0.9 M, the pH initially decreases to pH lower than the pH reached at steady-state, but rapidly rise to the final pH.

In **Figure 5.10** (b), the initial solution pH is varied for the [NaCl] = 0.1 M case. The pH transient for the cases in which the initial solution pH is 4, 7, and 10 is shown. Within 1 h, the pH adjacent to the

electrode/electrolyte interface either decreases or increases to neutral pH, and after 12 h it tends to the same steady-state value of ca. 6.4.

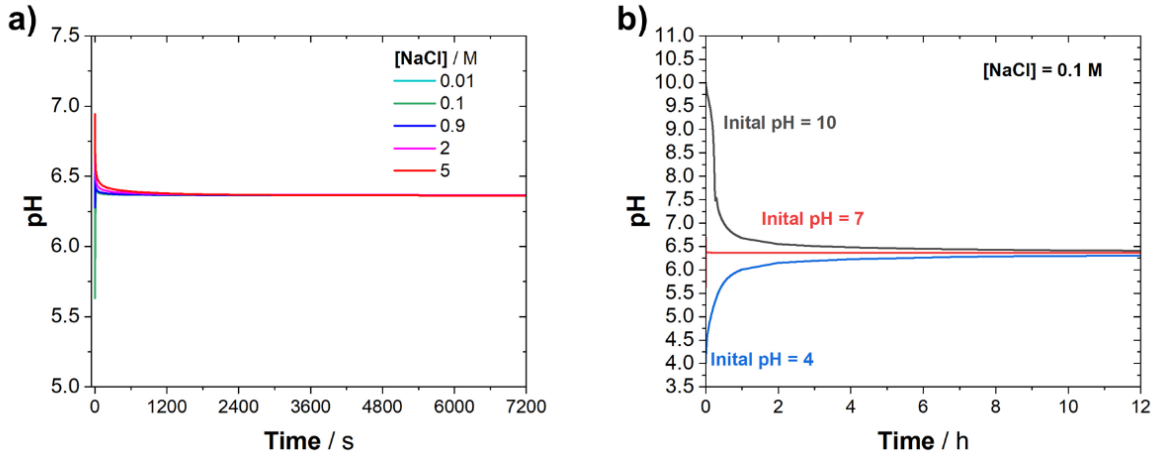

Figure 5.10. pH transient adjacent to the electrode/electrolyte interface at the center of the cathode as a result of the electrochemical reactions occurring at the Al boundary and the subsequent hydrolysis of the Al species for the various NaCl concentrations (a), for different initial solution pH (b).

5.4.8.2. pH and corrosion potential transients for an "inert" Al surface

Figure 5.11 (a) shows the corrosion potential transient and solution pH at the center of the scribe for a case in which the electrolyte chemistry changes only due to the Mg dissolution (Mg^{2+} and OH^- release from self-corrosion or dissolution of MgO pigments). Because the rate at which Mg-based dissolution occurs was considered equal in all cases, the pH transient is the same for all cases. The time it takes for the corrosion potential to fall below the repassivation potential changes depending on the concentration of the NaCl solution, because the pH_{crit} at each NaCl concentration is different. The corrosion potential drop occurs first (after 120 s) on the 5 M solution, which has the lowest pH_{crit}. Then, it occurs on the 2 M solution (after 180 s), 0.9 M (after 540 s), 0.1 M (after 1080 s), and finally on the 0.01 M NaCl solution, after 1320 s. **Figure 5.11** (b) shows the corrosion potential and pH transients calculated for 12 h. The pH reaches a steady-state of 10.98, mainly determined by the solubility product of $Mg(OH)_2$.

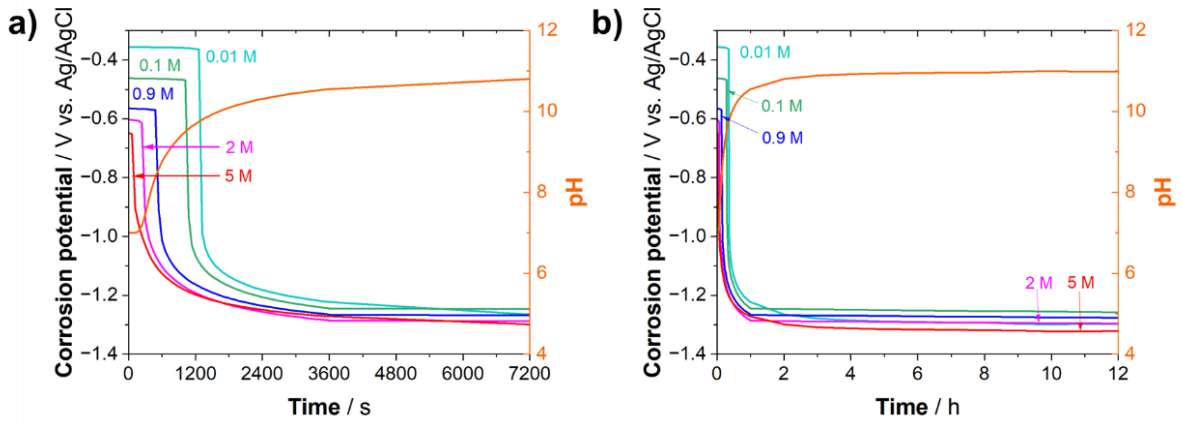

Figure 5.11. Corrosion potential and pH transient calculated at the center of the scribe in 7200 s (a) and 12 h (b).

5.4.8.3. pH and corrosion potential transients for an "electrochemically-active" Al surface

However, if the Al dissolution and hydrolysis are taken into account in the model, then the pH transient and distribution across the electrolyte change with depending on the NaCl concentration. **Figure 5.12** (a) shows the pH transient in the first 7200 s of simulation at the center of the scribe (x = 10 mm). As observed in **Figure 5.10,** initially the pH adjacent to the Al electrode decreases from the initial value of 7 to more acidic values. The lower the [NaCl], the lower the pH that is reached within the first seconds. The pH then increases with time. The pH increase is faster in the more concentrated NaCl solutions. To reach a pH = 9, for example, it took 227, 318, 663, 1236, and 1320 s for the cases in which the NaCl concentration was 5, 2, 0.9, 0.1, and 0.01 M, respectively. As a result of the slower pH increase and the high values of pH_{crit}, the time it takes for the pit repassivation mechanism to occur increases for the lower [NaCl].

The simulation was performed for longer times to evaluate the steady-state conditions. **Figure 5.12** (c) and (d) show the pH and corrosion potential transients, respectively, obtained for 1000 h of simulation time. The pH adjacent to the Al electrode, at the center of the scribe, did not reach a steady-state. The pH increases rapidly in the first 2 h, but then it starts to decrease. For the 0.01 and 0.1 M NaCl solutions, the pH decreases to 8.5 after ca. 200 h, and then it starts to slowly rise up again. For the more concentrated NaCl solutions, the pH decreases after the initial rise. Interestingly, the decrease in the pH was sufficient to cause the shift of the AA2024 corrosion potential back to their initial values in the 0.01, 0.1, and 0.9 M NaCl cases, which occurs after 30, 34, and 108 h, respectively. In the [NaCl] = 2 and 5 M cases, the corrosion potential remains low, but it increases steadily as the pH steadily decreases.

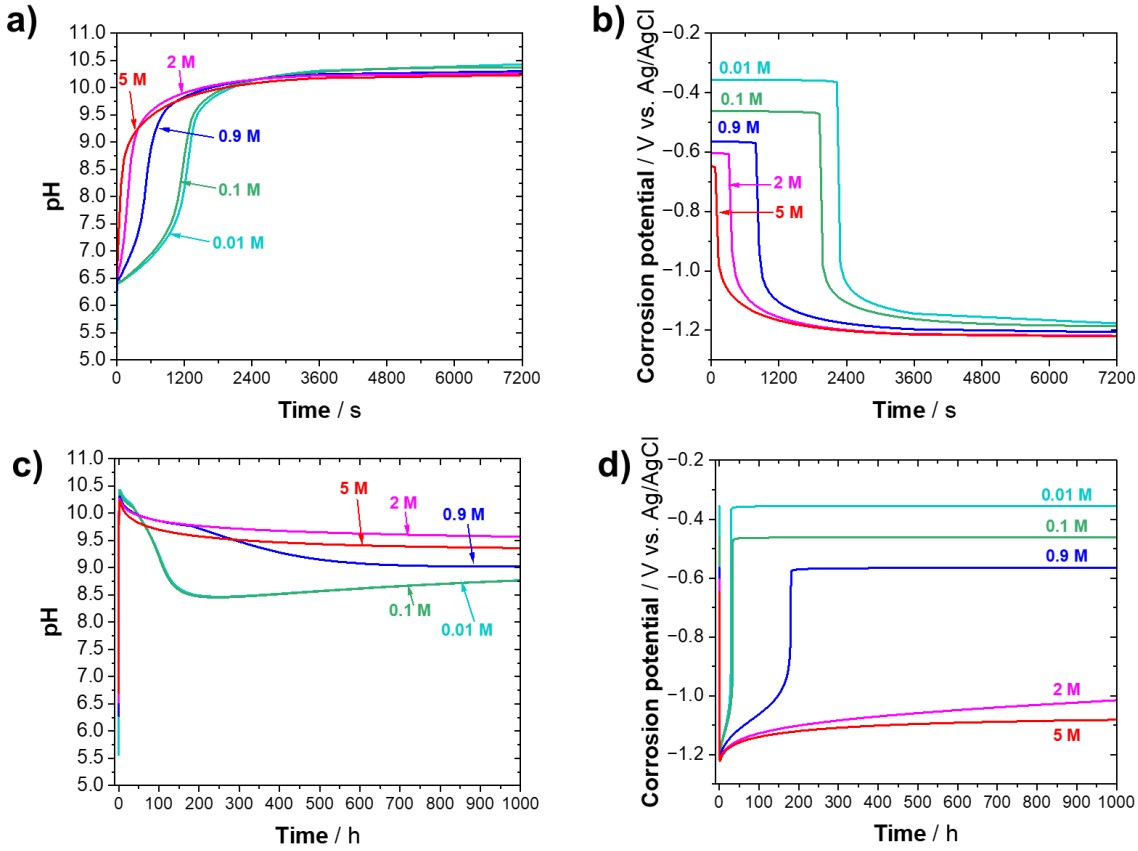

Figure 5.12. pH transient (a and c) adjacent to the electrode/electrolyte interface calculated at the center of the scribe and corrosion potential transient (b and d) calculated for the different NaCl concentrations for 7200 s (a and b), and 1000 h (c and d)

5.4.8.4. Net current density distribution at the AA2024 scribe

The model treats the AA2024 as a homogeneous metal, in which the anodic and cathodic electrochemical reactions are occurring at the same location. However, because the anodic and cathodic kinetics have a pH dependence, and the pH affects the anodic and cathodic kinetics differently, the establishment of a pH distribution across the electrode causes a separation of the anode and the cathode. **Figure 5.13** (a) and (b) show the net current density and pH profiles obtained at different times for [NaCl] = 0.9 M, respectively.

At t = 0 s, there are virtually no spatial differences in the electrolyte pH that could cause shifts in the cathodic and anodic reactions, and the net current density is virtually zero – as charge conservation must be obeyed. Only very near the MgRP boundaries (0 and 10 mm), the pH is higher due to the instantaneous flux of OH^-, but the effect on the current density is not observable in the scale of current densities shown.

At t = 60 s, however, there is a considerable pH gradient across the electrode. The pH is more than 3 orders of magnitude 0.6 mm away from the MgRP boundaries. As a note, the "noise" seen in the pH profile at t = 60 s could be due to numerical errors caused by the water auto-ionization reaction, which causes numerical instabilities when there is a fast change in the concentrations of OH^- and H^+. Because of the strong dependence of the passive current density on pH, these alkaline locations become anodic. At t = 850 s, the time at which the corrosion potential sharply decreases, the length of the electrode at which anodic currents are observed increases to 1.42 mm. The portion of the scribe that displays anodic current densities does not change much in the following times. After 12 h, a net anodic current occurs in 3 mm of the 10 mm scribe, and the remaining 7 mm of the scribe display a net cathodic current density.

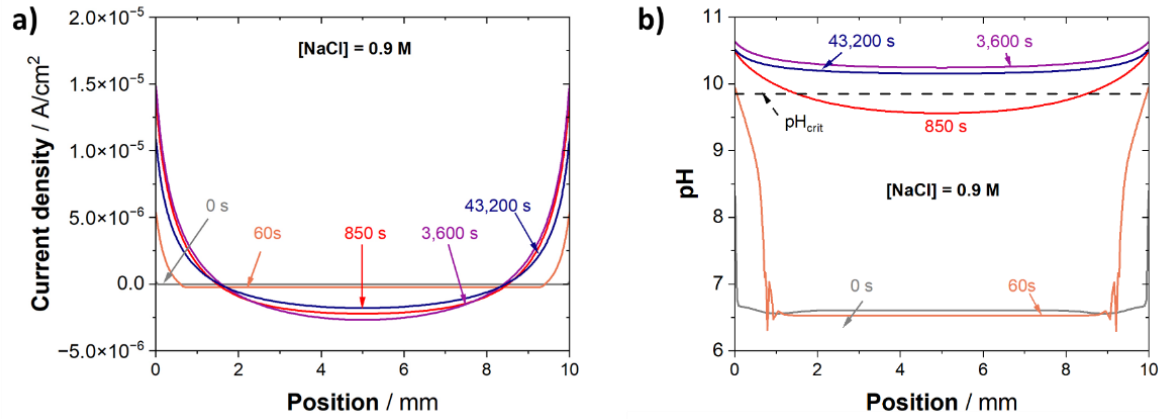

Figure 5.13. Net current density and pH profiles across the AA2024 electrode. The net current density (a) and pH (b) profiles obtained at different times for the NaCl concentration of 0.9 M.

Figure 5.14 (a)-(d) show the profiles of the anodic current density (a), cathodic current density (b), net current density (c) and pH adjacent to the electrode/electrolyte interface (d) obtained at t = 12 h for the different NaCl concentration cases. The current densities increase with the increase in the NaCl concentration, although the differences are small. For example, at x = 5 mm, the cathodic current density obtained for the [NaCl] = 5 M case is -1.18×10^{-5} A/cm^2, and for the [NaCl] = 0.01 M case is -8.9×10^{-6} A/cm^2. The portion of the scribe that exhibits a net positive current did not significantly change with the NaCl concentration. For the [NaCl] = 0.01 M, the net anodic behavior is observed within the first 1.62 mm length distant from the MgRP boundaries, representing 32.4% for the scribe. With the increase in the [NaCl] concentration, the net anodic portion slightly decreases. In the [NaCl] = 5 M case, for example, the net anodic behavior is observed within the 1.54 mm distant from the MgRP boundaries, representing 30.8% of

the scribe, and the anodic current density is higher. Contrarily to the current density behavior, **Figure 5.13** (d) shows that the pH is higher in the lower NaCl concentration cases.

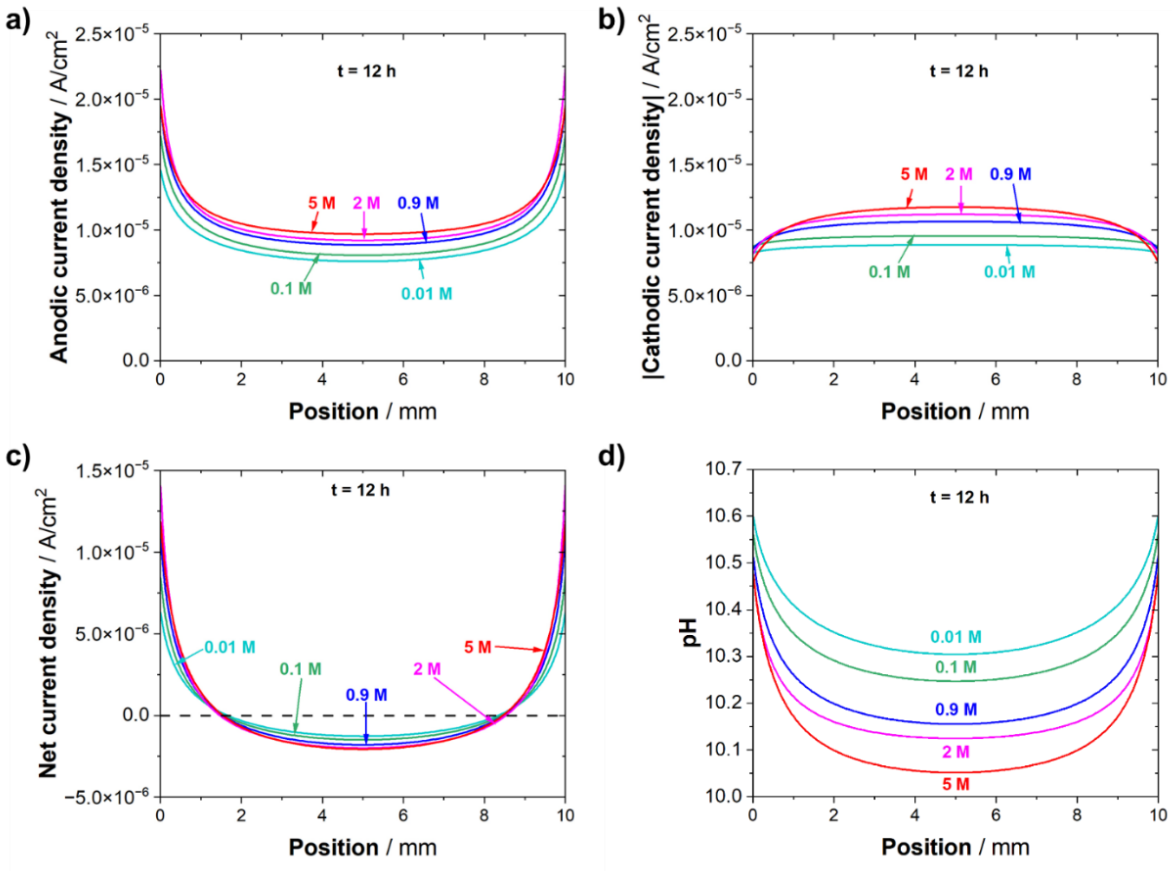

Figure 5.14. Current density and pH distributions obtained after 12 h for the different NaCl concentrations: (a) Anodic current density; (b) absolute value of the cathodic current density; (c) net current density; (d) pH profile across the AA2024 scribe adjacent to the electrode/electrolyte interface.

5.5. Discussion

5.5.1. Anodic and cathodic behavior in the varying NaCl solutions and the implications on pH_{crit}

The decrease in pH_{crit} with the increase in the NaCl concentration is due to contributions of both reduction in the ORR kinetics in the higher NaCl concentration, and the mild increase in the passive current density in moderately alkaline pH. **Figure 5.15** shows the passive current density as a function of pH obtained for [NaCl] = 0.01 and 5 M solutions, the linear regression fitting (solid lines), and the ORR current density extracted at -950 mV vs. Ag/AgCl. The intersection between the passive current density lines and the limiting ORR current density shows the pH_{crit} (calculated by mixed potential theory), indicated with arrows. The pH at which the combination of the ORR limiting current densities and the passive current

density slopes intersect determines the pH_{crit}, and they are indicated in the graph. The combination of both ORR and passive current density behavior found in the different NaCl solutions contribute to the pH_{crit}. For example, if the passive current density vs. pH behavior was invariant with Cl^- concentration, and equal to the relationship observed in 5 M, the pH_{crit} in the 0.01 M NaCl solution would be lower and equal to 9.77. If, on the other hand, the passive current density vs. pH behavior was equal to the relationship found for 0.01 M, the pH_{crit} would be higher in the 5 M solution and equal to 9.58. The combination of both decrease in the ORR limiting current density and an increase in the passive current density drives the pH_{crit} to be lower in the 5 M NaCl solution.

At the same time that the pitting susceptibility is significantly increased with the increase in the Cl^- concentration, the mechanism of localized corrosion protection via pH increase is facilitated in the higher concentrations. The lower ORR current densities at higher Cl^- concentrations also lower the cost of the localized corrosion stifling by the increased rates of uniform anodic dissolution, as lower anodic current densities are needed to surpass the ORR current density.

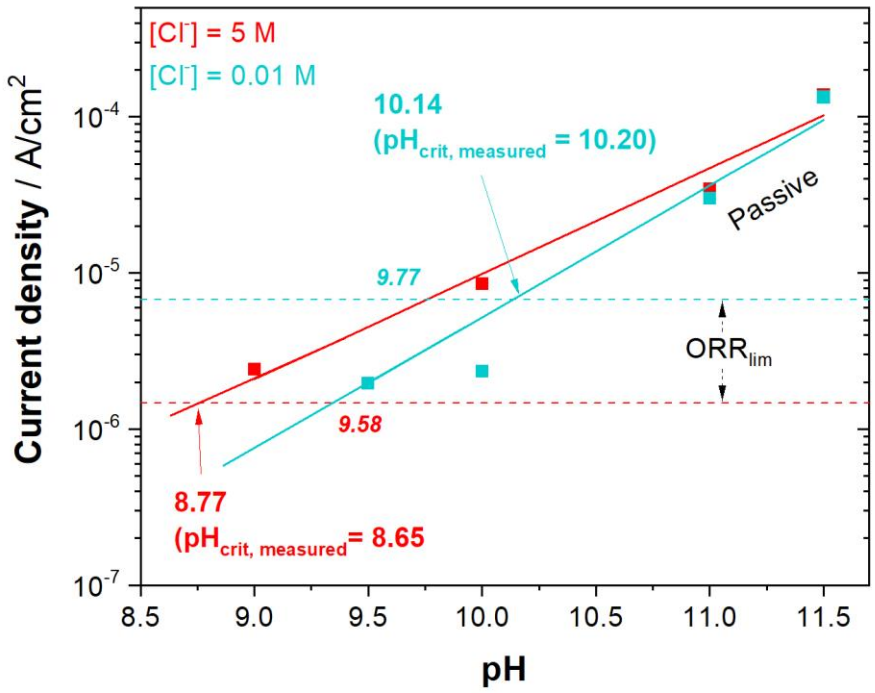

Figure 5.15. Passive current density as a function of pH, and ORR limiting current density (ORR_{lim}) obtained in solutions of NaCl concentration of 0.01 and 5 M. The intersection shows the pH_{crit} predicted by mixed potential theory.

The effect of Cl^- concentration on the passive dissolution appears to depend on pH and on the Cl^- concentration. The Cl^- concentration had a higher impact on the passive dissolution in the lower end of the pH range investigated herein, and, generally, the passive current density increased with the increase in the Cl^- concentration. With the increase in pH, the impact of Cl^- concentration on the passive current density was attenuated. For the highest pH investigated (pH =11.5) and NaCl concentration ([NaCl] = 5 M), an active to passive behavior was observed. Initially, the anodic dissolution is fast and it increases with the increase in potential reaching a maximum value. Upon further increasing the potential, anodic current density decreases, until the breakdown potential is reached and the current density rapidly increases again. The decrease in the anodic current density with the increase in the anodic polarization indicates the formation of a protective film on the surface of the alloy. The decrease in the anodic current density in potential below the pitting potential for pure Al in alkaline solutions with the increase in Cl concentration has been previously reported [212,220]. The authors suggested that Cl^- ions are incorporated into the passive layer through defect sites, and, in the presence of OH^- ions, compounds such as $Al(OH)_2Cl$ and $Al(OH)Cl_2$ are formed [212]. The phenomenon was observed in lower concentrations of Cl^-, but in a higher pH of 12. Perhaps the formation of such films is only significant at a combination of high OH^- and Cl^-.

The decrease in the ORR limiting current density with the increase in the Cl^- concentration can be explained by the decrease in the O_2 solubility and diffusivity in higher NaCl concentrations. **Figure 5.16** shows the equilibrium concentration of O_2, and its diffusivity calculated using OLI Studios (v. 11). The concentration of dissolved O_2 and its diffusivity decreases as the concentration of NaCl increases. The change is small in the lower NaCl concentrations - increasing the NaCl concentration from 0.01 M to 0.1 M decreases the equilibrium concentration by about 2%, and the diffusivity decreases by less than 1%. Indeed, the cathodic current densities obtained in the 0.01 M and 0.1 M solutions in the potential range at which ORR is the dominating cathodic reaction are virtually the same. In higher NaCl concentrations, the O_2 equilibrium concentration and diffusivity changes are more significant. In comparison to the 0.01 M NaCl solution, the equilibrium concentration in 5 M NaCl is ca. 3 times lower, and the O_2 diffusivity is 1.6 times lower. The cathodic current density extracted at -950 mV in 5 M was ca. 7 times lower than the cathodic current density measured in 0.01 M NaCl solution.

In the 5 M NaCl solution, the cathodic current densities were lower even at more negative potentials, at which HER is the dominating cathodic reaction. If films containing $Al(OH)_2Cl$ and $Al(OH)Cl_2$ indeed formed at the surface of the alloy, it is possible that the film decreased the rate of the charge-transfer controlled HER. More experimental investigation is needed to understand the behavior.

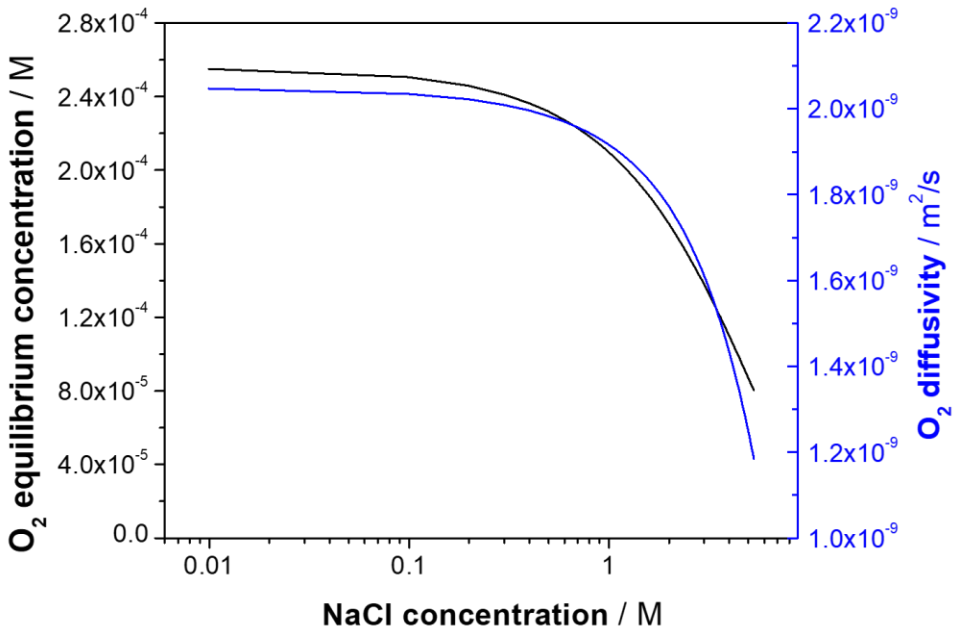

Figure 5.16. The equilibrium concentration of dissolved O_2 and O_2 diffusivity as a function of NaCl concentration calculated in OLI Studios.

5.5.2. The framework predicts the relationship between corrosion potential, pH and Cl^- concentration

The framework developed in Chapter 4 was extended to various compositions of NaCl is able to predict the sharp potential decrease occurring at the pH_{crit}. The agreement between the measured pH_{crit} and the ones obtained by the model (i.e., obtained by mixed potential theory) indicate that the pH-induced potential control mechanism described by Santucci [24] can be extended across different Cl^- concentrations. That is, there does not seem to occur additional effects that would interfere on the mechanism. The change in the ORR diffusion-limited current density observed in the different NaCl solutions and the passive current density-pH relationships obtained from the voltammetry are sufficient to explain and capture the corrosion potential shift.

The model was able to capture reasonably well the relationship between AA2024 corrosion potential and pH and Cl^- concentration. In aerated solutions of $pH < pH_{crit}$, the corrosion potential is at or near the pitting potential. The model predicted the decrease in the corrosion potential with the increase in the Cl^- concentration, as the pitting potential was defined to be inversely correlated to the log of the Cl^- concentration, in a linear fashion. The model slightly overestimated the corrosion potential for the $pH < pH_{crit}$. The model used potentiodynamic polarization data to fit the linear equation relating pitting potential

and Cl^- concentration. It is known that the pitting potential values can vary depending on the method which was used to determine them. For example, it has been shown that the pitting potential is dependent on the speed in which the polarization scan is performed [221]. Thus, the variation between the measured and predicted corrosion potentials can be attributed to the variability in the pitting potentials. Evidently the model cannot capture the large fluctuations observed in the 5 M solutions, as those are probably due to pitting and repassivation events, which are not modeled.

The corrosion potential is underestimated by the model for pH > 10 for the [NaCl] ≤ 2 M. The deviations are likely due to the differences in the HER kinetics. The HER kinetics were assumed to be independent of Cl^- concentration and were modeled utilizing an exchange current density obtained for pure Al [218]. In AA2024, the cathodic kinetics are enhanced due to the presence of Cu, which is more catalytic for cathodic reactions [61]. Additionally, in alkaline solutions, the surface becomes enriched in Cu due to the selective dissolution of Al and Mg from Al-Cu-Mg intermetallic particles and/or Cu replating [61], enhancing the catalytic properties of the surface for HER. The underestimation of the cathodic kinetics explains the underestimation of the corrosion potential.

Although the model assumed the HER kinetics to be independent from the NaCl concentration, **Figure 5.6** clearly shows that, in practice, the cathodic current density at low potentials decreases when [NaCl] approaches saturation, possibly as a consequence of the precipitation of a film. The overestimation of the cathodic kinetics leads to an overestimation of the corrosion potential. Indeed, for the [NaCl] = 5 M case, the model overestimated the corrosion potential for the pH range of 9 to 11. There is a better agreement for the pH = 11.5, which can be due to the increased cathodic kinetics in the more alkaline media.

The abstraction of the different anodic and cathodic kinetics observed on the AA2024 over the potential range investigated by the implementation of separate half-cell reactions increases the versatility of the model. In addition, the abstraction of the Cl^- and pH dependencies on the different half-cell reactions allows for the investigation of dynamic processes, in which Cl^- concentration and solution pH vary with time. The approach can be useful to improve predictive models of atmospheric corrosion, for example, as the dynamic variations in the electrolyte composition are important aspects of the process, and part of the challenges associated with the study of atmospheric corrosion. As the model adapts the boundary conditions according to the electrolyte, possible synergistic effects between the varying parameters can be captured.

The method can also be useful in the study of galvanic interactions between dissimilar alloys. Typically, the models are built such that anodic kinetics are imposed at the anode, and cathodic kinetics are imposed at the cathode. For situations in which the mixed potential between the two materials is distant from the corrosion potential, and the electrochemical kinetics do not considerably change, the approach is suitable. However, if changes in the electrolyte composition cause significant changes in the electrochemical reactions, important changes in the galvanic coupling behavior are not captured.

The drastic decrease in the corrosion potential of AA2024 with at pH > pH_{crit} can be an important factor in the study of cathodic protection. For example, if we were studying the cathodic protection provided by a hypothetical active metal, whose corrosion potential is – 1 V and invariant with pH, the anode and cathode behavior between the hypothetical metal and the Al alloy could reverse with time. At a neutral pH, the hypothetical active metal is anodic to AA2024, whose potential in aerated and neutral solutions is ca. -0.6 V. At such conditions, the hypothetical metal would act as the anode, and the Al alloy would act as the cathode. The cathodic reactions occurring at the Al alloy would cause an increase in the surface pH. If the surface pH increased to, for example, 11, the corrosion potential of AA2024 would decrease to -1.2 V. If the corrosion potential of the hypothetical active metal is not affected by the pH, and remained at -1 V, then the Al alloy would become anodic to the metal, and the cathodic protection would lead to a detrimental galvanic coupling (if the effects of Cu enrichment are not accounted for). For this hypothetical case, the change in electrochemical reactions with the solution composition is necessary to describe the galvanic coupling between the two materials, as the inevitable pH increase at the Al surface in the initial stages of the galvanic coupling would cause the polarization "inversion".

5.5.3. Interdependencies between chemical and electrochemical reactions

The description of pH-dependent boundary conditions and the numerical calculations of solution chemistry based on the electrochemical and chemical reactions occurring in the electrolyte allows the model to solve for complex, interdependent behaviors that are otherwise difficult to analyze and solve analytically.

In the absence of other chemical effects, the pH resulting from the uniform corrosion of Al is slightly acidic and equal to ca. 6.4. The various Al hydrolysis reactions buffer the solution [30]. The model showed that, independently of the initial solution pH, the solution pH tended to the same steady-state value of 6.4. The results agree with reports from the literature that showed that, in unbuffered solutions, the pH of a solution exposing Al alloys tended to near-neutral values within 24 h of exposure, independent of the initial solution pH [222]. The steady-state pH was independent of the NaCl concentration, as the equilibrium reactions between Cl^- and the Al ionic species were neglected. Although the cathodic and anodic kinetics vary with NaCl, charge conservation imposes that, for every Al^{3+} produced by the anodic reactions, three OH^- will be produced by the cathodic reactions. Thus, the differences in the anodic and cathodic rates found in the different NaCl solutions do not change the steady-state pH. For example, the higher rate of the cathodic reaction at open circuit potential observed in 0.01 M will cause a higher rate of anodic reaction, and this only changed the rate at which the steady-state is reached.

With the addition of an external source of OH^-, on the other hand, the different electrochemical kinetics impacted the pH distribution, which then in turn affected the electrochemical kinetics. For the cases in which ORR controlled the corrosion rate (pH < pH_{crit}), the higher ORR kinetics (and thus anodic kinetics)

of the lower [NaCl] decreased the rate at which the pH increased, as a result of the higher rates of Al^{3+} production and subsequent hydrolysis. The slower pH increase and the higher pH_{crit} contributed to an even a longer time necessary for the pH-induced pit repassivation mechanism to occur.

When performing the calculations for longer times, it was observed that there was a fast increase in the solution pH at earlier times. After reaching a maximum value, the pH decreased, probably due to higher dissolution of Al (caused by the higher pH), which increased the extent of the hydrolysis reactions. At lower NaCl concentrations, the pH decreased below pH_{crit}, and the corrosion potential eventually increased to its initial value. The shift caused the pH to decrease to even lower values. For the 0.01 and 0.1 M cases, the pH started to increase again after 200 h. A steady-state was not reached in 1000 h of simulation.

5.5.4. Implications of the non-uniformity of the local chemistry and chemistry-dependent boundary conditions on the current density distributions

The non-uniformity of the pH distribution associated with the different dependencies of the anodic and cathodic kinetics on pH caused a separation of anode and cathode in the initially uniformly-corroding electrode. The strong dependence of the anodic current densities on pH led to the net anodic behavior at the more alkaline locations. At the center of the scribe a net cathodic behavior was observed. The increase in the anodic kinetics eventually led to the decrease in the corrosion potential. For all cases, the pH_{crit} had to be reached in only ca. 30% of the scribe, as mixed potential theory is based on current, not on current density. The steep relationship between the passive current and pH led to the high anodic currents near the Mg-dissolving boundaries, so that 30% of the scribe with high anodic currents was enough to overcome the limiting cathodic current.

For the conditions in which the model was performed, the results imply that there would be a higher dissolution of the substrate near the protective coating, at which the dissolution of Mg/MgO increases the local pH. However, the model does not simulate a critical process in the protection provided by Mg-based coatings: the precipitation of protective hydroxides at alkaline locations, which can inhibit corrosion reactions. This effect has been largely reported [24,25,186,223], and it is a necessary mechanism to be taken into account in the development of models of corrosion protection mechanisms provided by Mg-rich primers.

5.5.5. Model limitations

The assumption of a homogeneous electrode to simulate the corrosion behavior of AA2024 is a major limitation of the model. Due to its heterogeneous microstructure, composed by a variety of intermetallic particles exhibiting unique electrochemical behavior, the corrosion behavior of Al alloys is complex. The electrochemical properties measured are a result of the contribution of each intermetallic

particle and the Al matrix. Many corrosion processes important to the corrosion of heterogeneous alloys such as AA2024 are described by the interactions between the Al matrix and the intermetallic particles, and those cannot be captured by the model described herein. The application of a heterogeneous electrode model to describe the boundary conditions at the AA2024 electrode, such as that developed by Jakab [61], could greatly improve the model. However, the use of the averaged anodic and cathodic behavior measured on the bulk of AA2024 was sufficient to capture the mechanism of the pH-induced pit repassivation, and to investigate the effect of Cl^- on the mechanism.

The evolution of the surface composition on AA2024 when exposed to alkaline solutions and the subsequent increase in the cathodic kinetics causes deviations of the model results from experimental measurements. The increased Cu content due to selective dissolution of Al and Mg, and Cu replating, increases the catalytic properties of AA2024 for cathodic reactions. This transient behavior poses a significant challenge to the development of models that simulate the corrosion behavior of AA2024, especially in cases in which the electrolyte becomes alkaline, or when it is in contact with more active metals, such as Mg.

The precipitation of corrosion products and their inhibiting effect on the corrosion reactions is another important aspect in the corrosion behavior of Al alloys. The precipitation of $Al(OH)_3$ is not modeled, only the equilibrium among the Al aqueous species is used in the model. As mentioned previously, Mg corrosion products, such as $Mg(OH)_2$ and $MgCO_3$ at the Cu-rich cathodic hotspots on AA2024, and the resulting inhibition of ORR, is an important aspect of the chemical protection mechanisms provided by Mg-based coatings.

5.6. Conclusions

The framework developed to model the chemical protection mechanisms provided by Mg-based rich primers was extended to solutions of varying NaCl concentrations. Through experimental and modeling studies, the impact of Cl^- concentration on the critical pH above which the corrosion potential of AA2024 decreases sharply was investigated. pH and Cl^- dependent boundary conditions were developed to capture the impact of these parameters on the corrosion potential of AA2024. The effectiveness of the method used to define the boundary conditions in the context of modeling dynamic behaviors is discussed. The following conclusions can be made:

- The critical pH above which the corrosion potential shifts from localized-corrosion prone potentials to potentials below the repassivation potential decreases with the increase in the Cl^- concentration, due to the combination of the increased anodic kinetics and decreased cathodic kinetics in higher Cl^- concentrations.

- The robustness of the modeling framework was tested by varying the solution chemistry. The model was able to capture the dependence of the corrosion potential behavior of AA2024 on the pH, indicating that the assumptions and abstractions used to build the model were sufficient to describe the phenomenon.
- For the conditions in which the model was performed, the results indicate that the mechanism of inhibiting localized corrosion by the pH-induced potential control is more feasible at higher Cl^- concentrations.
- In the absence of other effects, and for the dissolution rate of the Mg pigment used in the model, the corrosion potential of AA2024 eventually increased back to potentials near the pitting potential in lower NaCl concentrations.
- The development of chemistry-dependent boundary conditions allows for the investigation of the complex interplay between the electrochemical reactions and solution chemistry.

Part II: A modeling and experimental approach to investigate the impact of an ohmic resistance mediating the galvanic coupling between Mg and AA2024

5.7. Introduction

In Chapter 4, the effect of a polymer resistance on the mediation of the galvanic couple between AA2024 and the Mg pigments in a MgRP/AA2024 system was modeled using the approach developed by Lee, et al. [74]. The resistance can be afforded by the organic matrix in which the Mg pigments are embedded and by the topcoat that typically composes the coating system. It was found that a resistance greater than 10^5 $\Omega \cdot cm^2$ was sufficient to hinder the galvanic coupling and, therefore, the protection from localized corrosion by cathodic protection could not be afforded. However, if the dissolution of the self-corroding Mg pigment was taken into account, the model predicted that localized corrosion stifling could still occur due to the additional chemical protection mechanisms offered by Mg.

The objective of Part II of this chapter is to validate the effect of the resistance on the mediation of the galvanic coupling between Mg and AA2024. The mediation of the galvanic couple was tested by adding ohmic resistors of known resistances in the electronic path between Mg and AA2024, which were coupled with a zero-resistance ammeter. The current and potential at the AA2024 were measured during a 12 h exposure to a 0.9 M NaCl solution. The results obtained by this experimental approach were to assert the ability of the model to predict the galvanic potential and current densities as a function of resistance. The hypothesis that, even at large resistances, the potential at AA2024 can decrease to values below the repassivation potential due to the changes in the chemistry of the electrolyte caused by Mg corrosion is tested. Additionally, the applicability of the reduced-order modeling approach in simulating the mechanisms is evaluated.

5.8. Methods

5.8.1. Galvanic potential and current density measurements via zero resistance ammeter (ZRA) technique

An AA2024-T351 plate and 99.9% pure Mg rod were cut using a precision cut-off saw to obtain rectangular coupons. An insulating varnish was used to bind the coupons, which were then mounted in an epoxy resin. The area of the exposed Mg and AA2024 was 0.4 cm^2 to obtain an anode-to-cathode ratio of 1. Prior to performing the measurements, the sample was ground down to a 4000-grit paper, rinsed with deionized water, and dried with pressurized air.

Figure 5.17 shows a schematic drawing of the experimental setup. A vertical cell was used to expose the sample to 10 mL of 0.9 M NaCl solution. The galvanic potential and current density measurements were performed utilizing the zero-resistance ammeter (ZRA). AA2024 was set as the working electrode and Mg as the counter-electrode. Resistors of varying resistances (10, 100,

10^3,10^4,10^5,10^6, and 2x10^7 Ω) were added to the circuit between Mg and the zero-resistance ammeter. The resistances reported in the results section are multiplied by the area of the Mg electrode (0.4 cm^2). The measurements were performed with and without the resistors. The potential at the AA2024 electrode was measured utilizing an Ag/AgCl reference electrode.

The same mounted AA2024 and Mg sample was used to measure the corrosion potential of AA2024 as a function of time for a case in which the metals were *not* electrically coupled, but exposed to the same solution. The measurement was performed to investigate the impact of the corrosion products of the self-corrosion of Mg on the AA2024. The sample was exposed to 10 mL of 0.9 M NaCl solution in the vertical cell displayed in **Figure 5.17** (a). The corrosion potential of AA2024 was monitored utilizing an Ag/AgCl reference electrode.

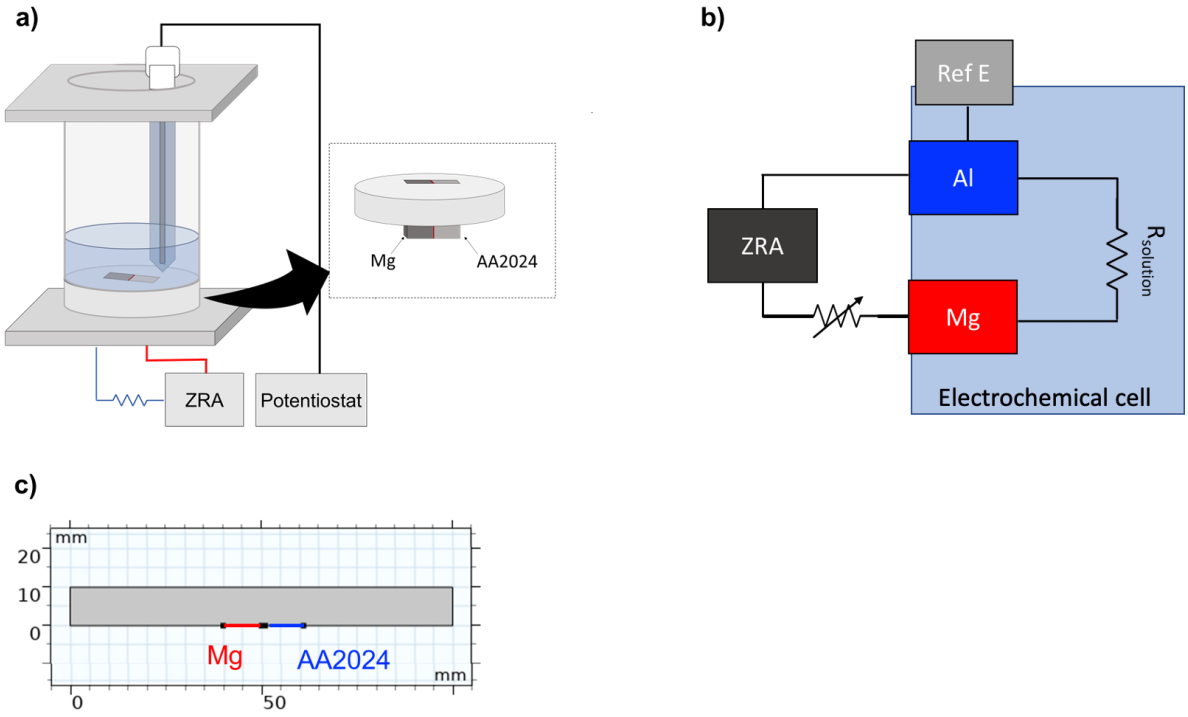

Figure 5.17. (a) Drawing of the experimental setup used to perform the ZRA measurements; (b) A simplified equivalent circuit of the experimental setup; (c) A 2D simplification of the geometry used to model the galvanic coupling of the AA2024 and Mg simulating the experimental setup.

5.8.2. Model description

The framework developed in Chapter 4 was applied to a geometry that simulates a cross-section of the experimental setup used to expose the Mg and AA2024 samples to the 0.9 M NaCl solution. **Figure 5.17** (c) shows the geometry applied in the model. The model was performed with different governing equations and boundary conditions. In Case I, the steady-state coupled potential and current density is

calculated utilizing the Laplace equation. In Case II, the transient of the coupled potential and current density is calculated utilizing the Laplace equation to solve for charge conservation and mass transport equations (Fick's second law with the addition of a reaction term) to solve for the concentration of the minor species. In Case II, the boundary conditions were dependent on the solution chemistry. The boundary conditions utilized in the two cases will be briefly described. More details of the model can be found in Chapter 4 and in [87].

5.8.2.1. Boundary conditions

The boundary conditions were defined according to the method described in Chapter 4 and in Part I of this chapter. Distinct half-cell electrochemical reactions were defined at the AA2024 boundary to describe the different kinetic behaviors observed in the potential range of ca. -1.6 to -0.5 V vs. Ag/AgCl, mainly: pitting and passive kinetics, ORR, and HER. The limiting passive current density was defined according to the relationship found by Santucci [24]

$$\log i_{pass} = 0.979 \times pH - 14.741 \quad [1]$$

In the steady-state calculation (Case I), the pH was assumed to be constant and equal to 7. In Case II, the pH was calculated at each time step, as described in the following section.

At the Mg boundary, the anodic Mg electrochemical kinetics were as in Chapter 4, using the pseudo-Tafel expressions, where the parameters A, i_0, and E_0 parameters were derived from experimental data and acquired from previous work [74]. The resistance was varied according to the resistances used in the experimental measurements. The HER kinetics at the Mg boundary was simplified by a Tafel fit in the cathodic region of the Mg polarization curve shown in the previous work [74]. The zero-dimension resistance was added to the Mg boundary. The resistance provided an additional ohmic drop across the surface of the Mg, which decreased the overpotential for the Mg dissolution, according to Equation 2:

$$\eta_{Mg} = E_{local,Mg} - \Delta\varphi_{film} - E_{eq,Mg} \quad [2]$$

In the limiting case of an infinite resistance, the overpotential at Mg is zero and it is corroding at its open-circuit potential. According to the boundary conditions described, the corrosion rate of Mg was ca. 0.3 mA/cm^2.

5.8.2.2. Heterogeneous and homogeneous reactions

As described in Chapter 4 and in Part I of this chapter, the local current densities calculated using the Laplace equation were used to calculate the flux of the species produced at the electrodes using Faraday's law. The local chemistry was only calculated in Case II. At the AA2024 boundary, the production of Al^{3+} and OH^- arising from the anodic and cathodic reactions was considered. At the Mg boundary, the production of Mg^{2+} and OH^- was considered.

The equilibrium between the H^+ and OH^- species, the hydrolysis reactions of the Al species, and the precipitation of $Mg(OH)_2$ were defined in the domain that represents the bulk of the electrolyte. Thus, the spatiotemporal distribution of pH is a result of all the heterogeneous and homogeneous reactions.

COMSOL Multiphysics (ver. 6.1) was utilized to perform the finite element analysis calculations. At the top, left, and right boundaries of the water layer domain in **Figure 5.1**, Neumann boundary conditions were applied, where the normal flux of all species was set to zero ($\boldsymbol{n} \cdot N_i = 0$). The Transport of Dilute Species and the Secondary Current Distribution interfaces of the Electrochemistry Module were used.

5.9. Results

5.9.1. Predicted galvanic potential and current density as a function of resistance – Case I: the steady-state model

Figure 5.18 (a) and (b) show the potential and current density as a function of position at the AA2024 for the different resistances between AA2024 and Mg. The position at x = 0 mm is the closest position from the Mg, which is separated from AA2024 by 1 mm. The coupled potential increases as the resistance increases. Accordingly, the cathodic current density decreases as the resistance decreases, as AA2024 is less cathodically polarized. For all resistances, there is a small ohmic drop across the electrodes. The highest ohmic drop, of 60 mV, is found in the case in which there is no resistance between AA2024 and Mg, and the coupled potential is -1.46 V vs. Ag/AgCl at the point closest to Mg and increases to -1.40 V vs. Ag/AgCl at x = 10 mm. The cathodic current density is highest at x = 0 mm (1.0×10^{-2} A/cm^2) and lowest at x = 10 mm (5.1×10^{-3} A/cm^2). As the current density decreases with the increase in the resistances, the ohmic drop across the electrolyte decreases, and the potential and current density becomes more uniform across the electrode.

Figure 5.18 (c) shows the modeled coupled potential and current density averaged across the length of the AA2024 electrode as a function of resistance. The coupled potential sharply increases from -1.08 to -0.61 V vs. Ag/AgCl when increasing the resistance from 4×10^4 to 4×10^5 Ω·cm^2. For the resistances of 4×10^5 and 8×10^6 Ω·cm^2, the predicted coupled potential is close to AA2024 open circuit potential. Essentially, the Mg and AA2024 are uncoupled at these higher resistances.

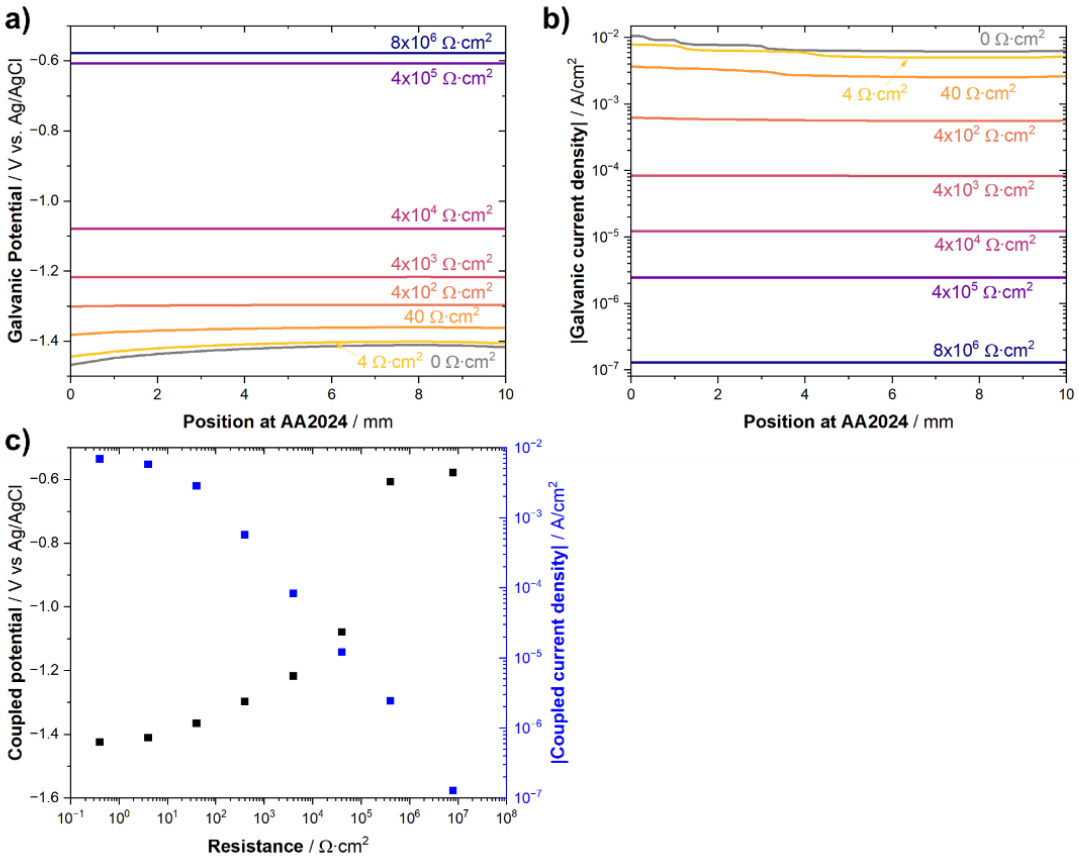

Figure 5.18. Potential (a) and current density (b) distributions at AA2024 as a function of the resistance between AA2024 and Mg; (c) average potential and current density on AA2024 as a function of resistance between AA2024 and Mg.

5.9.2. Predicted galvanic potential and current density as a function of resistance –transient model

In Case II, the species production from the electrochemical reactions, the homogeneous reactions in the electrolyte, and the pH-dependent boundary conditions were included in the model. **Figure 5.19** shows the transient of the averaged galvanic potential (a) and net current density (b) at AA2024 as a function of coating resistance. With the addition of the pH-dependent boundary conditions, the model predicts a decrease in the potential in the initial times of exposure. For the resistance = $4x10^5$ and $8x10^6$ Ω·cm^2, the calculated potential starts close to the AA2024 corrosion potential (in neutral solutions), then it decreases to more negative potentials. There was not a significant difference between the potential transients calculated with the resistances of 0 to 40 Ω·cm^2. In resistances higher than 40 Ω·cm^2, the galvanic potential increased with increasing resistance.

The calculated net current density, which is cathodic on AA2024, decreases with increasing resistances. As observed with the galvanic potentials, there was not a significant difference between the current densities obtained with the 0 and 4 $\Omega \cdot cm^2$ resistances. For the resistances lower than $4x10^5\ \Omega \cdot cm^2$, the magnitude of the net current density initially decreases, and then it stabilizes to a steady-state current density.

Figure 5.19 (c) and (d) shows the calculated average pH at the AA2024 surface as a function of time and the calculated local pH on the AA2024 surface as a function of distance from Mg after 12 h, respectively. The average pH near the AA2024 surface increased as the resistance decreased, which agrees with the higher magnitude of cathodic currents experienced on AA2024 when the metals are better coupled. Looking specifically at the pH on the AA2024 region adjacent to Mg (**Figure 5.19**-d) it becomes clear that, for resistances smaller than $4x10^4\ \Omega \cdot cm^2$, the pH on AA2024 is higher than on Mg as a result of its cathodic polarization. For resistances $\geq 4x10^4\ \Omega \cdot cm^2$, however, the pH on the surface of AA2024 is lower than on Mg. In this case, AA2024 and Mg behave as uncoupled metals corroding at their own corrosion potentials, and the lower pH calculated on AA2024 is likely due to the higher acidity of the Al^{3+} cations [224].

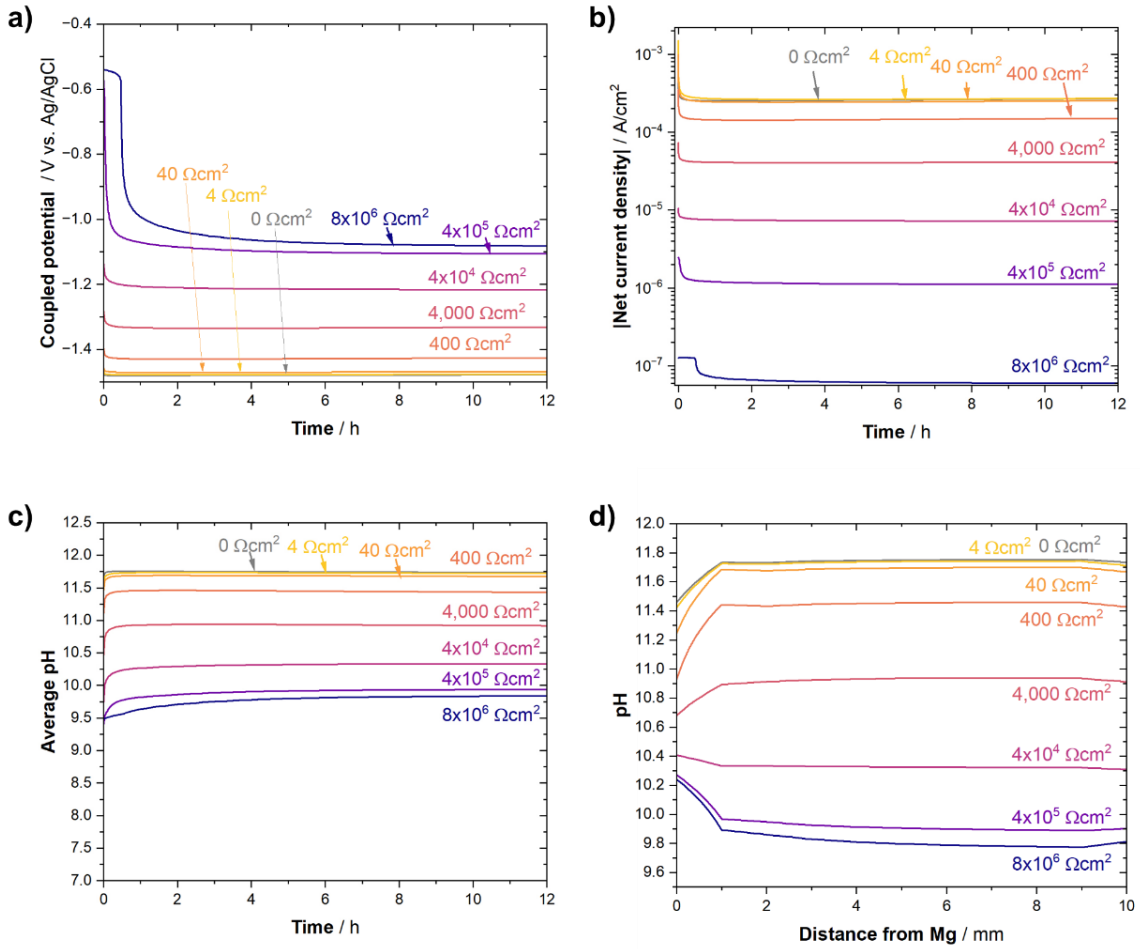

Figure 5.19. Transient of the average galvanic potential (a). and current density (b) as a function of resistance calculated in Case II.

5.9.3. Mg and AA2024 coupled potential and current density measured by ZRA

The galvanic potential and current densities of the coupled AA2024 and Mg were measured during a 12 h exposure. **Figure 5.20** shows the galvanic potential (a) and the absolute value of the current density (b) of the coupled Mg and AA2024 measured in 12 h of exposure to 0.9 M NaCl as a function of the additional ohmic resistance between the AA2024 and Mg electrode added by the resistors. Two other cases are shown: the open-circuit potential measured on AA2024 uncoupled from Mg, in a solution that exposes both electrodes – that is, AA2024 and Mg are corroding at their open-circuit potentials; the open-circuit potential measured on AA2024 "by itself," that is, without the Mg electrode exposed to the same solution. **Figure 5.20** (c) and (d) show the coupled potential and current density in the first 100 s obtained when using the resistances of $4x10^4$, $4x10^5$, and $8x10^6$ $\Omega \cdot cm^2$. The open-circuit potential was measured for the uncoupled case, and for the case in which only AA2024 is in solution.

The coupled potential decreases as the resistance between Mg and AA2024 increases. At the end of the exposure (at 12 h), the coupled potential is -1.44, -1.37, -1.28, -1.18, -1.14, -1.09, -1.02, and -0.96 V vs. Ag/AgCl for the 0, 4, 40, 400, 4000, $4x10^4$, $4x10^5$, $8x10^6$ $\Omega \cdot cm^2$ resistances, respectively. For the case in which the AA2024 is uncoupled from Mg, the open-circuit potential was -0.99 V vs. Ag/AgCl. For the case in which only AA2024 is in the 0.9 M NaCl solution, the open-circuit potential after 12 h was -0.58 V vs. Ag/AgCl.

The coupled current densities decrease with the increase in the resistance. The current density at the end of the exposure, the cathodic current density measured at AA2024 is $-2.6x10^{-2}$, $-2.0x10^{-2}$, $-7.0x10^{-3}$, $-1.0x10^{-3}$,- 5.9 $x10^{-5}$, $-1.3x10^{-5}$,- $1.3x10^{-5}$, $1.5x10^{-6}$ and $8x10^{-8}$ A/cm^2, for the 0, 4, 40, 400, 4000, $4x10^4$, $4x10^5$, $8x10^6$ $\Omega \cdot cm^2$ resistances, respectively. Note that it is possible to see large fluctuations in the current in the measurements performed with the 4000, $4x10^5$, $8x10^6$ $\Omega \cdot cm^2$ resistances, which could be due to issues in the connection of the electrodes.

It is possible to see a transient in the coupled potential and current density. For the resistances < $4x10^4$ $\Omega \cdot cm^2$, the coupled potential is more negative in the beginning of the exposure, and then it increases. The potential is more stable for the resistances $\leq 4x10^2$ $\Omega \cdot cm^2$. For the resistances of $4x10^3$ and $4x10^4$ $\Omega \cdot cm^2$, the potential initially rises, and after ca. 6 h it starts to decrease slightly. For resistances $\geq 4x10^5$ $\Omega \cdot cm^2$, the galvanic potential is higher in the beginning of the exposure. **Figure 5.20** (c) shows the measured potential in the first 100 s. The coupling started at 31 s. For the resistance = $4x10^4$ $\Omega \cdot cm^2$, the potential instantaneously decreased from -0.85 to -1.03 V vs. Ag/AgCl when the coupling started, and it continued to decrease in the first 100 s. For the resistances of $4x10^5$ $\Omega \cdot cm^2$ and $8x10^6$ $\Omega \cdot cm^2$, the potential did not significantly change when the samples were coupled – the potential decreased in 3.6 mV in the former case, and 1.05 mV for the latter. After ca. 1 h of exposure, the potential decreases to ca. -1 V vs. Ag/AgCl for the cases in which the added resistance was $4x10^5$ $\Omega \cdot cm^2$ and $8x10^6$ $\Omega \cdot cm^2$. The potential decrease occurs slightly earlier (ca. 10 min) for the $4x10^5$ $\Omega \cdot cm^2$. Interestingly, the corrosion potential of AA2024, exposed to the same solution as Mg but electrically uncoupled, follows the same behavior: it oscillates around higher potentials at the beginning of the exposure, and then it decreases and stabilizes around -1 V vs. Ag/AgCl. For the uncoupled sample, the time at which the potential decreased was longer, at ca. 3.2 h. As a comparison, the corrosion potential of AA2024 in the same solution, but without the presence of Mg, remained stable around -0.57 V. vs. Ag/AgCl for the entirety of the exposure.

Figure 5.20 (b) shows the transient of the absolute value of the current density as a function of the additional ohmic resistance added between Mg and AA2024. The current measured was negative for all cases, but the absolute value of the current normalized by the AA2024 area was plotted in a log scale to show the wide range of magnitudes of current densities measured in the different cases. The magnitude of the cathodic current density decreases with increasing resistances. At the end of the 12 h exposure, the

cathodic current density measured at AA2024 was -2.6x10^{-2}, -2.0x10^{-2}, -7.0x10^{-3}, -1.0x10^{-3},- 5.9 x10^{-5}, -1.3x10^{-5}, 1.5x10^{-6} and -8x10^{-8} A/cm^2, for the 0, 4, 40, 400, 4000, 4x10^4, 4x10^5, 8x10^6 Ω·cm^2 resistances, respectively.

For the resistances ≤ 400 Ω·cm^2, the current density increases rapidly in the first 10 min, then slowly reaches a steady-state. For the higher resistances, the current density does not change much with time – although it slightly decreases in the first 1 h.

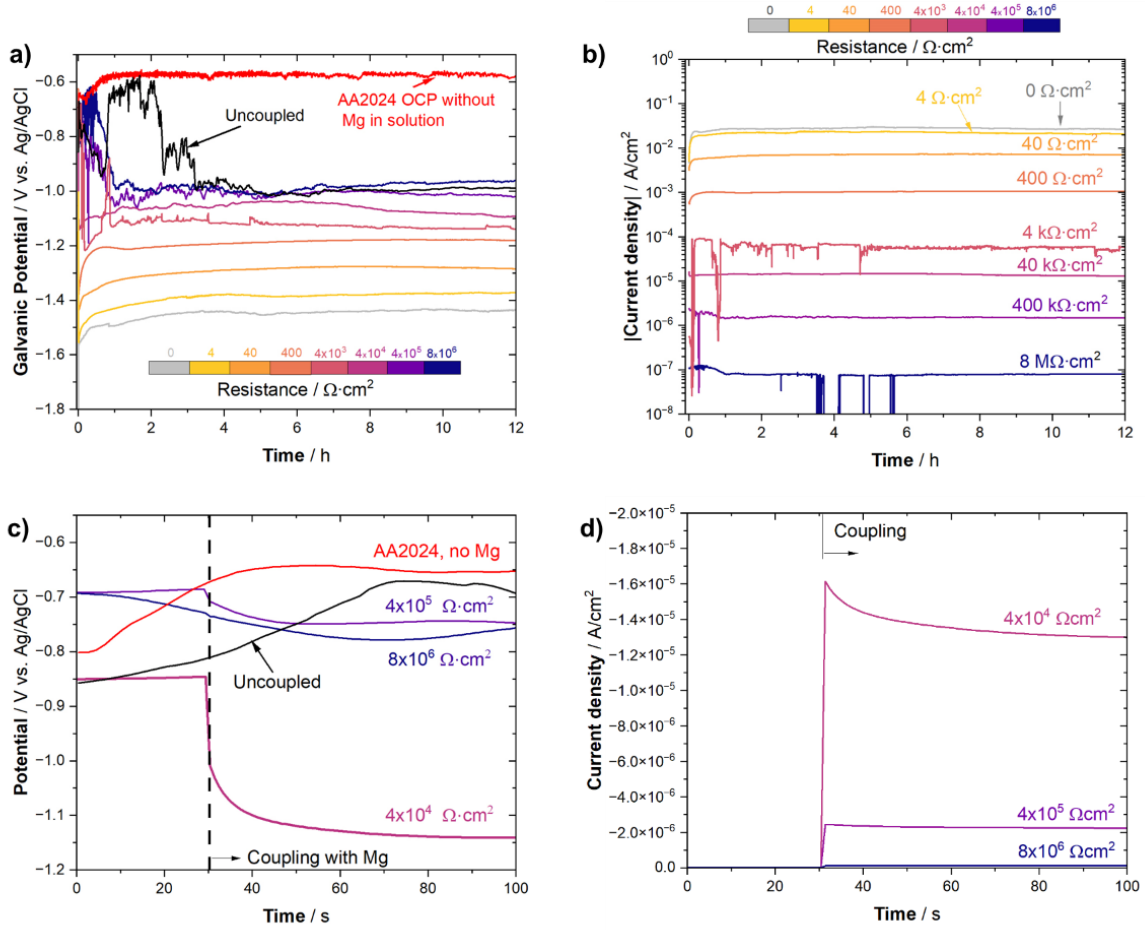

Figure 5.20. (a) Galvanic potential transient as a function of additional ohmic resistance added between AA2024 and Mg. The corrosion potential transient of AA2024 in solution with Mg (uncoupled) and without Mg in 0.9 M NaCl is also shown; (b) galvanic current density measured on AA2024 as a function of the additional ohmic resistance added between AA2024 Mg and. Note that the *absolute* value of the current density is plotted, but the currents values are negative (cathodic); (c) the galvanic potential in the first 100 s for selected cases; (d) the current density in the first 100 s for selected cases.

5.9.4. Images of the AA2024 and Mg surfaces during the galvanic coupling

Figure 5.21 (a) shows images of the galvanically coupled AA2024 and Mg with a 100 kΩ resistor ($4x10^4$ Ω·cm^2) at different times of exposure. Both the surfaces of AA2024 and Mg change with time. After 12 h, the color of AA2024 is darkened, showing a typical appearance of Al-Cu alloys after exposure to caustic solutions [24]. On Mg, corrosion initiates at an edge and spreads over time to the entire surface. Large bubbles are observed on the Mg surface, presumably due to hydrogen evolution. **Figure 5.21** (b) shows the potential and current density measured on AA2024. The potential varies from -1.15 to -1.05 V vs. Ag/AgCl. It slightly increases in the first 6 h of coupling, after which it slightly decreases. The cathodic current density varies from -1.3 to $-1.4 \cdot 10^{-5}$ A/cm^2. The magnitude of the current density slightly increases in the first 6 h, and then it decreases.

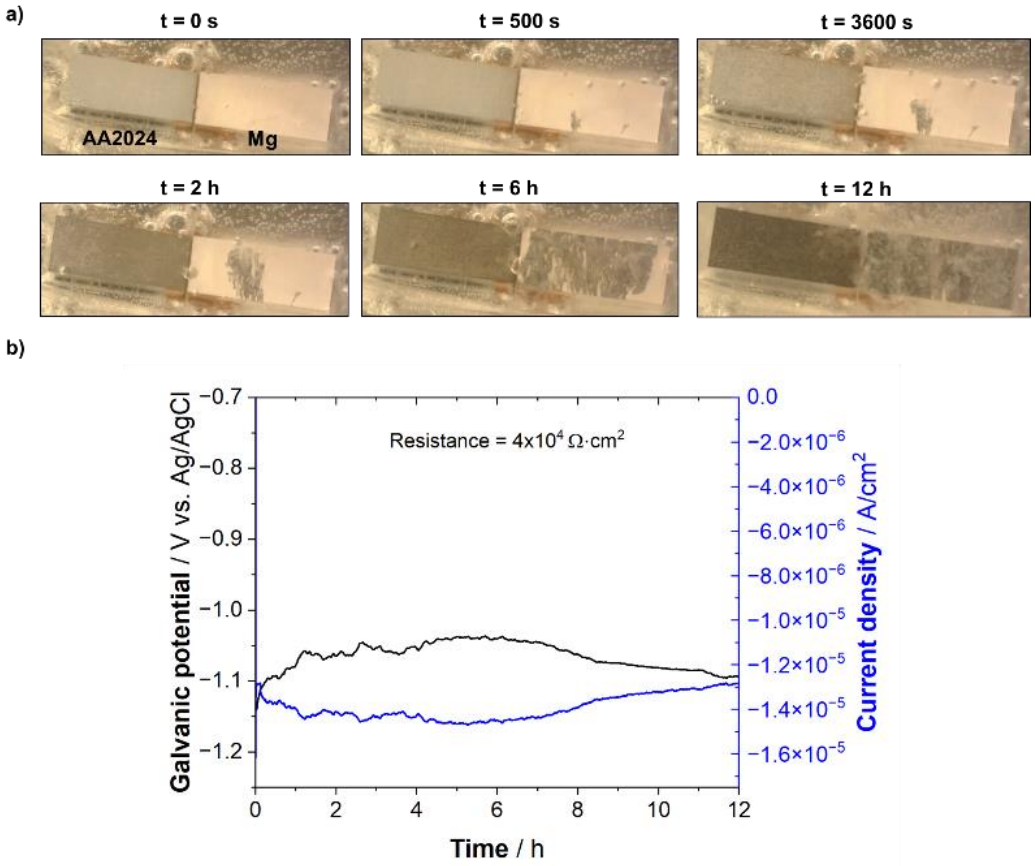

Figure 5.21. (a) images of galvanically coupled AA2024 and Mg with a 100 kΩ resistor ($4x10^4$ Ω·cm^2) at different times of exposure; (b) potential and current density measured for the AA2024 electrode.

5.9.5. Solution pH after 12 h of exposure

Figure 5.22 shows the solution pH after the 12 h exposure of the AA2024 and Mg sample to the 0.9 M NaCl solution as a function of resistance. The pH obtained for the cases in which the resistances were

not used are also plotted in the graph for comparison. In all cases in which the Mg electrode was present in the solution – either coupling or not with the Al alloy – the pH in the solution increased, as the initial pH of the 0.9 M NaCl solution was ca. 6. When an ohmic resistor was not added between AA2024 and Mg (and the only resistance between them was given by the solution resistance), the pH at the end of the 12 h exposure and coupling was 11.6. With the addition of the resistor between AA2024 and Mg, the pH varied from 10.2 to 9.45. In the case in which they were decoupled and corroded at their own corrosion potentials, the pH after 12 h was 10.1. The pH remained near 6 when only AA2024 was exposed to the 0.9 M NaCl solution.

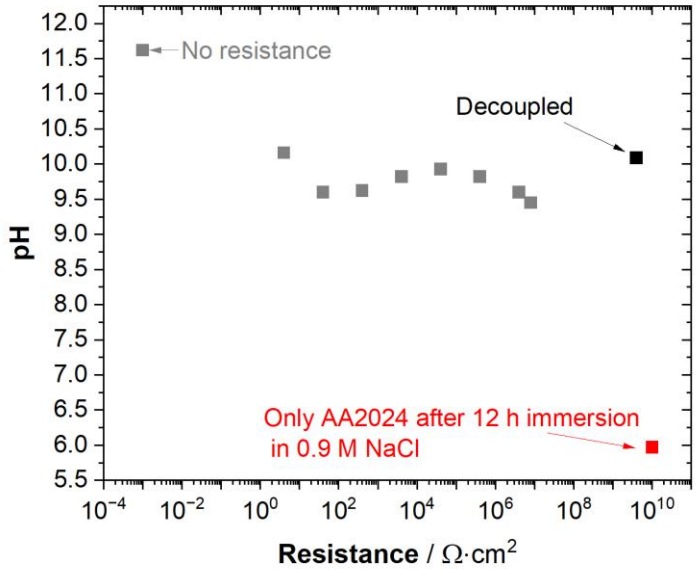

Figure 5.22. Solution pH after 12 h of exposure of the AA2024 and Mg sample, with and without galvanic coupling.

5.9.6. Comparison between the experimental measurements and the modeling results

Figure 5.23 (a) and (b) show the comparison between the galvanic potential and current density, respectively, as a function of resistance, obtained experimentally and by the modeling approaches (Case I and Case II). The potential and current densities measured at the onset of the coupling (t = 0 h) and after the 12 h are shown, along with the values obtained in the transient model at t = 0 and 12 h. The overall trend of the impact of the additional ohmic resistance between the AA2024 and Mg couple is captured in the models. There are higher discrepancies between the experimental and modeling results in the lower resistances.

When Mg and AA2024 are coupled without the addition of a resistor in their electrical connection, the steady-state model agrees well with the potential obtained after 12 h, while the transient model captures better the potential measured in the beginning of the exposure. The current density is underestimated by both models; the transient model predicts the opposite behavior than what was observed experimentally: it calculated a decrease in the current density with time, whereas the measured current density increased after 12 h.

For the resistances between 4 and $4x10^3$ $\Omega \cdot cm^2$, both steady-state and transient models underestimated the galvanic potential and the magnitude of the cathodic current density. The steady-state model agrees well with the current densities measured at t = 0 h. In the highest resistances, the potential measured at the onset of the galvanic coupling is 310 and 225 mV higher than after the 12 h of exposure for the resistances of $4x10^5$ and $8x10^6$ $\Omega \cdot cm^2$, respectively. The steady-state model does not predict the potential decrease, so the potential was significantly overestimated. The transient model captures the potential decrease, but it underestimates the potential obtained after 12 h. The galvanic current densities are in better agreement at the higher resistances.

Figure 5.23 (c) shows the average solution pH obtained by the model (averaged in the electrolyte domain) and the solution pH measured after the 12 h exposures. The model underestimated the pH for the case where there was no resistance between the Mg and AA2024, and overestimated the pH in the cases with the additional ohmic resistances.

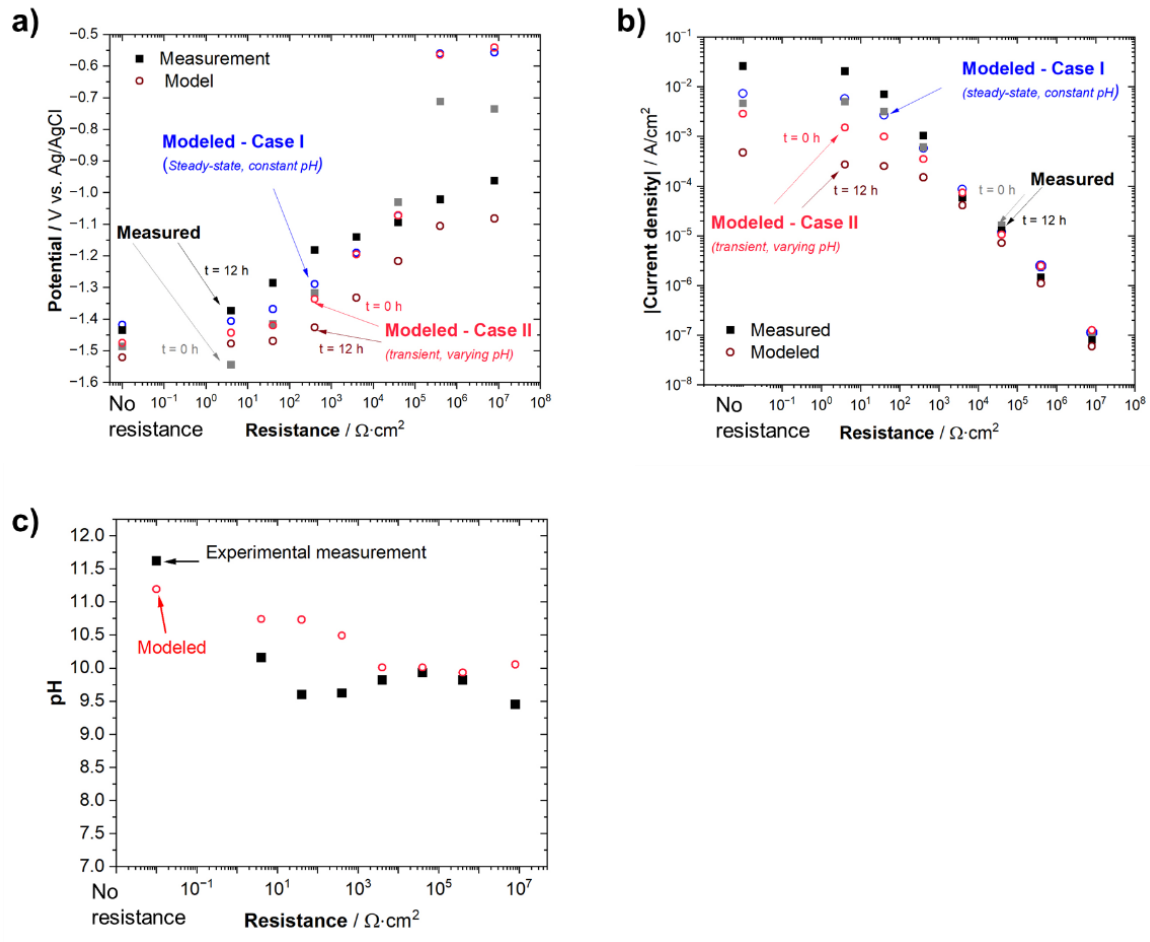

Figure 5.23. Comparison between the experimental and modeled potential (a) and current density (b) at the AA2024 coupled with Mg. The graph shows the experimental values measured at t = 0 and 12 h, and the values calculated at t = 0 and 12 h in the transient model (Case II). In (c), the solution pH measured after the 12 h exposure and the modeled average (in the domain) pH at t = 12 h.

5.9.7. Transient cathodic behavior of AA2024

Figure 5.24 shows the cathodic polarization scan performed on AA2024 in 0.9 M NaCl solution in different conditions. The black curve shows the behavior after 5 min exposure to the NaCl solution (referred to as "control"), at open circuit potential. The blue curve shows the behavior after 12 h of exposure to the 0.9 M NaCl solution at open circuit potential. The red curve shows the polarization behavior after 12 h of exposure to the 0.9 M NaCl solution, but in this case Mg electrode was also exposed to the solution, and both AA2024 and Mg were at their open-circuit potentials.

The open-circuit potential did not change with the exposure, regardless of the condition. However, the longer exposures increased the cathodic kinetics. In comparison to the control, the cathodic kinetics of

AA2024 are substantially faster after exposure to the solution containing the self-corroding Mg. Near the potential ranges in which ORR is the main cathodic reaction, the measured current densities are ca. 20 times faster. The kinetics also changed (to a much lower extent) after 12 h of exposure to the 0.9 M NaCl, but without the self-corroding Mg in the solution. In this case, the region commonly attributed to ORR does not seem mass-transport controlled, as the current increases with the lowering of the potential. At the higher cathodic overpotentials, the current density is slightly increased.

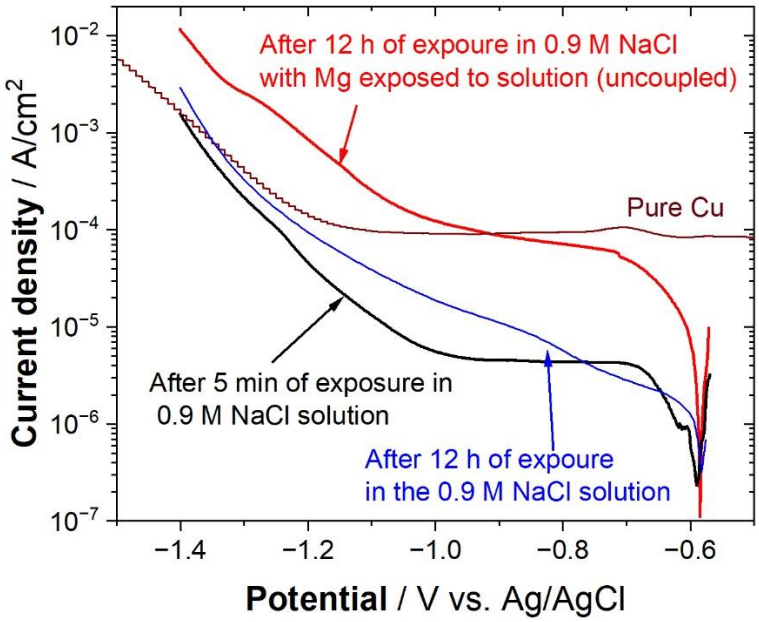

Figure 5.24. Cathodic polarization scan performed on AA2024 in 0.9 M NaCl for different conditions: after 5 min of exposure to the solution; after 12 h exposure to the solution; after 12 h exposure to the solution, in which Mg is also exposed to, but they are not galvanically coupled.

The time dependence of the cathodic kinetics on AA2024 was investigated by potentiostatic measurements. The potentiostatic holds were performed for 12 h in 0.9 M the NaCl solution. **Figure 5.25** shows the absolute value of the cathodic current density as a function of time for different applied potentials. At potentials -1.00 and -1.10 V vs. Ag/AgCl, the cathodic current density is stable during the 12 h. However, the absolute value of the cathodic current density increases significantly with time for the more negative potentials. In -1.18 V vs. Ag/AgCl, the current increases from $-2x10^{-5}$ to $-3x10^{-3}$ A/cm^2 after 12 h – a 150-fold increase. The increase in the cathodic current is faster in more negative potentials.

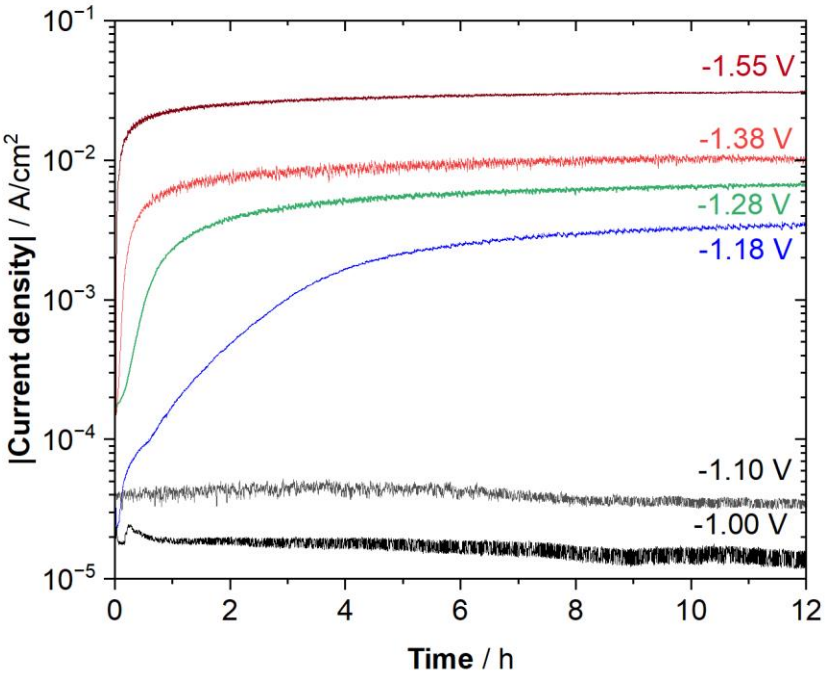

Figure 5.25. Absolute values of the current density of AA2024 as a function of time, measured at different potentials in 0.9 M NaCl.

5.10. Discussion

5.10.1. The models predict well the impact of an additional resistance mediating the galvanic coupling between Mg and AA2024

There was generally a good agreement between the current densities predicted by the model and the current densities measured experimentally via ZRA. In lower resistances, there is a higher discrepancy between the modeling and experimental results. In the lower resistances, the models agree well with the current densities obtained at onset of the galvanic coupling (t = 0 h). However, in the experiments, the current density measured increased with time. In the transient model, the anodic kinetics are dependent on the pH by an exponential expression. Thus, as the time progresses and the pH increases, the total net current decreases because of the increase in the anodic current. In reality, the cathodic current also increases in cases in which AA2024 is either held at low potential or in alkaline solutions, as observed in **Figure 5.24** and **Figure 5.25**. The fact that the transient model does not account for this transient cathodic behavior causes a deviation from the net current measured experimentally.

The models predicted well the resistance above which there was a large shift in the coupled potential at the onset of the galvanic couple. Experimentally, it was observed that for resistances lower than

$4x10^5$ Ω·cm^2, the potential measured at the Al alloy instantaneously decreased with the onset of the galvanic coupling and the measured potential increased steadily with the resistance. At the resistance of $4x10^5$ Ω·cm^2 and $8x10^6$ Ω·cm^2, the rapid decrease in potential with the onset of galvanic coupling was not observed. In the models, the coupled potential increased steadily from -1.42 to -1.07 V vs. Ag/AgCl with the decade of the resistance increasing from 0 to $4x10^4$ Ω·cm^2. Increasing from $4x10^4$ to $4x10^5$ Ω·cm^2, the coupled potential shifted from -1.07 to -0.57 V vs. Ag/AgCl, near the corrosion potential of AA2024 at neutral solutions.

The abrupt change in the potential above a critical resistance is due to the diffusion-limited ORR kinetics. In the diffusion-limited region, the metal behaves as a polarizable electrode - small changes in the current density causes large changes in potential. Thus, if the mixed current falls within or slightly below the ORR limiting current density, the potential can increase abruptly. By comparing the measured current densities calculated in the model using resistances equal or above $4x10^5$ Ω·cm^2, it is possible to see that they are below the diffusion-limited current density observed in the PDS (ca. $4.5x10^{-6}$ A/cm^2). When resistances lower than $4x10^5$ Ω·cm^2 were used, the measured coupled current densities were higher than the diffusion-limited current density and the potential fell within the HER-controlled region.

Because galvanic corrosion takes place by the passage of current between the two metals and the solution as a circuit in series, the position of a hypothetical resistor in this circuit does not change the total current flowing. It is important to note, however, that the experiments and models shown in this section consider the effect of a film resistance only between Mg and AA2024. In a real Mg-rich primer, however, a polymer film could possibly involve Mg particles and insulate them from the solution. In that case, the increase in film resistance would not only diminish the coupling of the metals, but also act as a barrier to Mg corrosion. As shown in **Figure 5.24**, the corrosion of Mg causes the increase in the solution pH, due to the weak hydrolysis of the Mg cations. In the conditions in which the experiment was performed – 1:1 area ratio between Mg and AA2024 – Mg shifted the solution pH to alkaline values. As shown in **Figure 5.24**, even when the two metals are uncoupled, the high pH results in an increased cathodic kinetics of Al, indicating that the changes in solution chemistry as a result of Mg dissolution can alone cause caustic dissolution of the aluminum and copper enrichment of AA2024 surface in the conditions in which the experiment was performed (1:1 Mg and AA2024 area ratio, and a 10 mL volume).

The important role of the resistance provided by the polymer present in the MgRP coating system is not only the mediation of the galvanic current passing between the Mg anodes and the Al substrate, but also by decreasing the rate at which Mg corrodes, as extensively discussed [20,21,23,74,83]. Not only the rapid dissolution causes the fast depletion of the protective pigment, but also leads to a fast increase in the local pH, causing the caustic attack on the Al substrate.

5.10.2. The transient model captures the decrease in the potential at high resistances

The sharp decrease in the measured potential with resistances of $4x10^5$ and $8x10^6$ $\Omega \cdot cm^2$, which was also observed when Mg and AA2024 were decoupled (infinite resistance), can be associated with the pH-induced potential control mechanism [24]. Indeed, the pH of the solutions increased to values near the pH_{crit} (9.86) during the exposures. For the case in which Mg and AA2024 were uncoupled and corroded at their open-circuit potential, the pH rose from 6.00 to 10, above the pH_{crit}. In the absence of Mg in solution, the self-corrosion of AA2024 did not change the solution pH; the pH remained slightly acidic, and the corrosion potential was stable near -0.58 V vs. Ag/AgCl during the entirety of the exposure to 0.9 M NaCl solution. The corrosion of Mg causes an increase in the solution pH, as a result of the weak hydrolysis of the Mg cations and relatively high solubility of $Mg(OH)_2$. Thus, the potential decrease observed at ca. 0.8, 1.0, and 3.2 h likely occurred when the pH at the Al surface reached values near the pH_{crit}, above which the passive current density surpassed the diffusion-limited ORR current density causing the potential shift (**Figure 5.20**-a).

The steady-state model is naturally unable to capture the change in the corrosion behavior of AA2024, as the boundary conditions used to describe its electrochemical behavior do not evolve with time. In the transient model, the pH-dependent boundary conditions developed in [24] and Chapter 3 are used, and the exponential relationship between the anodic passive current density of Al and pH is used. As the model predicts the pH rise in the electrolyte, the decrease in the potential due to the pH-induced potential control mechanism is predicted. The time at which the transition occurs is different in the model, and it occurs at much earlier times. One of the possible reasons why the model predicts a faster drop in potential could be due to the simplified description of Mg corrosion – the model does not account for any possible decrease in Mg dissolution kinetics due to the elevation of pH.

The transient model underestimated the coupled potential in all cases. The underestimation is likely due to the transient in the AA2024 cathodic kinetics in low potentials/alkaline conditions, as observed in the **Figure 5.24** and **Figure 5.25**. As the model did not take into consideration the increase in the cathodic kinetics, but it did take into consideration the increase in the anodic kinetics, the potential is underestimated.

5.10.3. Challenges in modeling the cathodic kinetics of AA2024

Modeling the electrochemical behavior of heterogeneous alloys is complex, as the overall electrochemical behavior is a contribution of the various phases that compose the alloy. The “averaged” electrochemical behavior observed in the bulk alloy depends on the phases present and their relative area ratios. Any changes in their relative area ratios change the overall behavior. In the case of Al-Cu alloys, such as AA2024, the surface composition changes dramatically in alkaline solutions, or under cathodic polarization, which results in local pH increase due to the cathodic reaction products. With the increase in

local pH, the Al matrix dissolves, and the surface becomes enriched in Cu particles of high surface area [5,6,225,226]. Because Cu has better catalytic properties for ORR and HER than an aluminum substrate, and because the surface area increases, the total cathodic current measured on a AA2024 electrode will increase with time, causing an even more intense local alkalinization.

Perhaps the most common approach utilized in FEM models to acquire the boundary conditions is performing potentiodynamic scans in the solution of interest. In the case of a dynamic cathodic behavior such as that of AA2024, this acquired boundary condition will depend strongly on the parameters utilized in the acquisition of the polarization experiments. As an example, **Figure 5.26** shows the polarization behavior of AA2024 obtained by different methods: potentiodynamically with different scan rates (solid lines), and potentiostatically, where each datapoint is acquired after a potential hold for the time indicated. The current density increases with time, and it surpasses the values obtained on a potentiodynamic scan on pure Cu, presumably because of the high surface area of the alkaline etched AA2024. Modeling such a complex and dynamic cathodic behavior with precision is a difficult task, and it makes the utilization of FEM models in the corrosion prediction of Al high-strength alloys more challenging.

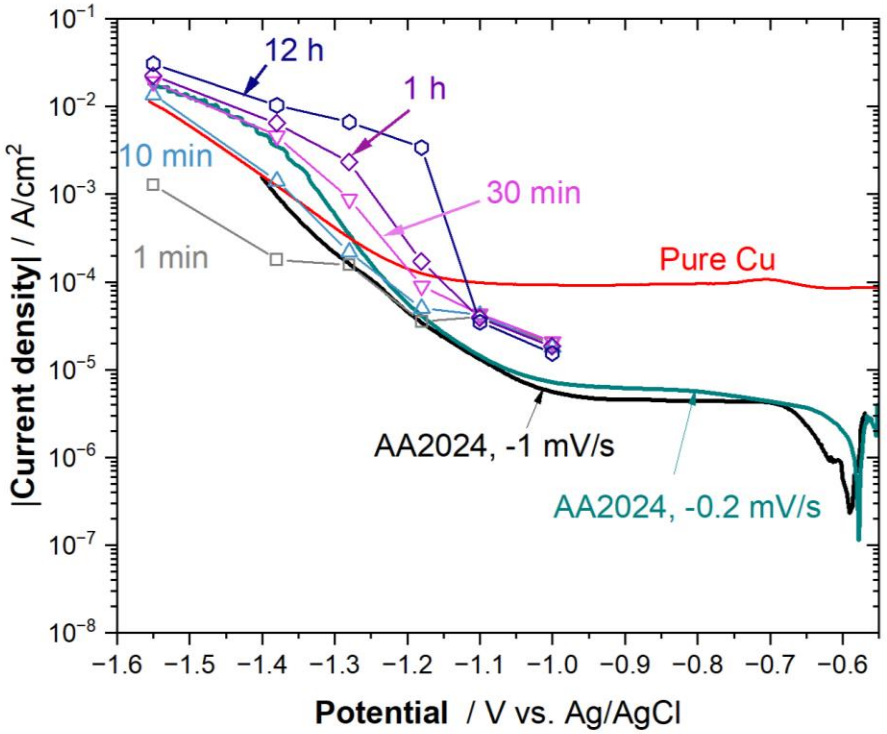

Figure 5.26. Comparison between the polarization behavior of AA2024 obtained via potentiodynamic methods at different scan rates and obtianed potentiostatically at different times. The polarization behavior of Cu obtained via potentiodynamic polarization is also shown.

5.11. Conclusions

In this section, models were used to describe the galvanic behavior of AA2024 and Mg by utilizing static or transient boundary conditions chemistry-dependent boundary conditions, and the modeling results were compared with experimental results. The main conclusions are summarized as follows:

1. The impact of the resistance on the galvanic currents is captured by the models.
2. The potential at the AA2024 decreased even without coupling with Mg, indicating that the pH-induced potential control takes place. By utilizing the pH-dependent anodic boundary conditions on the Al alloy, the model is able to predict the potential shift.
3. The transient model underestimates the coupled current density because it only considers the effect of pH on the anodic kinetics. The long exposure to the alkaline solution caused an increase in the cathodic kinetics of AA2024, which was not captured by this model.
4. Because of the mechanisms of aluminum alkaline dissolution and copper enrichment, the cathodic kinetics of AA2024 are complex and dynamic. The accurate modeling of an AA2024 cathode cannot be accomplished with static boundary conditions and it requires the use of chemistry-dependent cathodic kinetics.

Part III: Application of the pH-dependent anodic boundary conditions to model Al dissolution during cathodic polarization

5.12. Introduction

In Chapter 3 and in Part I and Part II of this chapter, an expression relating the passive current density of AA2024 and pH was empirically acquired from potentiodynamic polarization scans performed in deaerated, alkaline NaCl solutions, following the procedure performed by Santucci, et al. [24]. The expressions describe the increased rate of anodic dissolution kinetics that occur in alkaline solutions, due to the thermodynamic destabilization / increased solubility of the protective oxide/hydroxide film in pH > 9 [1].

The increased solubility at high pH explains the phenomenon of cathodic corrosion, in which an increased rate of *anodic* dissolution of Al is observed at *cathodic* overpotentials. This phenomenon is important during galvanic coupling of Al to less noble metals – such as Mg and Zn. This phenomenon also explains the trenching mechanisms observed due to the dissolution of the Al matrix surrounding cathodic Cu-rich intermetallics, which typically results in the initiation of localized corrosion [6–8,225–227].

In neutral pH, aluminum alloys are protected by a non-conducting oxide/hydroxide film which protects the metallic substrate from the oxidizing solution [22]. At low (pH < 4) and high pH (pH > 9) [1], the solubility of the oxide/hydroxide film increases. Because the equilibrium potential of the Al/Al^{3+} redox pair (E = -1.873 V vs Ag/AgCl) is far below both HER and ORR stability potential ranges, the oxidation of aluminum metal in water is thermodynamically favorable for a wide range of potentials below the open circuit potential of most aluminum alloys.

The dissolution of Al in alkaline solution was described by Moon and Pyun [228,229] as two competing processes occurring at the surface: the electrochemical dissolution of the Al metal and formation of Al hydroxide (Reaction I), and a chemical dissolution of the hydroxide film forming aluminate ($Al(OH)_4^-$), Reaction II:

$$Al + 3OH^- \rightarrow Al(OH)_3 + 3e^- \quad [I]$$

$$Al(OH)_3 + OH^- \rightarrow Al(OH)_4^- \quad [II]$$

Because HER and ORR result in local alkalization of the solution, the chemical dissolution of aluminum hydroxide (Reaction II) can be accelerated when an aluminum alloy is under cathodic polarization, resulting in a high rate of aluminum oxidation. Because the sum of cathodic reactions (HER and/or ORR) and anodic Al oxidation result in a net negative current at the interface, common electrochemical techniques cannot distinguish the two phenomena nor quantify the rate of Al oxidation under cathodic polarization.

A few authors have used a combination of electrochemical and non-electrochemical techniques to characterize this behavior. Baek et al. have used a quartz microbalance in association with electrochemical measurements to quantify Al mass loss under cathodic polarization [230]. The atomic emission spectroelectrochemistry (AESEC) was used to quantify Al oxidation while applying cathodic polarization by connecting a potentiostat-controlled electrochemical flow cell to an ICP-AES apparatus [22,39,40].

Oltra et al. developed an FEM model [52] to calculate the dissolution rate of Al due to local alkalinization to simulate trenching processes occurring around cathodic intermetallic particles. They used a pH-dependent kinetic law, in which the dissolution dependence on pH was expressed in the exchange current density in a Butler-Volmer expression. The issue with this approach resides in the assumption that charge transfer kinetics governs aluminum dissolution, which means that the estimated aluminum dissolution rate will be strongly dependent on potential. The experimental PDS data in alkaline solutions presented in this work (**Figure 5.3**) and in previous literature [24,220,228,231], however, show that aluminum dissolution in alkaline solution remains independent of the applied potential at a high pH. Thus, it can be hypothesized that the chemical dissolution of a thin interfacial layer by Reaction II is likely the rate-determining step.

In this section, the same concept of pH-dependent boundary conditions utilized in previous parts of this chapter is applied in the modeling of aluminum cathodic dissolution, employing a combination of theoretical and experimentally derived boundary conditions. It is hypothesized that the utilization of an empirical relation between passive current density and pH obtained from anodic polarizations can be utilized to describe aluminum dissolution under cathodic polarization, and the results obtained are compared to experimental results in the literature.

5.13. Model description

The model used to simulate the electrolyte chemistry evolution and its impact on the electrochemical reactions occurring on an Al alloy during a potentiodynamic polarization scan was developed. **Figure 5.28** show the model geometry along with a brief description of the conditions used. The use of the Laplace equation, in combination with the transport of minor species, was used to model the charge and mass conservation in the electrolyte.

The electrolyte composition was calculated at each time step and position by using Farday's law to calculate the flux of the ionic species produced as a result of the anodic and cathodic reactions, and by the homogeneous reactions that describe the equilibrium between H^+ and OH^- (water autoionization reaction) and among the Al species (Al hydrolysis reactions), as described in Part I.

5.13.1. Boundary conditions

At the upper boundary, referred to as the counter electrode, a potential was applied. The applied potential varied with time to simulate the scan speed utilized when performing the polarization scans. At the working electrode boundary, the overall electrochemical behavior was described by separate half-cell reactions, as described in Part I. The analysis was also performed for pure Al. The differences between the pure Al and AA2024 boundary conditions were in the description of the anodic kinetics (passive current density vs. pH relationship and pitting potential) and in the value of the ORR limiting current density. The passive current density vs. pH relationship of pure Al was acquired from the literature [24]. The pitting potential ($E_{pit,pure\ Al}$ = -0.65 V vs. Ag/AgCl) was obtained from the average value observed in anodic potentiodynamic polarization scans performed in pure Al deaerated solutions in 0.9 M NaCl. The cathodic boundary conditions used for the pure Al case were the same as those utilized for AA2024, except the ORR limiting current density was adjusted. The ORR limiting current density in pure Al was obtained from experimental cathodic PDS at -0.95 V vs. Ag/AgCl. The same HER kinetic parameters described in Part I were applied to the model (Tafel slope = -118 mV/dec, E_0 = -0.059xpH, and an $i_0 = 10^{-8}$ A/cm^2). **Figure 5.27** shows the anodic (a) and cathodic (b) PDS performed in pure Al at a scan rate of 1 mV/s.

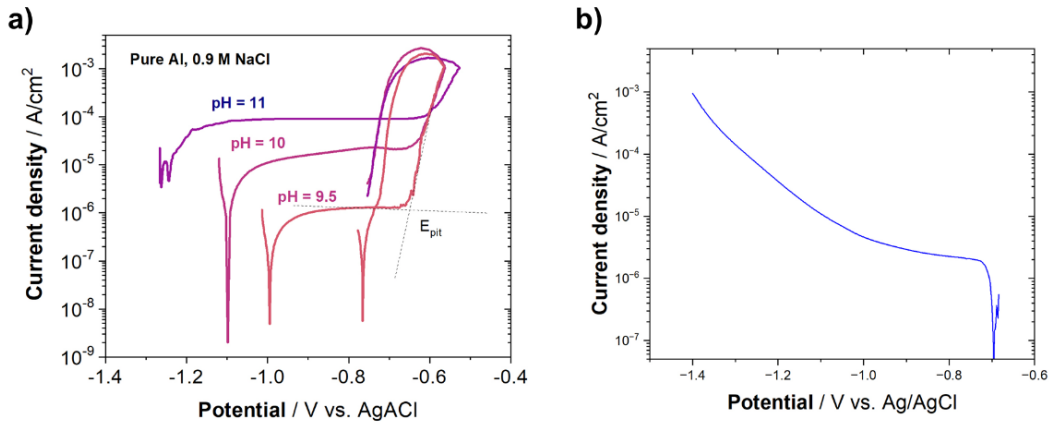

Figure 5.27 (a) PDS performed in pure Al in deaerated 0.9 M NaCl solutions; (b) Cathodic PDS performed in pure Al in 0.9 M NaCl solution.

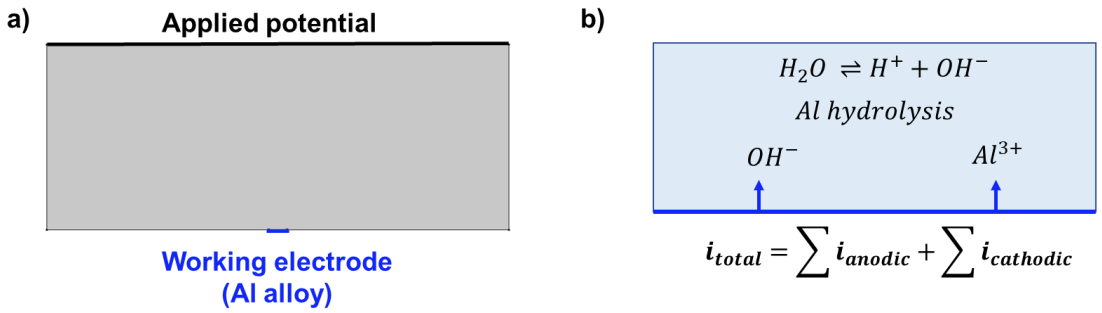

Figure 5.28. (a) Geometry of the model that simulates the electrolyte chemistry changes and its impact on the electrochemical reactions occurring at the Al alloy; (b) schematic drawing of the boundary conditions at the working electrode and the homogeneous reactions occurring in the electrolyte.

5.14. Results and Discussion

5.14.1. Modeled anodic, cathodic, and net current density as a function of applied potential in Pure Al

The boundary conditions defined on the Al surface were used to simulate the behavior of the electrode during a potentiodynamic polarization in a solution of initial pH = 8 (**Figure 5.30**). In this model, the polarization started at an applied potential near the open circuit, and the potential was scanned in the cathodic direction at a constant rate of -0.5 mV/s. The pH calculated on the surface of the electrode during the polarization is indicated on the right y-axis. From the beginning of polarization down to circa -1.0 V, the cathodic current is mainly due to diffusion-limited ORR, and pH increases slowly. As a consequence, Al anodic dissolution also increases slowly. Below -1.0 V, the cathodic current density increases continuously with a charge transfer behavior as a result of HER. The pH increases at a faster pace, and the anodic current density increases due to the faster aluminum dissolution. The anodic current increases as the applied potential decreases until a peak is reached, and it starts decaying. This peak marks the transition point when the rate of electrochemical oxidation becomes slower than chemical dissolution. Thus, the Al dissolution rate-limiting step changes from the chemical dissolution of the passive layer (Reaction II) to charge transfer-controlled Al oxidation.

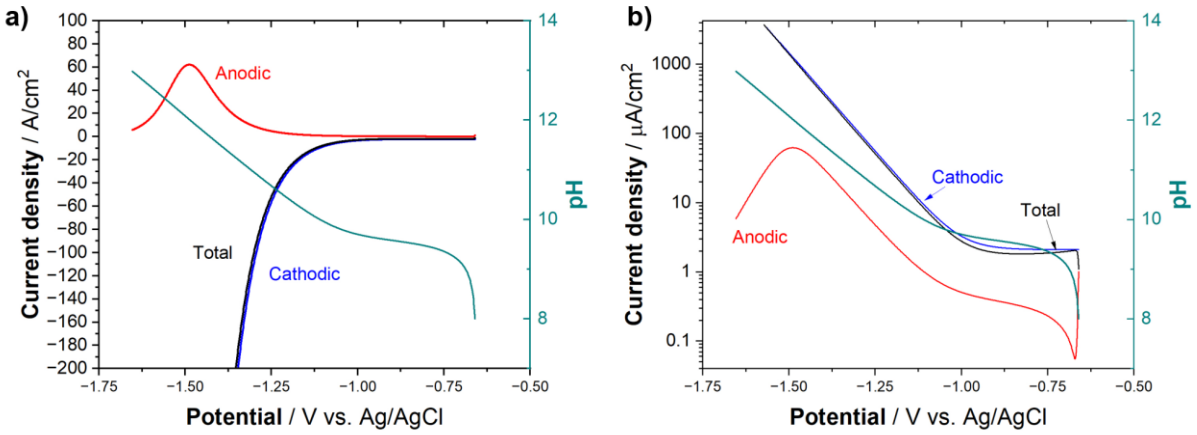

Figure 5.29. Modeled anodic, cathodic and net current density on pure Al under cathodic polarization at a scan rate of -1 mV/s; (a) shows the results in a linear scale and (b) in a log scale.

5.14.2. Comparison between modeled and experimental Al dissolution rates at cathodic potentials

The model results were compared to experimental data reported by Ogle, et al. [22], in which the AESEC technique was used to simultaneously measure the net current and the dissolution rate of Al. Details of the technique can be found in [22,39,40], but, in short, the potentiodynamic polarizations were performed in a flow cell, in which the Al electrodes were exposed to a flowing electrolyte in a flow cell (at a rate of 3 mL/min) coupled to the ICP-AES. The net current density was then measured by the potentiostat, while the dissolution rate was measured with ICP and converted to the anodic current density using Faraday's law. The experiments were performed in 0.5 M NaCl solution.

The applied potential in the model followed the experimental procedure implemented by Ogle, et al. [22]: first, the potential at the counter electrode was fixed at -1.4 V vs. Ag/AgCl for 120 s. Then, a potential sweep was applied at a rate of 0.5 mV/s. The model was performed using the passive current density vs. pH relationship obtained for AA2024 and for pure Al. In the model, the electrolyte flow was not considered, and the electrolyte chemistry was calculated assuming a quiescent electrolyte – one of the major differences between the experimental procedure and the model.

Figure 5.30 (a) shows the modeled and experimental Al dissolution rate as a function of time. The top axis shows the potential at the respective times. Ogle, et al. performed the analysis for pure Al and different Al alloys, and **Figure 5.30** (a) shows the results obtained by the authors for pure Al, AA7050 (an Al-Zn alloy), and AA2214 (an Al-Cu alloy). The calculated pH is shown by the green line and the right y-axis.

The Al dissolution increases in the first 120 s at a potential of -1.4 V vs. Ag/AgCl. The pH increases rapidly from 8 to 11.5. As the potential decreases from -1.4 to the open-circuit potential, the Al dissolution rate decreases, and so does the pH. At potentials slightly more positive than the open-circuit potential, the Al dissolution rate increases rapidly, and the pH decreases sharply.

During the potentiostatic hold at -1.4 V vs. Ag/AgCl, the dissolution of Al increases as the pH at the surface increases due to the fast rate of the cathodic reactions. The rate at which OH^- is produced is faster than the rate at which it diffuses away from the surface of the electrode. As the potential is scanned up towards the open-circuit potential, the rate of the cathodic reactions decreases. As such, the rate of OH^- decreases, and the concentration of OH^- at the surface of the electrodes decreases as OH^- diffuses away from the surface. As potential becomes slightly more anodic than the pitting potential, there is a sharp increase in the Al dissolution rate. The rapid decrease in the pH at the surface is a result of the low cathodic current densities and high anodic current density, which increases the rate of the hydrolysis reactions.

The Al dissolution rates calculated using the pure Al boundary conditions are lower than those obtained using the AA2024 boundary conditions. In comparison to the dissolution rates obtained by the AESEC technique, the model calculates lower dissolution rates at cathodic potentials in comparison to those obtained experimentally in AA7050 and AA2214, but higher than those measured in pure Al. In the model, the peak of the Al dissolution at cathodic potentials is found at the most negative potential (-1.4 V vs. Ag/AgCl), which agrees with the peak (at the cathodic potentials) measured in AA7050. In pure Al, however, the highest dissolution rate was measured at longer times and lower potentials for pure Al. The potential at which there is a rapid increase in the Al dissolution current is in good agreement with those observed by Ogle, et al [22]

Figure 5.30 (b) shows the anodic and net current densities as a function of potential reported by Ogle, et al. and calculated in the model using the AA2024 boundary conditions. The magnitude of the net and Al dissolution current densities was highest at AA2214, followed by AA7050 and pure Al, which is correlated to the Cu content of the alloys (4.5% in AA2214, 2.2% in AA7050, and 0% in pure Al). The modeled current densities using the AA2024 boundary conditions were generally lower than those measured in the AA7050 and AA2214 specimens. In the potential range from -1.4 to -1.3 V vs. Ag/AgCl, the model calculated a higher magnitude of the net current density in comparison to the measurements performed in AA7050.

Qualitatively, the model results agree reasonably well with the experimental measurements, and the model is able to show the “mirroring” behavior of the Al dissolution with the net current density.

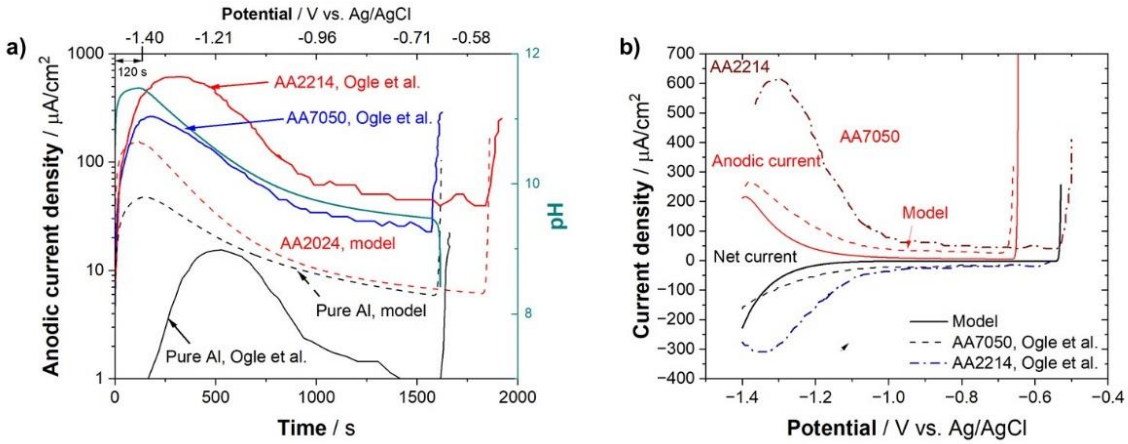

Figure 5.30. Comparison between the anodic and net current densities obtained in the model and obtained experimentally via AESEC technique reported in the literature [22]. In (a), the anodic current density as a function of time and potential is shown; in (b), the anodic and net current densities as a function of potential are shown.

Figure 5.31 shows the relationship between the Al dissolution and the net current density obtained by the model and by Ogle, et al [22]. In all cases, the Al dissolution is a linear function of the net current density, but in the model, the relationship is weaker, as observed by the smaller slopes. The smaller slopes indicate that higher currents are necessary to dissolve the Al oxide film. Ogle et al. found that the slope of the Al dissolution vs. net current density was nearly independent of the alloy system. In the model, different slopes were found because different anodic kinetics were used for the same cathodic kinetics.

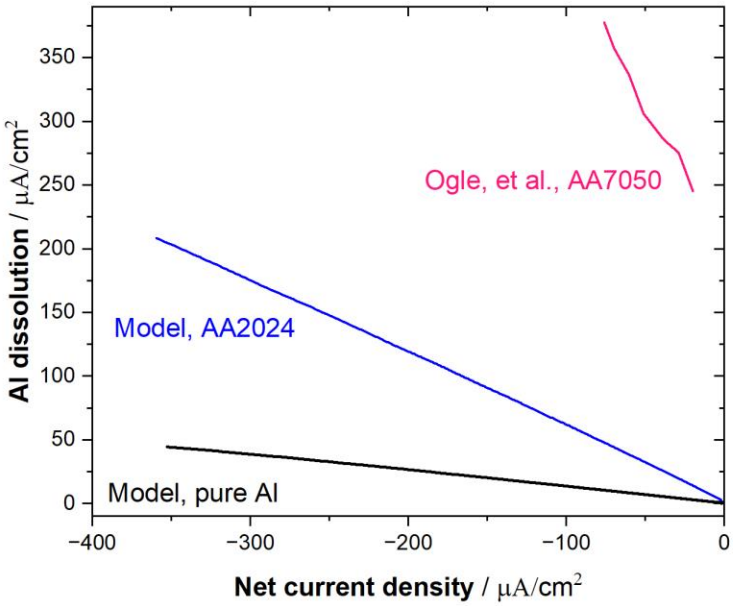

Figure 5.31. Relationship between Al dissolution and net current density calculated in the model and obtained experimentally by Ogle, et al. [22]

There are many factors that can contribute to the discrepancies between the models and the experimental data from Ogle, et al.[22]. A recurring topic is the cathodic kinetics of AA2024, which are oversimplified and underestimated, and explain the lower current densities obtained by the model. Another significant difference is the absence of a flow in the model – convection effects are not considered. The addition of a flow changes the transport of the species from the electrode surface to the bulk solution. Thus, the concentration of the species at the surface of the electrode can be quite different. As the dissolution of the Al involves a chemical reaction, differences in the concentration of the reactant and product species can change the rate of the reaction. Nevertheless, the phenomenon of the increase in the dissolution of Al at cathodic potentials is well captured in the models.

5.14.3. Comparison between modeled and experimental potentiodynamic behavior: apparent Tafel slope of the HER kinetics

The modeled potentiodynamic behavior of the Al was compared to the cathodic PDS performed in pure Al. The model mimicked the polarization scan: the potential applied at the counter electrode decreased from potentials slightly above the OCP (-0.66 V vs. Ag/AgCl) to -1.5 V vs. Ag/AgCl at a scan rate of -1 mV/s.

The model was performed in two different conditions. In one condition, the electrolyte composition was calculated at each time step. The electrolyte composition near the electrode was a result of the transport of the species, electrochemical reactions, and homogeneous reactions occurring in the electrolyte. The interdependence between the electrochemical reactions and chemical conditions at the electrodes was taken into account due to pH dependence in the electrochemical reactions (Al dissolution and equilibrium potential of ORR and HER using Nernst Equation). In the other condition, the chemical changes in the electrolyte were *not* taken into account, and the polarization was performed at a constant pH equal to 7.

Figure 5.32 (a) shows the results obtained by the model and the experimental PDS. There is a good agreement between the experimental and the modeled potentiodynamic behavior for the case in which the electrolyte chemistry is calculated. In the potential range in which ORR is the dominating cathodic reaction, the current densities are necessarily similar to the experimental PDS, as the ORR limiting current density was obtained from the experiment. However, as described in Part I, the HER kinetic parameters were *not* obtained from the experimental measurements. The theoretical Tafel slope of -118 mV/dec and the Nernst Equation were used, and the exchange current density was obtained in the literature [218]. That is, the parameters that describe HER are independent of PDS performed in this work.

There is a good agreement between the modeled and experimental potentiodynamic behavior, but only when the interdependence between the local chemistry and the electrochemical reactions is considered. The model slightly underestimated the current densities, but the transition from the ORR to the HER-controlled kinetics and the slope of the current-potential dependence were in good agreement.

If the changes in the electrolyte chemistry are not considered, and the pH is considered constant (and equal to 7), the HER kinetics is significantly overestimated. **Figure 5.32** (b) shows the equilibrium potential and the overpotential of HER as a function of the applied potential for the two cases modeled: constant pH = 7 and varying pH. If the change in pH due to the cathodic polarization is not considered, the overpotential of HER is overestimated, as the Her equilibrium potential is constant at -0.413 V. However, in reality, the pH is increasing as a result of the cathodic polarization. As a result, the equilibrium potential of HER decreases, and so does the overpotential.

The change in the equilibrium potential with the applied potential explains the higher, “anomalous” Tafel slope observed in the PDS. Interestingly, the model predicted the same slope. As observed in **Figure 5.32** (a), differences in the Tafel slope can lead to significant differences in the magnitude of the current density. Thus, when describing the boundary conditions using experimental Tafel slopes, one should be aware that the values measured will be impacted by local changes in solution chemistry.

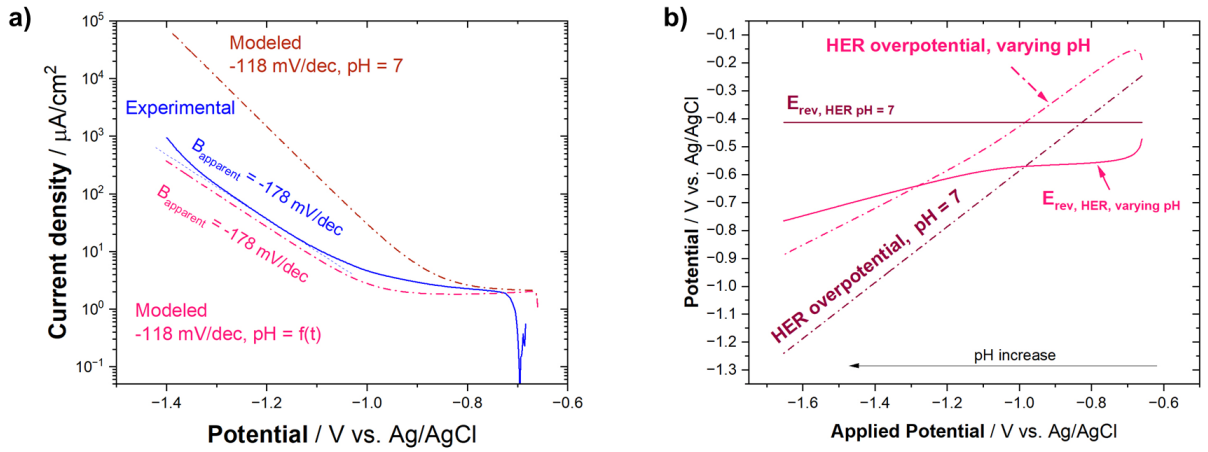

Figure 5.32. (a) Modeled potentiodynamic behavior of pure Al as a result of the sum of the anodic and cathodic reactions obtained in two conditions: i) the pH is calculated at each time step as a result of the heterogeneous and homogeneous reactions and transport; ii) chemistry variations are not accounted for, and the calculations were performed for constant pH of 7; (b) HER overpotential as a function of applied potential considering a constant pH and a varying pH, that is a function of the applied potential.

5.15. Conclusions

The FEM framework developed in this work was applied to model the potentiodynamic behavior of Al in cathodic potentials. The phenomenon of cathodic dissolution is captured by the use of an empirical expression that related the Al passive current density to pH, and the calculation of the chemical conditions at the Al surface as a result of the cathodic polarization. The modeling results agree qualitatively with experimental measurements. The comparison of the predicted cathodic polarization behavior of pure Al with experimental potentiodynamic scans allowed the understanding of the higher apparent Tafel slopes measured in unbuffered solutions. The work shows how FEM models can be used as a tool to understand the local conditions at the electrodes during potentiodynamic polarizations.

Chapter 6. Summary and Recommended Future Work

6.1. Summary

The use of reduced-order models for simulating potential, current density, and species distribution in an electrolyte are attractive due to the high computational costs required to solve the intricate set of highly nonlinear partial differential equations and boundary conditions characteristic of electrochemistry problems. In this work, the applicability of reduced-order models in simulating complex interdependent mechanisms occurring in galvanic systems was tested. The robustness of reduced-order models was increased by the development of chemistry-dependent boundary conditions that are adaptive to changes in the electrolyte composition. The work in this dissertation is summarized below.

The impact of governing equations used to describe charge and mass conservation in an electrolyte cell was verified. The loss in accuracy of the reduced-order models under varying degrees of simplifications was quantified by comparing the potential, current density, and species spatiotemporal distributions calculated by the different methods. Additionally, an improved pseudo-Laplace method, which calculates the spatiotemporal variations in the electrolyte conductivity, was developed. It was found that the reduced-order models could save substantial computational time without significant loss in accuracy in a sufficiently high ratio of non-reactive to electrochemically active species (SER). In these higher ratios, most of the errors in the potential, current density, and species distributions could be attributed to the absence of the diffusion potential term. In lower ratios, the error of the most reduced-order approach (**Lk**) was considerable, but the solutions were improved by the pseudo-Laplace approach (**Lvk**). The critical SER above which the error is below a desired threshold depended on the system and the critical ratio increased for the same percent error in the case in which a sink term simulating a precipitation reactions were modeled. The error associated with the **Lvk** approach was solely due to the absence of the diffusion potential term in the electric field calculation. The approach can be used to investigate the impact of diffusion potential on the potential, current density, and species distributions.

The suitability of the reduced-order models to calculate local current density distributions of an AA7050 and SS316 galvanic couple was verified by comparison with measurements obtained using SVET. It was found that the source of discrepancies associated with the model was mostly due to the boundary conditions used to describe the electrochemical behavior of the alloys and not by the simplified governing equation. Different methods used to generate anodic and cathodic boundary conditions were proposed. The use of an accelerated Al anodic electrochemical kinetics obtained by a modified voltammetry procedure represented its behavior better when coupled with SS316. The FEM model was also used to understand some of the limitations of the SVET technique, and it showed that a significant portion of the current density at the vicinity of the anode and cathode in a co-planar geometry is not measured due to the distance between

the probe and the electrode surface and the inability of the technique in measuring the component of the current density vector that is parallel to the surface.

A comprehensive framework for modeling of chemical and electrochemical protection mechanisms provided by Mg-based primers was developed. Chemistry-dependent boundary conditions were developed to simulate the transient behavior of an Al alloy in an evolving electrolyte chemistry. The framework was used to evaluate the environmental and coating parameters on the effectiveness of the protection mechanisms. For the conditions in which the model was performed, it was found a limiting water layer thickness below which the pH-induced pit repassivation mechanism was not viable because of the combination of high pH necessary for the mechanism to occur under thin films and the buffering capacity of $Mg(OH)_2$, unless the ORR inhibition by the precipitation of the Mg corrosion products were taken into account. The impact of Cl^- on the pH-induced pit repassivation mechanism was evaluated. It was found that the critical pH for the pit repassivation mechanism decreased with increasing Cl^- concentration. The framework was used to evaluate inhibitor parameters that could operate via a combination of the pH-induced potential control mechanism and ORR inhibition.

In the study of galvanic interactions between AA2024 and Mg, it was found that the use of the ORR kinetics in thin films can significant limit the galvanic throwing power, but only for electrolyte films thinner than 25 μm. The resistance provided by the polymeric films was shown to significantly mediate the galvanic interactions between Mg and AA2024 and thus reduced its throwing power. The results of the impact of the resistances were compared with experimental results. It was found that, even when there was a high resistance mediating the galvanic interactions, the potential measured on the Al alloy decreased with exposure to a solution containing the self-corroding Mg. These results corroborate with findings obtained by the modeling framework and indicate that the pH-induced pit repassivation mechanism can serve as an initial mode of protection in the case of high resistance films. The transient model developed with the pH-dependent boundary conditions was able to capture the behavior observed experimentally.

The FEM framework and the chemistry-dependent boundary conditions were used to simulate the behavior of Al alloys at cathodic potentials. The phenomenon of cathodic dissolution was captured by the model, and the results qualitatively agreed with experimental measurements reported in the literature. The model was able to predict the apparent Tafel slope observed in cathodic potentials.

6.2. Recommended Future Work

This work explores innovative methodologies for the development of simplified models that simulate complex corrosion mechanisms. The author suggests a few directions for further exploration, development, application, and validation of these modeling strategies.

- In this study, the impact of the choice of governing equations was assessed on a simplified planar geometry. However, this approach could be applied to occluded geometries, where more intense concentration gradients and electrolyte conductivity gradients are found. Relevant examples include the occluded cells found in pitting and crevice corrosion situations.
- The recent improvements in computational power and commercial software allow for the increase in the complexity of model input and efficient solving of highly nonlinear problems. Thus, it would be interesting to revisit works where the modeling of corrosion problems was performed analytically and required more simplifications as a consequence. Now the implications of these simplifications can be quantified, and the models can be expanded or improved.
- The effect of nucleation and growth of new phases as a result of alteration of chemical equilibria in solution was not included in this work. To use these FEM models as corrosion-predictive tools, the precipitation of corrosion products and their effect on corrosion kinetics should be accounted for in future work. The utilization of deformable meshing should also be implemented to describe the depth of corrosion.
- As mentioned in this work, the cathodic kinetics of Al-Cu alloys are highly dynamic. The cathodic boundary conditions utilized could be improved by implementing existing models that describe the heterogeneous behavior of the cathodic kinetics of aluminum alloys.
- As shown in Chapter 3, FEM can be used to aid the interpretation of advanced electrochemical techniques. This approach could be applied to other electrochemical techniques, such as AESEC, which requires specific experimental conditions that are not necessarily comparable to real service conditions.
- A few aspects of the models developed in this work still require validation. For example, the spatiotemporal distributions of pH and other species in solution are important features of the simulations and their validation could be accomplished by using pH microprobes and or/scanning electrochemical techniques.

References

[1] E. Deltombe, M. Pourbaix, The Electrochemical Behavior of Aluminum, Corrosion. 14 (1958) 16–20. https://doi.org/https://doi.org/10.5006/0010-9312-14.11.16.

[2] J.R. Scully, T.O. Knight, R.G. Buchheit, D.E. Peebles, Electrochemical characteristics of the Al2Cu, Al3Ta and Al3Zr intermetallic phases and their relevancy to the localized corrosion of Al alloys, Corros Sci. 35 (1993) 185–195. https://doi.org/10.1016/0010-938X(93)90148-A.

[3] G.S. Frankel, N. Sridhar, Understanding localized corrosion, Materials Today. 11 (2008) 38–44. https://doi.org/10.1016/S1369-7021(08)70206-2.

[4] A.P. Mouritz, Introduction to aerospace materials, 2012. https://doi.org/10.1533/9780857095152.

[5] G.O. Ilevbare, O. Schneider, R.G. Kelly, J.R. Scully, G.O. Ilevbare, J.R. Scully, R.G. Kelly, In Situ Confocal Laser Scanning Microscopy of AA 2024-T3 Corrosion Metrology: I. Localized Corrosion of Particles, J Electrochem Soc. 151 (2004) B453. https://doi.org/10.1149/1.1764781.

[6] R.G. Buchheit, R.P. Grant, P.F. Hlava, B. Mckenzie, G.L. Zender, Local Dissolution Phenomena Associated with S Phase (Al2CuMg) Particles in Aluminum Alloy 2024-T3, J Electrochem Soc. 144 (1997) 2621–2628. https://doi.org/10.1149/1.1837874/XML.

[7] O. Schneider, G.O. Ilevbare, J.R. Scully, R.G. Kelly, In Situ Confocal Laser Scanning Microscopy of AA 2024-T3 Corrosion Metrology: II. Trench Formation around Particles, J Electrochem Soc. 151 (2004) B465. https://doi.org/10.1149/1.1764781.

[8] M. Olgiati, P.J. Denissen, S.J. Garcia, When all intermetallics dealloy in AA2024-T3: Quantifying early stage intermetallic corrosion kinetics under immersion, Corros Sci. 192 (2021) 109836. https://doi.org/10.1016/J.CORSCI.2021.109836.

[9] J. Soltis, Passivity breakdown, pit initiation and propagation of pits in metallic materials – Review, Corros Sci. 90 (2015) 5–22. https://doi.org/10.1016/J.CORSCI.2014.10.006.

[10] A. Moran, J. Jennings, H. Nee, S. Pearson, B. Clark, R.S. Lillard, Coating breakdown and galvanically accelerated crevice corrosion of aluminum alloys 2024 and 7075 at cadmium-plated steel fasteners, Corrosion. 75 (2019) 484–498. https://doi.org/10.5006/2971.

[11] Z. Feng, G.S. Frankel, Galvanic test panels for accelerated corrosion testing of coated al alloys: Part 2 - Measurement of galvanic interaction, Corrosion. 70 (2014) 95–106. https://doi.org/10.5006/0907.

[12] Z. Feng, G.S. Frankel, W.H. Abbott, C.A. Matzdorf, Galvanic attack of coated al alloy panels in laboratory and field exposure, Corrosion. 72 (2016) 342–355. https://doi.org/10.5006/1899.

[13] R.S. Marshall, R.G. Kelly, A. Goff, C. Sprinkle, Galvanic Corrosion Between Coated Al Alloy Plate and Stainless Steel Fasteners, Part 1: FEM Model Development and Validation, Corrosion. 75 (2019) 1461–1473. https://doi.org/10.5006/3308.

[14] V.N. Rafla, J.R. Scully, Galvanic couple behavior between AA7050-T7451 and stainless steel in a fastener arrangement assessed with coupled multi-electrode arrays under atmospheric exposure conditions, Corrosion. 75 (2019) 12–28. https://doi.org/10.5006/2885.

[15] V.N. Rafla, A.D. King, S. Glanvill, A. Davenport, J.R. Scully, Operando Assessment of Galvanic Corrosion Between Al-Zn-Mg-Cu Alloy and a Stainless Steel Fastener Using X-ray Tomography, Corrosion. 74 (2018) 5–23. https://doi.org/10.5006/2561.

[16] C. Cocke, R.S. Marshall, C. Sprinkle, A. Goff, R.G. Kelly, J.T. Burns, The Effect of Corrosion Location Relative to Local Stresses on the Fatigue Life of Geometrically Complex, Galvanically Corroded AA7075-T6, Corrosion. 78 (2022). https://doi.org/10.5006/3908.

[17] M. Meeusen, L. Zardet, A.M. Homborg, M. Lekka, F. Andreatta, L. Fedrizzi, B. Boelen, H. Terryn, J.M.C. Mol, A Complementary Electrochemical Approach for Time-Resolved Evaluation of Corrosion Inhibitor Performance, J Electrochem Soc. 166 (2019) C3220–C3232. https://doi.org/10.1149/2.0271911jes.

[18] F. Presuel-Moreno, M.A. Jakab, N. Tailleart, M. Goldman, J.R. Scully, Corrosion-resistant metallic coatings, Materials Today. 11 (2008) 14–23. https://doi.org/10.1016/S1369-7021(08)70203-7.

[19] Occupational exposure to hexavalent chromium. Final rule., Fed Regist. (2006).

[20] D. Battocchi, A.M. Simões, D.E. Tallman, G.P. Bierwagen, Electrochemical behaviour of a Mg-rich primer in the protection of Al alloys, Corros Sci. 48 (2006) 1292–1306. https://doi.org/10.1016/j.corsci.2005.04.008.

[21] M.E. McMahon, R.J. Santucci, C.F. Glover, B. Kannan, Z.R. Walsh, J.R. Scully, A Review of Modern Assessment Methods for Metal and Metal-Oxide Based Primers for Substrate Corrosion Protection, Front Mater. 6 (2019) 1–24. https://doi.org/10.3389/fmats.2019.00190.

[22] K. Ogle, M. Serdechnova, M. Mokaddem, P. Volovitch, The cathodic dissolution of Al, Al2Cu, and Al alloys, Electrochim Acta. 56 (2011) 1711–1718. https://doi.org/10.1016/j.electacta.2010.09.058.

[23] B. Kannan, C.F. Glover, H.N. McMurray, G. Williams, J.R. Scully, Performance of a Magnesium-Rich Primer on Pretreated AA2024-T351 in Full Immersion: a Galvanic Throwing

Power Investigation Using a Scanning Vibrating Electrode Technique, J Electrochem Soc. 165 (2018) C27–C41. https://doi.org/10.1149/2.0711802jes.

[24] R. Santucci, J.R. Scully, Mechanistic Framework for Understanding pH-Induced Electrode Potential Control of AA2024-T351 by Protective Mg-Based Pigmented Coatings, J Electrochem Soc. (2020). https://doi.org/10.1149/1945-7111/abbd74.

[25] R.J. Santucci, M.D. Holleman, J.R. Scully, Laboratory accelerated and field exposure testing of MgRP and MgORP on AA2024-T351: Chemical and electrochemical protection effects, Surf Coat Technol. 383 (2020) 125245. https://doi.org/10.1016/j.surfcoat.2019.125245.

[26] A. Collazo, X.R. Nóvoa, C. Pérez, The role of Mg2+ ions in the corrosion behaviour of AA2024-T3 aluminium alloys immersed in chloride-containing environments, Electrochim Acta. 124 (2014) 17–26. https://doi.org/10.1016/j.electacta.2013.10.130.

[27] B. Kannan, A.D. King, J.R. Scully, Effect of pretreatments on Alloy 2024-T351 corrosion protection by magnesium-rich, nonchromium primer (MgRP): Laboratory characterization in full immersion, Corrosion. 71 (2015) 1093–1109. https://doi.org/10.5006/1700.

[28] E. Schindelholz, R.G. Kelly, Wetting phenomena and time of wetness in atmospheric corrosion: a review: , Corrosion Reviews. 30 (2012) 135–170. https://doi.org/doi:10.1515/corrrev-2012-0015.

[29] R.G. Kelly, J.S. Lee, Localized corrosion: Crevice corrosion, Elsevier, 2018. https://doi.org/10.1016/B978-0-12-409547-2.13420-1.

[30] J.R. Galvele, Transport processes in passivity breakdown—II. Full hydrolysis of the metal ions, Corros Sci. 21 (1981) 551–579. https://doi.org/10.1016/0010-938X(81)90009-3.

[31] J.R. Galvele, Transport Processes and the Mechanism of Pitting of Metals, J Electrochem Soc. 123 (1976) 464.

[32] C.F. Glover, T.W. Cain, J.R. Scully, Performance of Mg-Sn surface alloys for the sacrificial cathodic protection of Mg alloy AZ31B-H24, Corros Sci. 149 (2019) 195–206. https://doi.org/10.1016/j.corsci.2019.01.015.

[33] U.-E. Charles-Granville, C.F. Glover, J.R. Scully, R.G. Kelly, Effect of pH and Al Cations on Chromate Inhibition of Galvanic-Induced Corrosion of AA7050-T7451 Macro-Coupled to 316SS, J Electrochem Soc. 168 (2021) 121509. https://doi.org/10.1149/1945-7111/ac412a.

[34] H.S. Isaacs, The measurement of the galvanic corrosion of soldered copper using the scanning vibrating electrode technique, Corros Sci. 28 (1988) 547–558. https://doi.org/10.1016/0010-938X(88)90023-6.

[35] G. Williams, H.N. McMurray, Localized corrosion of magnesium in chloride-containing electrolyte studied by a scanning vibrating electrode technique, J Electrochem Soc. 155 (2008) 340–349. https://doi.org/10.1149/1.2918900.

[36] N.D. Budiansky, F. Bocher, H. Cong, M.F. Hurley, J.R. Scully, Use of Coupled Multi-Electrode Arrays to Advance the Understanding of Selected Corrosion Phenomena, Corrosion. 63 (2007) 537–554.

[37] H. Cong, F. Bocher, N.D. Budiansky, M.F. Hurley, J.R. Scully, Use of coupled multi-electrode arrays to advance the understanding of selected corrosion phenomena, J ASTM Int. 4 (2007) 537–554. https://doi.org/10.1520/JAI101248.

[38] L. Yang, N. Sridhar, O. Pensado, D.S. Dunn, An In-situ galvanically coupled multielectrode array sensor for localized corrosion, Corrosion. 58 (2002) 1004–1014. https://doi.org/10.5006/1.3280789.

[39] M. Serdechnova, P. Volovitch, F. Brisset, K. Ogle, On the cathodic dissolution of Al and Al alloys, Electrochim Acta. 124 (2014) 9–16. https://doi.org/10.1016/j.electacta.2013.09.145.

[40] M. Mokaddem, P. Volovitch, F. Rechou, R. Oltra, K. Ogle, The anodic and cathodic dissolution of Al and Al-Cu-Mg alloy, Electrochim Acta. 55 (2010) 3779–3786. https://doi.org/10.1016/j.electacta.2010.01.079.

[41] S.B. Inman, D. Sur, J. Han, K. Ogle, J.R. Scully, Corrosion behavior of a compositionally complex alloy utilizing simultaneous Al, Cr, and Ti passivation, Corros Sci. 217 (2023) 111138. https://doi.org/10.1016/J.CORSCI.2023.111138.

[42] C.F. Glover, M.J. Hutchinson, V.N. Rafla, L.G. Bland, J.R. Scully, Progress in Development of Electrochemical Methods in Corrosion Science and Engineering, Advances in Electrochemical Techniques for Corrosion Monitoring and Laboratory Corrosion Measurements. (2019) 32–58. https://doi.org/10.1520/stp160920170247.

[43] J. Han, O. Gharbi, Current state of electrochemical techniques and corrosion rate analysis for next-generation materials, Curr Opin Electrochem. 36 (2022) 101131. https://doi.org/10.1016/J.COELEC.2022.101131.

[44] A.C. Bastos, M.C. Quevedo, O. V. Karavai, M.G.S. Ferreira, Review - On the application of the scanning vibrating electrode technique (SVET) to corrosion research, J Electrochem Soc. 164 (2017) C973–C990. https://doi.org/10.1149/2.0431714jes.

[45] K. Ogle, Atomic emission spectroelectrochemistry: Real-time rate measurements of dissolution, corrosion, and passivation, Corrosion. 75 (2019). https://doi.org/10.5006/3336.

[46] B. Gangadharacharya, N. Van Den Steen, M. Haile, Y. Van Ingelgem, H. Terryn, Review on modelling of corrosion under droplet electrolyte for predicting atmospheric corrosion rate, Journal of Materials Science & Technology. 62 (2021) 254–267. https://doi.org/10.1016/j.jmst.2020.04.061.

[47] C. Liu, R.G. Kelly, The Use of Finite Element Models (FEM) in the Modeling of Localized Corrosion, Electrochemical Society Interface. 23 (2014) 0–5.

[48] C. Liu, R.G. Kelly, The Use of Finite Element Models (FEM) in the Modeling of Localized Corrosion, Electrochemical Society Interface. 23 (2014) 0–5.

[49] F. Thébault, B. Vuillemin, R. Oltra, C. Allely, K. Ogle, Protective mechanisms occurring on zinc coated steel cut-edges in immersion conditions, Electrochim Acta. 56 (2011) 8347–8357. https://doi.org/10.1016/j.electacta.2011.07.016.

[50] M. Hayase, T. Hatsuzawa, A. Fukuizumi, Electric field analysis in a dilute solution for the vibrating electrode technique, Journal of Electroanalytical Chemistry. 537 (2002) 173–181. https://doi.org/10.1016/S0022-0728(02)01268-8.

[51] M. Saeedikhani, K.X. Kuah, S. Wijesinghe, S. Vafakhah, D.J. Blackwood, Electrochemical Modeling of Scanning Vibrating Electrode Technique on Scratched and Inclined Surfaces, J Electrochem Soc. 168 (2021) 081505. https://doi.org/10.1149/1945-7111/ac1b50.

[52] R. Oltra, A. Zimmer, C. Sorriano, F. Rechou, C. Borkowski, O. Néel, Simulation of pH-controlled dissolution of aluminium based on a modified Scanning Electrochemical Microscope experiment to mimic localized trenching on aluminium alloys, Electrochim Acta. 56 (2011) 7038–7044. https://doi.org/10.1016/J.ELECTACTA.2011.06.002.

[53] E.J.F. Dickinson, H. Ekström, E. Fontes, COMSOL Multiphysics®: Finite element software for electrochemical analysis. A mini-review, Electrochem Commun. 40 (2014) 71–74. https://doi.org/10.1016/j.elecom.2013.12.020.

[54] J. Newman, K.E. Thomas-Alyea, Electrochemical Systems, Wiley, 2004. https://books.google.com/books?id=vArZu0HM-xYC.

[55] C. Liu, R.G. Kelly, A review of the application of finite element method (FEM) to localized corrosion modeling, Corrosion. (2019). https://doi.org/10.5006/3282.

[56] F. Gagnon, D. Ziegler, M. Fafard, Electrochemical modelling using electroneutrality equation as a constraint, J Appl Electrochem. 44 (2014) 361–381. https://doi.org/10.1007/s10800-014-0662-6.

[57] J. Zhang, M. Klasky, B.C. Letellier, The aluminum chemistry and corrosion in alkaline solutions, Journal of Nuclear Materials. 384 (2009) 175–189. https://doi.org/10.1016/j.jnucmat.2008.11.009.

[58] C. Liu, V.A. Yang, R.G. Kelly, Inhibition of Cathodic Kinetics by Zn 2+ and Mg 2+ on AA7050-T7451 , J Electrochem Soc. 166 (2019) C134–C146. https://doi.org/10.1149/2.0551906jes.

[59] P. Atz Dick, G.H. Knörnschild, L.F.P. Dick, Anodising and corrosion resistance of AA 7050 friction stir welds, Corros Sci. 114 (2017) 28–36. https://doi.org/10.1016/J.CORSCI.2016.10.015.

[60] A. Nishikata, Y. Ichihara, Y. Hayashi, T. Tsuru, Influence of Electrolyte Layer Thickness and pH on the Initial Stage of the Atmospheric Corrosion of Iron, J Electrochem Soc. 144 (1997) 1244–1252. https://doi.org/10.1149/1.1837578.

[61] M.A. Jakab, D.A. Little, J.R. Scully, Experimental and Modeling Studies of the Oxygen Reduction Reaction on AA2024-T3, J Electrochem Soc. 152 (2005) B311. https://doi.org/10.1149/1.1949047.

[62] C. Liu, J. Srinivasan, R.G. Kelly, Electrolyte Film Thickness Effects on the Cathodic Current Availability in a Galvanic Couple, J Electrochem Soc. 164 (2017) C845–C855. https://doi.org/10.1149/2.1641713jes.

[63] U.-E. Charles-Granville, C. Liu, J.R. Scully, R.G. Kelly, An RDE Approach to Investigate the Influence of Chromate on the Cathodic Kinetics on 7XXX Series Al Alloys under Simulated Thin Film Electrolytes, J Electrochem Soc. 167 (2020) 111507. https://doi.org/10.1149/1945-7111/aba935.

[64] O. Guseva, P. Schmutz, T. Suter, O. von Trzebiatowski, Modelling of anodic dissolution of pure aluminium in sodium chloride, Electrochim Acta. 54 (2009) 4514–4524. https://doi.org/10.1016/J.ELECTACTA.2009.03.048.

[65] O. Guseva, J.A. Derose, P. Schmutz, Modelling the early stage time dependence of localised corrosion in aluminium alloys, Electrochim Acta. 88 (2013) 821–831. https://doi.org/10.1016/j.electacta.2012.10.059.

[66] N. Murer, N. Missert, R. Buchheit, Towards the Modeling of Microgalvanic Corrosion in Aluminum Alloys : the Choice of Boundary Conditions, Proceedings of the COMSOL Users Conference. (2008) 1–32.

[67] L. Yin, Y. Jin, C. Leygraf, J. Pan, Numerical Simulation of Micro-Galvanic Corrosion of Al Alloys: Effect of Chemical Factors, J Electrochem Soc. 164 (2017) C768–C778. https://doi.org/10.1149/2.0691713jes.

[68] Y. Wang, L. Yin, Y. Jin, J. Pan, C. Leygraf, Numerical Simulation of Micro-Galvanic Corrosion in Al Alloys: Steric Hindrance Effect of Corrosion Product, J Electrochem Soc. 164 (2017) C1035–C1043. https://doi.org/10.1149/2.0871714jes.

[69] N. Murer, R. Oltra, B. Vuillemin, O. Néel, Numerical modelling of the galvanic coupling in aluminium alloys: A discussion on the application of local probe techniques, Corros Sci. 52 (2010) 130–139. https://doi.org/10.1016/j.corsci.2009.08.051.

[70] L. Yin, Y. Jin, C. Leygraf, J. Pan, A FEM model for investigation of micro-galvanic corrosion of Al alloys and effects of deposition of corrosion products, Electrochim Acta. 192 (2016) 310–318. https://doi.org/10.1016/J.ELECTACTA.2016.01.179.

[71] L. Yin, Y. Jin, C. Leygraf, N. Birbilis, J. Pan, Numerical Simulation of Micro-Galvanic Corrosion in Al Alloys: Effect of Geometric Factors, J Electrochem Soc. 164 (2017) C75–C84. https://doi.org/10.1149/2.1221702JES/XML.

[72] R.S. Marshall, R. Kelly, A. Goff, C. Sprinkle, Galvanic Corrosion Between Coated Al Alloy Plate and Stainless Steel Fasteners, Part 1:“ FEM Model Development and Validation, Corrosion. 75 (2019) 1461–1473. https://doi.org/10.5006/3308.

[73] R.S. Marshall, A. Goff, C. Sprinkle, A. Britos, R. Kelly, Estimating the Throwing Power of SS316 When Coupled with AA7075 Through Finite Element Modeling, Corrosion. 76 (2020) 476–484. https://doi.org/10.5006/3438.

[74] A.D. King, J.S. Lee, J.R. Scully, Finite Element Analysis of the Galvanic Couple Current and Potential Distribution between Mg and 2024-T351 in a Mg Rich Primer Configuration, J Electrochem Soc. 163 (2016) C342–C356. https://doi.org/10.1149/2.0171607jes.

[75] C. Liu, V.N. Rafla, J.R. Scully, R.G. Kelly, Mathematical modeling of potential and current distributions for atmospheric corrosion of galvanic coupling in airframe components, NACE - International Corrosion Conference Series. 2015-Janua (2015).

[76] F. Thébault, B. Vuillemin, R. Oltra, K. Ogle, C. Allely, Investigation of self-healing mechanism on galvanized steels cut edges by coupling SVET and numerical modeling, Electrochim Acta. 53 (2008) 5226–5234. https://doi.org/10.1016/j.electacta.2008.02.066.

[77] S. Palani, T. Hack, J. Deconinck, H. Lohner, Validation of predictive model for galvanic corrosion under thin electrolyte layers: An application to aluminium 2024-CFRP material combination, Corros Sci. 78 (2014) 89–100. https://doi.org/10.1016/j.corsci.2013.09.003.

[78] D. Snihirova, D. Höche, S. Lamaka, Z. Mir, T. Hack, M.L. Zheludkevich, Galvanic corrosion of Ti6Al4V -AA2024 joints in aircraft environment: Modelling and experimental validation, Corros Sci. (2019). https://doi.org/10.1016/j.corsci.2019.04.036.

[79] V. Topa, A.S. Demeter, L. Hotoiu, D. Deconinck, J. Deconinck, A transient multi-ion transport model for galvanized steel corrosion protection, Electrochim Acta. 77 (2012) 339–347. https://doi.org/10.1016/j.electacta.2012.06.021.

[80] M. Saeedikhani, N. Van den Steen, S. Wijesinghe, S. Vafakhah, H. Terryn, D.J. Blackwood, Moving Boundary Simulation of Iron-Zinc Sacrificial Corrosion under Dynamic Electrolyte Thickness Based on Real-Time Monitoring Data, J Electrochem Soc. 167 (2020) 041503. https://doi.org/10.1149/1945-7111/ab7368.

[81] F. Thébault, B. Vuillemin, R. Oltra, C. Allely, K. Ogle, Protective mechanisms occurring on zinc coated steel cut-edges in immersion conditions, Electrochim Acta. 56 (2011) 8347–8357. https://doi.org/10.1016/j.electacta.2011.07.016.

[82] M. Saeedikhani, S. Wijesinghe, D.J. Blackwood, Moving boundary simulation and mechanistic studies of the electrochemical corrosion protection by a damaged zinc coating, Corros Sci. 163 (2020) 108296. https://doi.org/10.1016/j.corsci.2019.108296.

[83] A.D. King, J.S. Lee, J.R. Scully, Galvanic Couple Current and Potential Distribution between a Mg Electrode and 2024-T351 under Droplets Analyzed by Microelectrode Arrays, J Electrochem Soc. 162 (2014) C12–C23. https://doi.org/10.1149/2.0121501jes.

[84] F. Thébault, B. Vuillemin, R. Oltra, C. Allely, K. Ogle, Reliability of numerical models for simulating galvanic corrosion processes, Electrochim Acta. 82 (2012) 349–355. https://doi.org/10.1016/j.electacta.2012.04.068.

[85] C.L. Alexander, C. Liu, A. Alshanoon, R.M. Katona, R.G. Kelly, J. Carpenter, C. Bryan, E. Schindelholz, Oxygen Reduction on Stainless Steel in Concentrated Chloride Media, J Electrochem Soc. 165 (2018) C869–C877. https://doi.org/10.1149/2.0181813jes.

[86] U.-E. Charles-Granville, R.S. Marshall, C. V. Moraes, C.F. Glover, J.R. Scully, R.G. Kelly, Application of Finite Element Modeling to Macro-Galvanic Coupling of AA7050 and SS316: Validation Using the Scanning Vibrating Electrode Technique, J Electrochem Soc. 169 (2022) 031502. https://doi.org/10.1149/1945-7111/ac55ce.

[87] C. Vicente Moraes, R. Santucci, J.R. Scully, R. Kelly, Finite Element Modeling of Chemical and Electrochemical Protection Mechanisms Offered by Mg-Based Organic Coatings to AA2024-T351, J Electrochem Soc. (2021). https://doi.org/10.1149/1945-7111/abfab8.

[88] C. Liu, R.G. Kelly, A review of the application of finite element method (FEM) to localized corrosion modeling, Corrosion. 75 (2019). https://doi.org/10.5006/3282.

[89] D. Höche, Simulation of Corrosion Product Deposit Layer Growth on Bare Magnesium Galvanically Coupled to Aluminum, J Electrochem Soc. 162 (2015) C1–C11. https://doi.org/10.1149/2.0071501JES/XML.

[90] D. Snihirova, D. Höche, S. Lamaka, Z. Mir, T. Hack, M.L. Zheludkevich, Galvanic corrosion of Ti6Al4V -AA2024 joints in aircraft environment: Modelling and experimental validation, Corros Sci. 157 (2019) 70–78. https://doi.org/10.1016/J.CORSCI.2019.04.036.

[91] K.B. Deshpande, Validated numerical modelling of galvanic corrosion for couples: Magnesium alloy (AE44)-mild steel and AE44-aluminium alloy (AA6063) in brine solution, Corros Sci. 52 (2010) 3514–3522. https://doi.org/10.1016/j.corsci.2010.06.031.

[92] F. Thébault, B. Vuillemin, R. Oltra, C. Allely, K. Ogle, Modeling bimetallic corrosion under thin electrolyte films, Corros Sci. 53 (2011) 201–207. https://doi.org/10.1016/j.corsci.2010.09.010.

[93] N. Van den Steen, Y. Gonzalez-Garcia, J.M.C. Mol, H. Terryn, Y. Van Ingelgem, Predicting the effect of droplet geometry and size distribution on atmospheric corrosion, Corros Sci. 202 (2022) 110308. https://doi.org/10.1016/J.CORSCI.2022.110308.

[94] R.M. Katona, J.T. Burns, R.F. Schaller, R.G. Kelly, Insights from electrochemical crack tip modeling of atmospheric stress corrosion cracking, Corros Sci. 209 (2022) 110756. https://doi.org/10.1016/J.CORSCI.2022.110756.

[95] J. Xiao, S. Chaudhuri, Predictive modeling of localized corrosion: An application to aluminum alloys, Electrochim Acta. 56 (2011) 5630–5641. https://doi.org/10.1016/J.ELECTACTA.2011.04.019.

[96] S.M. Sharland, C.P. Jackson, A.J. Diver, A finite-element model of the propagation of corrosion crevices and pits, Corros Sci. 29 (1989) 1149–1166. https://doi.org/10.1016/0010-938X(89)90051-6.

[97] J.W. Fu, S.K. Chan, A Finite Element Method for Modeling Localized Corrosion Cells, Corrosion. 40 (1984). https://doi.org/10.5006/1.3593890.

[98] K.B. Deshpande, Numerical modeling of micro-galvanic corrosion, Electrochim Acta. 56 (2011) 1737–1745. https://doi.org/10.1016/J.ELECTACTA.2010.09.044.

[99] W. Sun, L. Wang, T. Wu, G. Liu, An arbitrary Lagrangian–Eulerian model for modelling the time-dependent evolution of crevice corrosion, Corros Sci. 78 (2014) 233–243. https://doi.org/10.1016/J.CORSCI.2013.10.003.

[100] Y.-C. Chang, R. Woollam, M.E. Orazem, Mathematical Models for Under-Deposit Corrosion, J Electrochem Soc. 161 (2014). https://doi.org/10.1149/2.034406jes.

[101] X. Sun, J. Srinivasan, R.G. Kelly, R. Duddu, Numerical investigation of critical electrochemical factors for pitting corrosion using a multi-species reactive transport model, Corros Sci. 179 (2021) 109130. https://doi.org/10.1016/J.CORSCI.2020.109130.

[102] S.R. Cross, S. Gollapudi, C.A. Schuh, Validated numerical modeling of galvanic corrosion of zinc and aluminum coatings, Corros Sci. 88 (2014) 226–233. https://doi.org/10.1016/J.CORSCI.2014.07.033.

[103] M. Saeedikhani, D.J. Blackwood, Finite Element Method for Thin Film Corrosion Modelling: Where We Advanced and Where We would like to Advance?, Corrosion and Materials Degradation. 1 (2020) 273–281. https://doi.org/10.3390/cmd1020013.

[104] T. Nann, J. Heinze, Simulation in electrochemistry using the finite element method Part 1. The algorithm, Electrochem Commun. 1 (1999) 289–294. www.elsevier.nl/locate/elecom.

[105] S. Sarkar, W. Aquino, Electroneutrality and ionic interactions in the modeling of mass transport in dilute electrochemical systems, Electrochim Acta. 56 (2011) 8969–8978. https://doi.org/10.1016/j.electacta.2011.07.128.

[106] R.S. Marshall, K.A. Define, R.S. Rosner, A. Goff, C. Sprinkle, P.V. Balachandran, R.G. Kelly, Galvanic Corrosion Between Coated Al Alloy Plate and Stainless Steel Fasteners, Part 2: Application of Finite Element Method and Machine Learning to Study Galvanic Current Distributions, Corrosion. 79 (2023). https://doi.org/10.5006/4153.

[107] R. Alkire, T. Bergh, R.L. Sani, Predicting Electrode Shape Change with Use of Finite Element Methods, J Electrochem Soc. 125 (1978) 1981–1988. https://doi.org/10.1149/1.2131340.

[108] COMSOL Multiphysics (v 6.1), Electrochemistry Module User's Guide, Www.Comsol.Com. (n.d.).

[109] L.C. Abodi, J.A. Derose, S. Van Damme, A. Demeter, T. Suter, J. Deconinck, Modeling localized aluminum alloy corrosion in chloride solutions under non-equilibrium conditions: Steps toward understanding pitting initiation, Electrochim Acta. 63 (2012) 169–178. https://doi.org/10.1016/j.electacta.2011.12.074.

[110] C. V. Moraes, R.G. Kelly, A Comparison of FEM Results from the Use of Different Governing Equations in a Galvanic Cell Part I: In the Presence of a Supporting Electrolyte, Electrochim Acta. (n.d.).

[111] R. Alkire, T. Bergh, R.L. Sani, Predicting Electrode Shape Change with Use of Finite Element Methods, J Electrochem Soc. 125 (1978) 1981–1988. https://doi.org/10.1149/1.2131340.

[112] Z.Q. Wu, T. Zhou, K. Wang, J.R. Zhang, X.H. Xia, Current distribution at electrode surfaces as simulated by finite element method, Electrochim Acta. 55 (2010) 4870–4875. https://doi.org/10.1016/j.electacta.2010.03.079.

[113] J.-F. Yan, T. Nguyen, R. White, R. Griffin, Mathematical modeling of the formation of calcareous deposits on cathodically protected steel in seawater, Journal of The Electrochemical Society - J ELECTROCHEM SOC. 140 (1993) 733–741. https://doi.org/10.1149/1.2056150.

[114] J.R. Davis, Corrosion of Aluminum and Aluminum Alloys, 1999. https://doi.org/10.1361/caaa1999p001.

[115] D. Olson, T. Siewert, S. Liu, G. Edwards, ASM Handbook Vol 6: Welding, Brazing, and Soldering, ASM International, New York, 1993.

[116] U.-E. Charles-Granville, C. Liu, J.R. Scully, R.G. Kelly, An RDE Approach to Investigate the Influence of Chromate on the Cathodic Kinetics on 7XXX Series Al Alloys under Simulated Thin Film Electrolytes, J Electrochem Soc. 167 (2020) 111507. https://doi.org/10.1149/1945-7111/aba935.

[117] C.A. Matzdorf, W.C. Nickerson, B.C. Rincon Tronconis, G.S. Frankel, L. Li, R.G. Buchheit, Galvanic test panels for accelerated corrosion testing of coated al alloys: Part 1 - Concept, Corrosion. 69 (2013) 1240–1246. https://doi.org/10.5006/0907.

[118] Z. Feng, G.S. Frankel, Galvanic test panels for accelerated corrosion testing of coated al alloys: Part 2 - Measurement of galvanic interaction, Corrosion. 70 (2014) 95–106. https://doi.org/10.5006/0907.

[119] R.S. Marshall, R. Kelly, A. Goff, C. Sprinkle, Galvanic Corrosion Between Coated Al Alloy Plate and Stainless Steel Fasteners, Part 1:“ FEM Model Development and Validation, Corrosion. 75 (2019) 1461–1473. https://doi.org/10.5006/3308.

[120] R.S. Marshall, A. Goff, C. Sprinkle, A. Britos, R. Kelly, Estimating the Throwing Power of SS316 When Coupled with AA7075 Through Finite Element Modeling, Corrosion. 76 (2020) 476–484. https://doi.org/10.5006/3438.

[121] A. Moran, J. Jennings, H. Nee, S. Pearson, B. Clark, R.S. Lillard, Coating Breakdown and Galvanically Accelerated Crevice Corrosion of Aluminum Alloys 2024 and 7075 at Cadmium-Plated Steel Fasteners, Corrosion Journal. 75 (2019) 484–498.

[122] V. Rafla, A. Davenport, J.R. Scully, Operando Observation of Galvanic Corrosion Between Aluminum Alloy 7050-T7451 and 304 Stainless Steel in a Simulated Fastener Arrangement Using X-Ray Tomography, Corrosion. 71 (2015) 1300–1303. https://doi.org/10.5006/1871.

[123] V.N. Rafla, A.D. King, S. Glanvill, A. Davenport, J.R. Scully, Operando Assessment of Galvanic Corrosion Between Al-Zn-Mg-Cu Alloy and a Stainless Steel Fastener Using X-ray Tomography, Corrosion. 74 (2018) 5–23. https://doi.org/10.5006/2561.

[124] V.N. Rafla, J.R. Scully, Galvanic Couple Behavior Between AA7050-T7451 and Stainless Steel in a Fastener Arrangement Assessed with Coupled Multi-Electrode Arrays Under Atmospheric Exposure Conditions, Corrosion Journal. 75 (2019) 12–28.

[125] W.J. Clark, J.D. Ramsey, R.L. McCreery, G.S. Frankel, A Galvanic Corrosion Approach to Investigating Chromate Effects on Aluminum Alloy 2024-T3, J Electrochem Soc. 149 (2002) B179–B185. https://doi.org/10.1149/1.1469031.

[126] Z. Feng, G.S. Frankel, W.H. Abbott, C.A. Matzdorf, Galvanic attack of coated al alloy panels in laboratory and field exposure, Corrosion. 72 (2016) 342–355. https://doi.org/10.5006/1899.

[127] L. Shi, X. Yang, Y. Song, D. Liu, K. Dong, D. Shan, E.H. Han, Effect of corrosive media on galvanic corrosion of complicated tri-metallic couples of 2024 Al alloy/Q235 mild steel/304 stainless steel, J Mater Sci Technol. 35 (2019) 1886–1893. https://doi.org/10.1016/J.JMST.2019.04.022.

[128] V.N. Rafla, P. Khullar, R.G. Kelly, J.R. Scully, Coupled Multi-Electrode Array with a Sintered Ag / AgCl Counter / Reference Electrode to Investigate AA7050-T7451 and Type 316 Stainless Steel Galvanic Couple under Atmospheric Conditions, J Electrochem Soc. 165 (2018) 562–572. https://doi.org/10.1149/2.1001809jes.

[129] K.B. Deshpande, Experimental investigation of galvanic corrosion: Comparison between SVET and immersion techniques, Corros Sci. 52 (2010) 2819–2826. https://doi.org/10.1016/j.corsci.2010.04.023.

[130] B. Kannan, C.F. Glover, H.N. McMurray, G. Williams, J.R. Scully, Performance of a Magnesium-Rich Primer on Pretreated AA2024-T351 in Full Immersion: a Galvanic Throwing Power Investigation Using a Scanning Vibrating Electrode Technique, J Electrochem Soc. 165 (2018) C27–C41. https://doi.org/10.1149/2.0711802jes.

[131] L.B. Coelho, M.G. Olivier, The inhibition efficiency of different species on AA2024/graphite galvanic coupling models depicted by SVET, Corros Sci. 136 (2018) 292–303. https://doi.org/10.1016/j.corsci.2018.03.015.

[132] J.R. Kish, N. Birbilis, E.M. McNally, C.F. Glover, X. Zhang, J.R. McDermid, G. Williams, Corrosion Performance of Friction Stir Linear Lap Welded AM60B Joints, JOM. 69 (2017) 2335–2344. https://doi.org/10.1007/s11837-017-2504-6.

[133] C.F. Glover, T.W. Cain, J.R. Scully, Performance of Mg-Sn surface alloys for the sacrificial cathodic protection of Mg alloy AZ31B-H24, Corros Sci. 149 (2019) 195–206. https://doi.org/10.1016/j.corsci.2019.01.015.

[134] A.C. Bastos, M.C. Quevedo, O. V. Karavai, M.G.S. Ferreira, Review - On the application of the scanning vibrating electrode technique (SVET) to corrosion research, J Electrochem Soc. 164 (2017) C973–C990. https://doi.org/10.1149/2.0431714jes.

[135] S. Fajardo, C.F. Glover, G. Williams, G.S. Frankel, The Source of Anodic Hydrogen Evolution on Ultra High Purity Magnesium, Electrochim Acta. 212 (2016) 510–521. https://doi.org/10.1016/J.ELECTACTA.2016.07.018.

[136] G. Williams, H.N. McMurray, Localized corrosion of magnesium in chloride-containing electrolyte studied by a scanning vibrating electrode technique, J Electrochem Soc. 155 (2008) 340–349. https://doi.org/10.1149/1.2918900.

[137] C.F. Glover, T.W. Cain, J.R. Scully, Performance of Mg-Sn surface alloys for the sacrificial cathodic protection of Mg alloy AZ31B-H24, Corros Sci. 149 (2019) 195–206. https://doi.org/10.1016/j.corsci.2019.01.015.

[138] M. Saeedikhani, K.X. Kuah, S. Wijesinghe, S. Vafakhah, D.J. Blackwood, Electrochemical Modeling of Scanning Vibrating Electrode Technique on Scratched and Inclined Surfaces, J Electrochem Soc. 168 (2021) 081505. https://doi.org/10.1149/1945-7111/ac1b50.

[139] P. Atz Dick, G.H. Knörnschild, L.F.P. Dick, Anodising and corrosion resistance of AA 7050 friction stir welds, Corros Sci. 114 (2017) 28–36. https://doi.org/10.1016/J.CORSCI.2016.10.015.

[140] N. Murer, R. Oltra, B. Vuillemin, O. Néel, Numerical modelling of the galvanic coupling in aluminium alloys: A discussion on the application of local probe techniques, Corros Sci. 52 (2010) 130–139. https://doi.org/10.1016/j.corsci.2009.08.051.

[141] Z. Haque, B.A. Clark, R.S. Lillard, Experimental Considerations for Modeling Galvanic Corrosion in Aluminum and Its Alloys, Corrosion. 74 (2018) 903–913.

[142] K.B. Deshpande, Validated numerical modelling of galvanic corrosion for couples : Magnesium alloy (AE44)– mild steel and AE44 – aluminium alloy (AA6063) in brine solution, Corros Sci. 52 (2010) 3514–3522. https://doi.org/10.1016/j.corsci.2010.06.031.

[143] F. Thébault, B. Vuillemin, R. Oltra, C. Allely, K. Ogle, Reliability of numerical models for simulating galvanic corrosion processes, Electrochim Acta. 82 (2012) 349–355. https://doi.org/10.1016/j.electacta.2012.04.068.

[144] F. Thébault, B. Vuillemin, R. Oltra, C. Allely, K. Ogle, Modeling bimetallic corrosion under thin electrolyte films, Corros Sci. 53 (2011) 201–207. https://doi.org/10.1016/j.corsci.2010.09.010.

[145] D. Snihirova, D. Höche, S. Lamaka, Z. Mir, T. Hack, M.L. Zheludkevich, Galvanic corrosion of Ti6Al4V -AA2024 joints in aircraft environment: Modelling and experimental validation, Corros Sci. 157 (2019) 70–78. https://doi.org/10.1016/j.corsci.2019.04.036.

[146] O. Dolgikh, A. –S Demeter, S. V. Lamaka, M. Taryba, A.C. Bastos, M.C. Quevedo, J. Deconinck, Simulation of the role of vibration on Scanning Vibrating Electrode Technique

measurements close to a disc in plane, Electrochim Acta. 203 (2016) 379–387. https://doi.org/10.1016/j.electacta.2016.01.188.

[147] C. Liu, R.G. Kelly, A Review of the Application of Finite Element Method (FEM) to Localized Corrosion Modeling, CORROSION. 75 (2019). https://doi.org/doi.org/10.5006/3282.

[148] N. Murer, N.A. Missert, R.G. Buchheit, Finite Element Modeling of the Galvanic Corrosion of Aluminum at Engineered Copper Particles, J Electrochem Soc. 159 (2012) C265. https://doi.org/10.1149/2.102206jes.

[149] H. Wang, F. Presuel, R.G. Kelly, Computational modeling of inhibitor release and transport from multifunctional organic coatings, Electrochim Acta. 49 (2004) 239–255. https://doi.org/10.1016/j.electacta.2003.08.006.

[150] C. V. Moraes, R.J. Santucci, J.R. Scully, R.G. Kelly, Finite Element Modeling of Chemical and Electrochemical Protection Mechanisms Offered by Mg-Based Organic Coatings to AA2024-T351, J Electrochem Soc. 168 (2021) 051505. https://doi.org/10.1149/1945-7111/abfab8.

[151] H.S. Isaacs, The measurement of the galvanic corrosion of soldered copper using the scanning vibrating electrode technique, Corros Sci. 28 (1988) 547–558. https://doi.org/10.1016/0010-938X(88)90023-6.

[152] S. Böhm, H.N. McMurray, S.M. Powell, D.A. Worsley, Photoelectrochemical investigation of corrosion using scanning electrochemical techniques, Electrochim Acta. 45 (2000) 2165–2174. https://doi.org/10.1016/S0013-4686(99)00442-9.

[153] K.B. Deshpande, Validated numerical modelling of galvanic corrosion for couples : Magnesium alloy (AE44)– mild steel and AE44 – aluminium alloy (AA6063) in brine solution, Corros Sci. 52 (2010) 3514–3522. https://doi.org/10.1016/j.corsci.2010.06.031.

[154] C. Liu, P. Khullar, R.G. Kelly, Acceleration of the Cathodic Kinetics on Aluminum Alloys by Aluminum Ions, J Electrochem Soc. 166 (2019) 153–161. https://doi.org/10.1149/2.0571906jes.

[155] Z. Duan, C. Man, C. Dong, Z. Cui, D. Kong, X. Wang, Pitting behavior of SLM 316L stainless steel exposed to chloride environments with di ff erent aggressiveness : Pitting mechanism induced by gas pores, Corros Sci. 167 (2020) 108520. https://doi.org/10.1016/j.corsci.2020.108520.

[156] B. Zaid, D. Saidi, A. Benzaid, S. Hadji, Effects of pH and chloride concentration on pitting corrosion of AA6061 aluminum alloy, Corros Sci. 50 (2008) 1841–1847. https://doi.org/10.1016/j.corsci.2008.03.006.

[157] I.W. Huang, B.L. Hurley, F. Yang, R.G. Buchheit, Dependence on Temperature, pH, and Cl- in the Uniform Corrosion of Aluminum Alloys 2024-T3, 6061-T6, and 7075-T6, Electrochim Acta. 199 (2016) 242–253. https://doi.org/10.1016/j.electacta.2016.03.125.

[158] L. Yin, Y. Jin, C. Leygraf, J. Pan, Numerical Simulation of Micro-Galvanic Corrosion of Al Alloys: Effect of Chemical Factors, J Electrochem Soc. 164 (2017) C768–C778. https://doi.org/10.1149/2.0691713jes.

[159] U.-E. Charles-Granville, C. Glover, J.R. Scully, R. Kelly, Effect of pH and Al Cations on Chromate Inhibition of Galvanic-Induced Corrosion of AA7050-T7451 Macro-Coupled to 316SS, J Electrochem Soc. (2021). https://doi.org/10.1149/1945-7111/ac412a.

[160] E. Deltombe, M. Pourbaix, The Electrochemical Behavior of Aluminum, Corrosion. 14 (1958) 16–20. https://doi.org/https://doi.org/10.5006/0010-9312-14.11.16.

[161] M. Saeedikhani, D.J. Blackwood, Finite Element Method for Thin Film Corrosion Modelling: Where We Advanced and Where We would like to Advance?, Corrosion and Materials Degradation. 1 (2020) 273–281. https://doi.org/10.3390/cmd1020013.

[162] A.S. Demeter, O. Dolgikh, A.C. Bastos, D. Deconinck, S. Lamaka, V. Topa, J. Deconinck, Multi-ion transport and reaction model used to improve the understanding of local current density measurements in presence of concentration gradients around a point current source, Electrochim Acta. 127 (2014) 45–52. https://doi.org/10.1016/j.electacta.2014.02.009.

[163] L.B. Coelho, M.G. Olivier, The inhibition efficiency of different species on AA2024/graphite galvanic coupling models depicted by SVET, Corros Sci. 136 (2018) 292–303. https://doi.org/10.1016/j.corsci.2018.03.015.

[164] A.C. Bastos, M.C. Quevedo, M.G.S. Ferreira, The influence of vibration and probe movement on SVET measurements, Corros Sci. 92 (2015) 309–314. https://doi.org/10.1016/j.corsci.2014.10.038.

[165] N.E.C. Co, J.T. Burns, Effects of macro-scale corrosion damage feature on fatigue crack initiation and fatigue behavior, Int J Fatigue. 103 (2017) 234–247. https://doi.org/10.1016/j.ijfatigue.2017.05.028.

[166] T.Q. Ansari, J.-L. Luo, S.-Q. Shi, Modeling the effect of insoluble corrosion products on pitting corrosion kinetics of metals, Npj Mater Degrad. 3 (2019) 1–12. https://doi.org/10.1038/s41529-019-0090-5.

[167] M. Saeedikhani, N. Van den Steen, S. Wijesinghe, S. Vafakhah, H. Terryn, D.J. Blackwood, Moving Boundary Simulation of Iron-Zinc Sacrificial Corrosion under Dynamic Electrolyte Thickness Based on Real-Time Monitoring Data, J Electrochem Soc. 167 (2020) 041503. https://doi.org/10.1149/1945-7111/ab7368.

[168] L. Yin, Y. Jin, C. Leygraf, J. Pan, A FEM model for investigation of micro-galvanic corrosion of Al alloys and effects of deposition of corrosion products, Electrochim Acta. 192 (2016) 310–318. https://doi.org/10.1016/j.electacta.2016.01.179.

[169] M.E. McMahon, J.R. Scully, J.T. Burns, Mitigation of Intergranular Stress Corrosion Cracking in Al–Mg by Electrochemical Potential Control, JOM. 69 (2017) 1389–1397. https://doi.org/10.1007/s11837-017-2362-2.

[170] C.B. Crane, R.G. Kelly, R.P. Gangloff, Crack chemistry control of intergranular stress corrosion cracking in sensitized Al-Mg, Corrosion. 72 (2016) 242–263. https://doi.org/10.5006/1852.

[171] J. Zhao, L. Xia, A. Sehgal, D. Lu, R.L. McCreery, G.S. Frankel, Effects of chromate and chromate conversion coatings on corrosion of aluminum alloy 2024-T3, Surf Coat Technol. 140 (2001) 51–57. https://doi.org/https://doi.org/10.1016/S0257-8972(01)01003-9.

[172] K.A. Yasakau, M.L. Zheludkevich, M.G.S. Ferreira, Corrosion and corrosion protection of aluminum alloys, Elsevier, Oxford, 2018. https://doi.org/10.1016/B978-0-12-409547-2.13870-3.

[173] H.A. Katzman, G.M. Malouf, R. Bauer, G.W. Stupian, Corrosion-protective chromate coatings on aluminum, Applications of Surface Science. 2 (1979) 416–432. https://doi.org/10.1016/0378-5963(79)90073-4.

[174] M.E. Nanna, G.P. Bierwagen-North, P.A. Philadelphia, Mg-Rich Coatings: A New Paradigm for Cr-Free Corrosion Protection of Al Aerospace Alloys, JCT Research. 1 (2004).

[175] A.D. King, J.R. Scully, Sacrificial anode-based galvanic and barrier corrosion protection of 2024-T351 by a Mg-rich primer and development of test methods for remaining life assessment, Corrosion. 67 (2011) 1–22. https://doi.org/10.5006/1.3590330.

[176] A.D. King, J.S. Lee, J.R. Scully, Galvanic Couple Current and Potential Distribution between a Mg Electrode and 2024-T351 under Droplets Analyzed by Microelectrode Arrays, J Electrochem Soc. 162 (2014) C12–C23. https://doi.org/10.1149/2.0121501jes.

[177] A.D. King, B. Kannan, J.R. Scully, Environmental degradation of a Mg-rich primer in selected field and laboratory environments : part 1-without a topcoat, Corrosion. 70 (2014) 512–535.

[178] R.J. Santucci, B. Kannan, J.R. Scully, Electrochemical diagnostic cycle testing of magnesium and magnesium oxide-pigmented primers on AA2024-T351, Corrosion. 74 (2018) 96–111. https://doi.org/10.5006/2547.

[179] R.J. Santucci, B. Kannan, W. Abbott, J.R. Scully, Magnesium and magnesium oxide primer on AA2024-T351: Assessment of field performance, Corrosion. 73 (2017) 1196–1201. https://doi.org/10.5006/2545.

[180] A.M. Simões, D. Battocchi, D.E. Tallman, G.P. Bierwagen, SVET and SECM imaging of cathodic protection of aluminium by a Mg-rich coating, Corros Sci. 49 (2007) 3838–3849. https://doi.org/10.1016/J.CORSCI.2007.03.045.

[181] J. Lin, C. Orgon, D. Battocchi, G.P. Bierwagen, (Mg rich primer-powder topcoat) coating system for the corrosion protection of Al alloys, Prog Org Coat. 102 (2017) 138–143. https://doi.org/10.1016/j.porgcoat.2016.04.047.

[182] B.J.E. Merten, D. Battocchi, G.P. Bierwagen, Aluminum alloy 2024-T3 protection by magnesium-rich primer with chromate-free metal salts, Prog Org Coat. 78 (2015) 446–454. https://doi.org/10.1016/j.porgcoat.2014.09.013.

[183] A. Simões, D. Battocchi, D. Tallman, G. Bierwagen, Assessment of the corrosion protection of aluminium substrates by a Mg-rich primer: EIS, SVET and SECM study, Prog Org Coat. 63 (2008) 260–266. https://doi.org/10.1016/J.PORGCOAT.2008.02.007.

[184] D. Wang, D. Battocchi, K.N. Allahar, S. Balbyshev, G.P. Bierwagen, In situ monitoring of a Mg-rich primer beneath a topcoat exposed to Prohesion conditions, Corros Sci. 52 (2010) 441–448. https://doi.org/10.1016/j.corsci.2009.10.001.

[185] J. Nie, M.C. Yan, J. Wang, D.E. Tallman, D. Battocchi, G.P. Bierwagen, Cathodic Corrosion Protection Performance of Mg-Rich Primers: Effect of Pigment Shape and Pigment Volume Concentration, ECS Trans. C (2010) 261–275. https://doi.org/10.1149/1.3453621.

[186] S.S. Pathak, M.D. Blanton, S.K. Mendon, J.W. Rawlins, Investigation on dual corrosion performance of magnesium-rich primer for aluminum alloys under salt spray test (ASTM B117) and natural exposure, Corros Sci. 52 (2010) 1453–1463. https://doi.org/10.1016/j.corsci.2009.11.032.

[187] R.J. Santucci, B. Kannan, W. Abbott, J.R. Scully, Scientific investigation of the corrosion performance of magnesium and magnesium oxide primers on Al alloy 2024-T351 in field exposures, Corrosion. 75 (2019) 440–456. https://doi.org/10.5006/2879.

[188] R.J. Santucci, M.E. McMahon, J.R. Scully, Utilization of chemical stability diagrams for improved understanding of electrochemical systems: evolution of solution chemistry towards equilibrium, Npj Mater Degrad. 2 (2018) 1. https://doi.org/10.1038/s41529-017-0021-2.

[189] J.R. Scully, T.O. Knight, R.G. Buchheit, D.E. Peebles, Electrochemical characteristics of the Al2Cu, Al3Ta and Al3Zr intermetallic phases and their relevancy to the

localized corrosion of Al alloys, Corros Sci. 35 (1993) 185–195. https://doi.org/10.1016/0010-938X(93)90148-A.

[190] ASTM International, Standard Practice for Operating Salt Spray (FOG) Apparatus., Water (Basel). 03 (2003) 1–15. https://doi.org/10.1520/B0117.

[191] J. Lin, D. Battocchi, G.P. Bierwagen, Degradation of Magnesium-Rich Primers over AA2024-T3 During Constant Immersion in Different Solutions, Corrosion. 73 (2017) 408–416. https://doi.org/10.5006/2216.

[192] A. Turnbull, D.H. Ferriss, Mathematical modelling of the electrochemistry in corrosion fatigue cracks in structural steel cathodically protected in sea water, Corros Sci. 26 (1986) 601–628. https://doi.org/10.1016/0010-938X(86)90027-2.

[193] W. Sun, G. Liu, L. Wang, T. Wu, Y. Liu, An arbitrary Lagrangian-Eulerian model for studying the influences of corrosion product deposition on bimetallic corrosion, Journal of Solid State Electrochemistry. 17 (2013) 829–840. https://doi.org/10.1007/s10008-012-1935-9.

[194] A. Geochemistry, L. Emk, R. Carman, L.E. Bågander, R. Carman, A. Geochemistry, L. Emk, R. Carman, In situ determination of the apparent solubility product of amorphous iron sulphide, Applied Geochemistry. 9 (1994) 379–386. https://doi.org/10.1016/0883-2927(94)90060-4.

[195] W.H. Hartt, C.H. Culberson, S.W. Smith, Calcareous Deposits on Metal Surfaces in Seawater - a Critical Review., Corrosion. 40 (1984) 609–618. https://doi.org/10.5006/1.3581927.

[196] M. Mokaddem, P. Volovitch, F. Rechou, R. Oltra, K. Ogle, The anodic and cathodic dissolution of Al and Al-Cu-Mg alloy, Electrochim Acta. 55 (2010) 3779–3786. https://doi.org/10.1016/j.electacta.2010.01.079.

[197] J. Sinko, Challenges of chromate inhibitor pigments replacement in organic coatings, Prog Org Coat. 42 (2001) 267–282. https://doi.org/10.1016/S0300-9440(01)00202-8.

[198] S.M. Moon, S.I. Pyun, The corrosion of pure aluminium during cathodic polarization in aqueous solutions, Corros Sci. 39 (1997) 399–408. https://doi.org/10.1016/S0010-938X(97)83354-9.

[199] B. Kannan, D.M. Wolanski, J.R. Scully, Performance of a magnesium-rich primer on pretreated AA2024-T351 in selected laboratory and field environments: Anodization pretreatment, Corrosion. 74 (2018) 654–668. https://doi.org/10.5006/2424.

[200] V.N. Rafla, P. Khullar, R.G. Kelly, J.R. Scully, Coupled Multi-Electrode Array with a Sintered Ag/AgCl Counter/Reference Electrode to Investigate AA7050-T7451 and Type 316 Stainless Steel Galvanic Couple under Atmospheric Conditions, J Electrochem Soc. 165 (2018) C562–C572. https://doi.org/10.1149/2.1001809jes.

[201] A.D. King, N. Birbilis, J.R. Scully, Accurate electrochemical measurement of magnesium corrosion rates; A combined impedance, mass-loss and hydrogen collection study, Electrochim Acta. 121 (2014) 394–406. https://doi.org/10.1016/j.electacta.2013.12.124.

[202] R.G. Buchheit, L.P. Montes, M.A. Martinez, J. Michael, P.F. Hlava, The Electrochemical Characteristics of Bulk-Synthesized Al2CuMg, J Electrochem Soc. 146 (1999) 4424–4428. https://doi.org/10.1149/1.1392654.

[203] N. Birbilis, R.G. Buchheit, Electrochemical Characteristics of Intermetallic Phases in Aluminum Alloys, J Electrochem Soc. 152 (2005) B140. https://doi.org/10.1149/1.1869984.

[204] G.O. Ilevbare, O. Schneider, R.G. Kelly, J.R. Scully, G.O. Ilevbare, J.R. Scully, R.G. Kelly, In Situ Confocal Laser Scanning Microscopy of AA 2024-T3 Corrosion Metrology, J Electrochem Soc. 151 (2004) B465. https://doi.org/10.1149/1.1764781.

[205] M. Jönsson, D. Persson, D. Thierry, Corrosion product formation during NaCl induced atmospheric corrosion of magnesium alloy AZ91D, Corros Sci. (2007). https://doi.org/10.1016/j.corsci.2006.08.004.

[206] R. Lindström, J.-E. Svensson, L.-G. Johansson, The Influence of Carbon Dioxide on the Atmospheric Corrosion of Some Magnesium Alloys in the Presence of NaCl, J Electrochem Soc. 149 (2002) B103. https://doi.org/10.1149/1.1452115.

[207] C.F. Baes, R.E. Mesmer, The Hydrolysis of Cations, Wiley, 1976.

[208] W. Sun, G. Liu, L. Wang, Y. Li, A mathematical model for modeling the formation of calcareous deposits on cathodically protected steel in seawater, Electrochim Acta. 78 (2012) 597–608. https://doi.org/10.1016/j.electacta.2012.06.056.

[209] C.R. Bryan, A.W. Knight, R.M. Katona, A.C. Sanchez, E.J. Schindelholz, R.F. Schaller, Physical and chemical properties of sea salt deliquescent brines as a function of temperature and relative humidity, Science of the Total Environment. 824 (2022). https://doi.org/10.1016/j.scitotenv.2022.154462.

[210] S. Il Pyun, E.J. Lee, Effect of halide ion and applied potential on repassivation behaviour of Al-1 wt.%Si-0.5 wt.%Cu alloy, Electrochim Acta. 40 (1995) 1963–1970. https://doi.org/10.1016/0013-4686(94)00309-O.

[211] P.M. Natishan, W.E. O'Grady, Chloride Ion Interactions with Oxide-Covered Aluminum Leading to Pitting Corrosion: A Review, J Electrochem Soc. 161 (2014) C421–C432. https://doi.org/10.1149/2.1011409jes.

[212] W.J. Lee, S. Il Pyun, Effects of hydroxide ion addition on anodic dissolution of pure aluminium in chloride ion-containing solution, Electrochim Acta. 44 (1999) 4041–4049. https://doi.org/10.1016/S0013-4686(99)00164-4.

[213] D. Cicolin, M. Trueba, S.P. Trasatti, Effect of chloride concentration, pH and dissolved oxygen, on the repassivation of 6082-T6 Al alloy, Electrochim Acta. 124 (2014) 27–35. https://doi.org/10.1016/j.electacta.2013.09.003.

[214] D. Cicolin, M. Trueba, S.P. Trasatti, Effect of chloride concentration, pH and dissolved oxygen, on the repassivation of 6082-T6 Al alloy, Electrochim Acta. 124 (2014) 27–35. https://doi.org/10.1016/j.electacta.2013.09.003.

[215] H.-J. Lee, I.-J. Park, S.-R. Choi, J.-G. Kim, Effect of Chloride on Anodic Dissolution of Aluminum in 4 M NaOH Solution for Aluminum-Air Battery, J Electrochem Soc. 164 (2017) A549–A554. https://doi.org/10.1149/2.0171704jes.

[216] Z. Szklarska-Smialowska, Pitting corrosion of aluminum, Corros Sci. 41 (1999) 1743–1767. https://doi.org/10.1016/S0010-938X(99)00012-8.

[217] Effects of Cl-, No3, So3 ions on the anodic dissolution of pure Aluminum, (n.d.).

[218] S. Trasatti, Work function, electronegativity, and electrochemical behaviour of metals: III. Electrolytic hydrogen evolution in acid solutions, J Electroanal Chem Interfacial Electrochem. 39 (1972) 163–184. https://doi.org/10.1016/S0022-0728(72)80485-6.

[219] C. V. Moraes, R.J. Santucci, J.R. Scully, R.G. Kelly, Finite Element Modeling of Chemical and Electrochemical Protection Mechanisms Offered by Mg-Based Organic Coatings to AA2024-T351, J Electrochem Soc. 168 (2021) 051505. https://doi.org/10.1149/1945-7111/abfab8.

[220] S.I. Pyun, S.M. Moon, S.H. Ahn, S.S. Kim, Effects of Cl−, NO− 3 and SO2− 4 ions on anodic dissolution of pure aluminum in alkaline solution, Corros Sci. 41 (1999) 653–667. https://doi.org/10.1016/S0010-938X(98)00132-2.

[221] B.E. Wilde, CRITICAL APPRAISAL OF SOME POPULAR LABORATORY ELECTROCHEMICAL TESTS FOR PREDICTING THE LOCALIZED CORROSION RESISTANCE OF STAINLESS ALLOYS IN SEA WATER., Corrosion. 28 (1972) 283–291. https://doi.org/10.5006/0010-9312-28.8.283.

[222] I.W. Huang, B.L. Hurley, F. Yang, R.G. Buchheit, Dependence on Temperature, pH, and Cl- in the Uniform Corrosion of Aluminum Alloys 2024-T3, 6061-T6, and 7075-T6, Electrochim Acta. 199 (2016) 242–253. https://doi.org/10.1016/j.electacta.2016.03.125.

[223] B.J.E. Merten, D. Battocchi, G.P. Bierwagen, Aluminum alloy 2024-T3 protection by magnesium-rich primer with chromate-free metal salts, Prog Org Coat. 78 (2015) 446–454. https://doi.org/10.1016/j.porgcoat.2014.09.013.

[224] C.E. Paul L. Brown, Hydrolysis of Metal Ions, Wiley Vch, 2016. https://doi.org/10.1002/9783527656189.

[225] R.G. Buchheit, M.A. Martinez, L.P. Montes, Evidence for Cu Ion Formation by Dissolution and Dealloying the Al[sub 2]CuMg Intermetallic Compound in Rotating Ring-Disk Collection Experiments, J Electrochem Soc. 147 (2000) 119. https://doi.org/10.1149/1.1393164/XML.

[226] S. Lebouil, J. Tardelli, E. Rocca, P. Volovitch, K. Ogle, Dealloying of Al2Cu, Al7Cu2Fe, and Al2CuMg intermetallic phases to form nanoparticulate copper films, Materials and Corrosion. 65 (2014) 416–424. https://doi.org/10.1002/MACO.201307550.

[227] A.E. Hughes, R. Parvizi, M. Forsyth, Microstructure and corrosion of AA2024, Corrosion Reviews. 33 (2015) 1–30. https://doi.org/10.1515/corrrev-2014-0039.

[228] S. Il Pyun, S.M. Moon, Corrosion mechanism of pure aluminium in aqueous alkaline solution, Journal of Solid State Electrochemistry. 4 (2000) 267–272. https://doi.org/10.1007/s100080050203.

[229] S.M. Moon, S.I. Pyun, The corrosion of pure aluminium during cathodic polarization in aqueous solutions, Corros Sci. 39 (1997) 399–408. https://doi.org/10.1016/S0010-938X(97)83354-9.

[230] Y. Baek, G.S. Frankel, Electrochemical Quartz Crystal Microbalance Study of Corrosion of Phases in AA2024, J Electrochem Soc. 150 (2003) B1. https://doi.org/10.1149/1.1524172/XML.

[231] S.-M. Moon, S.-I. Pyun, The formation and dissolution of anodic oxide ®lms on pure aluminium in alkaline solution, n.d.